

TNO-report
NITG 00-223-B

Transport of Radionuclides disposed of in Clay of Tertiary Origin (TRACTOR)

Nederlands Instituut voor
Toegepaste Geowetenschappen TNO Final report
Archiefexemplaar

Date

October 2000

Author(s)

A.F.B. Wildenborg
B. Orlic
G. de Lange
C.S. de Leeuw
W. Zijl
F. van Weert (TUD)
E.J.M. Veling (TUD)
S. de Cock (UCL)
J.F. Thimus (UCL)
C. Lehnen-de Rooij (GeoDelft)
E.J. den Haan (GeoDelft)

Terrein University College Utrecht
Kriekenpitplein 18 and 25
P.O.Box 80015
3508 TA Utrecht
The Netherlands

Project number

005.70095

All rights reserved.

No part of this publication may be reproduced and/or published by print, photoprint, microfilm of any other means without the previous written consent of TNO.


In case this report was drafted on instructions, the rights and obligations of contracting parties are subject to either the Standard Conditions for Research Instructions given to TNO, or the relevant agreement concluded between the contracting parties. Submitting the report for inspection to parties who have a direct interest is permitted.

© 2000 TNO


Principal

Ministry of Economic Affairs

Approved

I. Ritsema 

Project manager

A.F.B. Wildenborg 



Uitgebreide samenvatting

Terughaalbaarheid van radioactief afval dat is opgeslagen in klei of steenzout, is een centraal onderzoeksthema in Fase 1 van het CORA Programma. Uit technische overwegingen is de gegarandeerde periode van terughaalbaarheid begrensd. Het geologisch barrièresysteem zal uiteindelijk in staat moeten zijn om het opgeborgen afval voor lange tijd afdoende van de biosfeer te isoleren. Dit wordt ook wel het 'fail-safe' mechanisme genoemd. Het project TRAKTOR is gericht op de geologische stabiliteit van klei op de middellange termijn, een tijdspanne van enige 100.000-en jaren omvattend. De periode van terughaalbaarheid van het radioactieve afval is hierin buiten beschouwing gelaten.

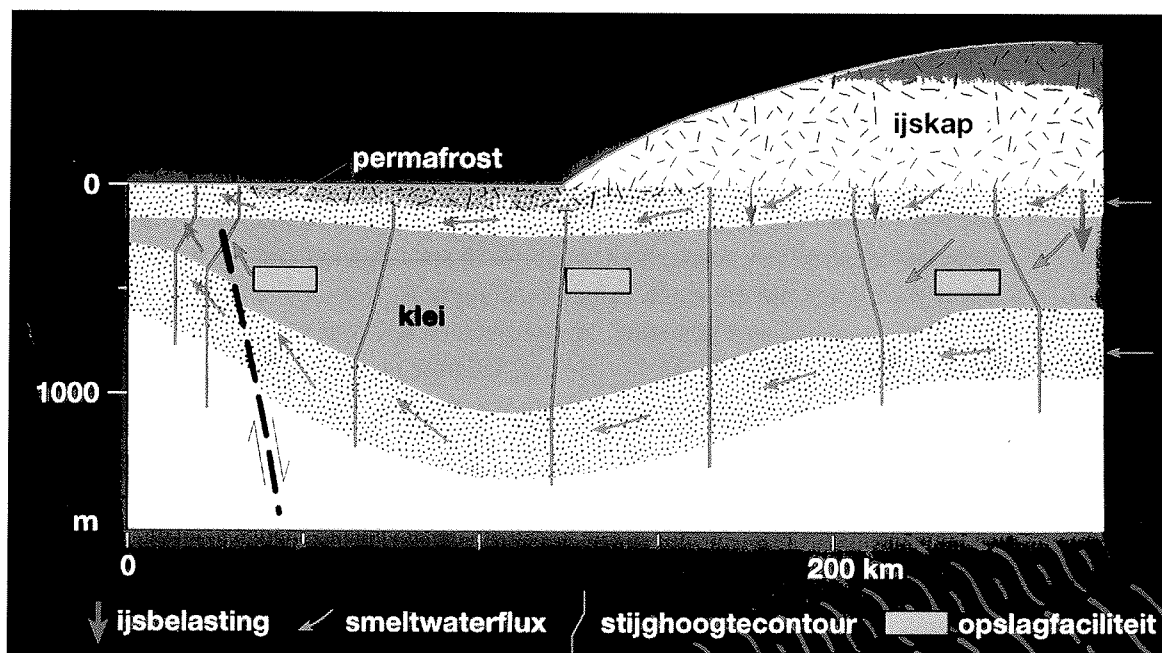
Voor opslag in het *gastgesteente klei* is reeds veel kennis en kunde bij het SCK in Mol en gelieerde onderzoeksinstituten opgebouwd. In het bijzonder is aandacht besteed aan de geologische, hydrologische en mechanische karakterisering van de Boomse klei (Klei van Rupel) op de locatie Mol en aan de mechanische en hydraulische processen in deze klei. Een vraag is in hoeverre de eigenschappen van de klei bij Mol extrapoleerbaar zijn naar Nederlandse voorkomens van deze klei op dieptes van 500 meter of meer.

Onder de huidige klimaatcondities vindt stroming van grondwater en transport van radionucliden in klei in een zeer laag tempo plaats. Diffusie vormt het belangrijkste transportmechanisme in intacte klei, d.w.z. in klei die niet door breuken of scheuren doorsneden wordt. Een proces dat buiten het bestek van het Belgische onderzoek valt, maar wel van belang kan zijn voor eventuele opslag in klei in de Nederlandse ondergrond, is het effect van een mogelijke toekomstige ijsbedekking (figuur 1).

Klei is, in tegenstelling tot steenzout, sterk waterhoudend en samendrukbaar. Door de *mechanische belasting* van een ijskap zou met radionucliden gecontamineerd water uit de klei gedreven kunnen worden (compactie gedreven grondwaterstroming). Radionucliden kunnen hierdoor versneld in het ondiepe grondwatersysteem terechtkomen.

Gelijktijdig met de mechanische belasting vindt infiltratie van smeltwater onder de ijskap plaats, wat leidt tot een *toename in de waterdruk* en de waterdrukgradiënt, zo bleek uit een door de Universiteit v. Edinburgh, RGD en RIVM uitgevoerd EG-onderzoek.

De opgewekte mechanische en hydraulische drukken t.g.v. de ijsbedekking zijn onderling gekoppeld. Zij leiden, mede afhankelijk van de driedimensionale opbouw van de ondergrond onder de ijskap, tot uitstroming van compactiewater afkomstig uit de klei of tot doorstroming van het gastgesteente door water afkomstig van de ijskap.



Figuur 1 Gebruikt concept voor modelstudie van grondwaterstroming onder invloed van ijsbelasting en smeltwaterproductie onder het ijs.

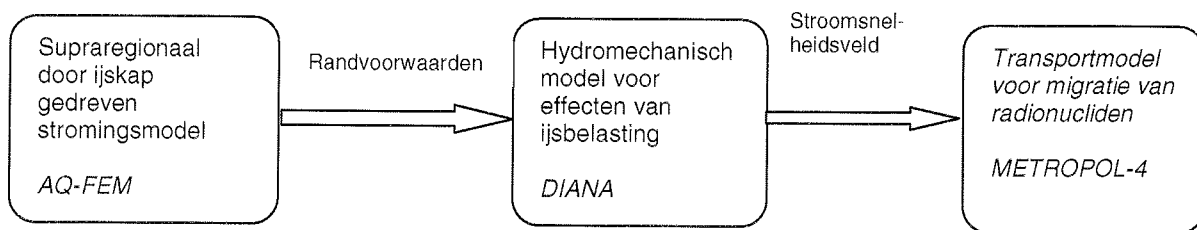
Vóór de ijskap en deels eronder is een aanzienlijk deel van de bodem boven het ondiepe grondwatersysteem in permanent bevroren toestand (permafrost). In de permafrost vindt dus geen stroming plaats, waardoor de transportroute van radionucliden naar de biosfeer verlengd wordt. Door de aanwezigheid van de permafrost wordt het ondiepe stromingsdomein ingesnoerd en zal dientengevolge de stromingssnelheid in het ondiepe systeem toenemen.

Een ander aspect dat bij de transportberekeningen aandacht verdient, is het ruimtelijke verloop van mogelijke *migratiepaden*. De aanname dat de verticale route naar de biosfeer de snelste migratieroute oplevert, hoeft a-priori niet waar te zijn. Een weliswaar langere horizontale transportweg via een watervoerende laag onder de kleibarrière en een verderop aanwezige verticale breuk zou uiteindelijk kunnen resulteren in een kortere migratietijd van radionucliden.

De *hoofddoelstelling* van het project TRAKTOR is het kwantificeren van de invloed van een ijsbedekking op het transport van radionucliden door de kleibarrière en vervolgens door de geosfeer. Dit doel wordt bereikt door computersimulatie van het effect van ijsbelasting op stroming in klei en haar invloed op het transport van radionucliden. Met labexperimenten op klei worden de geomechanische en geohydrologische parameters gemeten en wordt de graad van voorbelasting vastgesteld.

Met behulp van het hydromechanische eindige-elementen model DIANA is het effect van een ijsbelasting op het mechanisch gedrag van de ondergrond en op stroming van het grondwater gesimuleerd. De benodigde randvoorwaarden zijn overgenomen van een grootschalig stromingsmodel AQ-FEM, waarmee de effecten van een ijskap op het grondwatersysteem zijn gesimuleerd (figuur 2). De hydromechanische berekeningen zijn in twee fasen verlopen: aanvankelijk is een vrij eenvoudig model geconstrueerd waarmee een groot aantal verschillende situaties is geanalyseerd. Met het opgebouwde inzicht uit de eerste berekeningen is een meer gedetailleerd hydromechanisch model opgebouwd. De hieruit resulterende stroomsnelheden zijn gebruikt om het transport van radionucliden te modelleren met behulp van METROPOL-4.

Om de effecten van ijsbelasting op diepgelegen kleilichamen in de Nederlandse ondergrond te kwantificeren, is het noodzakelijk de grondmechanische parameters te kennen. Grondmechanische proeven zijn uitgevoerd, gericht op de consolidatie-eigenschappen, de doorlatendheid, de sterkte en stijfheid van de klei. Het materiaal voor de proeven is hoofdzakelijk afkomstig van de Klei van Rupel ('Boomse klei'), gelegen op verschillende diepteniveaus in België en Nederland.



Figuur 2 Relatie tussen het hydromechanische model en de andere modellen die in de studie zijn gebruikt.

Het TNO-NITG heeft de hydromechanische berekeningen uitgevoerd en de TUD heeft het transport van de radionucliden gemodelleerd. De mechanische proeven hebben plaatsgevonden bij de Universit  catholique de Louvain (UCL). GeoDelft heeft mogelijke oorzaken van overbelasting van de Klei van Rupel nagetrokken. De algehele co rdinatie van het project was in handen van het TNO-NITG.

Mechanische experimenten

Mechanische experimenten zijn uitgevoerd om de mechanische eigenschappen van Tertiaire klei, en die van de Klei van Rupel in het bijzonder, te karakteriseren. De proeven verschaffen onder meer inzicht in de mate waarin klei consolideert als functie van de opgelegde belasting. Twee typen van mechanische belastingsexperimenten zijn uitgevoerd: de uni-axiale consolidatieproef (oedometrie) en de tri-axiale proef (CTU).

In de tri-axiale proef wordt een bodemmonster in een kamer gevat, geconsolideerd en daarna onderworpen aan een axiale druk die hoger is dan de laterale druk totdat het materiaal bezwijkt. Deze proef is geschikt voor de voorspelling van de parameters cohesie, wrijvingshoek en glijdingsmodulus. Oedometrie is een ééndimensionale consolidatieproef waarmee de zetting- en zwelcapaciteit van het bodemmonster te bepalen is.

De gebruikte monsters zijn afkomstig van zes diepteniveaus op vier locaties in België en één locatie in Nederland. Voor de studie van ijsbelastingeffecten lag het accent op de analyse van materiaal uit het diepste bereik. Dit betreft diepteniveaus in één Nederlandse boring en één Belgische boring. Op één na, behoren alle monsters tot de Rupel Klei. Het diepste kleimonster, genomen op een diepte van ca. 562 m, behoort tot het Asse Laagpakket, een eenheid die onder de Rupel Klei ligt. Het gemonsterde kleimateriaal bestaat in alle gevallen uit een mengsel van de mineralen smectiet, illiet en kaoliniet. Het aandeel smectiet in het kleimonster van het Asse Laagpakket bedraagt ongeveer 50%; het smectiet-gehalte in de monsters uit Klei van Rupel varieert tussen 30 en 50%.

De drukbelastingen die zijn opgelegd in de mechanische experimenten, zijn afgestemd op de diepte waarvan het kleimonster afkomstig is en op de extra belasting die een toekomstige ijsbedekking in Nederland maximaal teweeg zou kunnen brengen (tabel 1). De beschikbare apparatuur voor de tri-axiale proeven liet geen belastingen hoger dan 10 MPa toe.

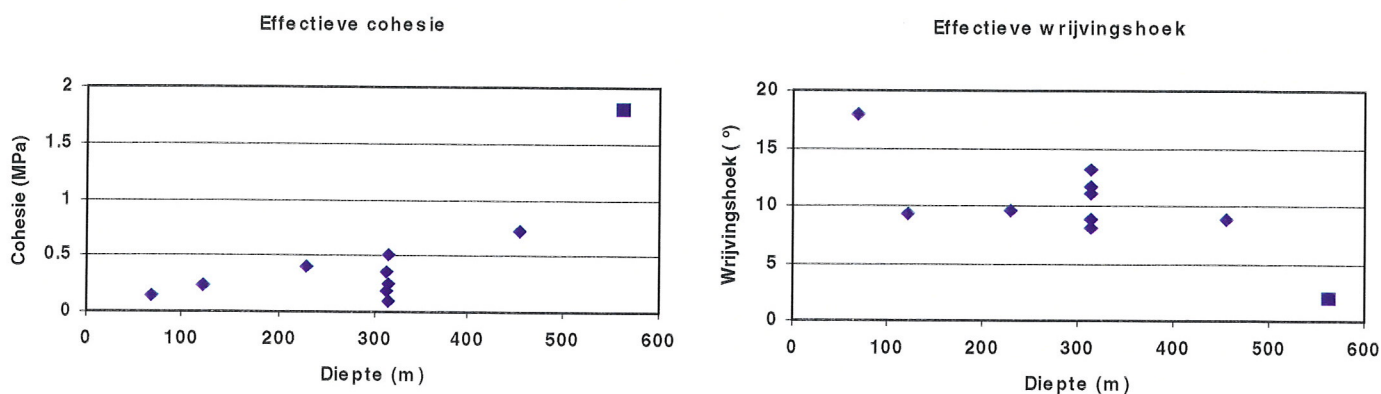
Tabel 1 Overzicht van uitgevoerde tri-axiale en oedometerproeven met belastingcondities.

Type experiment/ herkomst monster	Diepte- bereik (m)	Verticale belasting (MPa)
<i>Tri-axiaal/Weelde (B)</i>		
<i>Case 1 (3 monsters)</i>	<i>313 - 314</i>	<i>3,1 - 6,3</i>
<i>Case 2 (3 monsters)</i>	<i>314 - 315</i>	<i>2,3 - 4,1</i>
<i>Case 3 (3 monsters)</i>	<i>314 - 315</i>	<i>3,6 - 6,4</i>
<i>Case 5 (3 monsters)</i>	<i>314 - 315</i>	<i>5,4 - 9,4</i>
<i>Tri-axiaal/Blija (NL)</i>		
<i>Case 1 (3 monsters)</i>	<i>454 - 455</i>	<i>4,6 - 9,2</i>
<i>Case 4 (3 monsters)</i>	<i>561 - 562</i>	<i>4,8 - 9,8</i>
<i>Oedometer/Weelde (B)</i>		
<i>Case 1 (1 monster)</i>	<i>313 - 314</i>	<i>0,6 - 9,0</i>
<i>Case 2 (1 monster)</i>	<i>314 - 315</i>	<i>0,6 - 12,0</i>
<i>Case 3 (1 monster)</i>	<i>313 - 314</i>	<i>0,6 - 16,0</i>
<i>Case 4 (1 monster)</i>	<i>313 - 314</i>	<i>0,6 - 19,0</i>
<i>Oedometer/Blija (NL)</i>		
<i>Case 1 (1 monster)</i>	<i>453 - 454</i>	<i>0,6 - 20,0</i>
<i>Case 2 (1 monster)</i>	<i>561 - 562</i>	<i>0,6 - 20,0</i>

Tri-axiale proeven

De meeste tri-axiale proeven laten een normaal consoliderend gedrag van het kleimateriaal zien. Behalve voor de experimenten op monsters van de boring Blija en voor case 5 van de boring Weelde, is dit niet vanzelfsprekend, daar de opgelegde spanning onder de pre-consolidatiedruk ligt. Het normale consolidatiegedrag wordt geweten aan versterking van de oorspronkelijke conditie van de monsters. Door de lange tijd die ligt tussen de uitvoering van de experimenten en de extractie uit de monsterbuizen, zijn de kleimonsters waarschijnlijk gezwollen.

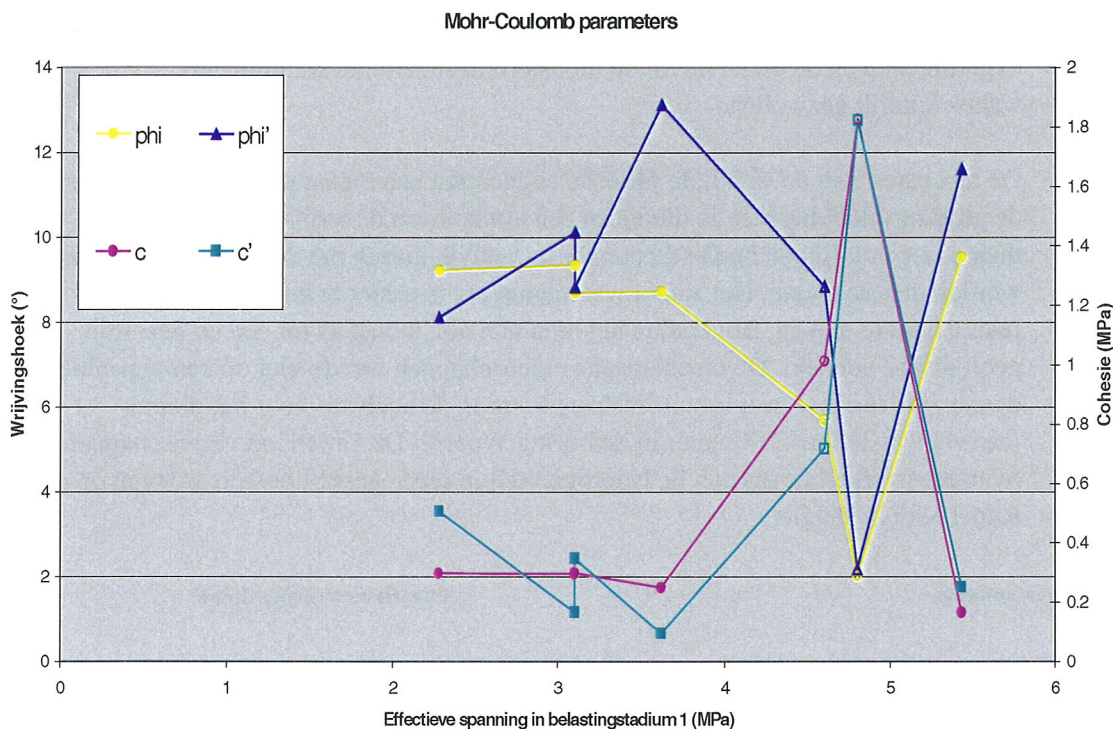
De resultaten van de tri-axiale proeven suggereren een toename van de cohesie en de glijdingsmodulus met de diepte en een afname van de wrijvingshoek met de diepte (zie ook figuur 3). De diepterelatie wekt de indruk dat de klei plastischer zou worden met de diepte. Het aantal waarnemingen is echter te beperkt om deze relatie hard te maken. Bovendien behoren niet alle monsters tot een en dezelfde geologische eenheid. De mechanische eigenschappen van de klei op een bepaalde diepte zijn variabel, wat tot uitdrukking komt in de analyses voor het diepte-interval van 313 tot 314 meter in de boring Weelde. De variatie in eigenschappen is overigens vergelijkbaar met de heterogeniteit in reeds gepubliceerde proeven op de Rupel Klei in België.



Figuur 3 Resultaten van de tri-axiale proeven; het diepste monster is afkomstig uit de klei van het Asse Laagpakket (■); de rest behoort tot de Rupel Klei (◆).

Mede gelet op de variabiliteit in de uitkomsten voor de boring Weelde, is het aantal proeven op materiaal uit de Nederlandse boring te laag om definitieve conclusies te trekken over de te gebruiken parameterwaarden. De waarden van de mechanische parameters die zijn bepaald voor het kleimonster uit het Asse Laagpakket, zijn extreem. Deze zullen in verder onderzoek geverifieerd moeten worden.

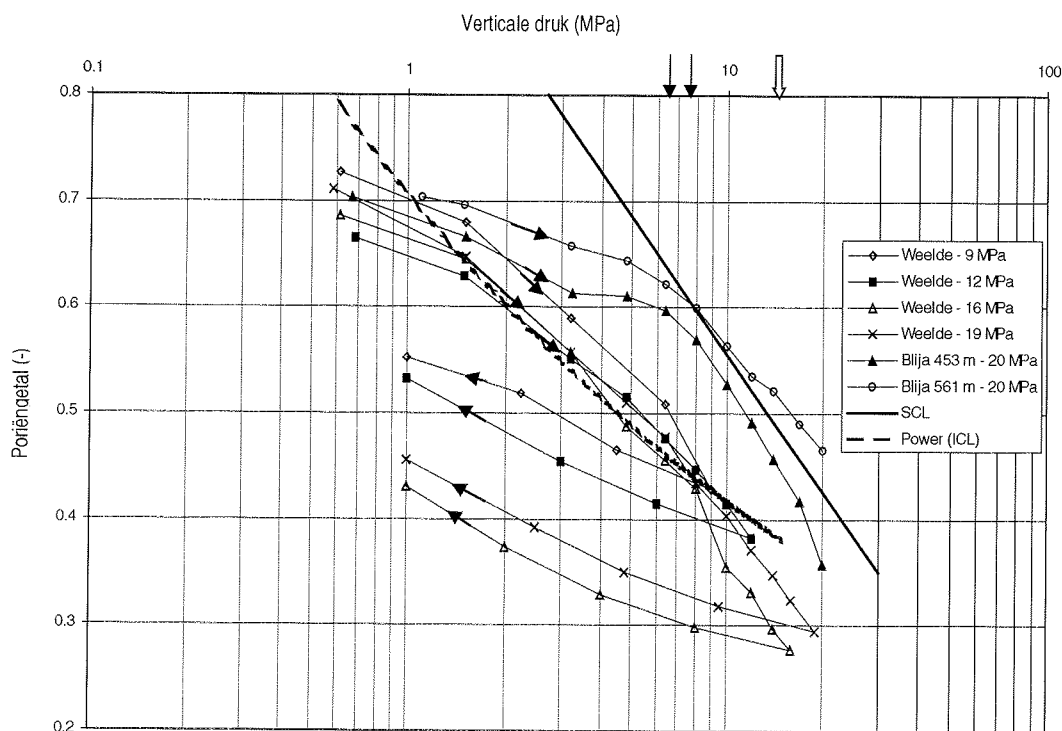
De waarden voor de cohesie en de wrijvingshoek die bepaald zijn voor de monsters op een diepte van 313 m (boring Weelde), vertonen geen duidelijke relatie met de opgelegde reeks van consolidatiespanningen (zie figuur 4). Voor dit bereik van (ijs-)belastingcondities lijken de mechanische parameters niet drukafhankelijk te zijn. De gemiddelde wrijvingshoek voor de monsters van de boring Weelde bedraagt 9° en de gemiddelde cohesie is 0,3 MPa.



Figuur 4 Relatie tussen effectieve spanning in eerste belastingstadium en de wrijvingshoek en de cohesie, open symbolen = boring Blija en gesloten symbolen = boring Weelde; c = cohesie, c' = effectieve cohesie, phi = wrijvingshoek, phi' = effectieve wrijvingshoek.

Oedometerproeven

De oedometrische experimenten tonen een goede reproduceerbaarheid van de resultaten voor het materiaal van Weelde en Blija afzonderlijk (figuur 5). Het belasting- en ontlastingsdeel in de curven voor de Belgische monsters zijn goed vergelijkbaar. Om dezelfde zetting voor de Nederlandse monsters te bereiken zijn hogere belastingsdrukken noodzakelijk.



Figuur 5 Resultaat van de oedometrische experimenten – poriëngetal e versus verticale druk; ICL = Intrinsieke Compressielijn, die de theoretische compressie van een compleet herknede klei in het laboratorium benadert; SCL = Sedimentaire Compressielijn, die de compressie van een klei onder natuurlijke, geologische omstandigheden benadert; gesloten pijl = pre-consolidatiedruk, open pijl = effectieve in-situ druk inclusief ijslast van 1000 meter.

Een nadere inspectie van de belastingcurven laat een onderverdeling in drie stadia toe:

- een initieel stadium tot ongeveer 1,5 MPa,
- een tweede stadium tot ongeveer 6 à 7 MPa voor Weelde en 7 à 8 MPa voor Blija en
- een derde stadium tot de maximale belasting.

De verticale druk aan het einde van het tweede belastingsstadium is geïnterpreteerd als de grootte van de pre-consolidatiedruk. Voor Weelde stemt de waarde van 6 à 7 MPa goed overeen met de prognose die is gebaseerd op waarnemingen aan ondiepe kleivoorkomens onder de Westerschelde ($p_c = 350 + 20z$ (kPa); $z =$ diepte (m)). De bijbehorende overconsolidatie-ratio (verhouding tussen pre-consolidatiedruk en in-situ druk) bedraagt 1,9 tot 2,2. De steile gradiënt in stadium 2 wordt toegewezen aan versterking van het uitgangsmateriaal (zie ook de discussie van de resultaten uit de tri-axiale proeven voor Weelde). Het nagenoeg samenvallen van de

belastingcurven voor Weelde met de Intrinsieke Compressielijn (ICL), de maagdelijke belastingcurve voor compleet verkneede klei in laboratoriumexperimenten, bevestigt dit.

De overconsolidatie-ratio voor de monsters uit Blija ligt tussen 1,3 en 1,8. Dit is lager dan is voorspeld op basis van waarnemingen uit het ondiepe bereik. De belastingcurven voor Blija liggen dichterbij de Sedimentaire Compressielijn (SCL) en vertonen dus een gedrag dat meer vergelijkbaar is met natuurlijke belasting op een geologische tijdschaal.

De waargenomen overconsolidatie van de vele miljoenen jaren oude Tertiaire klei wordt voor een deel geweten aan de processen diagenese en kruip (veroudering) en voor een ander deel aan een belasting in het geologische verleden die groter is dan de huidige. Het is zeer lastig om de effecten van veroudering en overbelasting te scheiden.

In figuur 5 zijn de pre-consolidatiedrukken en de effectieve druk door een ijslast van 1000 m weergegeven. Een dergelijk extreme last zou leiden tot verdere consolidatie van de klei. De werkelijke effectieve druk van een ijslast kan lager zijn, doordat smeltwaterproductie onder de ijskap de waterspanning verhoogt en de effectieve spanning daarmee verlaagt.

De oedometerproeven leverden invoerparameters voor het Cam-Clay materiaalmodel, te weten de compressie-index λ en de zwelling-index κ (tabel 2).

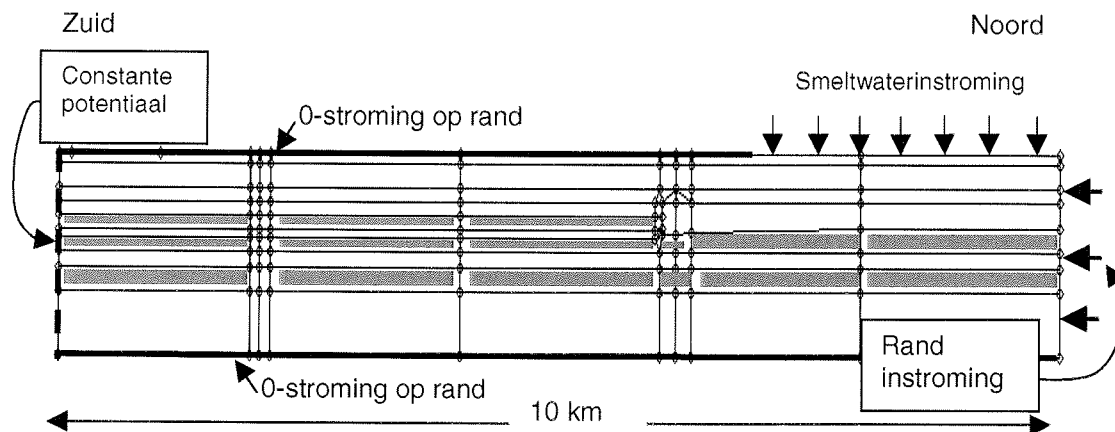
Tabel 2 Cam-Clay parameters κ (zwelling-index) and λ (compressie-index) afgeleid uit de oedometerproeven; eveneens zijn de waarden voor κ en λ afgeleid uit een isotrope tri-axiale proef (TRUCK-II) opgenomen. De waarden uit deze proef zijn gebruikt in de hydromechanische modellering. $p'c$ = pre-consolidatiedruk.

<i>Locatie/ type proef</i>	<i>Diepte (m)</i>	<i>Maximale belasting [MPa]</i>	<i>κ [-]</i>	<i>λ [-]</i>	<i>$p'c$ [MPa]</i>
<i>Weelde</i>					
<i>oedometer</i>	<i>313</i>	<i>9</i>	<i>0,06</i>	<i>0,24</i>	<i>6,4</i>
<i>oedometer</i>		<i>12</i>	<i>0,06</i>	<i>0,16</i>	<i>6,5</i>
<i>oedometer</i>		<i>16</i>	<i>0,06</i>	<i>0,21</i>	<i>8,0</i>
<i>oedometer</i>		<i>19</i>	<i>0,06</i>	<i>0,16</i>	<i>6,4</i>
<i>Blija</i>					
<i>oedometer</i>	<i>453</i>	<i>20</i>		<i>0,20</i>	<i>7,4</i>
<i>oedometer</i>	<i>561</i>	<i>20</i>		<i>0,14</i>	<i>7,5</i>
<i>tri-axiaal</i>	<i>478</i>	<i>-</i>	<i>0,02</i>	<i>0,12</i>	<i>6,9</i>

De doorlatendheidwaarden (K) voor de Rupel Klei onder de Westerschelde zijn geëxtrapoleerd naar grotere diepte en leverden een bereik van waarden tussen $1,2 \cdot 10^{-11}$ m/s and $5,4 \cdot 10^{-15}$ m/s op. De doorlatendheidwaarden uit de oedometerexperimenten liggen tussen $1,1 \cdot 10^{-13}$ en $7,6 \cdot 10^{-14}$ m/s en vallen binnen het geëxtrapoleerde bereik van de Westerschelde. De poriëntallen (e) afgeleid uit de experimenten voor Weelde en Blija zijn groter dan is voorspeld op basis van de waarnemingen uit de Westerschelde. Dit betekent uiteindelijk dat een extrapolatie van de relatie tussen e en K van ondiepe gegevens naar grotere diepte niet betrouwbaar is.

Hydromechanische berekeningen

De hydromechanische studie van ijsbelastingeffecten op Tertiaire klei is in twee fasen onderverdeeld. In de eerste fase is gebruik gemaakt van een relatief eenvoudig model waarin het effect van ijsbelasting op klei aan een eerste verkenning is onderworpen. Met de hieruit resulterende inzichten is voor de tweede fase een meer gedetailleerd model ontworpen, waarin tevens de dan beschikbaar gekomen laboratoriumresultaten zijn meegenomen.



Figuur 6 Type geohydrologische randvoorwaarden.

In de *eerste fase* van berekeningen is uitgegaan van een 2D ruimtelijk model, dat een representatieve doorsnede van de Nederlandse ondergrond met een lengte van 10 km en een diepte van 1200 meter omvat. Om de berekeningen uit te kunnen voeren is een aantal randvoorwaarden vastgelegd (zie figuur 6). Meer dan 10 scenario's zijn gedefinieerd om de gevoeligheid van het model voor variaties in de invoerparameters en randvoorwaarden te onderzoeken (tabel 3). De maximale dikte van de ijskap bedraagt in alle scenario's 1000 meter. De periode waarin het ijs over het modelgebied schuift varieert van 50 jaar tot 3.000 jaar en de totale periode van ijsbelasting neemt 600 dan wel 6.000 jaar in beslag.

Met het Mohr-Coulomb materiaalmodel (ideaal elastisch - perfect plastisch model) is het hydromechanisch gedrag van de Tertiaire afzettingen gesimuleerd.

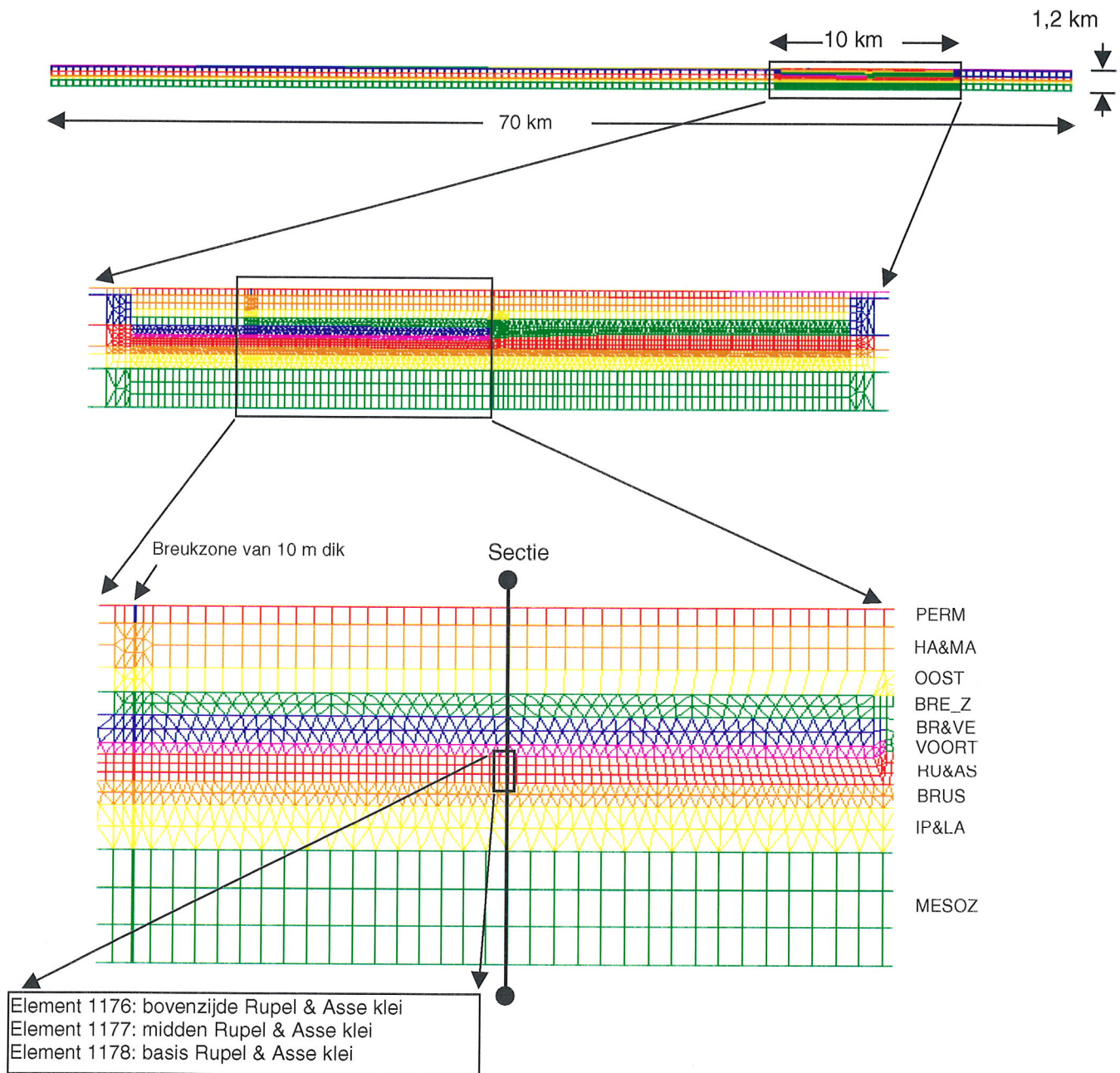
Tabel 3 Parameters en randvoorwaarden die zijn gevarieerd per ijsbelastingsscenario tijdens de eerste fase van modelberekeningen.

Variërende parameter	Gebruikte waarden
	$i=5 \times 10^{-4}$
Hydraulische gradiënt (-)	$i=4 \times 10^{-3}$
	$i=8 \times 10^{-3}$
Geomechanische parameters Rupel Klei	$c=100 \text{ kPa}, \Phi=20^\circ$
	$c=200 \text{ kPa}, \Phi=27^\circ$
Doorlatendheid Rupel Klei	$K=1 \times 10^{-10} \text{ m/s}$
	$K=1 \times 10^{-9} \text{ m/s}$

In de tweede fase van simulaties is het geometrisch model van 10 km uit de eerste fase verlengd tot 70 km (figuur 7). Deze lengte past beter bij de dimensies van de ijskap en de aan de ijskap gerelateerde hydraulische randvoorwaarden. In het ruimtelijk model is een breukzone opgenomen met een dikte van 10 meter. De gebruikte typen geohydrologische randvoorwaarden komen in grote lijnen overeen met de voorwaarden die in de eerste fase van berekeningen gebruikt zijn. Drie scenario's zijn doorgerekend, waarvan twee uitgaan van een Cam-Clay materiaalmodel voor de Klei van Rupel en de klei van het Asse Laagpakket (tabel 4). Voor de overige eenheden is het Mohr-Coulomb materiaalmodel gebruikt. De gebruikte waarden voor de wrijvingshoek zijn beduidend lager dan in de eerste fase van simulaties. Dit geldt ook voor de gebruikte doorlatendheidwaarden. De ijskap schuift in 350 jaar over het gehele modelgebied en de totale belasting duurt 20.000 jaar. Het gesimuleerde stroomsnelheidsveld is gebruikt als invoer voor de berekening van het radionuclidentransport.

Tabel 4 Gebruikte parameterwaarden voor een Cam-Clay materiaalmodel van de Klei van Rupel en de klei in het Asse Laagpakket in de tweede fase van hydromechanische simulaties.

Parameter	Gebruikte waarden
Hydraulische gradiënt (-)	$i = 8 \times 10^{-3}$
Geomechanische parameters Rupel Klei	$\Phi = 15^\circ$ $\Phi = 12^\circ$
	$\lambda = 0,12; \kappa = 0,02$
	$p_c = 10,4 \text{ MPa}$ $p_c = 6,9 \text{ MPa}$
Doorlatendheid Rupel Klei	$K = 3 \times 10^{-12} \text{ m/s}$ $K = 1 \times 10^{-11} \text{ m/s}$



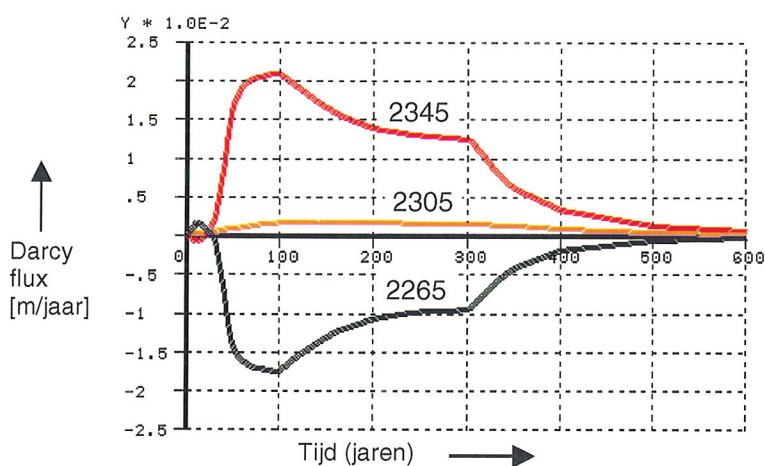
Figuur 7 Het netwerk van eindige elementen dat is gebruikt in de meer gedetailleerde hydromechanische berekeningen (fase 2). De opslagfaciliteit is geprojecteerd in element 1177 van het rooster.

Eenvoudige simulatie met Mohr-Coulomb materiaalmodel (fase 1)

De hoge laterale instroming leidt tot een opwaartse doorstroming van de Tertiaire klei. De verticale stroomsnelheid in de Rupel Klei en de klei van het Asse Laagpakket loopt op tot 0,4 mm per jaar bij een doorlatendheid van 1×10^{-10} m/s. Bij een snelle tot gematigd snelle voortschrijding van het ijsfront wordt het stromingsbeeld in de klei gedomineerd door consolidatie van de klei (figuur 8). Aan zowel de onder- als bovenzijde van het kleilichaam vindt uitstroming van grondwater plaats. Is de voortschrijdingssnelheid daarentegen laag dan neemt het effect van consolidatie-gedreven stroming in de klei af en gaat de regionale opwaartse stroming overheersen.

De invloed van de regionale opwaartse stroming door de klei is tijdens ijsbelasting sterker merkbaar bij een hogere waarde voor de doorlatendheid van de klei ($K = 1 \times 10^{-9}$ m/s). Een hogere doorlatendheid van de klei leidt verder tot een hogere maximale flux en een snellere dissipatie van de overdruk in de klei.

De klei wordt elastisch vervormd als de ijskap langzaam over het modelgebied schuift. Bij een hoge snelheid van het ijsfront wordt de klei wel plastisch vervormd.



Figuur 8 Verticale stroming in de Rupel Klei en de klei van het Asse Laagpakket ($K = 1 \times 10^{-10}$ m/s) gedurende een gematigd snelle voortschrijding van het ijsfront en een hoge laterale flux; 2265 = element aan onderzijde kleipakket, 2305 = element in midden kleipakket en 2345 = element aan bovenzijde van kleipakket.

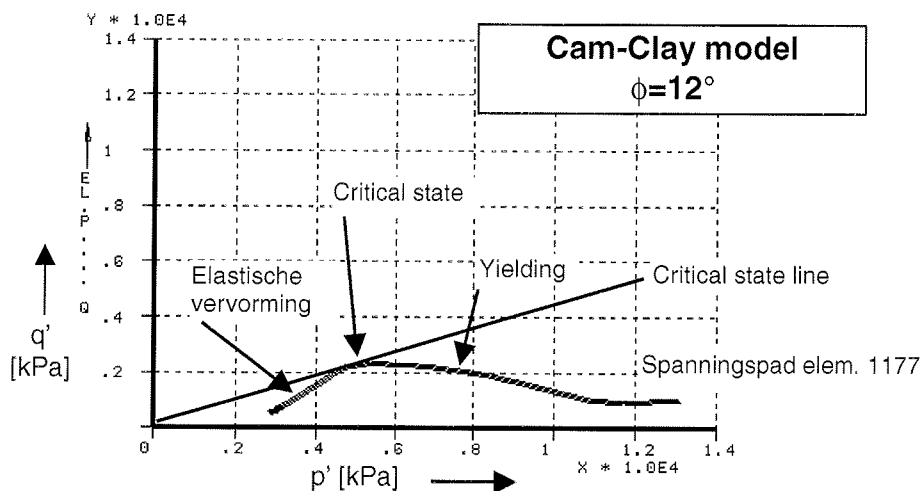
Meer gedetailleerde simulatie met het Mohr-Coulomb en het Cam-Clay materiaalmodel (fase 2)

De stroomsnelheid in de klei zonder ijsbelasting bedraagt 10^{-6} tot 4×10^{-7} meter per jaar. Onder glaciële condities zonder ijsbedekking draineert de doorlatende

breukzone de dieper gelegen Mesozoïsche aquifer, waardoor de poriëndruk in deze watervoerende laag daalt. In de Mesozoïsche aquifer stroomt water van beide zijden naar de breuk, vervolgens vindt opwaartse stroming door de breukzone plaats en instroming in de ondiepe aquifer.

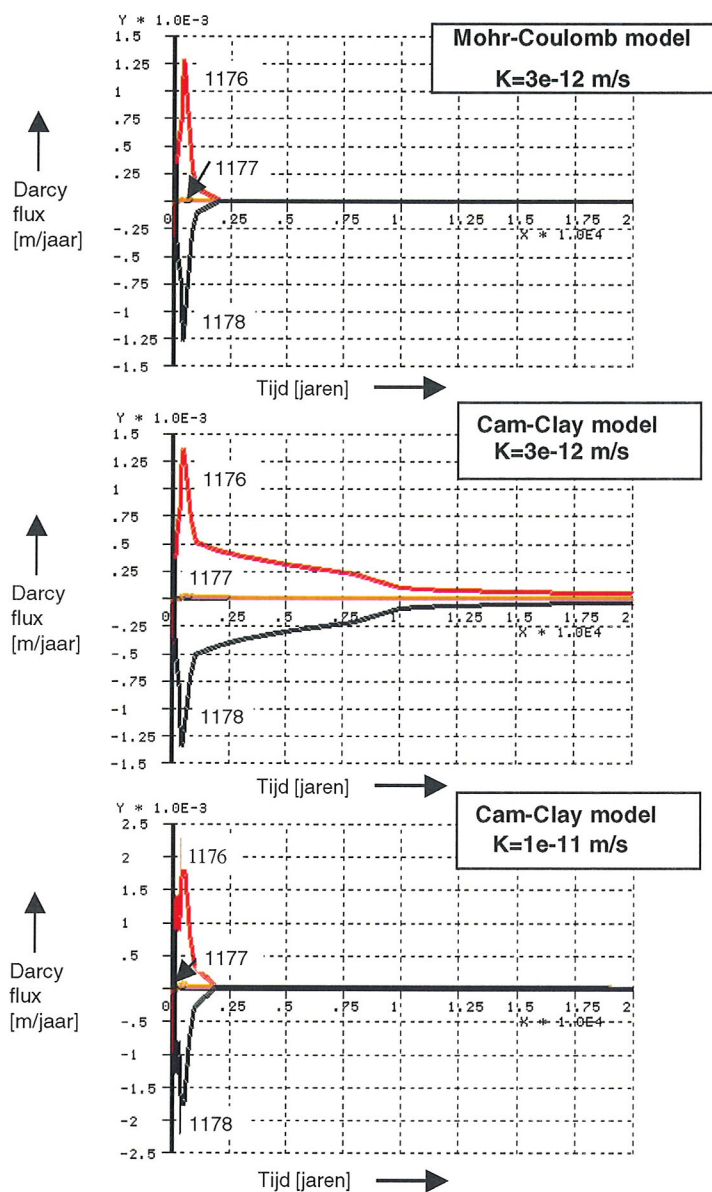
De druk ten gevolge van de ijsbelasting wordt vertraagd aan het sediment doorgegeven. Na 350 jaar als het ijs het gehele modelgebied bedekt, is ongeveer de helft van de ijsdruk aan het sediment doorgegeven. Een belangrijk deel van de ijsbelasting wordt dan nog gedragen door het poriënwater. Afhankelijk van de doorlatendheid van de klei en het gebruikte materiaalmodel, bedraagt de vertraging vele honderden jaren tot 20.000 jaar. Aan het eind van de simulatie is de effectieve spanning toegenomen met de maximale belasting van de ijskap en is de druk in het poriënwater weer teruggekeerd tot de initiële waarden.

De Rupel Klei en de klei van het Asse Laagpakket vertoont plastisch gedrag door de ijsbelasting. Vooral de lage waarde van de wrijvingshoek ϕ versterkt het plastisch gedrag. In figuur 9 is het vervormingsgedrag van een element in de klei weergegeven. Duidelijk is dat na aanvankelijke elastische vervorming, de klei plastisch gaat deformeren.



Figuur 9 Effectief spanningspad voor een element in het midden van het kleipakket.

Door de ijsbelasting consolideert de Rupel Klei en de klei van het Asse Laagpakket en leidt tot verticale stroming in de klei (figuur 10). Voor een realistische waarde van de doorlatendheid van $3 \cdot 10^{-12}$ m/s houdt de consolidatie aan gedurende de gehele belastingsperiode van 20.000 jaar. De stroomsnelheid loopt tot maximaal 1 mm per jaar op. Deze waarde is ongeveer 3 grootteordes hoger dan de stroomsnelheid in de klei, voordat de ijskap het modelgebied belast.



Figuur 10 Verticale stroming door de Rupel Klei en de klei van het Asse Laagpakket door ijsbelasting; 1176 = element aan de bovenzijde van de klei; 1177 = element in het midden van de klei; 1178 = element aan de basis van de klei.

De stroomsnelheid in de watervoerende lagen neemt met ongeveer een grootteorde toe ten opzichte van de toestand voor de ijsbelasting. De toename houdt ongeveer gelijke tred met de druktoename door de ijsbelasting. Als de ijsbelasting eenmaal zijn maximum bereikt heeft dan neemt de stroomsnelheid in de aquifer weer snel af.

Transportberekeningen

Het effect van ijsbelasting op het transport van radionucliden is zichtbaar gemaakt door het effect te vergelijken met radionuclidentransport onder de huidige omstandigheden (referentiescenario). De uitkomsten van de transportberekeningen zijn dus van relatieve betekenis. Met behulp van het programma Metropol is het transport van 17 radionucliden gesimuleerd gedurende een periode van 1 miljoen jaar. De radionuclidenbron, waarvan de samenstelling is overgenomen uit de veiligheidstudie METRO, is geprojecteerd in de Rupel Klei op een diepte van 545 meter. Acht vervalketens, waarvan drie met vier leden en vijf met slechts één lid, zijn beschouwd. Aangenomen is dat vrijzetting van de radionucliden instantaan, zonder vertraging, aan het begin van de simulatie plaatsvindt. Het transport van de radionucliden vindt plaats door diffusie, stroming en dispersie, en sorptie van de radionucliden aan de klei (met behulp van de retardatiefactor R). Daarbij is rekening gehouden met het natuurlijk verval van de radioactieve stoffen.

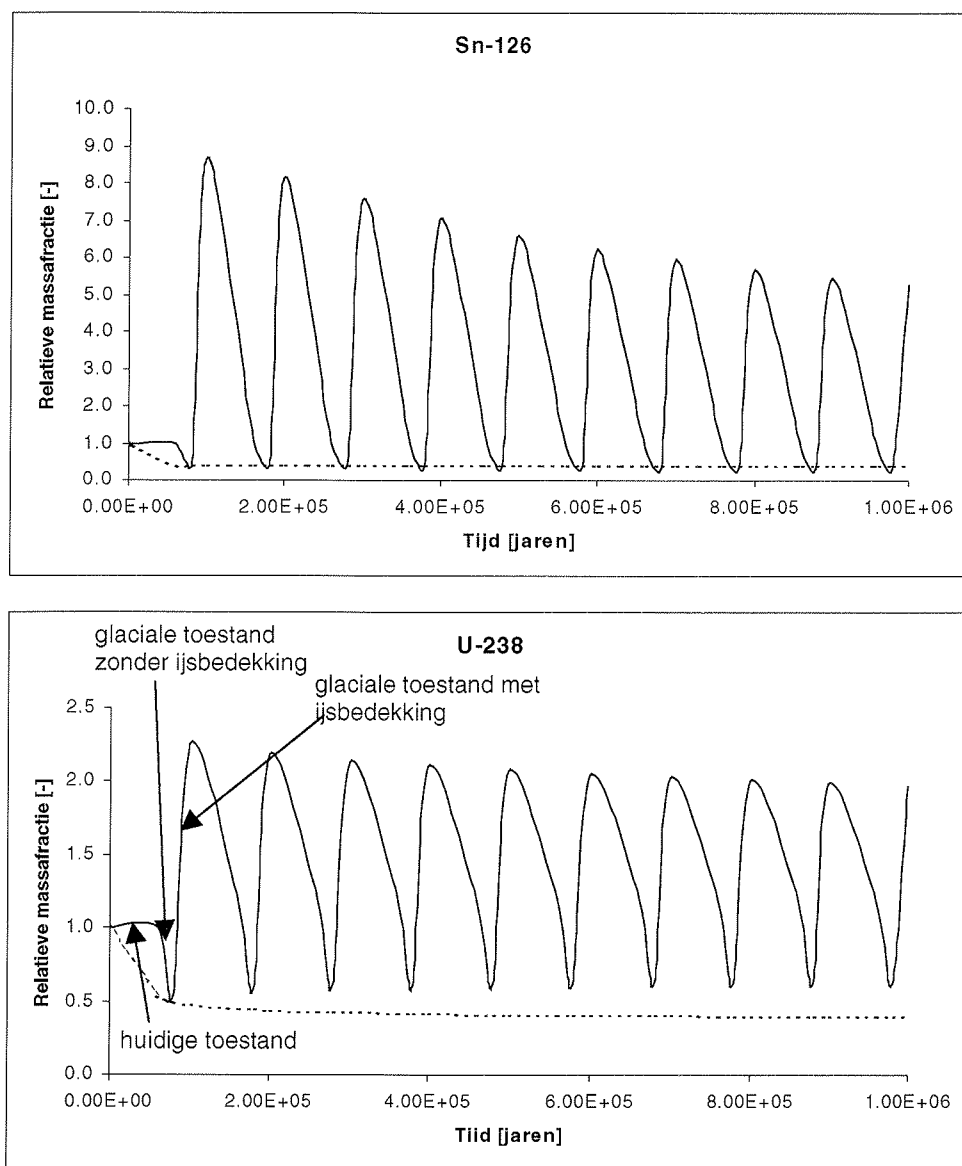
Een uitsnede uit het ruimtelijke model voor de hydromechanische berekeningen is gebruikt; de lengte bedraagt 10 km. Het profiel is vervolgens in de derde dimensie uitgebreid, zodat sprake is van een semi-driedimensionaal model. Het stroomsnelheidsveld is berekend met behulp van het meer gedetailleerde hydromechanische model, waarin de doorlatendheid van de klei een waarde van $3 \cdot 10^{-12}$ m/s aanneemt. Drie representatieve snelheidsvelden zijn gegenereerd: een huidige toestand en twee glaciële toestanden, waarvan één zonder ijsbedekking en één met ijsbedekking.

In de modellering van radionuclidenmigratie zijn deze gebruikt om drie verschillende situaties te door te rekenen:

1. Huidige toestand gedurende $1 \cdot 10^6$ jaar. Dit referentiescenario met huidige randvoorwaarden is gebruikt voor de berekening van de relatieve massafracties in de scenario's 2 en 3.
2. Glaciële toestand met permafrost situatie gedurende $1 \cdot 10^6$ jaar. Dit scenario met glaciële randvoorwaarden zonder ijsbedekking is gebruikt voor de evaluatie van het meer realistische scenario 3.
3. Cyclische afwisseling van de huidige situatie met een duur van $6 \cdot 10^4$ jaar, permafrost situatie met een duur van $2 \cdot 10^4$ jaar en een situatie met ijsbedekking met een duur van $2 \cdot 10^4$ jaar. Deze opeenvolging is 10 keer herhaald zodat de totale duur uiteindelijk $1 \cdot 10^6$ jaar bedraagt.

Ook onder invloed van een ijsbelasting is het transport in de klei hoofdzakelijk diffusief. De grootteorde van de stroomsnelheden voor de huidige toestand en de glaciële toestanden zonder en met ijsbedekking zijn respectievelijk 10^{-7} , $2,5 \cdot 10^{-7}$ en $1,7 \cdot 10^{-5}$ meter per jaar. Zij dragen respectievelijk voor 0,08%, 0,2% en 14% bij aan het totale transport. Deze waarden gelden onder de aanname dat de longitudinale dispersiviteit 50 m bedraagt.

In de aquifers boven en onder de klei wordt het transport sterk door stroming beïnvloed, waardoor de migratie van radionucliden veel sneller verloopt. Het versterkende effect van de breuk op de migratie van de radionucliden is duidelijk te zien aan het verloop van het contourbeeld bij de breuk.



Figuur 11 Massafracties van twee radio-isotopen op de grens tussen de klei en de bovenliggende aquifer ten opzichte van de massafractie voor de huidige toestand (referentiescenario); getrokken lijn = relatieve massafractie voor het scenario met cyclische veranderingen; streepjeslijn = relatieve massafractie voor het scenario met permafrost zonder ijsbedekking.

Het effect van afwisselende klimaatomstandigheden, en van glaciële condities in het bijzonder, op de massafractie radionucliden is zichtbaar gemaakt in figuur 11.

Het glaciële scenario zonder ijsbedekking resulteert in lagere massafracties dan het referentiescenario. De radionucliden worden door de grote stroomsnelheid in de bovenliggende aquifer snel verdund. Ijsbelasting leidt tot hogere massafracties radionucliden op de overgang van de klei naar de bovenliggende aquifer. Afhankelijk van de nuclide kan de massafractie maximaal 2 tot 9 maal hoger zijn dan in het referentiescenario.

Conclusies en aanbevelingen

IJstijd en radionuclidenmigratie

- Verkennende berekeningen geven aan dat cyclische ijsbelasting kan leiden tot een versnelling van de migratie van radionucliden in klei. De berekende bijdragen van dispersief transport aan de totale diffusiecoëfficiënt in klei bedragen 0,08% onder huidige omstandigheden, 0,2% onder glaciële omstandigheden zonder ijsbedekking en 14% onder glaciële omstandigheden met ijsbedekking. Deze waarden gelden onder de aanname dat de longitudinale dispersiviteit 50 m bedraagt. In de genoemde percentages komt sorptie van radionucliden door klei niet tot uitdrukking.
- Het cyclisch optreden van een ijsbelasting met een duur van 20.000 jaar en een periode van 100.000 jaar leidt tot verhoging van de massafractie radionucliden op het grensvlak van de kleibarrière en de bovenliggende aquifer. De verhoging is, afhankelijk van de radionuclide, maximaal 2 tot 9 maal de massafractie in het referentiescenario (huidige klimaat). De verhoging valt naar verwachting binnen de onzekerheidsmarge van de geschatte snelheid van diffusief transport. De genoemde waarden zijn berekend met inbegrip van radionuclidensorptie door klei.

IJstijd en grondwaterstroming

- De poriëndruk in diepgelegen aquifers vóór een ijskap neemt toe onder invloed van deze ijskap. Deze toestand kan leiden tot versterkte doorstroming van kleilichamen met een doorlatendheid van 1×10^{-10} m/s of meer. Langs aanwezige doorlatende verticale breuken treedt preferentiële stroming op.
- In een diepgelegen kleipakket onder een ijskap wordt water uitgedreven naar boven- en onderliggende watervoerende lagen. De uitstroming wordt versterkt door een hogere doorlatendheid; tegelijkertijd wordt de periode van verhoogde uitstroming verkort.
- In het meest realistische ijsbelastingsscenario (zie ook conclusies onder 'Laboratoriumexperimenten en rekenmodellen') dat is beschouwd, is de consolidatie van de Rupel Klei en de klei in het Asse Laagpakket over de gehele periode van ijsbelasting uitgesmeerd. De maximale waarde van de

uitstroomsnelheid bedraagt 1 mm per jaar. Deze waarde is ongeveer 3 grootteordes hoger dan de stroomsnelheid in de klei vóór de ijsbelasting.

Laboratoriumexperimenten

- De proeven met de monsters uit de Rupel Klei in het dieptebereik van 313 tot 454 meter hebben geresulteerd in de vaststelling van een aantal mechanische en hydraulische parameters met de volgende bereiken:

<i>Parameter</i>	<i>Bereik</i>
ϕ'	8,1 - 13,1°
c'	0,09 - 0,72 MPa
p'_c	6 - 8 MPa
λ	0,14 - 0,24
κ	0,06
K	$1,1 \cdot 10^{-13}$ - $7,6 \cdot 10^{-14}$ m/s.

Analyse van het monster uit de Klei van Asse heeft een ϕ' -waarde van 2° opgeleverd. Deze extreem lage waarde moet met aanvullende experimenten worden onderbouwd.

- Sommige mechanische parameters, zoals de wrijvingshoek, cohesie en de glijdingsmodulus, tenderen met de diepte te veranderen. De gegevensbasis is te smal om van een duidelijke diepterelatie te spreken. Extrapolatie van waarnemingen uit de Belgische regio naar Nederland wordt daardoor bemoeilijkt.
- De geanalyseerde kleien zijn alle overgeconsolideerd. De oorzaak hiervan is niet eenduidig vast te stellen: er kan sprake zijn van diagenetische veranderingen, van kruip of van daadwerkelijke overbelasting. Bij een extreme effectieve belasting met 1000 meter ijs zal de Rupel Klei verder consolideren.

Laboratoriumexperimenten en rekenmodellen

- In het meest realistische scenario dat is doorgerekend zijn parameterwaarden gebruikt, die grotendeels aan de experimenten voor TRUCK II zijn ontleend. Ten tijde van de hydromechanische modellering waren de resultaten uit het experimentele programma voor TRAKTOR nog niet beschikbaar.

De gebruikte parameterwaarden in dit scenario van de hydromechanische modellering zijn:

<i>Parameter</i>	<i>Waarde</i>
ϕ'	15°
p'_c	10,4 MPa
λ	0,12
κ	0,02
K	$3 \cdot 10^{-12}$ m/s

De gebruikte waarde voor de wrijvingshoek is hoger dan de experimenteel bepaalde waarden. In Cam-Clay modellen wordt een hogere waarde voor ϕ gebruikt om te compenseren voor de cohesie-parameter. Deze is namelijk niet in het Cam-Clay model opgenomen.

De lagere experimentele waarde voor de effectieve pre-consolidatiedruk p'_c en de hogere experimentele waarde voor de compressie-index λ zullen uiteindelijk leiden tot een enigszins hogere Darcy-flux dan in het meest realistische scenario van het project TRAKTOR is doorgerekend.

Aanbevelingen

- Het wordt aanbevolen om de Rupel Klei voor de doeleinden van radioactief afvalberging verder te karakteriseren en daarbij gebruik te maken van materiaal uit het gewenste dieptebereik en regio. Voorts wordt geadviseerd om boorgatmeettechnieken in te zetten, die, na calibratie aan de hand van laboratoriumanalyses, geschikt zijn om mechanische eigenschappen van de klei af te leiden. Ook zal de natuurlijke spanningstoestand *in situ* vastgesteld moeten worden.
- Om de bruikbaarheid van andere Tertiaire kleipakketten, zoals de kleien in het Asse en Ieper Laagpakket, voor de berging van radioactief afval vast te stellen, zijn eveneens meer veldgegevens noodzakelijk.
- Tenslotte wordt in overweging gegeven om enkele aanvullende hydromechanische modelberekeningen uit te voeren op basis van de nu beschikbaar gekomen geomechanische parameterwaarden voor de Klei van Rupel in de boringen Weelde en Blija.

Contents

Uitgebreide samenvatting	i
List of figures	xxv
List of tables	xxxi
1 Introduction.....	1
2 Modelling concept of ice-sheet loading	3
2.1 Literature review	3
2.2 Modelling concept in TRACTOR	5
3 Data inventory	11
3.1 Description of 2-D-transect	11
3.2 Hydromechanical parameters derived from literature	15
3.2.1 Geohydrological parameters	15
3.2.2 Geomechanical parameters	16
4 Additional mechanical experiments	21
4.1 Brief review of the test programme for TRUCK II	21
4.1.1 Characteristics of the samples	22
4.1.2 Sedimentation analysis	23
4.1.3 Results	24
4.2 The initial test programme for TRACTOR	26
4.3 Description of sample material	26
4.3.1 Characteristics of the samples	30
4.3.2 Sedimentation analysis	30
4.3.3 Mineralogical analysis	31
4.3.4 Atterberg limits	32
4.4 Methods and techniques used for testing	33
4.4.1 The consolidated and undrained triaxial test (CTU).....	33
4.4.2 The oedometer consolidation test.....	34
4.5 Results of mechanical experiments	36
4.5.1 The consolidated and undrained triaxial tests (CTU)	36
4.5.2 The oedometer consolidation tests	39
4.6 Discussion	42
5 The hydromechanical model and coupling with other models	49
5.1 Mathematical description of the flow-stress analysis	49
5.1.1 Basic equations and assumptions	49

5.1.2	The numerical code DIANA.....	53
5.2	Coupling between the supraregional groundwater model and DIANA.....	57
5.2.1	Brief description of the supraregional model.....	58
5.2.2	Simulation with supraregional model	60
5.2.3	Results	61
5.2.4	Boundary conditions for 2-D model.....	63
5.3	Coupling between DIANA and the transport model.....	63
6	Simulation of glacially-driven hydromechanical processes using a simple model.....	67
6.1	Simple hydromechanical model	67
6.2	Schematisation and model mesh	67
6.3	Conditioning of the model.....	71
6.4	Practical approach in the simulations.....	73
6.5	Initialisation of the stress and groundwater flow in the model.....	77
6.5.1	Loading by gravity.....	79
6.5.2	Hydrodynamic loading	79
6.5.3	Initialisation of stresses for a nonlinear transient analysis	80
6.6	Loading by ice for a medium fast advance of ice sheet.....	81
6.6.1	Stress and deformation	81
6.6.2	Plasticity	89
6.6.3	Groundwater flow in aquifers.....	93
6.6.4	Groundwater flow in aquitards.....	103
6.7	Loading by ice for a very fast advance of ice sheet.....	105
6.8	Loading by ice for a very slow advance of ice sheet	113
6.9	Discussion	120
7	Simulation of glacially-driven hydromechanical processes using a detailed model.....	125
7.1	Approach.....	125
7.2	Description of the hydromechanical model	126
7.2.1	Schematisation and mesh.....	126
7.2.2	Material models and hydromechanical parameters.....	128
7.2.3	Boundary conditions	130
7.2.4	Ice-loading scenarios	130
7.3	Initialisation of the stress and groundwater flow	133
7.4	Loading by ice.....	134
7.4.1	Stress and deformation	134
7.4.2	Plasticity	136
7.4.3	Groundwater flow in aquifers.....	141
7.4.4	Groundwater flow in aquitards.....	145

7.4.5	Preparation of the groundwater velocity fields for the transport model	149
8	Migration of radionuclides	151
8.1	Introduction	151
8.2	Description of METROPOL-4	151
8.3	Input description	153
8.3.1	METROMESH and METROREF	153
8.3.2	METROPOL-4.....	155
8.4	Results	160
8.5	Discussion	162
9	Conclusions and recommendations.....	167
10	References.....	171
Appendices		
A	Analysis of the permeability of the Boom clay at high pressure	
B	Stress paths in the tri-axial tests	
C	Mineralogical analyses	
D	Physical input parameters of METROPOL	

List of figures

Figure 2.1	Schematic cross-section showing the groundwater flow pattern during glaciation	7
Figure 3.1	Representative geological cross-section through the subsurface in the Netherlands.....	12
Figure 3.2	Structural map.....	13
Figure 4.1	Dry, saturated and specific weights versus depth.....	22
Figure 4.2	Initial and saturated water content versus depth.....	23
Figure 4.3	Sedimentation analysis for Doel (69 m), Zoersel (120 m), Mol (224 and 229 m), Weelde (313 m) and Blija (455 m).....	23
Figure 4.4	Cohesion versus depth.....	24
Figure 4.5	Friction angles versus depth.....	24
Figure 4.6	Shear modulus (G) versus the mean effective stress.....	25
Figure 4.7	Geophysical logs of boring Blija.....	29
Figure 4.8	Sedimentation analysis for Weelde (313 m) and Blija (454 m and 561 m).....	32
Figure 4.9	Fixed-ring cell adapted for high pressures.....	37
Figure 4.10	Shear modulus (G) versus mean effective stress.....	38
Figure 4.11	Shear modulus (G) versus mean effective stress for TRUCK II and TRACTOR.....	40
Figure 4.12	Undrained shear strength versus mean effective stress.....	44
Figure 4.13	Results of the consolidated and undrained triaxial tests (CTU) - cohesion and angle of friction versus depth.....	45
Figure 4.14	Relation between effective vertical stress of first loading stage and friction angle and cohesion.....	48
Figure 4.15	Results of oedometric tests – void ratio e versus axial pressure.....	48
Figure 5.1	Relation between the various models used in the project TRACTOR.....	49
Figure 5.2	Schematic position of the 2-D profile model in the quasi 3-D supraregional model.....	59
Figure 5.3	This palaeogeographical situation forms a (extreme) but representative snapshot of a cold climatic period in Europe during the Pleistocene.....	61
Figure 5.4	Calculated hydraulic heads in the upper aquifer for the palaeogeographical situation	62
Figure 5.5	Supraregional model results on the location of the vertical boundaries in the DIANA model.....	64
Figure 5.6	Coupling between the groundwater velocity field calculated by the hydromechanical model and the radionuclides transport modelling	65

Figure 6.1	Schematisation for simplified hydromechanical finite element model.	69
Figure 6.2	Finite element mesh and structural boundary conditions for the simplified hydromechanical model.	71
Figure 6.3	Geohydrological boundary conditions.	73
Figure 6.4	Division of ice-loading scenarios into three major groups on the basis of the speed of ice sheet movement.....	76
Figure 6.5	Loading of the model by a steadily advancing and thickening ice sheet is achieved through five load cases.	76
Figure 6.6	Effective vertical stresses in the model initialised in a linear elastic finite element analysis.	82
Figure 6.7	Effective stresses for hydrostatic conditions along a vertical section shown in Figure 6.6.	82
Figure 6.8	Pore pressure distribution initialised for a low influx through the northern lateral boundary.	84
Figure 6.9	Pore pressure distribution initialised for a high influx through the northern lateral boundary.	86
Figure 6.10	Initial effective vertical stresses in the model at the beginning of a nonlinear transient finite element analysis.....	87
Figure 6.11	Initial effective stresses at the beginning of a nonlinear transient finite element analysis.	87
Figure 6.12	Effective vertical stresses during a medium fast advance of ice sheet for a low lateral influx in the model.	90
Figure 6.13	Vertical displacement during a medium fast advance of ice sheet for a low lateral influx in the model.....	91
Figure 6.14	a) Vertical effective stress, b) pore pressure, and c) vertical displacement with depth during a medium fast advance of ice sheet for a low lateral influx in the model.....	92
Figure 6.15	Effective vertical stresses during a medium fast advance of ice sheet for a high lateral inflow into the model.....	94
Figure 6.16	Vertical displacement during a medium fast advance of ice sheet for a high lateral inflow in the model.....	95
Figure 6.17	a) Vertical effective stress, b) pore pressure, and c) vertical displacement with depth during a medium fast advance of ice sheet for a high lateral inflow in the model.....	96
Figure 6.18	a) Vertical displacement of the characteristic nodes in the clay layers during a medium fast advance of ice sheet for a high lateral inflow in the model. b) Vertical strain for a middle element of the Rupel Clay and Asse Member layer, for medium and high hydraulic.	97
Figure 6.19	Principal plastic strain in the Tertiary sand layers during a medium fast advance of ice sheet for a high lateral influx in the model.....	98

Figure 6.20	Formation of the zone of plasticity during a medium fast advance of ice sheet, for low values of cohesion and the angle of internal friction.	99
Figure 6.21	Horizontal Darcy flux during a medium fast advance of ice sheet for a low lateral inflow into the model.....	101
Figure 6.22	Pore pressure along two horizontal sections during a medium fast advance of ice sheet and for a low lateral inflow into the model.....	102
Figure 6.23	Horizontal Darcy flux during a medium fast advance of ice sheet for a high lateral inflow into the model.....	106
Figure 6.24	a) Pore pressure along two horizontal sections during a medium fast advance of ice sheet and for a high lateral inflow into the model.....	107
Figure 6.25	Excess pore pressure during a medium fast advance of ice sheet for a high lateral inflow into the model.....	108
Figure 6.26	Vertical Darcy flux in the Rupel Clay and Asse Member during a medium fast advance of ice sheet for a low lateral inflow into the model.....	109
Figure 6.27	Vertical Darcy flux in the Rupel Clay and Asse Member during a medium fast advance of ice sheet for a high lateral inflow into the model.....	110
Figure 6.28	Vertical Darcy flux in the Rupel Clay and Asse Member during a medium fast advance of ice sheet and for a high lateral inflow into the model and high hydraulic conductivity.....	111
Figure 6.29	Formation of the zone of plasticity during a very fast advance of ice sheet for a high lateral inflow into the model.....	114
Figure 6.30	Horizontal Darcy flux during a very fast advance of ice sheet for a high lateral inflow into the model.	115
Figure 6.31	Pore pressure during a very fast advance of ice sheet and for a high lateral inflow into the model.....	116
Figure 6.32	Excess pore pressure during a very fast advance of ice sheet for a high lateral inflow into the model.....	117
Figure 6.33	Vertical Darcy flux in the Rupel Clay during a very fast advance of ice sheet, for a high lateral inflow into the model and high hydraulic conductivity	118
Figure 6.34	Pore pressure during a very slow advance of ice sheet and for a high lateral inflow into the model.....	121
Figure 6.35	Excess pore pressure during a very slow advance of ice sheet for a high lateral inflow into the model.....	122
Figure 6.36	Vertical Darcy flux in the Rupel Clay and Asse Member during a very slow advance of ice sheet, for a high lateral inflow into the model and high hydraulic conductivity	123
Figure 7.1	Finite element mesh for the detailed hydromechanical model	127

Figure 7.2	Geohydrological boundary conditions in the detailed hydromechanical model.....	131
Figure 7.3	Dynamics of the ice sheet movement.....	132
Figure 7.4	Initial hydrodynamic pore pressures	135
Figure 7.5	Initial effective stresses in the model.	136
Figure 7.6	a) Vertical effective stress, b) pore pressure, and c) vertical displacement with depth (Mohr-Coulomb model).....	137
Figure 7.7	a) Vertical effective stress, b) pore pressure, and c) vertical displacement with depth (Cam-Clay model) Average values of the Cam-Clay parameters were used.....	138
Figure 7.8	a) Vertical effective stress, b) pore pressure, and c) vertical displacement with depth (Cam-Clay model). Low values of the Cam-Clay parameters were used	139
Figure 7.9	Mohr-Coulomb material model for the Rupel Clay and Asse Member used in an ice-loading scenario	141
Figure 7.10	Modified Cam-Clay material model for the Rupel Clay and Asse Member used in two ice-loading scenarios	142
Figure 7.11	Effective stress path for element 1177 located in the middle of the Rupel Clay and Asse Member. a) Ice-loading scenario with low Cam-Clay parameters. b) Scenario with average parameters	143
Figure 7.12	Formation of the plasticity zone in the Rupel Clay and Asse Member modelled by a Cam-Clay model.	144
Figure 7.13	Horizontal Darcy flux shown for a 10 km long refined part of the detailed hydromechanical model.....	146
Figure 7.14	Pore pressure along horizontal sections	147
Figure 7.15	Vertical Darcy flux in the Rupel Clay and Asse Member during glaciation for various material models and values of hydraulic conductivity.	148
Figure 7.16	Preparation of the groundwater velocity fields for the transport model (METROPOL).....	149
Figure 8.1	Mesh used in the transport model.....	155
Figure 8.2	Contours mass fractions.....	161
Figure 8.3	Mass fraction of radio-isotope Se-79 relative to present-day condition.....	163
Figure 8.4	Mass fraction of radio-isotope Sn-126 relative to present-day condition.....	163
Figure 8.5	Mass fraction of radio-isotope Th-230 relative to present-day condition.....	164
Figure 8.6	Mass fraction of radio-isotope Np-237 relative to present-day condition.....	164
Figure 8.7	Mass fraction of radio-isotope U-238 relative to present-day condition.....	165

Figure 8.8	Mass fraction of radio-isotope Pu-242 relative to present-day condition.....	165
Figure A.1	Graph of void ratio (e) versus logarithm of the permeability (k) at various loadings.....	A.2
Figure B.1	Deviatoric stress versus the mean effective stress for Weelde (Belgium): 313.22 – 313.55 m (Case 1).....	B.1
Figure B.2	Deviatoric stress versus the mean effective stress for Weelde (Belgium): 314.22 – 315.10 m (Case 2).....	B.2
Figure B.3	Deviatoric stress versus the mean effective stress for Weelde (Belgium): 314.22 – 315.10 m (Case 3).....	B.2
Figure B.4	Deviatoric stress versus the mean effective stress for Weelde (Belgium): 314.22 – 315.10 m (Case 5).....	B.3
Figure B.5	Deviatoric stress versus the mean effective stress for Blija (The Netherlands): 454.50 - 455.00 m (Case 1).....	B.3
Figure B.6	Deviatoric stress versus the mean effective stress for Blija (Belgium): 561.50 – 561.85 (Case 3).	B.4
Figure B.7	Deviatoric stress versus the mean total stress for Weelde (Belgium): 313.22 – 313.55 m (Case 1).....	B.4
Figure B.8	Deviatoric stress versus the mean total stress for Weelde (Belgium): 314.22 – 315.10 m (Case 2).....	B.5
Figure B.9	Deviatoric stress versus the mean total stress for Weelde (B): 314.22 – 315.10 m (Case 3).	B.5
Figure B.10	Deviatoric stress versus the mean total stress for Weelde (Belgium) 314.22 – 315.10 m (Case 5).	B.6
Figure B.11	Deviatoric stress versus the mean total stress for Blija (The Netherlands): 454.50 - 455.00 m (Case 1).	B.6
Figure B.12	Deviatoric stress versus the mean total stress for Blija (The Netherlands): 561.50 – 561.85 m (Case 3).....	B.7
Figure C.1	Mineralogical analysis: Spectra on the clay for Weelde (B) - 313 m.....	C.1
Figure C.2	Mineralogical analysis: Spectra on the clay for Blija (NL) - 561 m.....	C.1

List of tables

Table 3.1	Stratigraphy of the Tertiary and Quaternary in the geological cross section (top down).	14
Table 3.2	Generic stratigraphic column, representative of a generic nuclear waste storage site, with description of geological units and an overview of their hydrogeological parameters.	17
Table 3.3	Strength parameters of the Rupel Clay and Asse Member.	18
Table 3.4	Geomechanical parameters, which characterise geological units along a generic stratigraphic column, representative of a generic nuclear-waste storage site.	19
Table 4.1	Origin of the samples	21
Table 4.2	Characteristics of the samples.	22
Table 4.3	Numerical values for the shear modulus (G).	27
Table 4.4	Planned consolidated and undrained triaxial tests (CTU) on the samples from Weelde (Belgium).	27
Table 4.5	Planned consolidated and undrained triaxial test (CTU) on the samples from Blija (The Netherlands).	28
Table 4.6	Planned oedometer tests on the samples from Weelde (Belgium) and Blija (The Netherlands).	28
Table 4.7	Samples from boring Weelde-1.	28
Table 4.8	Available samples from boring Blija.	30
Table 4.9	Characteristics of the samples – consolidated and undrained triaxial tests (CTU).	31
Table 4.10	Parameters determined from the oedometer tests.	31
Table 4.11	Atterberg limits for samples from Weelde and Blija.	33
Table 4.12	Shear strength parameters – consolidated and undrained triaxial tests (CTU).	36
Table 4.13	Numerical values for the shear modulus (G).	40
Table 4.14	Numerical values for the compressibility index.	41
Table 4.15	Numerical values for the swelling index.	41
Table 4.16	Permeability.	42
Table 4.17	Cam-Clay parameters.	47
Table 6.1	Schematisation of a generic geological cross-section in a simplified hydromechanical model and the parameters.	69
Table 6.2	Additional parameters required for Cam-Clay model for the Rupel Clay and Asse Member	70
Table 6.3	Parameters characterising friction along the fault according to the Coulomb friction model.	70
Table 6.4	Overview of the defined ice-loading scenarios.	78
Table 7.1	Geomechanical and geohydrological parameters for the model units in the detailed hydromechanical model.	129

Table 7.2	Fluxes and potentials used to define geohydrogeological boundary conditions in the detailed hydromechanical model	132
Table 8.1	Structure of the finite element mesh used for the transport simulations	154
Table 8.2	Retardation factor and K_d	157
Table 8.3	Amount of nuclides per container.	158
Table 8.4	Nuclide chains.....	159
Table A.1	Range of permeabilities resulting from the analysis of samples from the Boom Clay in the Western Scheld tunnel project.....	A.1

1 Introduction

The present document establishes the final report of the project TRACTOR, which is part of the CORA Research Programme, Phase 1 (1996-2000).

A central research theme in this programme is the retrievability of radioactive waste. Because of practical considerations, the guaranteed period of retrievability is limited. The geological barrier system in case of geological disposal must be able to isolate the waste for a long time after the period of retrievability.

One of the main research fields of radioactive waste management deals with the transport of radionuclides from the repository to the biosphere. There are a number of natural, climate driven mechanisms that may affect radionuclide migration. A number of aspects of these processes occurring in nature have already been studied, in particular in the OPLA Research Programme (1984-1993).

An aspect related to the transport in clays that deserves more attention finds its origin in the specific properties of clays, in particular in its compressibility and water content. Under present climate conditions the transport of radionuclides in structural undisturbed clay is mainly determined by diffusion, which is a slow process.

During a glacial period an ice sheet with a large thickness may cover the earth's surface. The ice exerts a *load* on the subsurface and might change the properties of the clay by water overpressure, compaction, or even hydro-fracturing of the sediment. This may have a substantial effect on the transport of radionuclides released from the waste, which is disposed in the clay.

Another important item refers to the *migration pathways* of radionuclides. The shortest vertical pathway is not necessarily the fastest transport route. A longer transport route via an aquifer below the clay barrier and through a vertical fault zone may lead to a shorter transport time and a higher radionuclide concentration in the shallow subsurface.

The *objective* of this project is to assess the influence of ice loading on the transport of radionuclides through the clay barrier. The project TRACTOR will exclusively deal with the natural flow system. Man- or waste-induced effects will not be considered.

The project will especially result in transport rates in clay under the influence of ice-loading, potential migration paths of radionuclides and related radionuclide doses in the shallow fresh groundwater system.

The project consists of two main parts:

- Modelling study of ice loading and radionuclide migration (TRACTOR).
- Experimental study of the potential effects of ice loading on clay (TRACTOR and TRACTOR- Appendices).

TNO-NITG is the main contractor in the project TRACTOR. Three subcontractors of TNO-NITG are involved in the project:

- Delft University of Technology (TUD): provenance of boundary conditions for the hydromechanical modelling and, modelling of radionuclide migration.
- Université Catholique de Louvain (UCL): execution of the experimental geomechanical programme for the purposes of TRACTOR. This project included also an experimental programme dedicated to the objectives of the mining design study in the project TRUCK-II. The results of this part of the experimental programme are extensively dealt with in the TRUCK-II report. In the present report a synopsis of the TRUCK-II experimental results is presented.
- GeoDelft (formerly Grondmechanica Delft): evaluation of available geomechanical information on ice-loading effects.

The subcontractors GeoDelft and UCL delivered four reports. Summarised versions of these reports are included in the present report. The contribution of the TUD is directly integrated in the final report of the project TRACTOR.

The reports of GeoDelft and UCL are:

- GeoDelft (1999a). Authors: C. Lehnen-de Rooij, E.J. den Haan & G.A.M. Kruse. Analyse van de doorlatendheid van de Klei van Boom bij hoge belastingen, nr. CO-383970/4, 18 p.
- GeoDelft (1999b). Authors: E.J. den Haan & G.A.M. Kruse. Bronnenonderzoek naar overconsolidatie van dikke Tertiaire kleipakketten in Nederland: Klei van Boom, nr. CO-383970/06, 24 p.
- Université catholique de Louvain (1999). Authors: S. de Cock & J.F. Thimus. Project TRUCK II – test results, 75 p.
- Université catholique de Louvain (2000). Authors: S. de Cock & J.F. Thimus. Project TRACTOR – test results, 146 p.

The final report starts with a brief review of earlier research on loading phenomena and the description of the modelling concept adopted for this study (Chapter 2). Next, in Chapter 3 the available data are described. The results of the geomechanical test programme are presented in Chapter 4. Chapter 5 provides a description of the various modelling tools and the way they are mutually coupled. The core of the report form the hydromechanical simulations described in Chapters 6 and 7. In Chapter 8 the effect of ice loading on the transport of radionuclides is presented. Conclusions are drawn in Chapter 9. The final chapter contains the references. A number of appendices at the end of the report contain background information.

2 Modelling concept of ice-sheet loading

2.1 Literature review

The studies investigating the effects of ice loading on the subsurface have been undertaken in different contexts and within different scientific disciplines such as glaciology, soil mechanics, geotechnics, etc. Of direct relevance to this project are studies related to the safety assessment of the underground waste repositories. In these studies the ice-loading effects are usually considered as a factor that can influence the superficial and ground water flow pattern. The response of geohydrological system is important in the long-term risk assessment studies as groundwater plays a dominant role in future release of radionuclides from repositories.

Several authors have carried out extensive studies of the subglacial hydrology. Shoemaker (1986) investigated subglacial hydrology for an ice sheet where the substrate consists of a deformable aquifer. This study focused on the creation of a system of subglacial water channels to evacuate basal melt water from beneath the ice and on the near-surface deformations near the terminus of ice sheet. Boulton & Hindmarsh (1987) studied the role of glacial hydrology in relation to sediment deformation beneath glaciers. Mooers (1990) studied the groundwater flow and thermal regime in relation to the occurrence of deformations in the marginal parts of ice sheets. Comprehensive studies of the glacier hydrology have been undertaken and published in several papers by Boulton and various co-workers (e.g. Boulton & Dobbie, 1993; Boulton et al., 1993; Boulton & Curle, 1997). They have developed an ice sheet model and assessed the influence of glaciation on the groundwater system. Further, a theory of subglacial consolidation is developed from which important properties of past glaciations can be inferred. Profiles through the sediments in the Netherlands were used to illustrate the concepts developed.

Van Weert & Leijnse (1996) also studied the effects of the Pleistocene glaciations on the Northwest European geohydrological system. A large-scale two-dimensional vertically integrated groundwater model was created for which boundary conditions were defined from palaeoenvironmental reconstruction of the last three glacial cycles. Results showed relatively high groundwater velocities and pressures in the subglacial areas and the ice-marginal permafrost area. Discharge of highly pressurised groundwater system mainly occurred in proglacial lakes, ice-marginal seas and zones of discontinuous permafrost, such as river valleys.

Various scenarios for groundwater flow studies that consider the effects of glaciation are often defined by using results of other modelling studies in which the climate and thermal regime of the past are simulated. A comprehensive, integrated

study of this type was undertaken in order to assess the effects of climatic changes on the safety of geological disposal sites (Boulton & Curle, 1997; EUR 17793). In this study the Mid- and Late Quaternary climate in west-Europe was reconstructed over the last 700 000 years including the last three cold stages.

The effects of ice loading in sedimentary basins were studied by Lerche et al. (1997). The main objectives of this study, for which the data set from the Barents Sea was utilised, were to simulate excessive pressure development, temperature development, hydrocarbon accumulation, porosity-permeability changes and basin geometry changes. The numerical model study showed that the overpressure could increase under steadily increasing ice cover and reduce under cyclic ice cover. Certain qualitative conclusions about the ice-induced fracturing and faulting were also drawn in this study.

The study of particular relevance to the project, in which glaciation is treated as a possible realistic scenario of natural evolution of a potential site for storage of nuclear waste, has been carried out by Modaresi et al. (1990; EUR 12503). The authors described simulations carried out to assess the rate of compaction of the subsurface and the change in the ground water flow system caused by a possible future ice loading. The sedimentary sequence of the Parisian basin in France was used to derive a generic geological cross-section and to develop a two-dimensional finite element hydromechanical model. Transient simulations were carried out in order to simulate the effects caused by steadily growing and advancing ice sheet over the study area. The behaviour of the modelled layers was assumed pure elastic. The most important parameters, which influenced the model response, were the speed of ice advance and hydraulic boundary conditions.

One of the important conclusions from this study is that the ground water flow system undergoes considerable changes with respect to the present situation. Gradients and fluxes in top layers increase one to two orders of magnitude. Ground water flows mainly in horizontal direction towards the terminal zone of ice sheet. At the same time, the excessive water pressure develops in low permeability layers under the weight of ice. This over-pressure decreases in time as the pore water dissipates from low permeability layers.

Prij & Benneker (1989) have simulated the dynamics of the temperature and stress fields around salt domes in case of a glaciation. According to their findings the permafrost in the Netherlands can reach a thickness of 200 m during a glacial stage. The ice-induced stress changes in the subsurface become stationary already after a few hundreds of years, if the soil materials are pure elastic.

Other important sources of information relevant to this project are geotechnical studies. Geological characterisation of the subsurface, which is regularly a part of these studies, requires estimation of the soil and rock properties. Previous (ice)

loading history of clay in particular has a considerable influence on the physical and mechanical properties of the clay as well as on its deformability. A study of this type was carried out by Schokking (1990) by investigating the properties and the deformation patterns of the overconsolidated Pot Clay. According to this author, the overconsolidation of the Pot Clay in the Northern Netherlands occurred under the weight of a 195 m thick Saalian ice sheet.

2.2 Modelling concept in TRACTOR

This section presents conceptualisation of hydromechanical processes caused by the impact of glaciation on the Tertiary clays and the groundwater system. First a brief review of the general aspects of glaciation is given, followed by description of its effects on the geohydrology and geomorphology of an area. Description of a glacial groundwater model is mainly based on the works of Boulton et al. (1993) and Van Weert & Leijnse (1996). This model is further expanded to incorporate geomechanical aspects related to the consolidation of the Rupel Clay and Asse Member, possible occurrence of plastic deformation in soil layers and fault reactivation.

Glaciation, glacial hydrology and deformation

The global cooling of the atmosphere marks the beginning of a glaciation. The drop in air temperature causes freezing of the uppermost parts of the subsurface and forming of the permanently frozen zone, i.e. permafrost. Over the permafrost accumulate masses of snow, that grow each year with every snowfall. The snow masses compact under their own weight to form the glacier ice. During glaciation large amounts of ocean water are stored in continental ice. Because of this, the sea level drops globally (usually more than 100 m) and the precipitation rates decrease in the periglacial zones marginal to the continental ice sheets.

Various types of soil deformations occur in the shallow subsurface under the weight of ice and abrasion caused by the movement of ice over the ground surface. Ice-pushed ridges and deep glacial basins are common examples of geomorphological forms typically found near the ice sheet terminus. Soils in particular are prone to subglacial deformations caused by shearing, fissuring, folding and consolidation. Schokking (1998) gives an indication of the depth within which such deformations can take place. According to his subglacial deformation model, a 40 m thick Pot Clay sequence was affected by intense shearing and folding in the northern Netherlands during the Saalian glaciation. At greater depths dominant mechanisms of soil deformation were consolidation and fissuring of (at present) overconsolidated very stiff Pot Clay. An important

conclusion that can be derived from this work was that various types of subglacial deformations mainly occur in the permafrost zone.

Ice sheets advance at various rates varying from a few centimetres to a few tens of metres per day. Because of thermal friction due to basal sliding of the ice over the ground, and the geothermal heat flux, glaciers melt basally. Meltwater from the base of ice sheets is discharged in a relatively thin subglacial zone and into the uppermost aquifers. Meltwater tends to flow radially outwards towards the ice sheet margin. The subglacial discharge at the ice/bed interface transports large quantities of sediments to varying distances, depending on its transporting power. The discharge of the surface run-off takes place beyond the margins of ice sheet, in rivers and other accumulations of water. The dynamics of the ice sheet affects the whole glacial drainage system. As the ice sheet advances and retreats, the river systems at the margins of the ice sheets shift and become buried. Large lakes along the ice margin and new glacial valleys beneath the ice form.

The groundwater flow pattern during glaciation is considerably different with regard to present. The continental scale of the ice sheet mainly controls the general flow pattern. Hydraulic gradients and groundwater flow velocities are increased one to two orders of magnitude in comparison with their present values. General direction of groundwater flow, as in the case of surface run-off, is radial outwards towards the ice sheet margin. High hydraulic pressure gradients in the near surface aquifers result in their complete flushing out during glaciations. On the other hand, the high gradients initiate soil deformation and eventually failure. Mechanical discontinuities (e.g. hydrofractures, tensile fractures) and processes such as liquefaction and hydraulic piping often occur. These features and processes initiate forming of various geomorphological phenomena such as near-terminus bulging, heaving (soil boiling, upwelling), forming of diapiric sand dykes, etc. Critical conditions for creation of these phenomena are commonly met ahead of ice sheet margins where the water outlets and gaps in permafrost occur. The gaps in permafrost, which acts as a low permeability layer, represent local zones of pressure release and convergent flow of groundwater. Generally, the processes of soil failure caused by increased hydraulic pressure lead to the forming of the preferential groundwater flow paths and to an increase in porosity and hydraulic conductivity.

Processes and key features incorporated in the model

Modelling objectives, scale of modelling and available modelling tools constrain selection of the processes to be modelled as well as the level of detail that can conveniently be incorporated into the model. The scale of the model in this study is regional and therefore small-scale features can neither be taken into account nor modelled. Both hydrogeological and geomechanical processes will be modelled by

the hydromechanical model which will be developed in this study. The processes related to the surface hydrology and sediment transport will be omitted as these can affect shallow subsurface only and as such are not of direct relevance. However, the boundary conditions for the hydromechanical model will take into account some important features derived from the glacial groundwater model.

In modelling the groundwater flow the following important factors will be taken into account (Figure 2.1):

- Meltwater infiltration, which provides significant discharge of water into the subglacial aquifer. Melting rates depend on several factors and can reach values of $m=0.02$ m/year.
- Permafrost, which represents an impermeable layer and acts as a confining layer to the subglacial aquifer. Permafrost reduces the aquifer thickness and therefore its transmissivity.
- Rivers, lakes and other water accumulations represent outlets where discharge of surface run-off and groundwater takes place.

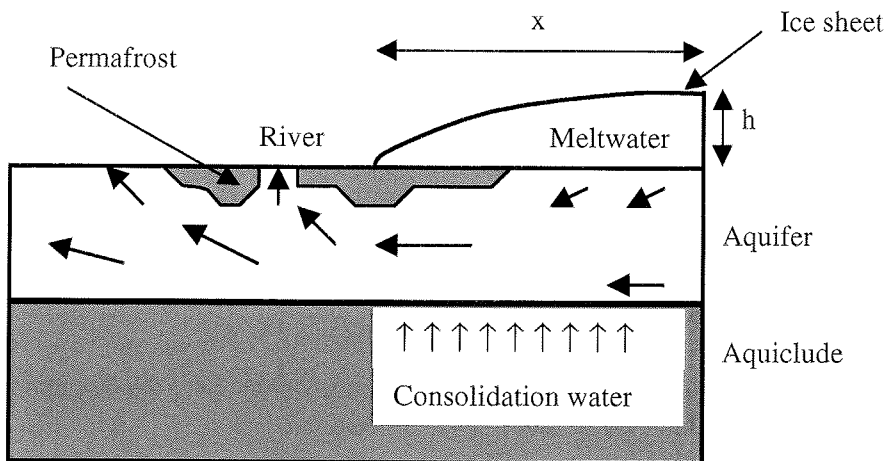


Figure 2.1 Schematic cross-section showing the groundwater flow pattern during glaciation. Subglacial meltwater is forced into a subglacial aquifer beneath the permafrost. Under the ice load an aquiclude compacts and releases consolidation water. Discharge takes place beyond the ice sheet margins where the permafrost terminates and unfrozen gaps in the permafrost, caused by rivers and lakes, occur (modified after Boulton et al., 1993).

In contrast to the previous glacial groundwater flow models, the consolidation of the Rupel Clay and Asse Member, which is a combined hydro- and geomechanical process, will be modelled and fully integrated with the groundwater flow model. Compression and consolidation of the subsurface, caused by the weight of ice, lead to the release of pore water from aquicludes into adjacent aquifers. Dissipation of

water from low permeability layers is a slow, long-term process. Consolidation-driven flow in low permeability layers, such as the Rupel Clay and Asse Member, may exceed the flow under natural hydraulic gradients several times.

Another important geomechanical aspect that will be explored is the deformability of the Rupel Clay and Asse Member under the weight of ice. The ice loads the subsurface, induces changes in the stress field and causes soil deformation. Plastic deformation in particular may lead to the forming of mechanical discontinuities in clays and subsequently to an increase in their permeability. In order to define the spatial and temporal extent of an ice sheet and the permafrost, a brief review of their geometry and dynamics is given below.

Geometry of ice-sheet

Ice-sheet profiles are frequently approximated by a parabolic shape:

$$h = A \sqrt{x} \quad (2.1)$$

- where: h = height above a horizontal base
 x = distance upstream from the terminus (see Figure 2.1).
 A = coefficient with a value of $A=4.7 \text{ m}^{1/2}$ for both the Antarctic ice sheet and the West Greenland ice sheet. In studies of late Pleistocene ice-sheet lobes within mountainous terrain of North America it has been estimated that A values range from 2.9 to 4.1.

The maximum thickness of an ice-sheet that in the future could cover the modelled area is estimated to be 1 km (J. v.d. Meer, pers. comm.).

The geometry of ice-sheet is needed to calculate the additional load due to the weight of ice. This load is a uniformly distributed load, which can be calculated by multiplying the ice thickness and the density of ice, which is equal to $\rho=917 \text{ kg/m}^3$.

Dynamics of ice-sheet

Three glaciations have affected The Netherlands during the Quaternary: the Weichselian (the youngest), the Saalian and the Elsterian stage. During the Weichselian glaciation the ice sheet did not reach The Netherlands. During the Saalian glaciation the ice sheet reached from Scandinavia down to the central parts of The Netherlands and the river Rhine. Schokking (1998) estimated that the minimum thickness of ice sheet during the Saalian in the northern Netherlands was

195 m. During the Elsterian glaciation only northern parts of The Netherlands were covered by ice sheet.

Comprehensive studies were carried out in order to reconstruct Mid- and Late Quaternary climate and to simulate spatial variation of the European ice sheet during the last glaciations (e.g. report EUR 17793). These have indicated the complexity of a glacial stage, which may comprise more than one glacial sub-stage alternating with the warming phases of temperate interglacial magnitude. In the Saalian stage, for which the climate and the dynamics of ice sheet movement have been simulated by Boulton et al. (1993), three distinct glacial sub-stages were determined. In The Netherlands these correspond to the maximum extent of ice sheet towards the south (peaks at 135, 145 and 155 ka B.P.; ka = thousand of years; B.P. = Before Present). The speed of ice sheet movement (advance and retreat) obtained in the same study varies from a few tens of metres to 200-300 m per year.

Permafrost

Before the ice starts accumulating and advancing over an area, the uppermost parts of the subsurface freeze and form a permanently frozen zone, i.e. permafrost. The permafrost represents impermeable ground that acts as a confining layer. It is often assumed that a permafrost zone spreads continuously and it has a constant thickness. Van Weert & Leijnse (1996) use a transmissivity value of $5 \text{ m}^2/\text{d}$ (i.e. hydraulic conductivity $K=6 \times 10^{-7} \text{ m/s}$), which is thought to be representative for permafrost.

The thickness of permafrost has been calculated by Marivoet et al. (1996) for the conditions at the Mol repository site in Belgium. For a realistic glaciation scenario, which assumes lowering of the groundwater table for a few tens of metres, the maximum thickness of permafrost is limited to about 100 m. If the present groundwater level stays unchanged during a future glaciation, which is a less likely scenario, permafrost would reach a depth of about 350 m. The time needed to reach the maximum thickness of permafrost is in most analysed cases 10,000 years.

At present day the thickness of the continuous permafrost in Inuvik, Canada, North West Territories, with an average air temperature of $-9 \text{ }^\circ\text{C}$, is about 100 m. At higher temperatures the permafrost becomes non-continuous and its thickness varies between 13 and 100 m (French, 1996). According to Brown (1970) the thickness of permafrost in the transition zone reaches 45 m. Furthermore, it is known that several other factors influence permafrost, such as the characteristics of ground surface, local and microclimate, hydrology, vegetation, and ground parameters such as grain size distribution, humidity and thermal conductivity. The geothermal conductivity of coarse sand is for example two times greater than that

of clay. In extreme cases this can cause differences in average temperatures of 5 - 10 °C over a distance of less than 160 m (Smith, 1975).

For the drilled tunnel underneath the Western Scheld, a traffic link currently under construction, the following reconstruction of permafrost during the last two glaciations has been made. Van Vliet-Lanoë (1989) suggested that continuous permafrost was present in the study area during the Weichselian glaciation in two time intervals: in the period about 60.000 years before present (BP), and from 28000 and 19000 years BP. The average air temperatures were ranging between -5 and -8 °C, and -5 en -9 °C, respectively. Morphological forms indicative of permafrost, about 50,000 years old, can be found in the Vlaamse valley (De Moor, 1983). In the interglacials, the permafrost was partly absent. During the Saalian glaciation, when the ice terminus advanced more to the south, the permafrost was continuous. It is, however, possible that unfrozen patches (*taliks*) interrupted some parts of the ground. In Alaska and Canada it has been shown that the transition between continuous and discontinuous permafrost takes place at an average air temperature of -6 to -8 °C (Brown, 1966). In conclusion, during the two last glaciations the area of the Western Scheld underwent the transition between the continuous and discontinuous permafrost a number of times. The maximum depth of permafrost likely did not exceed 45 m below the ground surface.

Next, the lateral extents of the permafrost underneath and ahead of the ice-sheet have to be estimated. The permafrost is discontinuous along rivers and underneath seas and lakes. River systems, located ahead of an ice-sheet terminus, follow the dynamics of the ice advance or retreat. This often limits the extent of the permafrost ahead of the terminus to a few kilometres. The extent of permafrost underneath the ice-sheet can considerably vary and ranges from a few kilometres to a few tens of kilometres.

3 Data inventory

This chapter presents a description of the geological section used to develop a hydromechanical finite element model and gives an overview of the available hydrogeological and geomechanical parameters.

3.1 Description of 2-D-transect

A geological profile was constructed for the specific needs of the hydromechanical modelling. This profile is considered to show a representative regional cross section through the Tertiary and the underlying and overlying formations in the subsurface of the Netherlands. The cross section is used for the construction of a generic model profile, as is described in Chapter 6. The outline of the geological profile is not determined by a specific location of the repository site. To this end, attention was given particularly to the presence of structural elements, stratigraphic relations and the depth and thickness of the Rupel Clay and Asse Member.

Data used to select the location of and to interpret the geological cross-section originate from the existing reports related to:

- Investigation of the geothermal potential of the Tertiary sands.
- Investigation of the low permeability formations of the Tertiary.
- CAR1 and CAR2 projects, carried out within the framework of the CORA Research Programme.

Preconditions for the selection of the geological profile are:

- The potential repository is assumed to be located in the Boom Clay (the Rupel Clay and Asse Member).
- The depth window of the Boom Clay lies within 500 and 800 metres below NAP.
- The repository lies at a depth ranging from 500 and 800 m below NAP.

From a geological perspective the following aspects were also taken into consideration:

- A favourable position in relation to areas in which rock deformation has taken place.
- A favourable, large thickness of the Rupel Clay and Asse Member.
- A favourable stratigraphic position in relation to directly underlying and overlying water bearing formations.
- A tighter control of the geological interpretation by the existing borehole data and the available data in the used reports.

Short description of the cross section

The geological profile runs in a north-south direction, along the expected direction of ice movement during a next ice age. The profile starts in Belgium, near the town of Mol and runs from there through Nijmegen, Apeldoorn, Steenwijk, Akkrum and Leeuwarden to the Waddenzee in northern Friesland. The profile crosses the Roer Valley Graben, the Mid Netherlands High and runs subsequently along the eastern extension of the Zuiderzee Low towards the north (Figure 3.1).

The locations of the most important structural elements in the Cenozoic are given in Figure 3.2. The formations distinguished in the profile are summarised in Table 3.1. Some formations are not present over the entire length of the cross section. A number of formations pinch out laterally or have been eroded completely or have not been deposited at all.

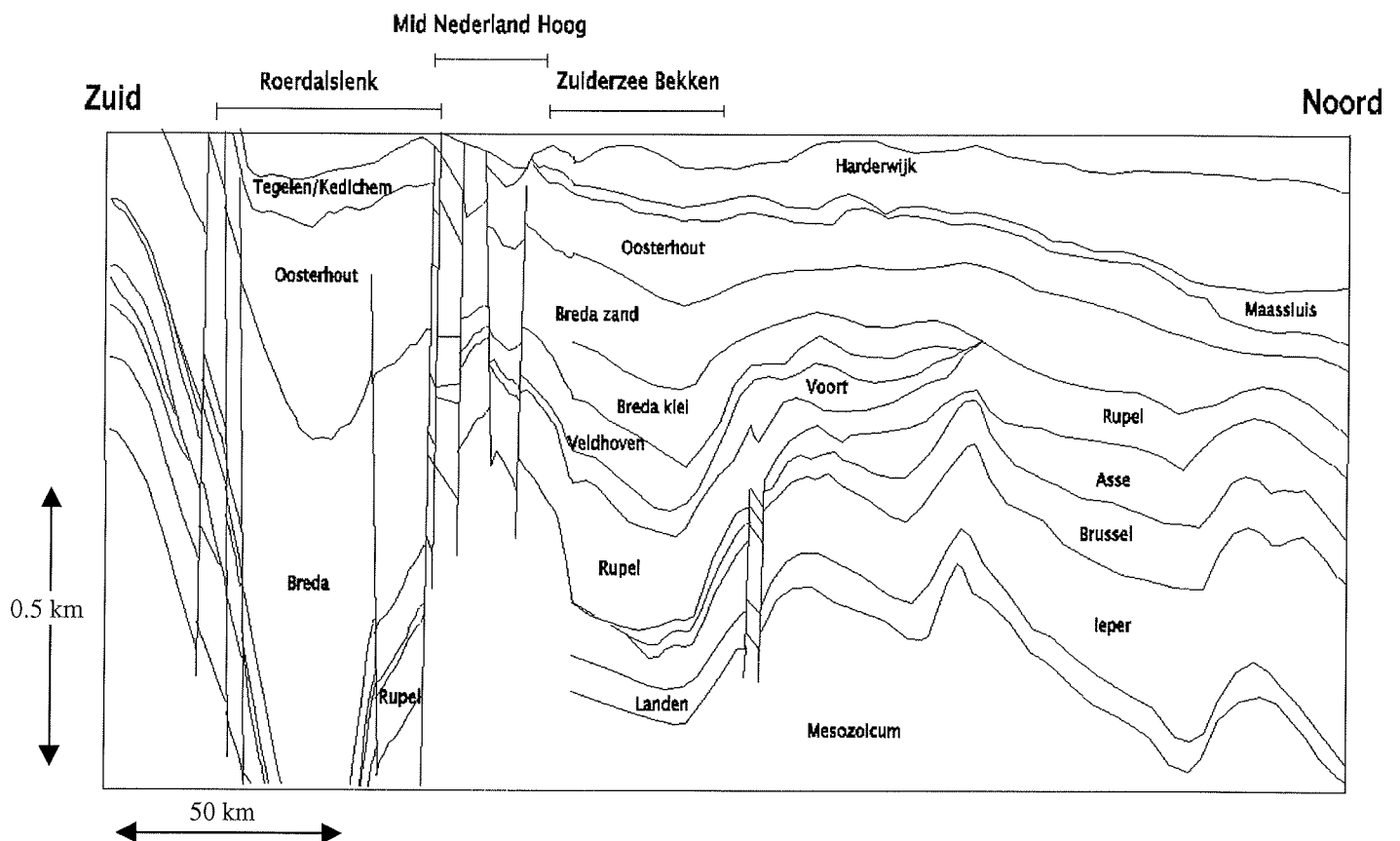


Figure 3.1 Representative geological cross-section through the subsurface in the Netherlands.

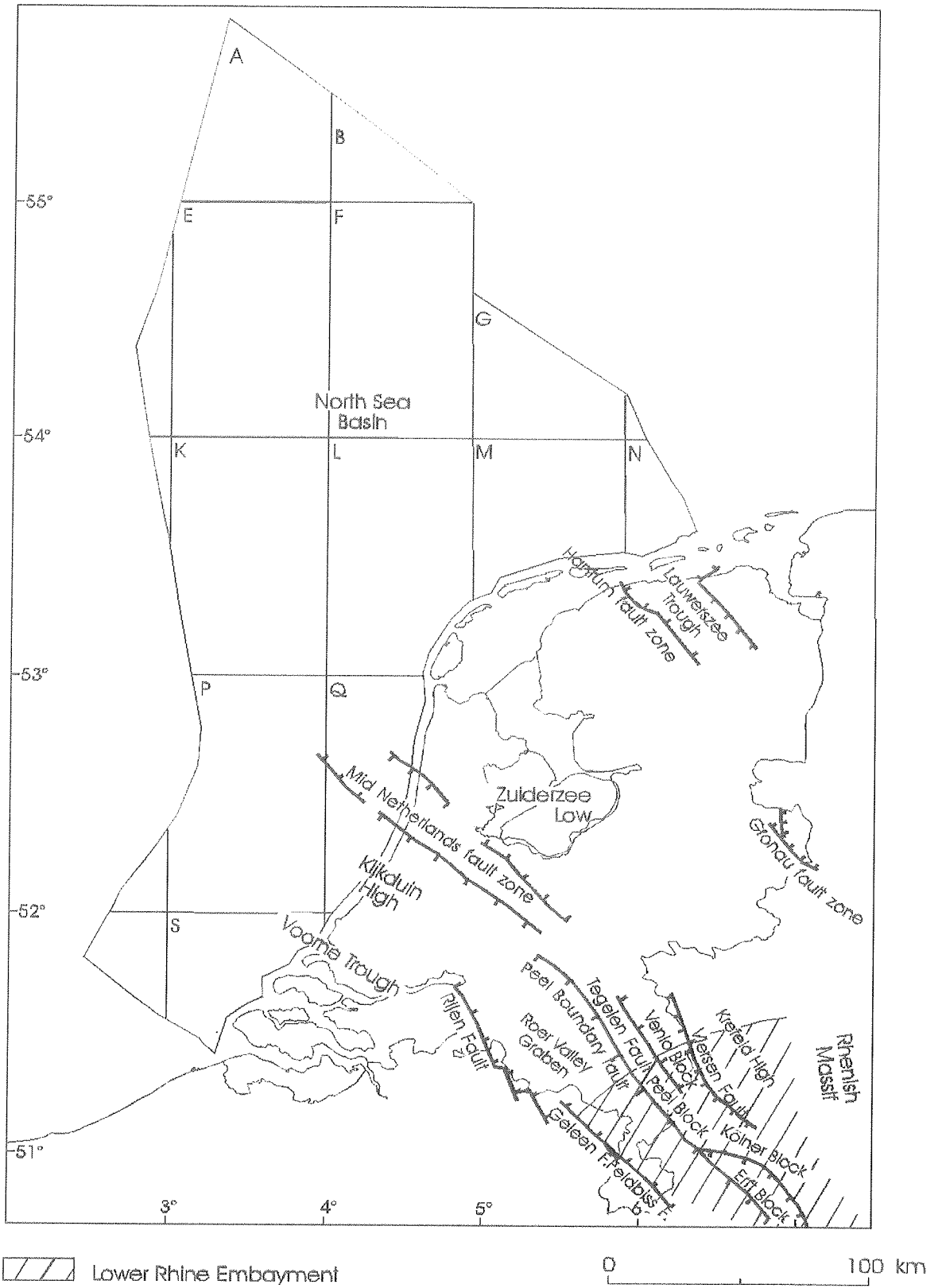


Figure 3.2 Structural map.

Table 3.1 Stratigraphy of the Tertiary and Quaternary in the geological cross section (top down).

Unit	Lithology	Thickness (m)	Remarks
<i>Div. Quaternary fm.</i>	<i>sand/clay</i>	<i>30-100</i>	<i>alternating discontinuous sand and clay</i>
<i>Tegelen/Kedichem</i>	<i>clay</i>	<i>50-100</i>	<i>clay bodies in Roer Valley Graben</i>
<i>Harderwijk</i>	<i>sand</i>	<i>0-200</i>	<i>highly permeable Quaternary sand</i>
<i>Maassluis</i>	<i>sand</i>	<i>25-100</i>	<i>shelly sand, intercalated clay layers</i>
<i>Oosterhout</i>	<i>sand/clay</i>	<i>50-400</i>	<i>sandy clay alternating with sand lenses</i>
<i>Breda</i>	<i>sand/clay</i>	<i>50-300</i>	<i>local clay basis, rest sandy clay</i>
<i>Veldhoven</i>	<i>clay</i>	<i>0-75</i>	<i>sandy clay, present in the south</i>
<i>Voort</i>	<i>sand</i>	<i>0-75</i>	<i>present in the south</i>
<i>Rupel</i>	<i>clay</i>	<i>50-200</i>	<i>Boom clay with 20 m Berg sand at base</i>
<i>Asse</i>	<i>clay</i>	<i>0-100</i>	<i>plastic clay; in northern half</i>
<i>Brussel</i>	<i>sand</i>	<i>0-100</i>	<i>present in northern half</i>
<i>Ieper</i>	<i>clay</i>	<i>50-300</i>	<i>base up to 30 m thick Dongen sand/tuffite</i>
<i>Landen</i>	<i>clay</i>	<i>50-100</i>	<i>base ± 20 m thick Heers sand</i>
<i>Mesozoic</i>	<i>carbonate</i>	<i>>400</i>	<i>chalk group, bad permeability</i>

The Boom Clay is part of the Rupel Formation (Middle North Sea Group) and was deposited in a marine environment. It consists of stiff, dark-brown to grey clays. A gradual transition to sands occurs towards the base and top of the Boom Clay.

The sands at the base of the Boom Clay belong to the Vessem Formation (Berg Sand, according to the old nomenclature) and are up to 20 m thick along the length of the profile. A gradual transition in the top of the Boom Clay results in the sandy Steensel Member (Rupel Formation). The Vessem Formation is discernible in the boreholes used along the profile.

Overlying formations are the Voort Sand and the Veldhoven Clay (Middle North Sea Group), which are subsequently overlain by the Breda Formation (Upper North Sea Group). The Breda Formation is present along the entire cross section, whereas the Voort Sand and the Veldhoven Clay pinch out towards the North.

Consequently, north of the pinch out clayey sands of the Breda Formation overlie the Boom Clay.

The underlying formations consist of respectively the Asse Clay and the Brussel Sand belonging to the Dongen Formation (North Sea Group). Both cover the Ieper Clay of the same formation. The Ieper Clay Member is present in the entire profile, whereas the Asse Clay and the Brussel Sand pinch out towards the south and subsequently reappear near the Belgium border.

Characteristic elements in the geological profile are:

- The presence of the Mid Netherlands Fault Zone (Mid Netherlands High). It is present in the southern part of the profile.
- The presence of highs and depressions which are clearly visible in the central and northern parts of the profile.
- Lateral pinch out of rock units, resulting in changing rock characteristics of the over and underlying units of the Boom Clay.

3.2 Hydromechanical parameters derived from literature

The parameters were derived from the existing available reports and literature, and, whenever possible, they rely on data published in reports that have been carried out within the scope of the CORA research programme. In this sense the parameters characterising the Tertiary clay layers were mainly derived from the CAR2 project (NITG-TNO, 1998) which gives a summary of the hydromechanical parameters relevant to this study.

3.2.1 Geohydrological parameters

The two geohydrological parameters required in this study are effective porosity (n) and hydraulic conductivity (K). An overview of these parameters, representative of the geological units found along a generic geological cross-section, is presented in Table 3.2. For each of the differentiated geological units, whenever possible, a range of values published in the literature is given rather than a representative average value. For most units data on directional dependence of hydraulic conductivity, i.e. anisotropy, were not available.

The review of data sources shows that abundant and reliable data are available to characterise the Quaternary and the upper Tertiary sandy layers (down to the Maassluis Formation and the Oosterhout Formation). In various parts of the Netherlands these layers represent aquifers important for water supply. Their geohydrological properties are locally well known and they are based on direct in-situ (well test) and lab test, as well as on indirect relationships derived from the granulometry and borehole logs.

The geohydrological properties of deeper Tertiary aquifers, not exploited for water-supply purposes, are based on lab-measurements on cores taken from deep boreholes and derived indirectly from geophysical logs. Typically, 10 to 20 boreholes were available for each geological unit.

The geohydrological properties of the Tertiary clay layers were taken over from the CAR2 report (NITG-TNO, 1998) and, for the Rupel Clay and Asse Member, from

the results obtained by the laboratory testing programme carried out within the scope of this project. The amount of available data was very small and some of the parameters had to be derived indirectly from geophysical logs. The exception is the Rupel Clay and Asse Member whose geohydrological properties were extensively tested at the Mol site in Belgium and at the Western Scheld site (see also Appendix A). The parameters from these two sites are rather indicative than representative of a potential nuclear-waste storage site in the Rupel Clay and Asse Member in the Netherlands. This is because the Rupel Clay and Asse Member are lithologically heterogeneous, with the rhythmic succession of clayey and silty beds. Consequently, its hydrological properties will vary spatially. Furthermore, neither of the two sites is at a depth approximately corresponding to the depth at which a potential nuclear-waste repository may be located (500 to 800 m deep from the ground surface).

3.2.2 Geomechanical parameters

An overview of geomechanical parameters, representative of the geological units along a generic geological cross-section, is presented in Table 3.3 and Table 3.4. These parameters determine physical and mechanical properties of the materials that compose geological units. Physical parameters of interest here are unit weight in saturated condition (γ), dry unit weight (γ_d), and porosity (n).

A range of mechanical parameters, which for most of the geological units were not available, determines the strength and deformability of geological materials. This implies that even for a commonly used Mohr-Coulomb model of material's behaviour the shear strength parameters, such as the angle of internal friction (ϕ) and cohesion (c), as well as the parameters on deformability, such as Young's modulus (E) and Poisson's ratio (ν), will have to be derived indirectly. Generally, the lack of geomechanical data at greater depths is common due to the fact that most of the construction activity, in the context of which geomechanical parameters need to be acquired, takes place within a few tens of metres from the ground surface.

Additional geomechanical parameters are required to adequately represent and model elasto-plastic behaviour of the Rupel Clay and Asse Member by using the Cam-Clay model for soil. Besides the angle of internal friction (ϕ) and cohesion (c), the model parameters comprise compression index (λ), swelling index (κ) and preconsolidation stress (p_c'). In order to determine these parameters additional geomechanical laboratory tests were carried out (see Chapter 4). For comparative purposes both the newly obtained Cam-Clay parameters and the existing parameters determined on the soil samples taken at the Mol site (Belgium) are presented in Table 3.3.

Table 3.2 Generic stratigraphic column, representative of a generic nuclear waste storage site, with description of geological units and an overview of their hydrogeological parameters.

Stratigraphy		Lithology	Porosity n [%]	Hydraulic conductivity K [m/s]	Reference*	
Quaternary	Various formations	Sand, silt, clay and peat	35 - 40	$<1.15 \times 10^{-7}$	EUR	
	Harderwijk Formation	Sand, coarse	-	$2.3 \times 10^{-4} - 2.3 \times 10^{-3}$	GHK	
	Tegelen Formation	Clay, peat	-	$5.8 \times 10^{-5} - 2.3 \times 10^{-4}$	GHK	
	Kedichem Formation	Clay	-	$<5.8 \times 10^{-5}$		
Tertiary	Maassluis Formation	Sand, fine to coarse, interbedded with clay intervals	32 - 35	5×10^{-5}	RGD(83,4)	
	Oosterhout Formation	Sand, at the base and top of formation, and clay, sandy	35	$2.1 \times 10^{-4} - 1 \times 10^{-9}$	CAR2	
				$1 \times 10^{-7} - 1 \times 10^{-9}$	CAR1	
	Breda Formation	Sand, very fine, interbedded with siltstone	27 - 30	$2 \times 10^{-5} - 6 \times 10^{-5}$	RGD(83,4)	
				$1 \times 10^{-6} - 2 \times 10^{-5}$	CAR2	
	Veldhoven Formation	Clay, interbedded with layers of sand	40 - 50	$1.9 \times 10^{-6} - 2.5 \times 10^{-6}$	RGD(83,4)	
				1×10^{-9}	CAR2	
	Veldhoven Formation	Veld. Clay Mb.	Clay, silty to sandy	40 - 50	$8 \times 10^{-6} - 2.1 \times 10^{-7}$	CAR2
		Voort Mb.	Sand, very fine and clayey	-	$1 \times 10^{-5} - 1 \times 10^{-6}$	RGD(85)
	Rupel Formation	Offshore	Clay	36	-	CAR2
		Western Scheld	Clay, moderately to very silty	33 - 49	$1 \times 10^{-11} - 40 \times 10^{-9}$ (hor. - vert.)	-in situ
	Mol (Belgium)	Clay, silty clay and sand in rhythmic succession	35 - 40	$1.3 \times 10^{-12} - 3.4 \times 10^{-12}$	-lab.	
				$2.1 \times 10^{-12} - 4.5 \times 10^{-12}$ (hor. - vert.)	-in situ	
	Asse Mb.	Clay, homogeneous, plastic	-	-	CAR2	
Dongen Formation	Brussels sand Mb.	Sand, very fine, silty and clayey	30 - 35	$0.6 \times 10^{-5} - 6 \times 10^{-7}$	RGD(83,4)	
				$2 \times 10^{-6} - 6 \times 10^{-6}$	RGD(85)	
leper Mb.	Clay, homogeneous, plastic	40 - 50	5×10^{-7} (sand, clayey)	CAR2		
Landen Formation	Clay, sandy and silty, compact	15- 17	$<1 \times 10^{-8}$	CAR2		
Mesozoic	Jurassic/Triassic	Various lithology	<25	$<1 \times 10^{-7}$	EUR	
	Triassic Buntsandstone	Sandstone	<25	$<1 \times 10^{-5}$	EUR	
Paleozoic (non-differentiated)	Paleozoic	Evaporites	Impervious base	impervious base		

* Complete overview of the used references can be found in the References according to the following scheme: CAR1 = Rijks Geologische Dienst (1996); CAR2 = Nederlands Instituut voor Toegepaste Geowetenschappen TNO (1998); EUR = EUR 17793 EN (1997); GHK = TNO, Rijksinstituut voor Drinkwatervoorziening, Rijks Geologische Dienst (1976); RGD(83,4) = Rijks Geologische Dienst en TNO (1983), *ibid.* (1984); RGD(85) = Rijks Geologische Dienst (1985); see also Appendix A.

The parameters on the undrained shear strength of the Rupel Clay and Asse Member at Western Scheld are about five times lower than those determined at the Mol site. The observed difference in strength can be explained by a higher preconsolidation stress at the Mol site.

Table 3.3 Strength parameters of the Rupel Clay and Asse Member.
*For explanation of the references see Table 3.4.

Strength parameters	Location				
	Western Scheld	Mol, Belgium		Doel 2b, Zoersel, Mol, Weelde, Blija	
	Reference*				
	CAR2	Volckaert, 1997		TRACTOR / TRUCK II	
	Undrained	Undrained	Drained	Undrained	Drained
Undrained strength q_u [Mpa]	0.2 - 0.45	2.0 - 2.2	-	0.8 - 2.6**	-
Young's modulus E [Mpa]		200 - 400 (stat)	300	180 - 600	
Poisson's ratio ν		0.4 - 0.45	0.125 - 0.2		
Cohesion c [kPa]		0.9 - 1 (triaxial test) 0.7 - 0.8 (direct shear)	300	125 - 1110 300 - 1800 (CTU - consolidated and undrained test)	135 - 715 100 - 1800 (effective cohesion)
Angle of internal friction ϕ' [°]		4	18 - 22	15 - 6 2 - 9.5	18 - 9 2 - 13
Compression index λ		-	0.11 - 0.16		0.07 - 0.22 0.14 - 0.24
Swelling index κ		-	0.02 - 0.05		0.01 - 0.02 0.06
Preconsolidation stress p_c' [MPa]	1 - 2	-	5 - 6		6.5 - 8.7

**Low stiffness for shallow sites.

Table 3.4 Geomechanical parameters, which characterise geological units along a generic stratigraphic column, representative of a generic nuclear-waste storage site.

Stratigraphy		Saturated unit weight γ [kN/m ³]	Dry unit weight γ_d [kN/m ³]	Young's modulus E [MPa]	Seismic velocity V_p [m/s]	Reference*
Various formations						
Quaternary	Harderwijk Formation (sand, coarse)					
	Tegelen Formation					
	Kedichem Formation (clays)					
Tertiary	Maassluis Formation (sand, fine)					
	Oosterhout Formation (sand and clay)					
	Breda Formation (sand, at the top and clay, at the base)					
	Veldhoven Formation					
Quaternary	Veld. Clay Mb.					
	Voort Mb.					
	Offshore			2250-3500 (dyn)	1825-2073	CAR2
	Rupel Formation Western Scheld	19 - 21	15 - 16			CAR2
	Mol (Belgium)	20.1	16.3	200-400 (stat)	1852	CAR2
	Various locations	19.2 - 20.2	15.1 - 16.3	180 - 600		TRACTOR
	Asse Mb.	20.1	16.3		1742-2898	CAR2
Dongen Formation	Brussels Sand Mb.					
	Ieper Mb.	20.5	16.1			CAR2
		17.5 - 19.5	13 - 15			Thimus, p.c.
Landen Formation				1847-2258	CAR2	
		17.9	13.1			Thimus, p.c.
Mesozoic	Jurassic/Triassic					
	Triassic Buntsandstone					

* Complete overview of the used references can be found in the References according to the following scheme: CAR2 = Nederlands Instituut voor Toegepaste Geowetenschappen TNO (1998); Thimus, p.c. = Thimus, J.F., personal communication.

4 Additional mechanical experiments

The project TRACTOR contains an experimental programme on the hydromechanical behaviour of the Rupel Clay (Boom clay). The Université Catholique de Louvain has carried out hydromechanical tests on sample material from Belgium and the Netherlands.

The test programme is composed of 12 triaxial tests and 4 oedometric tests on samples coming from Weelde (Belgium) and additional 6 triaxial tests and 2 oedometric tests on samples coming from Blija (NL). The methods and techniques used for testing are described in Section 4.4.

This programme is the follow-up of the test series carried out for the project TRUCK II, in which the mine design is modelled (SCK·CEN et al.). A few important results are presented here to characterise the samples from Weelde and Blija in relation to the others samples coming from 3 other sites in Belgium. For more in-depth information on the test programme for the project TRUCK II reference is made to the draft report of the Université Catholique de Louvain (1999) and to reports of the project TRUCK II itself.

4.1 Brief review of the test programme for TRUCK II

The samples in the experimental programme for TRUCK II came from 5 different places, 4 situated in Belgium and 1 in the Netherlands. Each site corresponds with a different depth interval (Table 4.1).

Table 4.1 *Origin of the samples in the TRUCK II programme. The sample intervals of interest for the test programme designed for the objectives in the project TRACTOR are in bold type.*

Well site	Depth interval (m)
Doel 2b (B)	69.23 - 69.68
Zoersel (B)	120.47- 121.22
Mol (B)	224.52- 225.06
	229.18 229.28
Weelde (B)	313.22- 313.55
Blija (NL)	454.50- 455.00
	478.00- 478.50

Sedimentologically two groups of clays can be differentiated:

- The first group with the samples from Doel (69m), Zoersel (120m) and Mol (229m) with less fines than in the samples from the second group.

- The second group consisting of the samples from Mol (224m), Weelde (313m) and Blija (455m).

4.1.1 Characteristics of the samples

The selection of the geomechanical samples in the Doel, Zoersel, Mol, Weelde and Blija cores has been done after tomographic scanning of the cores.

Table 4.2 summarises the dry, saturated and specific weights and the initial and saturated water contents of the samples. Figure 4.1 and Figure 4.2 represent respectively the evolution of the dry, saturated and specific weights and the evolution of the initial and saturated water contents versus the depth. The wet and dry densities increase linearly with depth, indicating an increasing consolidation with depth.

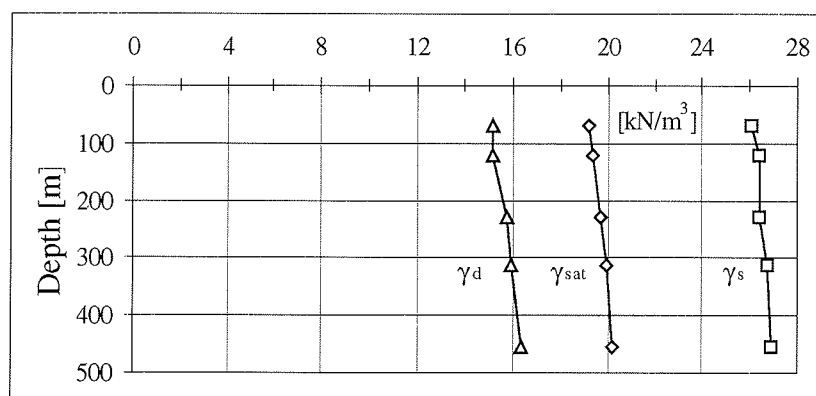


Figure 4.1 Dry, saturated and specific weights versus depth.

Table 4.2 Characteristics of the samples.

Origin	γ_d [kN/m ³]	γ_{sat} [kN/m ³]	γ_s [kN/m ³]	$w_{initial}$ [%]	w_{sat} [%]	S_r [%]	n [%]
Doel (B)	15.11	19.19	26.07	27.25	27.00	100.93	42.03
Zoersel (B)	15.11	19.30	26.41	27.30	27.70	98.56	42.76
Mol (B)	15.69	19.68	26.43	25.20	25.42	99.12	40.64
Weelde (B)	15.79	19.79	26.70	24.92	25.35	98.30	40.88
Blija (NL)	16.34	20.15	26.89	23.31	23.52	99.09	39.23

4.1.2 Sedimentation analysis

To verify the homogeneity of the samples, a particle size analysis by sedimentation was done for each site, one for Doel, Zoersel, Weelde and Blija, but two for Mol, due to the 5 m depth difference between the samples. These analyses are given in Figure 4.3.

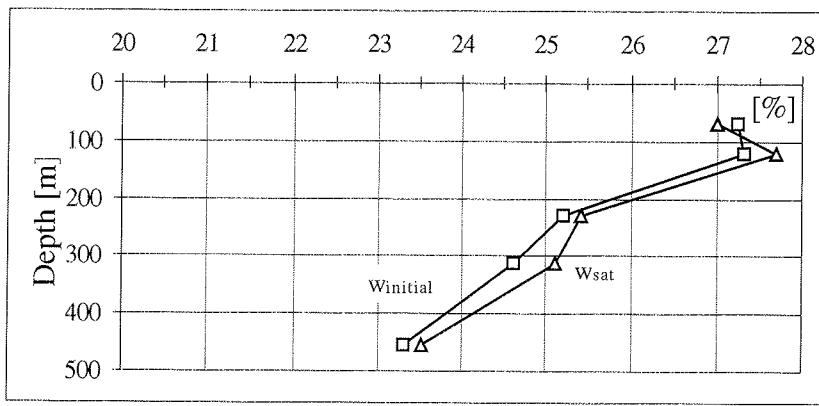


Figure 4.2 Initial and saturated water content versus depth.

Particle size analysis

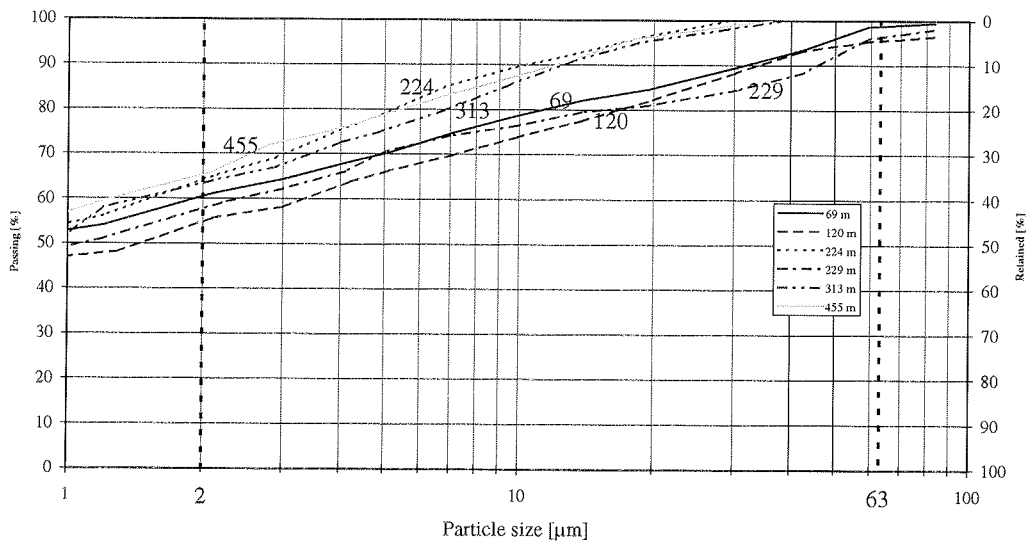


Figure 4.3 Sedimentation analysis for Doel (69 m), Zoersel (120 m), Mol (224 and 229 m), Weelde (313 m) and Blija (455 m).

4.1.3 Results

Shear strength parameters

Each triaxial test was performed on a series of 3 samples, confined at about in situ effective stress σ'_o , $1.5 \cdot \sigma'_o$ and $2 \cdot \sigma'_o$.

The values of the shear strength parameters for the soil are calculated from the linear regression coefficients in the p'-q and p-q diagrams and are given in Figure 4.4 and Figure 4.5. The mechanical test results are coherent, except for the cohesion at failure (shear strength parameter, see Figure 4.4). Due to the difference in terms of cohesion between the results of Weelde (313 m) and the others, a second series of tests on samples from Weelde was realised. The new values are plotted with ■ and ▲ in the Figure 4.4 and Figure 4.5.

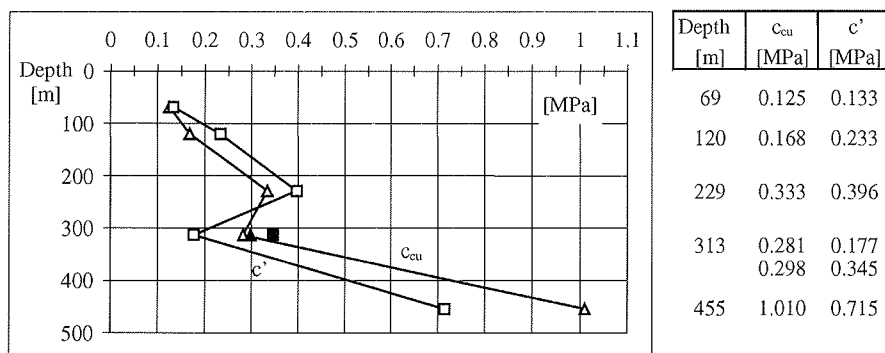


Figure 4.4 Cohesion versus depth.

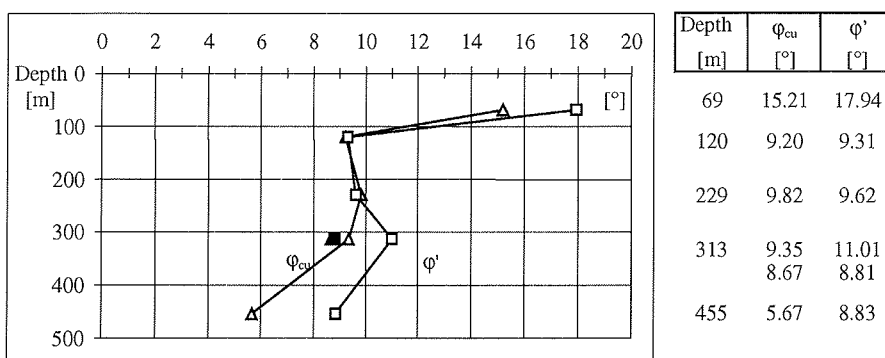


Figure 4.5 Friction angles versus depth.

Modulus of shear deformation

The shear modulus (G) is the ratio between a given shear stress change and the corresponding shear strain change. We can estimate its value owing to the loading-unloading cycle realised during the consolidated and undrained triaxial test (CTU). The loading-unloading loop provides Young's modulus because the relationship between shear modulus and Young's modulus for uniaxially compressed samples is:

$$E = 2(1 + \nu) G \quad (4.1)$$

where: E = Young's modulus,
 ν = Poisson's ratio,
 G = shear modulus.

For undrained conditions, if we assume that $\nu = 0.5$, it follows that $E = 3 \cdot G$. Therefore, G is one third of the mean slope of the cycle in the p - q' diagram. Then we have 18 values of this modulus (Figure 4.6 and Table 4.3).

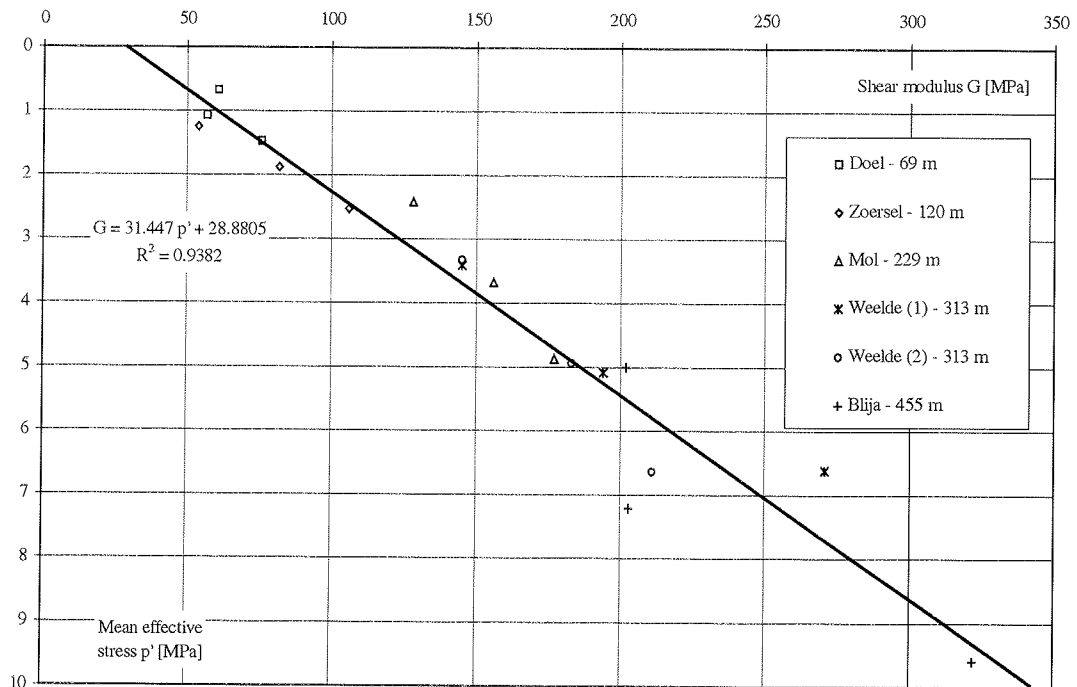


Figure 4.6 Shear modulus (G) versus the mean effective stress.

4.2 The initial test programme for TRACTOR

The tests planned to undertake on the clay samples from Weelde consist of 9 consolidated undrained triaxial tests and 6 oedometer consolidation tests. The characteristics of the planned consolidated and undrained triaxial tests (CTU) are given in Table 4.4 and Table 4.5. The characteristics of the planned oedometer tests are given in Table 4.6.

The CTU tests for case 1 of Weelde and case 1 of Blija were performed in the project Truck II. Due to the maximum cell pressure of the equipment of 10 MPa, case 4 for Weelde and case 4 for Blija were not performed. Case 2 for Blija was not performed due to a misunderstanding about availability of sample material. Case 3 for Blija was performed on the Asse member.

4.3 Description of sample material

In order to obtain characteristics from the Tertiary clays at levels as close as possible to the modelled depth (500 to 800m), fresh samples were secured from deep boreholes in Belgium and the Netherlands. Then samples were derived from a borehole commissioned in 1998 by NIRAS in Weelde, approximately 30 km north of Mol, and from a borehole performed for scientific purposes by NITG-TNO in Blija, approximately 20 km north of Leeuwarden.

Samples from Weelde

Three samples from boring Weelde-1 were obtained for the TRUCK II and TRACTOR tests (Table 4.7). In order to permit correlation between the results from the different Belgian boreholes all samples were taken from the Putte Member. The samples were taken with a sample tube of 1 m length and 100 mm diameter, which was pushed into the bottom of the borehole. The samples were retrieved by wireline after overcoring with a hollow 244 mm drillstring. The samples were extruded after retrieval and packed under vacuum in aluminium-lined plastic foil. It was noted that the samples had a tendency to swell when they were extruded directly after retrieval. In one instance a sample exploded upon extrusion and there was evidence of gas bubbles in the sample. All care was taken to prevent these effects of rapid unloading from the relatively deep levels.

Table 4.3 Numerical values for the shear modulus (G).

Location	Sample	Depth [m]	Mean effective stress p' [MPa]	Shear modulus G [MPa]
Doel (B)	a	69.42	0.67	61
	b	69.42	1.07	57
	c	69.42	1.48	76
Zoersel (B)	a	120.57	1.25	54
	b	120.57	1.88	82
	c	120.67	2.54	106
Mol (B)	a	229.23	2.42	128
	b	224.52	3.68	156
	c	224.52	4.87	177
Weelde (B)	a	313.30	3.42	145
	b	313.30	5.09	194
	c	313.30	6.62	271
Weelde (B)	a	313.30	3.34	145
	b	313.30	4.95	183
	c	313.30	6.64	211
Blija (NL)	a	454.75	5.00	202
	b	454.75	7.21	203
	c	454.75	9.60	322

Table 4.4 Planned consolidated and undrained triaxial tests (CTU) on the samples from Weelde (Belgium).

Test	Sample	Depth [m]	Consolidation of the samples σ_c' [MPa]	Simulated condition
Case 1	a	313.22	3.10	Present in situ stress
	b	to	4.70	
	c	313.55	6.26	
Case 2	a	314.22	2.28	Elevated pore pressure, no ice load
	b	to	3.20	
	c	315.10	4.12	
Case 3	a	314.22	3.62	Ice load and elevated pore pressure
	b	to	5.00	
	c	315.10	6.38	
Case 4	a	314.22	9.30	Ice load and normal pore pressure
	b	to	12.40	
	c	315.10	15.50	
Case 5	a	314.22	5.43	Intermediate ice load and pore pressure
	b	to	7.41	
	c	315.10	9.39	

Table 4.5 *Planned consolidated and undrained triaxial test (CTU) on the samples from Blija (The Netherlands).*

Test	Sample	Depth [m]	Consolidation of the samples σ_c' [MPa]	Simulated condition
Case 1	a	454.50	4.60	Present in situ stress
	b	to	6.90	
	c	455.00	9.20	
Case 2	a	454.00	0.50	Elevated pore pressure, no ice load
	b	to	0.70	
	c	454.30	0.90	
Case 3	a	561.50	5.00	Ice load and elevated pore pressure
	b	to	7.50	
	c	561.85	9.80	
Case 4	a	478.50	10.80	Ice load and normal pore pressure
	b	to	14.65	
	c	479.00	21.50	

Table 4.6 *Planned oedometer tests on the samples from Weelde (Belgium) and Blija (The Netherlands).*

Origin	Depth [m]	Maximum load [MPa]
Weelde	313.55 – 314.05	9
	314.22 – 315.10	12
	313.55 – 314.05	16
	313.55 – 314.05	19
Blija	453.50 – 453.80	20
	561.50 – 561.85	20

Table 4.7 *Samples from boring Weelde-1.*

Sample no.	Depth interval
86	312.3 – 313.1m
87	313.1 – 314.05m
88	314.05 – 315.1m

Samples from Blija

The samples that were available from the boring Blija, are listed in Table 4.8. The samples were taken with a percussion sampler. All samples are present in steel tubes with a length of 40 cm and a diameter of 63 mm, which were sealed with wax and rubber caps at both ends.

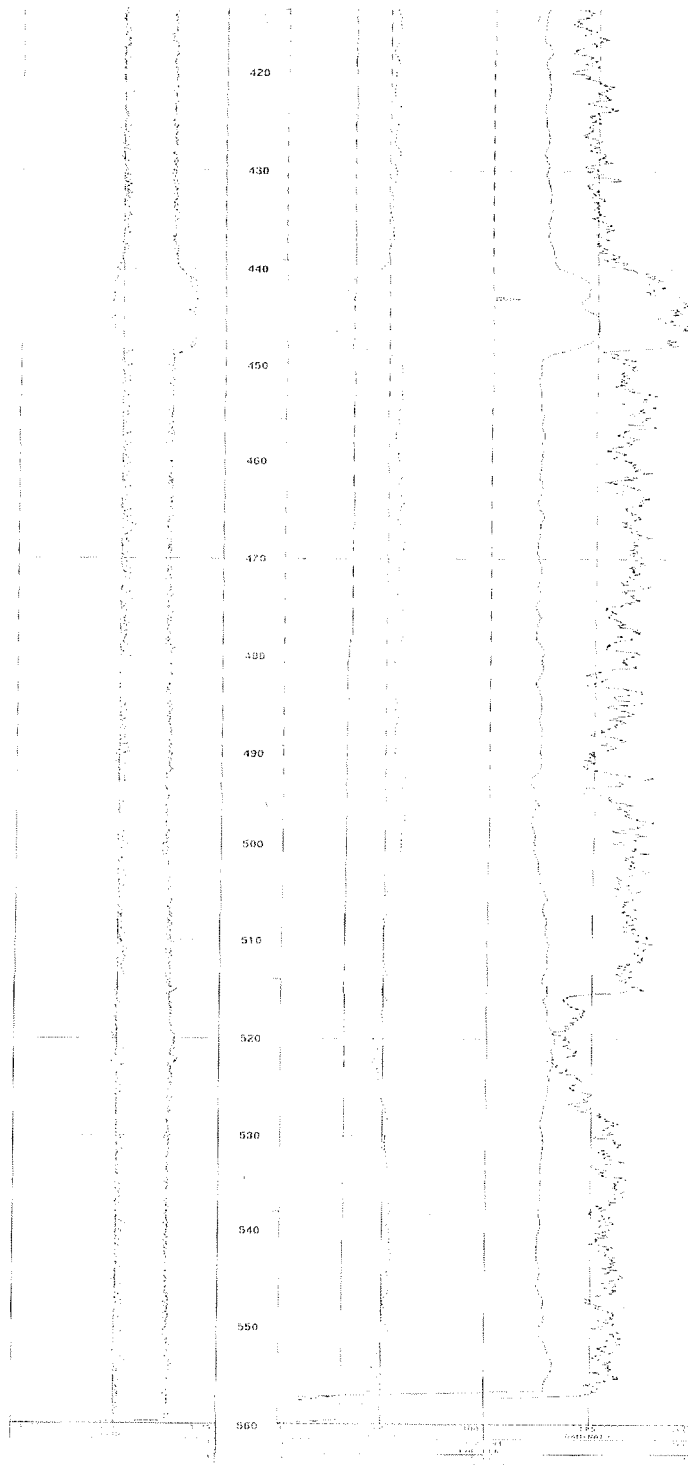


Figure 4.7 Geophysical logs of boring Blija. The right-most curve is the natural gamma log. The following preliminary stratigraphy can be given:
 448.5 m - Oosterhout/Breda Formation, between 440 m and 448 m very rich in glauconitic sand;
 448.5 - 515.5 m - Rupel Clay Member (old name: Boom Clay);
 515.5 - 527.5 m - Vesseem Member (old name: Berg Sand);
 527.5 m - Dongen Formation, represented here by the Asse Clay Member.

Additionally, a suite of geophysical well logs available from the depth window of interest.

Table 4.8 Available samples from boring Blija.

Start depth [m]	End depth [m]	Recovery [cm]
443	443.5	18
443.5	443.65	15
453	453.15	13
453.5	453.8	30
454	454.3	30
454.5	455	40 (full)
478	478.5	40 (full)
478.5	479	25
479.5	480	40 (full)
561.5	561.85	35
562	562.31	31

4.3.1 Characteristics of the samples

The selection of the geomechanical samples from the Weelde and Blija cores was done after inspection of x-ray tomographic scans of the cores. Table 4.9 and Table 4.10 summarise the dry, saturated and specific weights and the initial and saturated water contents determined on the samples.

The main observations are:

- The values of dry, saturated and specific weights of Blija specimens confirm the trends observed for the TRUCK-II experimental program:
 - γ_d increases from 15.11 to 16.34 kN/m³,
 - γ_{sat} increases from 19.19 to 20.15 kN/m³,
 - γ_s increases from 26.07 to 27.08 kN/m³.
- The saturated water content decreases from 27 % (Doel specimens) to 26 % (Blija specimens).
- The porosity generally decreases from 42.03 % (Doel specimen) to 39.23 % (Blija specimens).

4.3.2 Sedimentation analysis

To verify the homogeneity of the samples, a particle size analysis by sedimentation was done for each site, at each depth. These analyses are given in the Figure 4.8. The sedimentation curves of the Blija specimens are very similar to those of the Weelde specimens and thus confirms the existence of two types: the first type

encompasses the specimens from Doel, Zoersel and Mol at –224 m; the second type the specimens from Mol at –229 m, Weelde and Blija with finer sediments.

Table 4.9 Characteristics of the samples – consolidated and undrained triaxial tests (CTU).

Case	Origin	Depth [m]	γ_d [kN/m ³]	γ_s [kN/m ³]	$W_{initial}$ [%]	S_r [%]	n [%]
1	Weelde	313.22 – 313.55	15.79	26.70	24.92	98.3	40.88
2	Weelde	314.22 – 315.10	15.76	26.60	25.33	100.1	40.73
3	Weelde	314.22 – 315.10	15.60	26.60	26.14	100.7	41.35
4	Weelde	314.22 – 315.10	Not performed				
5	Weelde	314.22 – 315.10	15.81	26.60	25.38	101.0	40.56
1	Blija	454.50 – 455.00	16.34	26.89	23.31	99.1	39.23
2	Blija	454.00 – 454.30	Not performed				
3	Blija	561.50 – 561.85	15.70	27.08	25.75	99.4	41.53
4	Blija	478.50 – 561.85	Not performed				

Table 4.10 Parameters determined from the oedometer tests.

Load [MPa]	Origin	Depth [m]	γ_d [kN/m ³]	γ_s [kN/m ³]	$W_{initial}$ [%]	S_r [%]	n [%]
9	Weelde	313.55 – 314.05	15.46	26.70	25.38	95.0	42.11
12	Weelde	314.22 – 315.10	15.97	26.60	25.20	(102.7)	39.95
16	Weelde	313.55 – 314.05	15.83	26.70	23.90	94.8	40.70
19	Weelde	313.55 – 314.05	15.61	26.70	24.28	93.1	41.53
20	Blija	453.50 – 453.80	16.10	26.86	22.97	94.0	40.08
20	Blija	561.50 – 561.85	16.09	27.08	22.97	92.9	40.57

4.3.3 Mineralogical analysis

Mineralogical analyses were done for Weelde (313 m) and Blija (561 m). The results for each sample consist of 3 curves (see Appendix C). For the analysis, the clay ($d \leq 2 \mu\text{m}$) is separated from the sample by sedimentation. The black curve corresponds to the unprocessed clay, the red one to the clay saturated by an atmosphere of glycol (it increases the heaving of the clay), and the blue one to the clay after burning at 500 °C.

Several remarks can be made about the analysis of the clay:

- For each sample, there are 3 different peaks :
 - 6 ° Smectite (Montmorillonite),
 - 8.5 ° Illite,
 - 12 ° Kaolinite.

- Between 6° and 8.5° , the diffractions of interstratifieds of montmorillonite and illite are present. There is no difference between the samples.
- The glycol acts on the swelling sheets (montmorillonite principally): the thickness of the sheets increases and the peak moves to the left of the graphs.
- The burning at 500°C eliminates the kaolinite.
- The clay consists of 30 to 50% of smectite, and for 50% of smectite in the Blija sample (561 m). Illite and kaolinite are in same proportion as in the Weelde sample.
- The mineralogical analysis shows that the clay is the same from a mineralogical point of view.

4.3.4 Atterberg limits

The determination of the Atterberg limits is made for the samples from Weelde (313 m) and Blija (454 m and 561 m). The results are given in the Table 4.11.

The Atterberg limits exhibit trends with depth as expected: increase of liquid limit, plastic limit and plasticity index.

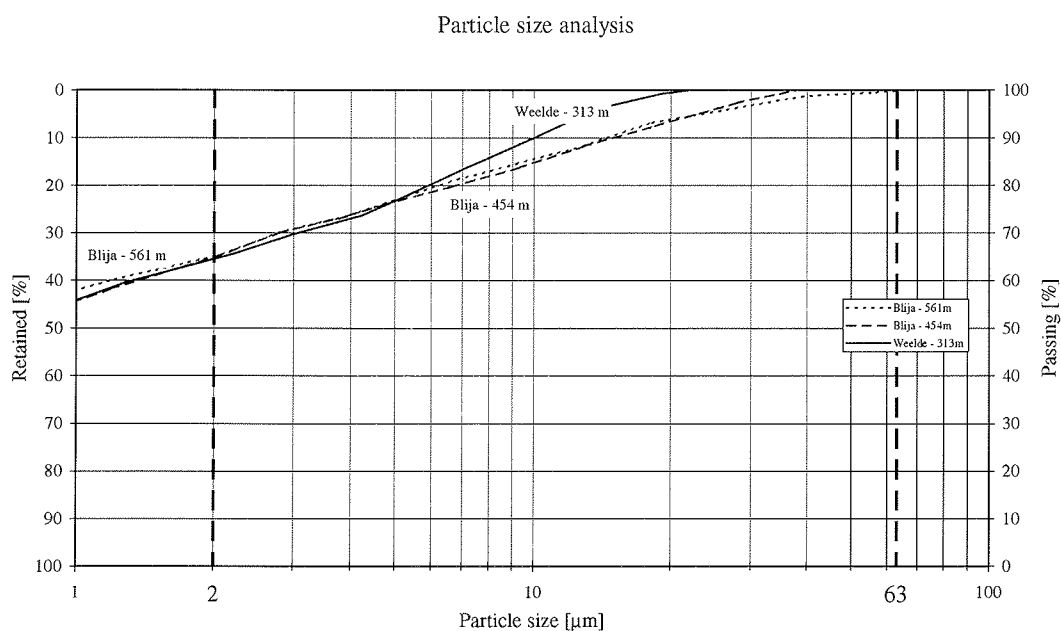


Figure 4.8 Sedimentation analysis for Weelde (313 m) and Blija (454 m and 561 m).

Table 4.11 Atterberg limits for samples from Weelde and Blija.

Origin	Depth [m]	W_L [%]	w_P [%]	I_P [%]
Weelde	313.55 – 314.05	75.2	28.5	46.7
Weelde	314.22 – 315.10	93.2	29.8	63.5
Blija	453.50 – 453.80	103.9	31.2	72.7
Blija	561.50 – 561.85	105.1	32.5	72.6

4.4 Methods and techniques used for testing

4.4.1 The consolidated and undrained triaxial test (CTU)

The triaxial tests are compression tests induced by a vertical deformation performed on three separate cylindrical specimens at three different load levels. This enables the determination of the angle of internal friction and cohesion, and deformation modulus. The load levels chosen generally are :

- 1 σ'_c : the in-situ stress situation of the particular model scenario
- 2 $1.5 \cdot \sigma'_c$
- 3 $2 \cdot \sigma'_c$

Preparation of the samples

In order to exclude possible disturbance caused by the sampling process or by inclusions in the samples, the cores were X-rayed after extrusion from their containers. Based on the tomographic images the suitable levels were chosen. The Weelde samples are approximately 100 mm in diameter and allow the preparation of three cylindrical specimens of 38 mm diameter and 76 mm height at the same level. The samples from Blija are 64 mm in diameter and allow the preparation of one specimen at each level.

Outline of test stages

Test stage 1: Saturation

The specimen is capped with a porous end plate and a filter sheet around the side surface, after which it is wrapped in a thin rubber membrane and placed in the loading cell. The loading cell is filled with water. The saturation of the samples with de-aired water is done by application of a pore water pressure of 0.2 MPa in the sample so the air as a separate phase in the void spaces is eliminated. This

enables reliable readings of pore pressure changes to be obtained during subsequent testing stages for the determination of the effective stresses. The time required for saturation depends upon the type of soil and size of sample, as well as the degree of saturation. Due to the high degree of saturation of the samples, this saturation is almost instantaneous.

Test stage 2: Consolidation

The specimen is isotropically consolidated to the required initial effective pressure by elevating the confining pressure in the loading cell by allowing water to drain out. Drainage of water results in a decrease in volume and an increase in the effective stress, which after consolidation is equal to the difference between the confining pressure and the mean pore pressure remaining in the sample. The consolidation is complete when the sample is stabilised and does not expel water. Permeability controls the time required for the sample to consolidate. Consolidation must be allowed to continue until at least 95% of the excess pore pressure, caused by the increase in confining pressure has dissipated. This may take from less than an hour to many days, depending upon the type of soil and size of the sample. In order to avoid failure of the specimen by excessive pore pressures due to the low permeability of the clays the consolidation is performed in load steps of 1 MPa. Each load step lasts seven days at least. Use of side drains appreciably shortens the consolidation time for soils of low permeability.

Test stage 3: Compression

The rate of excess pore pressure dissipation from the consolidation stage is used to derive a suitable rate of strain for the compression test. An undrained test can be run at a faster rate of strain than a drained test on similar material because no movement of water through and out the sample is involved. However, the rate of strain must be slow enough to permit equalisation of pore pressure within the sample. Pore pressure is measured at the base, but it is the value within the middle third that most affects the measured shear strength. For soils of low permeability, shearing to failure usually requires a day or two. At approximately 50% of the estimated peak strength, an unload-reload loop is performed, to enable the accurate determination of the deformation modulus.

4.4.2 The oedometer consolidation test

The oedometer consolidation test is used for the determination of the consolidation characteristics of soils of low permeability. The two parameters normally required are:

- The compressibility of soil, which is a measure of the amount by which the soil will compress when loaded and allowed to consolidate.

- The time related parameter, which indicates the rate of compression, and hence the time-period over which consolidation settlement will take place.

The test is carried out by applying a sequence of eight to eleven vertical loads to a laterally confined specimen. The vertical compression under each load is observed over a period of time. Since no lateral deformation is allowed it is a one-dimensional test, from which the one-dimensional consolidation parameters are derived. The parameters represent the consolidation behaviour at loads lower than the preconsolidation pressure, dominated by elastic behaviour, at loads higher than the preconsolidation pressure, dominated by plastic behaviour, and during unloading. The resulting compression and swelling coefficients can be used in the CAM-CLAY constitutive model. Additionally, the time related parameters are presented as vertical permeabilities.

Preparation of the samples

The size of a consolidation test specimen is important for several reasons. The advantages of smaller specimens are:

- The thinner the specimen, the smaller the distance the escaping pore water must flow and, therefore, the shorter time required for consolidation. The time for consolidation varies as the square of the specimen thickness
- The thinner the specimen for a given diameter, the less the side friction.

In view of the foregoing considerations, a ratio of specimen diameter to thickness of about three to four is recommended. In our case, the samples are 20 mm height and 63 mm diameter.

Laboratory equipment

The fixed-ring cell is the most standard cell. The specimen is held in the cutting-ring, which is accurately located and rigidly restrained by a retainer or the cell body, which avoids damaging the cutting edge. Setting up and dismantling are simple operations, which entail little risk of disturbing the specimen.

The large range of the applied pressure (from 0.1 to 19 MPa) is not realisable on this standard cell because the maximum pressure is limited to about 3.2 MPa. The utilisation of a hydraulic jack to apply the highest pressures is necessary. The procedure used was to apply the pressure until 3.2 MPa with the standard cell and then place the sample underneath the jack. The standard cell is adapted to permit this operation. Figure 4.9 shows the new cell with a steal sheet, which fixes the deformation of the sample at the reached value for a pressure of 3.2 MPa.

Consolidation test

The test is performed in steps of 1.6 MPa up to 8 MPa, steps of 2 MPa up to 16 MPa and steps of 3 MPa up to 20 MPa. Unloading is achieved in steps of 50% of the previous load. The load is maintained until the secondary ("creep") phase of consolidation has clearly replaced the primary, hydrodynamic, phase. This usually takes more than one day, for the lower load steps, up to more than 10 days for the higher load steps, because of decreasing permeability. The unloading stage ends at 1MPa. Care is taken that no side friction occurs due to a sliding end plate. In a few cases this happened still and the test was repeated.

4.5 Results of mechanical experiments

This section contains a selection of the results acquired in the experimental programme. A full description of the experimental results can be found in the report from the UCL (2000).

4.5.1 The consolidated and undrained triaxial tests (CTU)

Shear strength parameters

The values of the shear strength parameters for the soil are calculated from the linear regression coefficients in the p'-q and p-q diagrams (Figure B.1 to Figure B.6 and Figure B.7 to Figure B.12) and are given in Table 4.12.

Table 4.12 *Shear strength parameters – consolidated and undrained triaxial tests (CTU).*

Case	Origin	Depth [m]	c_{cu} [MPa]	c' [MPa]	ϕ_{cu} [°]	ϕ' [°]
1	Weelde	313.22 – 313.55	0.299	0.345	8.7	8.8
2	Weelde	314.22 – 315.10	0.296	0.504	9.2	8.1
3	Weelde	314.22 – 315.10	0.247	0.093	8.7	13.1
5	Weelde	314.22 – 315.10	0.164	0.249	9.5	11.6
1	Blija	454.50 – 455.00	1.010	0.715	5.7	8.8
3	Blija	561.50 – 561.85	1.823	1.818	2.0	2.1



Figure 4.9 Fixed-ring cell adapted for high pressures.

The following conclusions can be drawn:

- c_{cu} and c' are varying not only with depths but also samples of Weelde within one specific depth:
 - For Doel, $c' = 0.133$ MPa
 - For Zoersel, $c' = 0.233$ MPa
 - For Mol, $c' = 0.396$ MPa
 - For Weelde $c' = 0.093$ to 0.504 MPa
 - For Blija $c' = 0.715$ and 1.818 MPa (respectively 455 m and 561 m)
- ϕ_{cu} and ϕ' are also varying as a function of the same parameters :
 - For Doel, $\phi' = 17.9^\circ$
 - For Zoersel, $\phi' = 9.3^\circ$
 - For Mol, $\phi' = 9.6^\circ$
 - For Weelde $\phi' = 8.1^\circ$ to 13.1°
 - For Blija $\phi' = 8.8^\circ$ and 2.1° (respectively 455 m and 561 m)

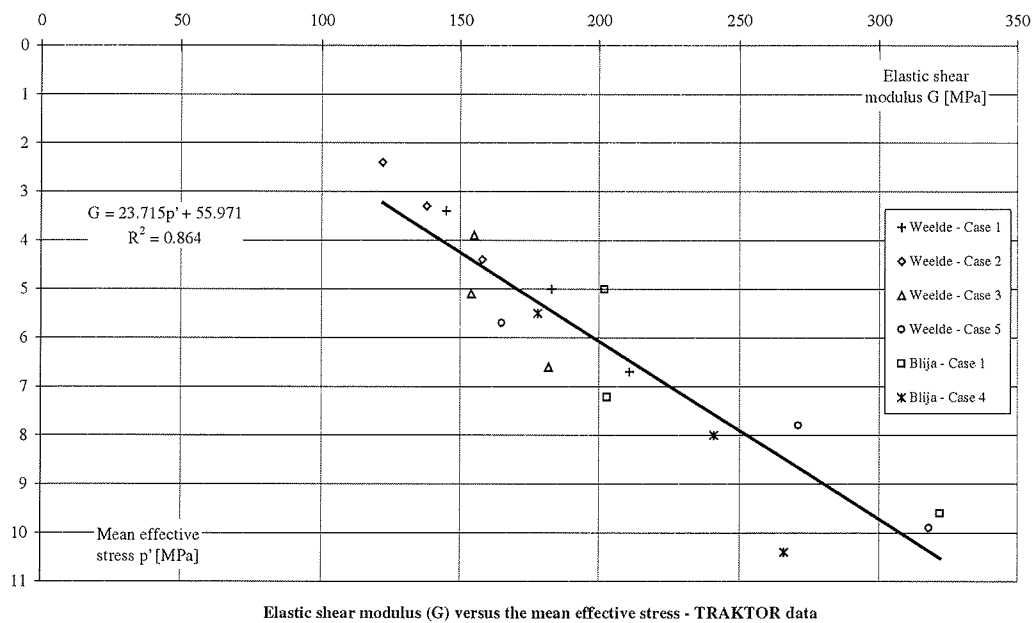


Figure 4.10 Shear modulus (G) versus mean effective stress.

Modulus of shear deformation

The shear modulus (G) is the ratio between a given shear stress change and the corresponding shear strain change. We can estimate its value from the loading-unloading cycle realized during the CTU test: G is 1/3 of the mean slope of the cycle in the p - q' diagram. Thus, we have 18 values of this modulus. Figure 4.11 and Table 4.13 give the numerical values of this modulus.

The values of shear modulus (G) can be related with the mean effective stress p' . We observe the same evolution as for the TRUCK II experimental programme.

For TRUCK II:	$G = 31.48 * p' + 28.88$	with $R^2 = 0.94$
For TRAKTOR:	$G = 23.72 * p' + 55.97$	with $R^2 = 0.86$
All data:	$G = 26.11 * p' + 46.51$	with $R^2 = 0.90$.

4.5.2 The oedometer consolidation tests

Characteristics of compressibility

From the oedometer consolidation tests, a diagram of linear strain vs. log of pressure can be plotted. We can also estimate the values of the compressibility and the swelling index.

$$\text{Compressibility index} \quad C = \frac{h}{\Delta h} \ln \frac{\sigma' + \Delta \sigma'}{\sigma'}$$

$$\text{Swelling index} \quad A = -\frac{h}{\Delta h} \ln \frac{\sigma'}{\sigma' - \Delta \sigma'}$$

The values are given in Table 4.14 and Table 4.15.

Due to the hydraulic jack, the pressure applied on the samples is not strictly constant as done with the standard cell. The pressure varies slightly (3 % maximum) with temperature and time. The daily adjustment of the pressure produced some irregularities in the height-time curves.

From the obtained results the following can be concluded:

- For Weelde specimens:
 - The initial void ratio varies from 0.67 to 0.73.
 - The value of Compression Index increases when pressure is increasing from 2 to 8 MPa. C_c tends to an average value of 0.35 to 0.40 at pressures over 9MPa. These values are in agreement with results of empirical formulas (based on Liquid Limit and/or void ratio) even if these values are slightly higher (0.47 to 0.52).
 - The value of C_s varies between 0.07 and 0.12 for the beginning of the unloading curve. The average ratio of C_s to C_c is 1/5, which is a value commonly encountered for the higher loading steps.

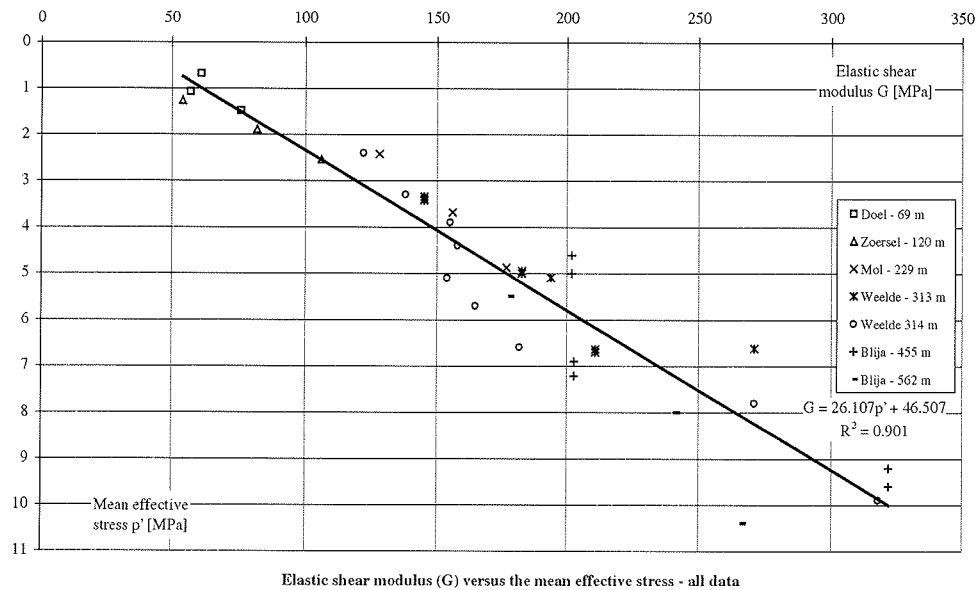


Figure 4.11 Shear modulus (G) versus mean effective stress for TRUCK II and TRACTOR.

Table 4.13 Numerical values for the shear modulus (G).

Case	Origin	Depth [m]	Mean effective stress p' [MPa]	Shear modulus G [MPa]
1	Weelde	313.22 – 313.55	3.4	145
			5.0	183
			6.7	211
2	Weelde	314.22 – 315.10	2.3	122
			3.4	138
			4.4	158
3	Weelde	314.22 – 315.10	3.9	155
			5.1	154
			6.6	182
5	Weelde	314.22 – 315.10	5.7	165
			7.8	271
			9.9	318
1	Blija	454.50 – 455.00	5.0	202
			7.2	203
			9.6	322
3	Blija	561.50 – 561.85	5.5	178
			8.0	241
			10.4	266

Table 4.14 Numerical values for the compressibility index.

Stresses [MPa]	Compressibility index					
	Weelde 9 MPa	Weelde 12 MPa	Weelde 16 MPa	Weelde 19 MPa	Blija – 453 m 20 MPa	Blija – 561 m 20 MPa
1.5	31	35	35	25	37	(71)
3.2	13	15	13	13	2	3
4.8		(17)	(9)	13	(218)	(46)
6.4	13	11	13	13	(35)	(21)
8		11	13	7	13	16
9	6					
10		10	4	10	8	10
12		8	10	8	7	10
14			6	9	7	17
16			8	8		
17					7	9
19				7		
20					4	9

The values in brackets are calculated values that are not reliable.

Table 4.15 Numerical values for the swelling index.

Stresses [MPa]	Swelling index					
	Weelde 9 MPa	Weelde 12 MPa	Weelde 16 MPa	Weelde 19 MPa	Blija – 453 m 20 MPa	Blija – 561 m 20 MPa
10					37	60
9.5				38		
8			41			
6		30				
5					23	25
4.75				30		
4.5	27					
4			30			
3		25				
2.5				21	23	14
2			21			
2.25	(20)					
1	38	22	17	21		

- For Blija specimens
 - The initial void ratio is similar to these of the Weelde specimens (0.67 and 0.68).
 - The values of C_c are on average similar to the Weelde specimens: we observe an increase of C_c to about 0.35 for one sample (from 561 m) and

0.45 to 0.50 for the other (from 453 m). For this last specimen, we have a value 0.83 for the last loading step.

- The value of C_s varies between 0.08 and 0.06 for the beginning of the unloading curve.

Permeability

From the height-time curves, and after locating the time for 50 % of primary compression, the coefficient of consolidation C_v is calculated by:

$$C_v = \frac{0.197 H^2}{t_{50}} \quad (4.2)$$

The method of locating assumes that the early portion of the curve is a parabola. The coefficient of compressibility a_v can be found from C_c (the compression index) by:

$$a_v = \frac{0.435 C_c}{p} \quad (4.3)$$

Having the values of a_v and C_v , we can compute the permeability from:

$$k = \frac{C_v a_v \gamma_w}{1 + e} \quad (4.4)$$

The values of the permeability are given in Table 4.16.

Table 4.16 Permeability.

Origin	Maximum load [MPa]	Permeability [m/s]
Weelde	9	$5.3 \cdot 10^{-13}$
	12	$7.6 \cdot 10^{-14}$
	16	$1.1 \cdot 10^{-13}$
	19	$1.3 \cdot 10^{-13}$
Blija	453 m 20	$6.5 \cdot 10^{-14}$
	561 m 20	$6.9 \cdot 10^{-14}$

4.6 Discussion

The two experimental programmes for TRACTOR and TRUCK-II make possible to draw conclusions about the behaviour of Tertiary clays taken from depths of 450 to 560 m.

From the mineralogical point of view, the clay samples consist of the same minerals: smectite, illite, and kaolinite. The proportion of smectite in the sample from clay of the Asse Member (about 50%) is higher than in the Rupel Clay samples (between 30 and 50%).

Atterberg Limits

The Atterberg Limits, Liquid Limit, Plastic Limit and the Plasticity Index, related by:

$$I_p = w_L - w_P \quad (4.5)$$

where: I_p = plasticity index,
 w_L = liquid limit: water content at which clay behaviour changes from plastic to liquid,
 w_P = plastic limit: water content at which clay behaviour changes from brittle to plastic.

have been shown by various researchers to correlate with strength parameters and overconsolidation ratio. As such, they are a means to check the results of the present tests with values reported in the literature.

Plasticity index vs shear strength

The drained friction angle decreases with the Plasticity Index. In the data gathered by Olson it is shown that at high Plasticity Indices comparable to the present values the friction angle lies in the range of 13° to $11^\circ \pm 5^\circ$. Factors, which result in lower friction angles at the same level of plasticity values, are the presence of smectites, the percentage of clay size fraction and the effective normal stress. Higher values of these factors result in lower friction angles.

Bishop et al. (1965) have shown that the Mohr envelope for London Clay is curved. At low effective normal pressures, i.e. in the range of 1 to 2 MPa, the effective friction angle is 20° , and the effective cohesion 310 kPa. These values would greatly overestimate the strength at higher pressures. Beyond the preconsolidation pressure of 4.1 MPa the effective friction angle is less than 10° and the effective cohesion is greater than 750 kPa.

The explanation for this effect is that at high pressures dilatancy, which causes the mechanical friction of the particles is no longer a major contributor to the strength. In other words, the clay particles are deformed.

An alternative for the use of c' and ϕ' in the models is the maximum deviator stress or undrained shear strength. A plot of shear strength vs mean effective stress is given in Figure 4.12.

Liquid Limit and Intrinsic Compression Line

The Liquid Limits have been used to calculate the Intrinsic Compression Lines according to the GeoDelft report (1999). It can be seen that with increasing depth, the ICL moves closer to the Sedimentation Compression Line, leaving the Weelde tests below the ICL (Figure 4.12). A possible explanation is that for the Boom Clay it is not possible to remove aging effects, even with thorough remoulding. This corresponds with observations made earlier in the experience of the "Université catholique de Louvain" on another research programme supported by the National Fund of Scientific Research of Belgium, which showed that remoulding was hindered by the texture of the material. In addition, it confirms the valid results for the Blija samples and the possible relaxation of the Weelde samples.

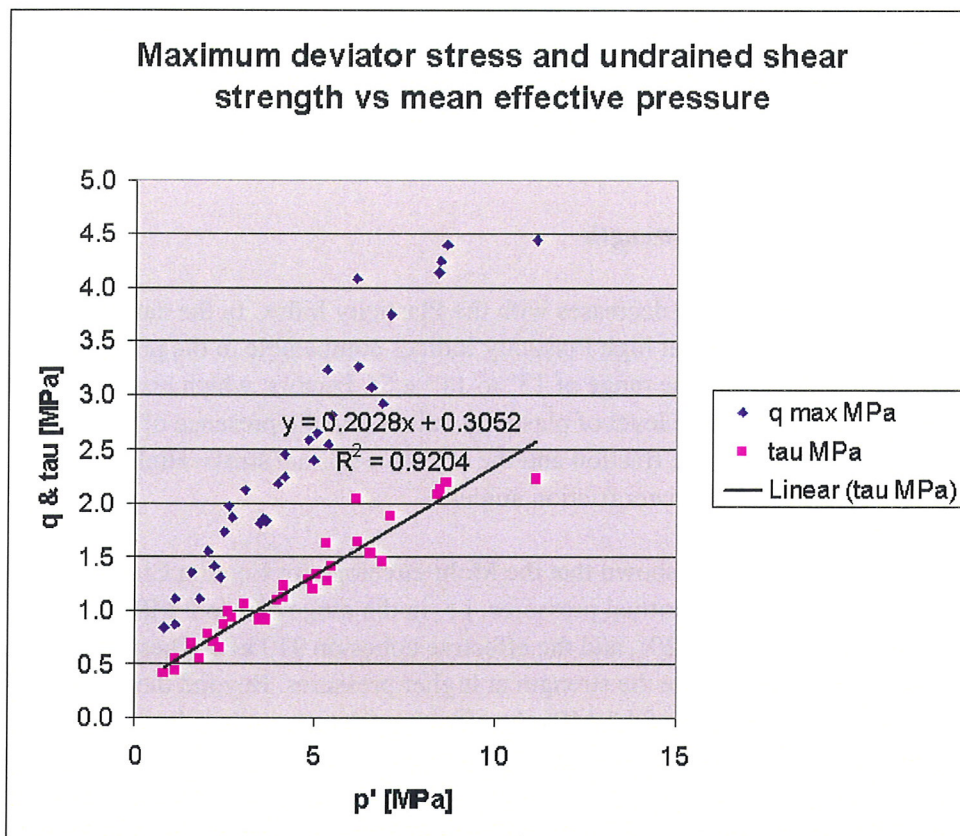


Figure 4.12 Undrained shear strength versus mean effective stress.

Tri-axial tests

Most tests exhibit a normally consolidated behaviour. This is not obvious, because except for Case 5, high effective pressures due to ice-loading, and the tests on the Blija samples, the stress conditions in the tests are below the pre-consolidation pressure. This can be explained by disturbance of the original condition of the samples. Due to a long time of loss of constraint after extrusion of the sampling tubes, it is likely that the samples have swollen.

The results of the CTU tests suggest an increase of cohesion and a simultaneous decrease of friction angle with depth (see Figure 4.13). For the specimens at a depth level of 313 m, one has a variation of values of cohesion and angle of friction. For the specimens from the Asse Member at a depth of 561 m, extreme values were observed, which needs to be confirmed by further testing.

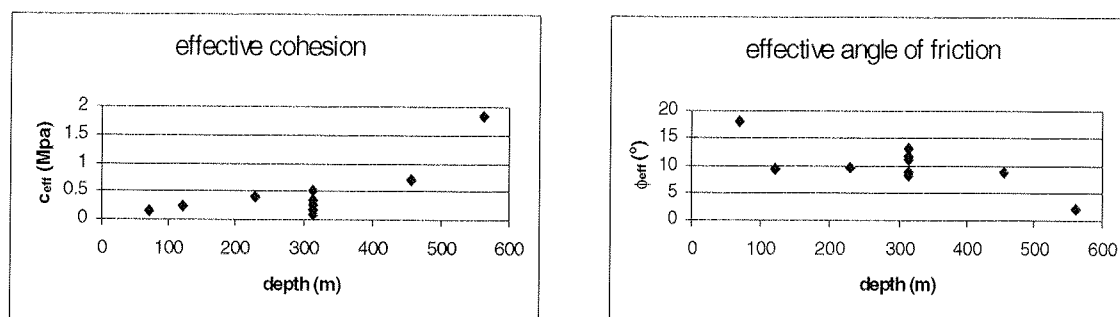


Figure 4.13 Results of the consolidated and undrained triaxial tests (CTU) - cohesion and angle of friction versus depth. The deepest sample is from the clay of the Asse Member; the others were taken from the Rupel Clay.

In general, the heterogeneity of the results for the Rupel Clay is comparable to the variability observed in already published tests in the equivalent Belgian Boom Clay. The shear modulus is increasing with depth. It could be argued that the clay becomes more plastic with depth. This conclusion is however not firm, because it is based on too few data, but it is confirmed by the Atterberg limits.

The values of cohesion and angle of friction obtained for the specimens at a depth level of 313 m don't show a clear relation between these values and the consolidation pressure (Figure 4.14). The average undrained friction angle is 9 degrees. The average cohesion is 0.3 MPa. Consequently, it doesn't appear that the potential effect of ice loading on soil will lead to a modification of Mohr-Coulomb criterion as would be expected for over-consolidated clay. The average value of the friction angle is 9 degrees; the average cohesion is 0.3 MPa. For the results from

the Blija specimens, the small number of performed tests doesn't permit to draw definitive conclusions concerning the values of mechanical parameters to be used in the models.

Oedometric tests

The results of the oedometric tests in Figure 4.15 show a good reproducibility of the performed tests. The Belgian specimens give very close results for the loading and for the unloading parts of the different curve. The Dutch specimens necessitate higher pressures to obtain the same settlement.

The values of Compression Index (C_c) are nearly 0.35 to 0.4 for pressures higher than 10 MPa. One observes this tendency for the four Weelde specimens and for the first Blija specimen. The other specimen of Blija gives a value of average 0.45 to 0.50. The value of Swell Index (C_s) for Weelde specimens is average 0.07 to 0.12. The value of initial void ratio (e_0) for the two clays varies between 0.67 and 0.73. The Cam-Clay parameters derived from the oedometric tests are given in Table 4.17.

Inspection of the load-settlement curves of the oedometric tests reveals that the loading curve is made up of three stages:

- an initial stage to about 1.5 MPa,
- a second stage to about 6-7 MPa for Weelde and about 7-8 MPa for Blija,
- a third stage to the final load, before unloading starts.

According to previous studies, summarised in the GeoDelft report (1999b), the pre-consolidation pressure is expected to be about 6-7 MPa for Weelde. This corresponds well with the second transition load of the tests. The steep gradient of the second stage is attributed to sampling disturbance. This is also indicated by the fact that the Weelde samples fall on the Intrinsic Compression Line, which is the virgin laboratory compression curve for completely remoulded clay. It is therefore concluded that the overconsolidation ratio of 1.9-2.2 (ratio of the pre-consolidation pressure and the in-situ pressure) is confirmed by the tests on the Weelde samples. The Blija samples have an overconsolidation ratio of 1.3-1.8. This is lower than predicted from previous work on the Rupel Clay from shallower depths ($p_c' = 350 + 20z$ (kPa)). Sample disturbance explains why the curves for the Weelde samples plot below the Sedimentation Compression Line. The curve for the Rupel sample at Blija also falls below the SCL, but well within the 30% range of literature data. The Asse clay results plot on the SCL.

The overconsolidation is to a large degree caused by ageing effects, which includes the processes of creep and diagenesis. There is no conclusive evidence for ice loading consolidation in the samples from the formerly glaciated northern part of the Netherlands. In the graph, the preconsolidation pressures and the effective

pressure due to 1000 m ice-load are represented by solid and open arrows respectively. This load would lead to further consolidation of the Tertiary clay. The actual effective pressure of an ice load could be lower because of melt-water production below the ice sheet.

Table 4.17 *Cam-Clay parameters κ (dimensionless swelling index) and λ (dimensionless compression index) derived from the oedometric tests. p'_c is the pre-consolidation pressure.*

Location	Depth (m)	Test [MPa]	κ	λ	p'_c [MPa]
Weelde	313	9	0.06	0.24	6.4
		12	0.06	0.16	6.5
		16	0.06	0.21	8.0
		19	0.06	0.16	6.4
Blija	453	20	0.06	0.20	7.4
		561	0.07	0.14	7.5
Isotrope test (TRUCK II)	475		0.02	0.12	6.9

Calculated *permeabilities* for the Rupel Clay at shallow depths below the Westerschelde were extrapolated to equivalent permeabilities at larger depths between 1.2×10^{-11} m/s and 5.4×10^{-15} m/s. The permeabilities found in the oedometer tests fall in the lower part of this range. The void ratios of the tests for the samples of Weelde and Blija are greater than the range observed for the Westerschelde samples. This means that a simple extrapolation of the relationship between void ratio and permeability from shallow data is not reliable for estimating parameter values at larger depth.

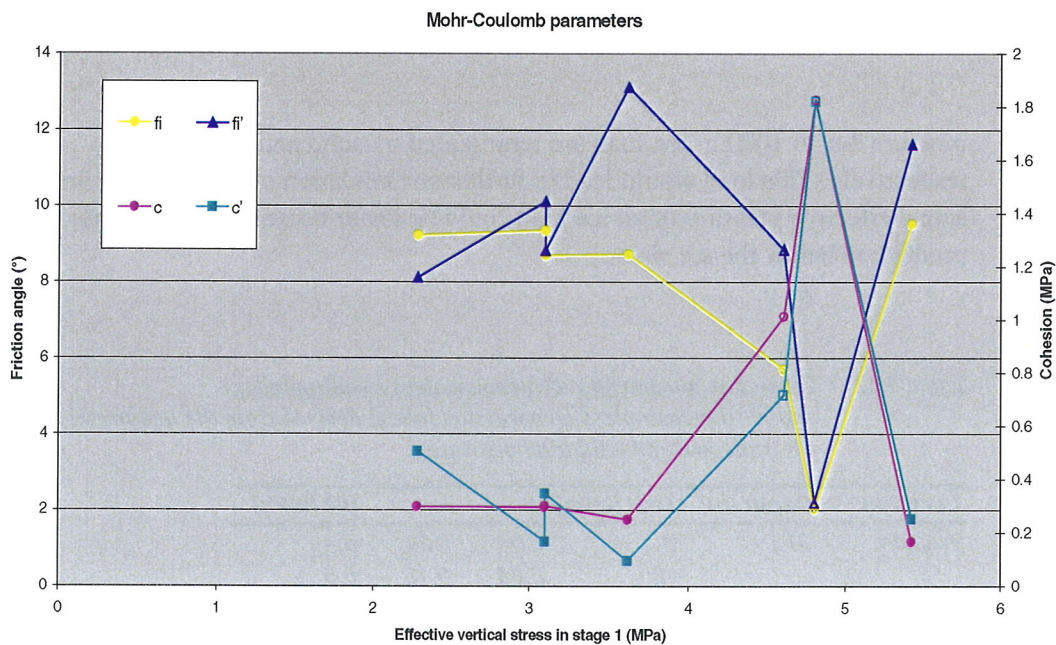


Figure 4.14 Relation between effective vertical stress of first loading stage and friction angle and cohesion. Open symbols = Blija samples and closed symbols = Weelde samples; c = cohesion, c' = effective cohesion, f_i = friction angle, f_i' = effective friction angle.

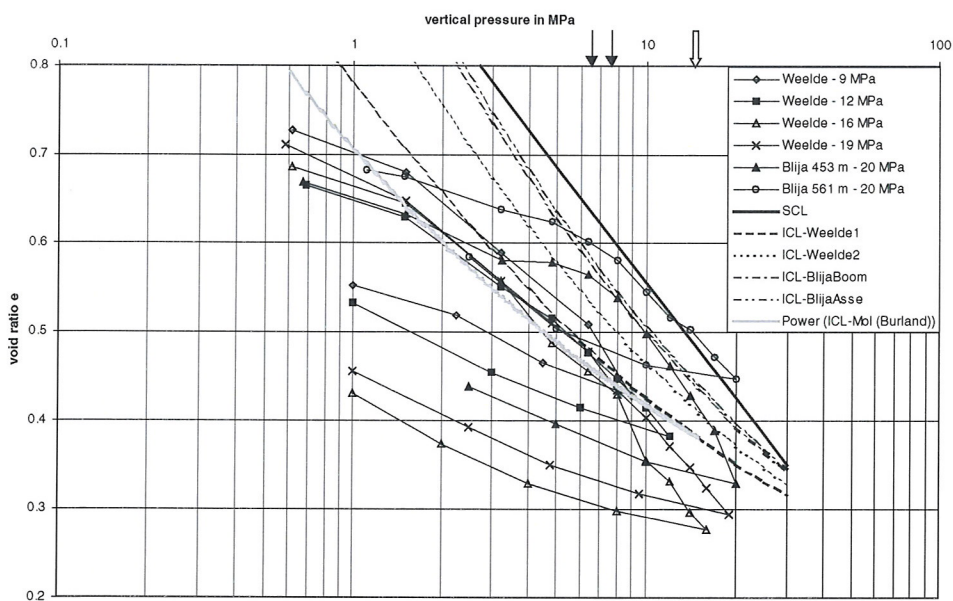


Figure 4.15 Results of oedometric tests – void ratio e versus axial pressure. ICL = Intrinsic Compression Line, which shows theoretical compression of a completely remoulded clay in the laboratory; SCL = Sedimentation Compression Line, which shows theoretical compression of clay in nature.

5 The hydromechanical model and coupling with other models

The hydromechanical modelling discussed in Chapter 4 is related to two other modelling exercises:

- Simulation of supraregional groundwater flow on the scale of North-western Europe to provide geohydrological boundary conditions for the hydromechanical model.
- Simulation of the transport of radionuclides on the basis of the flow field calculated by the hydromechanical model (Figure 5.1).

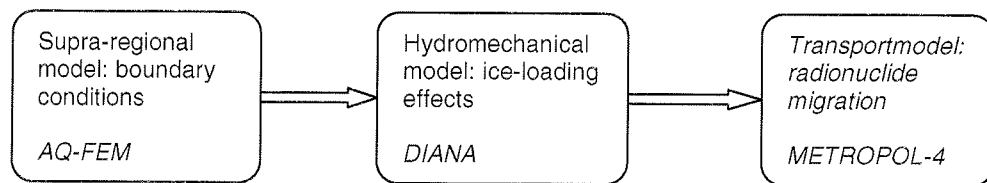


Figure 5.1 Relation between the various models used in the project TRACTOR.

5.1 Mathematical description of the flow-stress analysis

The physical processes that will be simulated by using the hydromechanical model are consolidation of the host rock (the Tertiary clays, namely the Rupel Formation) and groundwater flow.

Ice loading causes change in stresses and deformations in the subsurface that influence the groundwater flow, and vice versa. As this interaction is two-directional, a simultaneous calculation of flow and stress is necessary. The numerical code used in this project - DIANA, developed by TNO Building and Construction - relies on the full Biot theory to describe the interaction between the pore fluid pressure and the solid particles (Biot, 1941). A short explanation of the background theory, mathematical equations and assumptions describing coupled stress-flow analysis, which is mainly based on the User's Manual of DIANA (version 7.1, distributed on compact disk) is presented below.

5.1.1 Basic equations and assumptions

The equations and assumptions in this chapter relate the stresses and pore pressures to deformations and fluid flow, using material parameters for elastic compressibility, drained elastoplasticity, density, porosity and permeability.

Stress separation

The theory is based on the Terzaghi's principle of effective stress (1962) which states that the total stress in soil can be separated into effective, i.e. intergranular stress and pore pressure, i.e. neutral stress. All measurable effects of a change in stress in soils (such as compression, distortion, or a change in shearing resistance) are due to changes in effective stresses. The relationship between the stresses is as follows:

$$\sigma' = \sigma - p \quad (5.1)$$

where: σ' = effective stress [ML⁻¹T⁻², e.g. Pa]
 σ = total stress [ML⁻¹T⁻², e.g. Pa]
 p = pore pressure [ML⁻¹T⁻², e.g. Pa]

Following the notation convention of DIANA, the equations for the soil-pore fluid analysis can be written as follows.

The equation for stress separation, in its more complex form, reads as follows:

$$\sigma' = \sigma - (1 - \gamma) I p \quad (5.2)$$

$$\gamma = \frac{K_D}{K_S} \quad (5.3)$$

where: γ = function of compressibility [-], for soils $\gamma \rightarrow 0$,
 I = a unity matrix
 K_D = compression modulus of the drained porous soil skeleton [ML⁻¹T⁻², e.g. Pa]
 K_S = compression modulus of the non-porous solid [ML⁻¹T⁻², e.g. Pa]

DIANA determines the pore pressure p from the pore pressure potential, using the initial position vector and the displacement:

$$\phi = p - \rho_f g(x - x_{ref}) \quad (5.4)$$

$$x = x_{init} + u \quad (5.5)$$

where: ϕ = pore pressure potential [ML⁻¹T⁻², e.g. Pa]
 ρ_f = fluid density [ML⁻³, e.g. kg m⁻³]
 g = gravity acceleration [LT⁻², e.g. m s⁻²]
 $x - x_{ref}$ = position vector [L, e.g. m]

u = displacement [L, e.g. m].

Porosity, saturation and apparent density

DIANA uses the following equation to determine the deformation and saturation dependent density during the analysis, assuming a deformation dependent porosity:

$$\rho = \rho_{dry} + S n \rho_f \quad (5.6)$$

where: ρ = total density of the soil [ML⁻³, e.g. kg m⁻³]
 ρ_{dry} = density of the dry porous solid [ML⁻³, e.g. kg m⁻³]
 S = degree of saturation dependent on the pore pressure
 n = porosity
 ρ_f = fluid density [ML⁻³, e.g. kg m⁻³]

Momentum conservation

The momentum conservation, which is the basic equilibrium law in stress analysis, is formulated as follows:

$$\text{div}(\sigma') - S(1 - \gamma)\nabla I p + \rho g + \rho \ddot{u} = 0 \quad (5.7)$$

where: div = divergence of vector
 S = pore pressure dependent degree of saturation [-]
 ∇ = gradient of the function
 \ddot{u} = acceleration of the solid [LT⁻², e.g. m s⁻²]

Mass conservation

The mass conservation for a fully saturated soil means that both fluid and undrained compression or expansion will cause volumetric changes. The storage equation, which is derived from the general mass conservation law, can be expressed in the following form:

$$\alpha \text{div}(\dot{u}) + \text{div}(q) + \frac{p}{Q} = 0 \quad (5.8)$$

$$\alpha = 1 - \gamma \quad (5.9)$$

$$\frac{1}{Q} = \frac{n}{K_f} + \frac{\alpha - n}{K_s} \quad (5.10)$$

where: \dot{u} = velocity vector [LT⁻¹, e.g. m s⁻¹]

q	= fluid flux vector [LT^{-1} , e.g. $m\ s^{-1}$]
α	= first Biot material parameter
Q	= second Biot material parameter
n	= porosity
K_f	= compressibility module of the fluid [$ML^{-1}T^{-2}$, e.g. Pa]

Darcy flow

The Darcy's law describes the fluid flow in porous media. In case of dynamic behaviour, DIANA uses the following extended formulation of the Darcy's law:

$$q = -K'(\nabla\phi - \rho_f \ddot{u}) \quad (5.11)$$

$$K' = \frac{K}{\mu} \quad (5.12)$$

where:	q	= specific discharge [LT^{-1} , e.g. $m\ s^{-1}$]
	K'	= modified permeability [L^3TM^{-1} , e.g. $m^2\ Pa^{-1}\ s^{-1}$]
	∇	= gradient of a function [-]
	ϕ	= pore pressure potential [$ML^{-1}T^{-2}$, e.g. Pa]
	ρ_f	= fluid density [ML^{-3} , e.g. $kg\ m^{-3}$]
	\ddot{u}	= acceleration of the solid [LT^{-2} , e.g. $m\ s^{-2}$]
	K	= hydraulic conductivity [LT^{-1} , e.g. $m\ s^{-1}$]
	μ	= dynamic viscosity [$ML^{-1}T^{-1}$, e.g. Pa s]

The porosity and saturation dependent modified permeability can directly be provided to DIANA in the form of user-specified diagrams.

In geotechnical practice the hydraulic head is often used instead of the pore pressure potential. The relationship between these two quantities is:

$$\phi_{head} = \frac{\phi}{\rho_f g} \quad (5.13)$$

where: ϕ_{head} = hydraulic head [L]

Also, the hydraulic gradient is more conveniently used instead of the pore pressure potential gradient. A unit hydraulic gradient corresponds to a pore pressure potential gradient of $10\ kPa\ m^{-1}$.

Elastoplastic stiffness

Elastoplasticity relates stress to strain via the stiffness matrix:

$$\sigma' = D' \varepsilon \quad (5.14)$$

where: σ' = effective stress [ML⁻¹T⁻², e.g. Pa]
 D' = stiffness matrix, based on the effective stress parameters
 ε = strain

5.1.2 The numerical code DIANA

Simultaneous solution of deformations and pore pressures was achieved by using DIANA finite element code (developed by TNO Building and Construction). Pre- and post-processing of the obtained results was done by using FEMGV software package (version 5.2, developed by Femsys Ltd., UK). FEMGV consists of two parts: FEMGEN, which is a pre-processor, and FEMVIEW, which is a postprocessor. DIANA and FEMGV are currently loosely coupled and generate compatible input/output files. Some features related to the functionality and limitations of these packages of relevance to the project will be discussed below. Detailed description of both packages can be found in accompanied User's documentation.

Mixture analysis

Coupled stress-flow analysis can be performed by the *mixture analysis* in DIANA. In order to achieve two-directional interaction between load-induced stresses and pore pressure in the mixture of a fluid and a porous soil it is necessary to utilise *transient* mixture analysis. Typically, transient mixture analysis is used to analyse consolidation and swelling caused by mechanical loading and unloading of low permeability porous media. These processes are expected to take place in the Tertiary clays under the weight of an ice sheet.

Appropriate types of finite elements for mixture analyses are quadrilateral and triangular plane strain elements extended with a special *mixture* option. Mixture option is also available for interface elements, which are suitable to model fault zones. By extending structural elements to mixture elements a scalar pore pressure potential is added to the set of element degrees of freedom in each element node.

Material models

The behaviour of soil is non-linear. It is strongly dependent on the state of stress, both isotropic as well as shear stress. Density also has an influence on the results.

When soil is loaded isotropically it is found that the deformation behaviour experiences a transition at the so-called pre-loading pressure:

At pressures below the pre-loading pressure the soil behaves stiffer than at pressures higher than the pre-loading pressure. This behaviour is most prominent in clays. The term pre-loading is misleading in the sense that this effect is not solely brought about by the actual loading history of the soil. Several diagenetic effects, which are summarised in the term "ageing", have a similar effect on the soil.

These constraints result in a complex volumetric behaviour in clays. Several constitutive models can describe this behaviour, each having its own set of parameters. These parameters can be derived from a suite of tests in which the test conditions more or less resemble the model.

Deformation and strength are described in terms of elastic and plastic behaviour. Elastic behaviour describes reversible deformations. Elastic behaviour can be linear and non-linear. There is a direct relation between stresses and strains, which is described by the elastic parameters:

- modulus of elasticity (or Young's modulus),
- shear modulus,
- compression modulus (isotropic and constrained),
- Poisson's ratio.

Plastic behaviour describes the irreversible deformations and is always non-linear. Plasticity is governed by three factors:

- The failure envelope: is a function of stresses and parameters determining the boundary between elastic and plastic behaviour.
- Plastic deformations: which deformations occur when the failure envelope is reached.
- Hardening/softening relations: determine how the strength parameters change with strain.

For clay two constitutive models are used:

- Mohr-Coulomb, which describes the behaviour as perfectly elastic/perfectly plastic,
- Cam-Clay, which describes the behaviour with hardening plasticity.

A major drawback in the modelling of soil behaviour with parameters derived in the laboratory is the visco-elastic component, which means that the parameters are time-dependent.

Mohr-Coulomb parameters

The Mohr-Coulomb model describes the failure of the soil by the transition from elastic to plastic behaviour. The model is well suited to estimate failure loads.

The stiffness, or modulus, of the soil governs the elastic part of the model. Two moduli are important:

- the shear modulus G ,
- the compression, or bulk modulus K .

They can be described by the modulus of elasticity E and Poisson's ratio ν . E can be derived directly from triaxial tests. ν cannot be derived from Consolidated Undrained tests. In this type of test incompressibility and $\nu = 0.5$ is assumed.

The value of E to be used in the model has to relate to the stress levels involved in the problem to be solved and the type of loading. The stiffness is considerably lower during unloading than during loading. Stiffness increases at higher stress levels. In the results of triaxial tests E is usually determined as secant modulus at 50 % of the peak strength

The failure envelope is described by three parameters:

- friction angle (ϕ)
- angle of dilatation (assumed to be 0 for clays)
- cohesion (c).

The position and size of the Mohr circle determine the strength of the material: the position is a measure of the isotropic stress level and is the determining factor at depth. At low isotropic levels, such as experienced close to the surface, the cohesion becomes more important.

Cam-Clay parameters

The Cam-Clay model describes the soil behaviour by an integrated elastic and plastic formulation. It describes a failure envelope, but also the stresses and strains before failure. The relation between volume change and the logarithm of the isotropic stress is linear, as well in the elastic stage as in the plastic stage, with a different gradient. This is comparable to the one-dimensional consolidation model of Terzaghi-Buisman. The Cam-Clay model is the three-dimensional equivalent of this consolidation model.

In the elastic range:

$$e = e_k - \kappa \ln p \quad (5.15)$$

In the plastic range:

$$e = e_\lambda - \lambda \ln p \quad (5.16)$$

where: κ = gradient of elastic stage (= swelling index in oedometer test),

- λ = gradient of Critical State line in the e - $\ln p$ curve (= compression index in oedometer test),
 e = void ratio,
 p = effective isotropic stress.

Plasticity occurs when the isotropic stress increases above the transition stress level, the so-called cap in the p - q graph. This stress level is the equivalent of the pre-consolidation stress. The pre-consolidation stress is related to the plastic volumetric strain: the pre-consolidation pressure increases during compression and decreases during dilatation.

The parameters describing the initial situation of the ground are the preconsolidation stress, the present stress level and the initial porosity e_0 . e_0 is also a Cam-Clay parameter, because deformations are determined in relation to this value.

The present stress state is determined with the ratio of horizontal to vertical pressure. This parameter can be approximated by the relationship:

$$K_0 = 1 - \sin \phi \quad (5.17)$$

In an overconsolidated material this formula underestimates the value of K_0 .

The pre-consolidation pressure or the OCR , the over-consolidation ratio, which is the ratio of past maximum stress and present stress level, can be derived from the pre-consolidation pressure of the oedometer test. The pre-consolidation pressure in the Cam-Clay model is calculated according to the cap-formula used (drop, ellips or egg) with the one-dimensional p and q values derived from this pressure with the relationships:

$$\begin{aligned}
 p'_{1\text{dim}} &= (1/3) * (p'_g + 2 K_0) \\
 q'_{1\text{dim}} &= (1 - K_0) * p'_g
 \end{aligned} \quad (5.18)$$

In the Cam-Clay model a stress-dependent shear modulus is used. Poisson's ratio is held constant. The initial values are derived from triaxial tests.

The gradient of the Critical State Line in the p - q diagram is:

$$M = 6 \sin \phi (3 - \sin \phi) \quad (5.19)$$

in which ϕ is determined at failure.

FEM Analysis

Transient mixture analysis in DIANA is carried out through the following steps:

- A preliminary static linear analysis must be performed first to check the model, setup mass and elastic stiffness matrices and calculate an initial stress and flow field. As the time derivatives in static analysis are zero, two-directional stress-flow interaction reduces to single-sided coupling, i.e. flow influences stress but stress does not influence flow.
- In the second step an initial stress field is initialised in the model. This is particularly useful to initialise in situ stresses for geotechnical analysis. Usually, loading the model with the downward directed gravity loading initialises the drained stress and flow fields. This may yield an initial equilibrium state, i.e. no deformation. During stress initialisation, DIANA adapts the initial stress according to the lateral pressure ratio, i.e. the ratio between the horizontal effective stress and the vertical effective stress.
- Transient analysis is then performed on the model by applying external non-linear loads. Loads are composed of the load sets from the linear elastic analysis. The variation of non-linear loads in time must be specified. DIANA applies loads incrementally. During analysis, the behaviour of low permeability soils can be specified as either drained or undrained.

Pre- and post-processing

Preparation of a finite element mesh for very simple model geometries, definition of supports and mechanical loads can efficiently be achieved by FEMGV. In case of other but very simple geometries, considerable amount of time-consuming editing is usually required to build up a mesh. With respect to presentation and visualisation of results, FEMGV provides sufficient capabilities except for the visualisation of vector fields.

5.2 Coupling between the supraregional groundwater model and DIANA

The DIANA model will be used to simulate the coupled processes of groundwater flow and sediment consolidation under glacial loading on a 2-D vertical section. In order to solve the governing equations describing groundwater flow and geomechanical processes, the boundary conditions for the model have to be specified. This section describes how the boundary conditions have been derived.

The modelled 2-D section is generic and resembles the underground in the northwestern part of The Netherlands. The vertical boundaries (A-A' and B-B') do not coincide with physical boundaries such as large lakes or rivers and hence, the specification of boundary conditions is not straightforward. To circumvent these problems boundary conditions for the sides A-A' and B-B' will be obtained from a large-scale quasi 3-D groundwater flow model (see Figure 5.2).

Ideally, the 2-D section should be aligned with the stream plane in the quasi-3-D model. Furthermore, the hydrogeological properties, aquifer geometry and ice sheet properties (thickness, gradient and subglacial meltwater production) should be similar in both models.

5.2.1 Brief description of the supraregional model

The supraregional model has been developed in the EC project 'Simulation of the effects of long-term climatic change on groundwater flow and the safety of geological waste disposal sites' by the RIVM, University of Edinburgh and the Geological Survey of the Netherlands (now TNO-NITG). The model is described in detail in a number of publications (Van Weert et al., 1997; Boulton & Curle, 1997). It is based on the AQ-FEM computer code. For a comprehensive understanding of the model one is referred to one of the publications mentioned above. A concise description of the supraregional model is given below.

The supraregional groundwater model is able to study the effects of cold climatic changes on the geohydrological system of Northwest Europe. Its model domain extends from Scandinavia to Belgium and from Great Britain to Poland (about 1000 * 1000 km²). It covers the current North Sea basin and the older Permian basins.

At this large scale it is assumed that the geohydrological system can be modelled by dividing the sedimentary layers into 3 units:

- an upper aquifer of mainly Quaternary permeable sediments;
- a separating aquitard consisting of semipervious Tertiary clays;
- a lower aquifer consisting of Mesozoic low permeability sediments like chalk, marl, lime and fine sands.

The model is quasi 3-D. In the aquifers groundwater flow is assumed strictly horizontal. In the aquitards groundwater flow is assumed to be strictly vertical. It is thought that Darcy's law is valid on this scale. Fluid density is assumed constant.

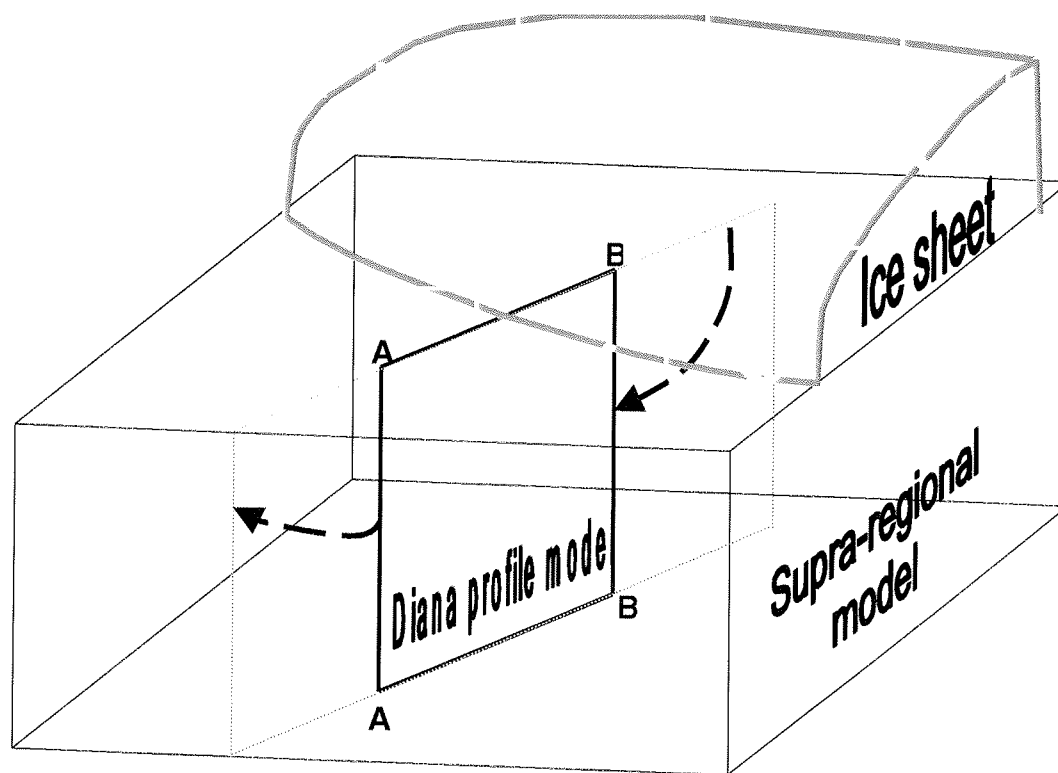


Figure 5.2 Schematic position of the 2-D profile model in the quasi 3-D supraregional model. The 2-D profile model will be used to calculate the coupled groundwater flow and sediment deformation under glacial loading. Hydraulic boundary conditions for the vertical boundaries A-A' and B-B' will be derived from the supraregional model. These boundary conditions will be specified as fluxes or hydraulic heads.

There are neither temperature effects, nor salt concentration effects in the model. Geomechanical effects due to glacial loading are neglected and porosity is taken as a constant. Because of these assumptions only steady-state calculations were performed. The hydraulic conductivity values of the various layers are assumed homogeneous and isotropic. For the lower aquifer two hydraulic conductivity values were used: a higher value for the outcropping lower aquifer and a lower value for the lower aquifer overlain by other sediments.

The boundary conditions for the top surface are dependent on the palaeogeography. Depending on the geographical feature covering the top surface different boundary conditions are applied. The zones covered by permafrost are modelled as no-flow boundaries. When covered by an ice sheet, sub-glacial infiltration of the smeltwater may occur. When overlain by large water bodies (lakes or seas) a direct contact between the groundwater system and surface water system is assumed.

5.2.2 Simulation with supraregional model

A hypothetical palaeogeographical situation is simulated with the aid of the supraregional model. The results of this simulation are used to provide boundary conditions for the vertical sides of the 2-D hydromechanical model. The ice sheet's properties are chosen such as to have strong effects on the geohydrological system. This means that especially the horizontal groundwater velocities in the aquifers will have extreme values. One has to consider that the supraregional model does not take into account any deformation processes. Extreme geohydrological situation calculated with this model does not necessarily imply strong deformation processes in the DIANA model.

The palaeogeographical situation is showed in Figure 5.3. This figure gives the spatial distribution of the ice sheet, continuous and discontinuous permafrost, proglacial lakes and major rivers. As mentioned above, this is a hypothetical palaeo-situation. This very situation may have not existed at all. However, similar climatic situations (although maybe not this extreme) may have existed during the cold periods (Elsterian, Saalian, and Weichselian) in the Pleistocene. The glacier's profile is defined as follows:

$$ice\ sheet\ height\ (m) = 4.7 \sqrt{dist.\ from\ ice\ sheet\ toe\ (m)} \quad (5.20)$$

This relation is based on data of current ice sheets in the Antarctic and in Greenland. It is assumed that the Pleistocene glaciers invading Europe had smaller gradients. To provide a smooth ice sheet surface the profile does not obey this relation everywhere. This relation implies that already 100 metres from the ice sheet's toe the ice sheet thickness is 47 metres. The maximal ice thickness in the model domain is about 3200 metres.

The subglacial melting rate is taken as a fixed value of 20 mm/year. In reality one would expect a spatial distribution of sub-glacial meltwater production due to differences in subglacial heat production (geothermal flux, frictional heat). The subglacial melting rate used in this study is relatively high.

The ice sheet extends into NE-part of the Netherlands and into northern part of Germany and Poland. Furthermore, it covers a large part of the United Kingdom. This extension existed during the Saalian period. In front of the ice sheet there are permafrost zones. This permafrost can be continuous (and hydraulically completely confining) or discontinuous. The thickness is 120 and 60 metres for the continuous and discontinuous permafrost areas, respectively. Directly in front of the ice sheet there are a number of proglacial lakes. These lakes develop in the topographical depressions (due to the ice sheet loading) directly at the toe. They are filled mainly

with supraglacial meltwater. Underneath these lakes, permafrost is absent enabling a contact between the groundwater system and the lake water.

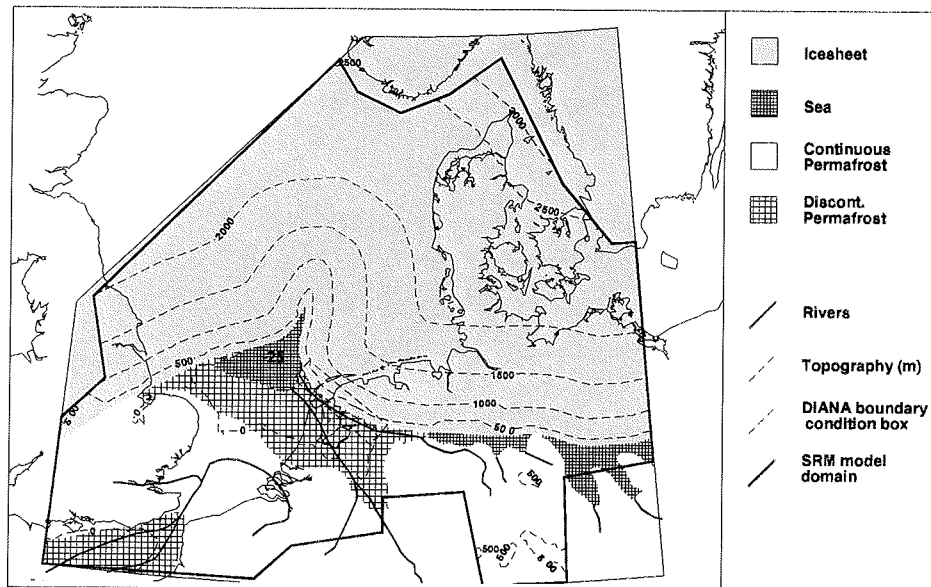


Figure 5.3 This palaeogeographical situation forms a (extreme) but representative snapshot of a cold climatic period in Europe during the Pleistocene. It gives the distribution of ice, permafrost, lakes and major rivers. A subglacial melting rate of 20 mm/year is assumed. Permafrost is assumed to be absent under lakes and rivers.

Some major rivers are shown in Figure 5.3. Permafrost is absent under these rivers. Lakes and rivers form the only unconfined zones in the model domain. One could therefore expect high drainage values in these features.

Two different runs are performed with this palaeo-situation. In the first run, all rivers shown on the map are allowed to drain and infiltrate. In the second run, the river flowing closest (10 km distance) to the glacier's snout is "switched off" - no infiltration or drainage possible.

5.2.3 Results

Figure 5.4 shows the calculated hydraulic heads in the upper aquifer for the runs described above. Maximal upper aquifer heads of about 2400 metres are reached at the maximal ice thickness in the very north-western part. The hydraulic gradients in the upper and lower aquifer follow more or less the ice sheet's profile. The upper

aquifer hydraulic potential is furthermore strongly affected by the draining lakes and rivers. Hydraulic heads in the upper aquifer are generally 10-100 metres less than the heads in the lower aquifer. The opposite situation of upper aquifer heads being 100's of metres higher than the lower aquifer head exists in an area in the northern part of Germany.

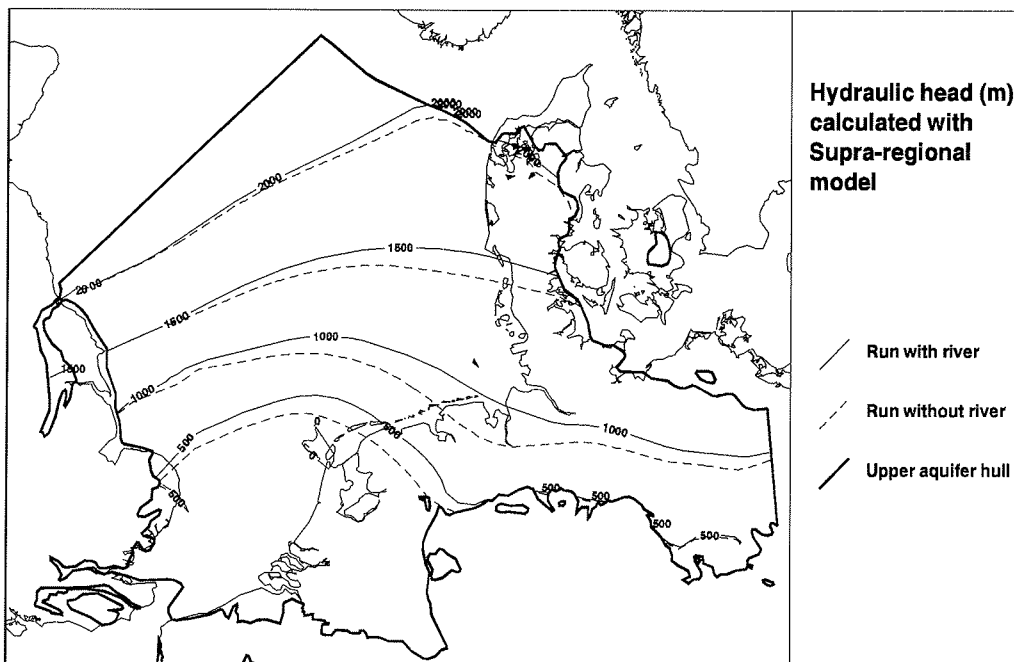


Figure 5.4 Calculated hydraulic heads in the upper aquifer for the palaeogeographical situation. Hydraulic heads are in metres. In the upper figure, all rivers are able of discharge/drainage. In the lower figure the river closest to the glacier's snout is "switched off".

The horizontal (Darcy) velocities in the upper aquifer range from 1-10 metres/year in the permafrost zones to 10-100 m/year in the zones under the glaciers' snout. Very high groundwater values (up to 300 m/year) can be found in northern Germany and Poland. Here, the hydraulic gradient is enhanced due to the drainage into the pro-glacial lakes. The horizontal groundwater velocities in the lower aquifer range from 0.01-1 m/year in the proglacial part and 0.1-0.5 m/year in the subglacial part.

Vertical fluxes through the Tertiary clays are generally in the order of 1 to 10 mm/year. Vertical fluxes (mainly drainage) in the rivers and proglacial lakes can reach up to hundreds of mm/year.

Note the strong effect of the river close to the glaciers' snout on the hydraulic heads. In case of a draining river hydraulic heads are much less than in the case of no river.

5.2.4 Boundary conditions for 2-D model

Figure 5.3 shows a box located in the northeastern part of the Netherlands. In this area the supraregional model geometry corresponds closely to the vertical 2-D model. Hence, results from this area are used to calculate boundary conditions for the 2-D profile model. Results from two series of nodes in the supraregional model are used. The first series of nodes lies directly on the ice sheet's toe. These results provide boundary conditions for the vertical side B-B'. This series of nodes lies at a distance of 10 kilometres from the glacier's snout. The nodes are located along the river. The results of this series are used to define boundary conditions for side A-A' of the DIANA model.

Figure 5.5 shows the hydraulic heads and Darcy velocities for the upper aquifer and lower aquifer obtained from both series of nodes. The heads are given in metres and the velocities in m/year. Averaged values and their standard deviation are given. Note the strong influence of the river on the hydraulic heads and hydraulic gradient in the upper aquifer. These effects are less, but still observable in the lower aquifer.

5.3 Coupling between DIANA and the transport model

With the aid of the computer code DIANA a 2-D groundwater velocity field will be calculated for the section under glacial conditions. This velocity field will be used to calculate the transport of radionuclides hypothetically leaking from a repository in the clay formation. These transport simulations will be carried out with the METROPOL-code.

Transport of radionuclides takes place due to the mechanisms of advection and diffusion. The advective transport takes place as the groundwater in which the nuclides reside is moving. Due to this type of transport the nuclides will tend to follow groundwater streamlines. Diffusion takes place due to the concentration gradient of radionuclides in the groundwater. This process tends to spread the nuclides in all directions. Even when the groundwater is stagnant transport of radionuclides will take place because of diffusion.

It is believed that the groundwater velocities in the deep-located clay formation are very small under current climate conditions. In the case of glacial loading the consolidation effects are assumed to occur and transport of the nuclides might be

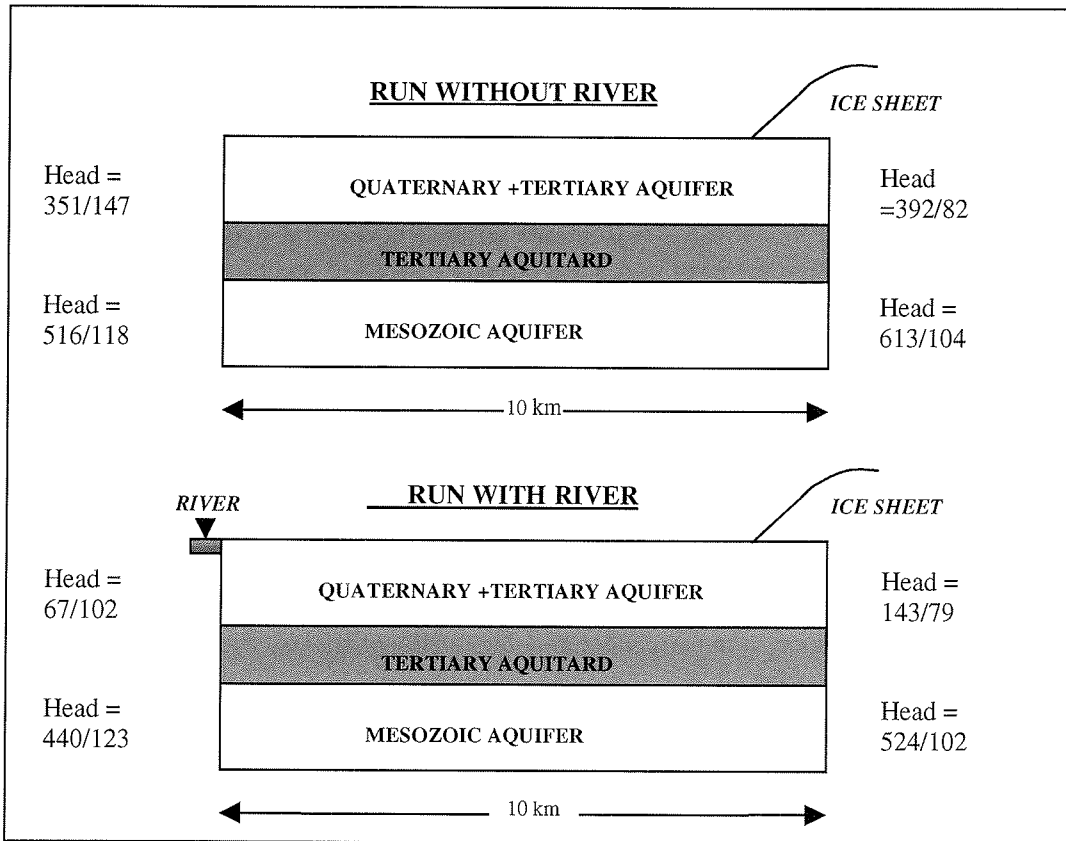


Figure 5.5 Supraregional model results on the location of the vertical boundaries in the DIANA model: A-A' and B-B'. Both hydraulic heads and horizontal (Darcy) groundwater velocities are given for the upper and lower aquifer. These values (number before slash sign) are based on an average of hydraulic heads and velocities in the box denoted in Figure 5.3). After the slash sign, the standard deviation around this average value is given.

driven by advection as well. Thus, transport of the radionuclides in the clay formation will be diffusion-dominant for most time periods and may be advection-driven under (glacial) loading conditions. In the aquifers where the groundwater velocities are much higher transport of nuclides is dominated by advection in all cases.

One would overestimate the mainly diffusion-driven transport of nuclides in the clay when only 2 dimensions are considered. Therefore, transport calculations are carried out on a 3-dimensional (3-D) model. This 3-D model is created by a repetition of the hydrogeology and velocity fields of the 2-D section model (Figure 5.6).

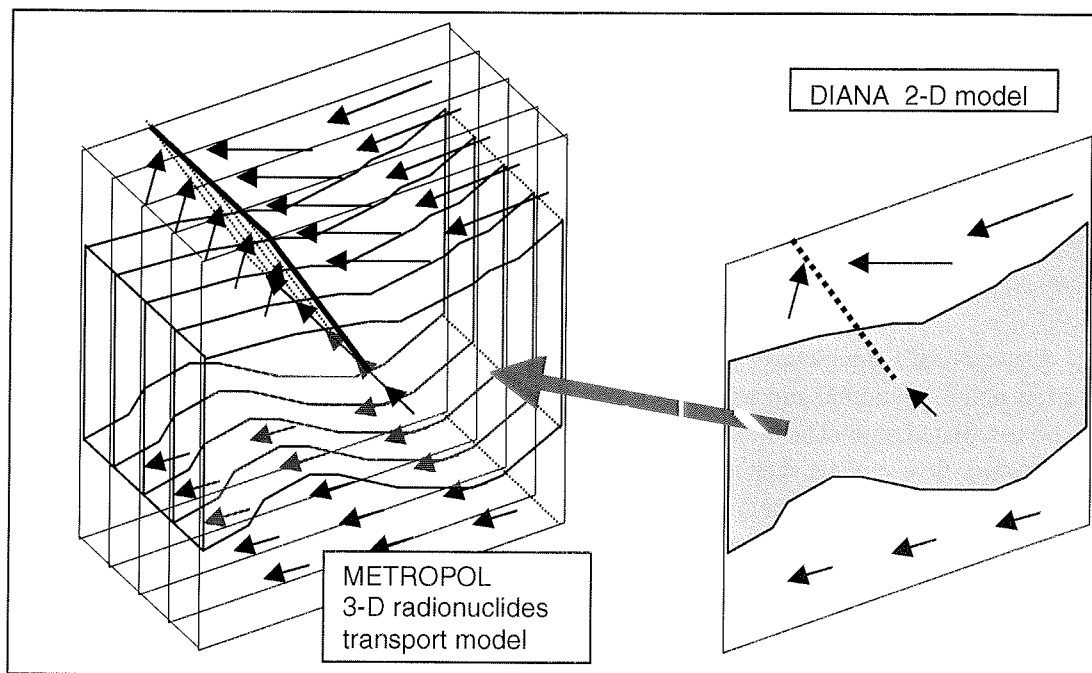


Figure 5.6 Coupling between the groundwater velocity field calculated by the hydromechanical model and the radionuclides transport modelling. The groundwater velocity field is calculated in the 2-D profile model (DIANA). The transport modelling will be performed in a 3-D fashion (METROPOL). If diffusion were considered a 2-D process only, transport of radionuclides would be overestimated. If faults were considered as linear features (instead of planar), possible transport through fractures would be underestimated.

The DIANA code is also able to incorporate faults into the models. Faults might increase the permeability locally and create conduit for groundwater flow. In the 2-D section model, faults will be modelled as 1-dimensional (1-D) features (lines). In the 3-D reality the faults will be planar. These fault planes can be schematised in the 3-D transport model as well. Modelling faults as a one-dimensional feature might cause a strong underestimation of radionuclide transport.

Brief Description of METROPOL-4

The transport of radionuclides will be simulated with a specially developed computer code: METROPOL-4. This code has been developed at the RIVM (Sauter, 1987; Sauter and Hassanizadeh; Sauter et al., 1990). METROPOL-4 is part of a larger simulation package able of calculating steady-state and transient groundwater flow with constant density or transient groundwater flow with transport of dissolved salt or adsorbing or decaying species (at low concentrations).

Pre- and post-processing programs include mesh generation, mesh refinement, particle tracking and plotting of data.

METROPOL-4 is a program for the simulation of the transport of low-concentration tracers (in this study the radionuclides) by groundwater flow. It calculates mass fractions of the radionuclides and takes into account linear adsorption and radioactive decay of unstable solutes into new species. METROPOL-4 calculates the concentration and transport of each species in the decay chain.

The dispersive-diffusive tensor is defined in a classical way as a function of Darcy velocity and longitudinal and transversal dispersivities. The Darcy velocity field can be calculated with other modules of the METROPOL-package or with other groundwater flow models such as DIANA. The Darcy velocity field can change in time in a step-like fashion. Retardation of the radionuclides due to adsorption to the solid matrix is taken into account. This adsorption is described by an isothermal linear adsorption coefficient. The decay of unstable species is taken into account.

The effective molecular diffusion coefficient, dispersivities, retardation factor and decay factor may change in space. Furthermore, different decay factors can be specified for each species in the decay chain.

6 Simulation of glacially-driven hydromechanical processes using a simple model

6.1 Simple hydromechanical model

In order to assess the effects of ice loading on the Tertiary clays, which may host a nuclear repository site, a simplified mathematical hydromechanical model is developed. The use of a simplified model in the first phase of this study is beneficial due to relatively short time required to prepare the model and run simulations. In this way a number of scenarios can be calculated in order to test the model, validate it and determine its sensitivity to the change of some input parameters. The results obtained will then be used to select a small number of scenarios that will be calculated in the second phase of this study on a detailed hydromechanical model.

The simplified hydromechanical model is based on the following assumptions:

- The model is a generic approximation of the regional geological cross-section and is considered to be representative for the Netherlands situation, but does not refer to a specific location in the subsurface of the Netherlands.
- Geometry of the model comprises the most important regional geological features derived from the regional geological cross-section (Figure 3.1).
- The model units are derived from the regional geological cross-section taking into account similarity in hydromechanical properties of geological units.
- Each of the differentiated model units has uniform thickness and it is homogeneous with respect to its hydromechanical properties.
- Mechanical behaviour of the Rupel Clay and Asse Member is described by using the Mohr-Coulomb material model for soils.
- Initial geohydrological boundary conditions are based on the groundwater model of Northwest Europe for glacial conditions (Van Weert & Leijnse, 1996).

6.2 Schematisation and model mesh

Model schematisation

Schematisation of the model cross-section is carried out in such a way to preserve important geological relationships and features identified on the geological cross-section shown in Figure 3.1. Another important constraint in model schematisation was to limit the total number of elements in a finite element mesh to a few thousands in order to reduce the computer calculation time.

Regional character of the geological cross-section implies it's large lateral extent and a depth of interest several orders of magnitude smaller than the lateral extent. Tessellation of such a section in relatively small number of finite elements would require the use of elongated quadrilaterals and triangles, which would lead to a mesh of poor quality and, consequently, to the numerical instabilities during calculations. For this reason the model cross-section has been considerably shortened to a length of 10 km and a depth of 1.2 km.

The model section is divided into two parts, the northern part and the southern part, each of which is characterised by a set of horizontal model units of uniform thickness (Figure 6.1). In this way important geological and hydrogeological relationships are preserved as follows:

- In the northern part of the section the Rupel Formation is in direct hydraulic contact with the overlying sands of the Breda Formation.
- In the southern part of the section fine sands of the Voort Formation and clays of the Veldhoven Formation subsequently overlay the Rupel Formation. The Breda Formation, which overlays the Voort Formation, is thus not in a direct hydraulic contact with the Rupel Formation.
- The fault zone, in the southern part of the cross-section, is simplified and represented by a single vertical fault.

The model units are differentiated using the following principle. Adjacent geological units, similar in lithology and hydromechanical parameters, are joined into a single model unit. On the other hand, single geological units, if they consist of lithologically different parts whose thickness exceed 30 m, are split into different model units (e.g. Breda Formation).

In total ten model units are differentiated. These are characterised by the hydromechanical parameters presented in Table 6.1 to Table 6.3. In geohydrological sense seven units represent aquifers (various formations of the Quaternary – KWAR; Harderwijk, Tegelen, Kedichem and Maassluis - HA&MA; Oosterhout – OOST; most of Breda Formation - BRE_Z; Voort - VOORT; Brussel - BRUS; and Mesozoic - MESOZ). Three units represent aquitards or semipervious units (part of Breda Formation and Veldhoven - BR&VE; Rupel Clay and Asse Member - RU&AS; and Ieper and Landen - IP&LA).

Finite element mesh

A finite element mesh was generated with the FEMGEN code (*DIANA, User's Manual, FemGV*). The generated mesh is shown in Figure 6.2. The total number of elements is 3585. Most of the elements are quadrilaterals, with a length of 250 m and a width of 30 to 80 m. In this manner the aspect ratio of an element (i.e. the length to width ratio) was kept below 10.

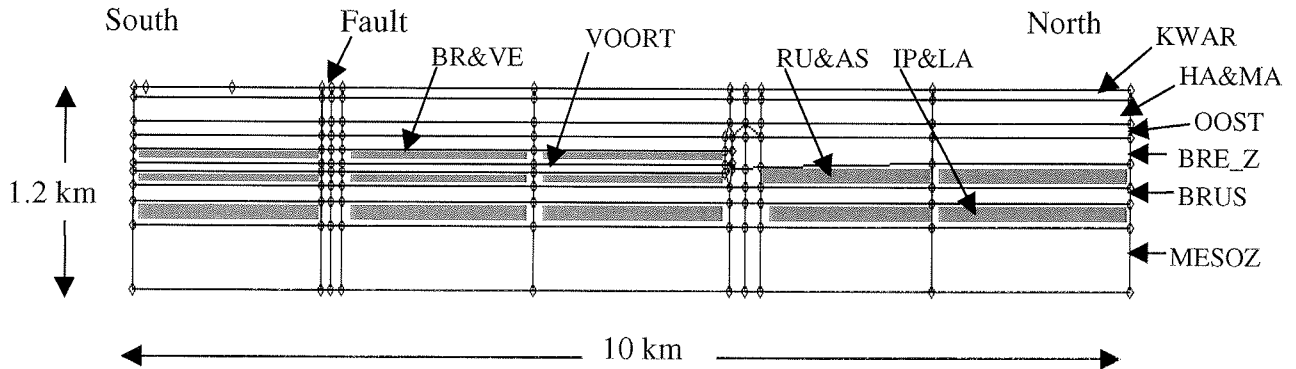


Figure 6.1 Schematisation for simplified hydromechanical finite element model. Units that act as aquicludes are shaded. Other units represent aquifers.

Table 6.1 Schematisation of a generic geological cross-section in a simplified hydromechanical model and the parameters which are characterising the differentiated model units; for legend is referred to Table 6.3.

Stratigraphic unit	Model unit	Thickness (m)	Geohydrological parameters		Geomechanical parameters for Mohr-Coulomb model						
			n (%)	K (m/s)	γ (kN/m ³)	E (MPa)	ν	Φ (°)	ψ (°)	c (kPa)	
Quaternary	Various formations	KWAR	60	35	1×10^{-5}	18	125	0.3	35	35	10
	Harderwijk Formation	HA&MA	150	35	1×10^{-5}	18	125	0.3	35	35	10
Tertiary	Tegelen Formation										
	Kedichem Formation										
e	Maasluis Formation										
	Oosterhout Formation	OOST	80	35	1×10^{-5}	18	125	0.3	35	25	10
r	Breda Formation	BRE_Z	150	35	1×10^{-5}	18	125	0.3	35	25	10
	Veldhoven Formation	BR&VE	150-90	50	1×10^{-10}	16	50	0.3	27	27	200
i	Voort Mb.	VOORT	40	35	1×10^{-5}	18	125	0.3	35	35	10
	Rupel Formation										
a	Asse Mb.	RU&AS	150-90	40	1×10^{-10}	16	50	0.3	27	27	200
	Brussels Sand Mb.	BRUS	80	30	1×10^{-5}	18	125	0.3	35	35	10
y	leper Mb.										
	Landen Formation	IP&LA	150	40	1×10^{-10}	16	50	0.3	27	27	200
Mesozoic	Jurassic/Triassic										
	Triassic Buntsandstone	MESOZ	380	20	1×10^{-6}	23	10000	0.3	25	25	3000

Table 6.2 Additional parameters required for Cam-Clay model for the Rupel Clay and Asse Member.

For legend is referred to Table 6.3.

Stratigraphic unit	Model unit	Geomechanical parameters for Cam-Clay model		
		λ	κ	OCR
Rupel Formation Asse Mb.	RU&AS	0.13	0.04	1.0

Table 6.3 Parameters characterising friction along the fault according to the Coulomb friction model.

Model unit	Lithological unit intersected by fault	Geomechanical parameters for Coulomb friction along the fault					Geohydr. parameters
		c (kPa)	ϕ (°)	ψ (°)	D_n (MPa)	D_s (Mpa)	K (m/s)
Fault	Sand unit				12500	4800	
	Clay unit	0	35	0	5000	1920	1×10^{-3}
	Mesozoic				1×10^7	4.34×10^6	

Legend:

n - porosity,	c - cohesion,
K - hydraulic conductivity,	λ - compression index,
γ - unit weight,	κ - swelling index,
E - Young's modulus,	OCR - over-consolidation ratio,
ν - Poisson's ratio,	D_n - normal stiffness,
ϕ - angle of internal friction,	D_s - shear stiffness.
ψ - dilatation angle,	

The Rupel Clay and Asse Members were represented by a uniform and relatively fine mesh, consisting of squares of 30 by 30 metres. Away from this unit the mesh was made coarser. Mesh quality tests were run to check and confirm that the whole mesh was of good quality.

Two types of plane strain elements are then generated using the FEMGEN code: quadrilateral elements with 8 nodes (CQ16E element type in DIANA) and triangular elements with 6 nodes (CT12E element type in DIANA; see *DIANA, User's Manual, Element Library*). In order to allow simultaneous calculation of flow and stress according to the Biot theory, all the structural elements were extended to the so-called mixture elements. In this way the pore pressure potential is added to the displacements as a nodal degree of freedom.

Quadrilateral interface elements with 6 nodes (type CL12I in DIANA) were used to model the fault. Interface elements allow sliding of (fault) blocks on either side of an element. The fault unit has a thickness of one interface element (1 m).

6.3 Conditioning of the model

Initial displacement conditions

Structural and geohydrological boundary conditions have to be imposed along the model boundaries. Structural boundary conditions consist of imposing displacement constraints. Along the lateral boundaries of the model displacements were allowed in vertical direction only. The lower boundary was fixed in the vertical direction, while the upper boundary was free to move in all direction (Figure 6.2).

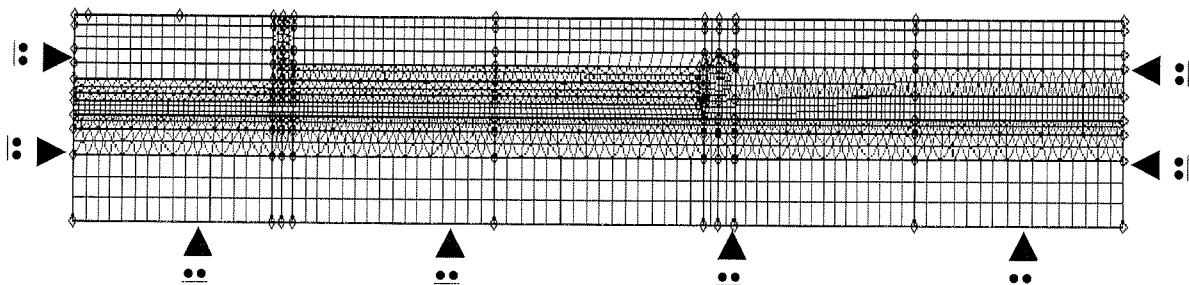


Figure 6.2 *Finite element mesh and structural boundary conditions for the simplified hydromechanical model.*

Displacements in vertical direction were also allowed along the interface between the fault and the surrounding model units. The interface represents a sort of internal boundary condition that is modelled by using a special type of interface structural elements (see previous section).

Initial in situ stress conditions

Initial in situ stresses are determined by the weight of soils, pressure of fluids in the soil pores and geological history of the modelled area. As the model in this study is generic, calculation of the initial stresses is based upon relatively simple assumptions:

- The total stresses in vertical direction are calculated from the depth below ground surface and unit weights of the model units.

- The effective stresses are obtained by subtracting the pore water pressure from the total stresses.
- Initial distribution of the pore water pressure is calculated taking into account initial hydraulic boundary conditions.
- The modelled area has been normally consolidated in the geological past. The horizontal effective stresses (σ'_h) can therefore be calculated from the vertical effective stresses (σ'_v) using the lateral pressure ratio (K_0) which follows from the theoretical relationship (ϕ is the angle of internal friction):

$$\sigma'_h = K_0 \sigma'_v \quad (6.1)$$

$$K_0 = 1 - \sin \phi \quad (6.2)$$

The initialisation of the *in situ* stresses in the finite element model can be achieved by applying gravity acceleration on the model.

Geohydrological boundary conditions

Geohydrological initial boundary conditions are determined on the basis of the developed model concept as presented in Chapter 2.2. The upper boundary conditions are determined by the palaeogeographical conditions. The model may be covered by a large ice sheet, permafrost and, possibly large lakes or rivers. Underneath the glacier there may be recharge of sub-glacial meltwater, Additionally, supra-glacial meltwater may percolate through the ice sheet and eventually recharge the underlying aquifers. The permafrost may be continuous or discontinuous. In the case of continuous permafrost no groundwater flow can take place. In the case of discontinuous permafrost some recharge/discharge may occur. In the case of coverage by lakes or major rivers permafrost is absent. The groundwater system will be connected with the surface water, possibly with some hydraulic resistance between the groundwater system and surface water system.

In accordance with the above the following boundary conditions for the simplified hydromechanical model are specified (Figure 6.3):

- The base of the model represents a no-flow boundary.
- The lateral side upglacier of the model represents a boundary with prescribed inflow. The inflow can be calculated as a function of the recharge from basal melting upglacier from that point.
- The lateral side of the model, beyond the glacier margin, can be represented as a boundary with prescribed potential. The potential can be inferred from groundwater drains such as rivers, lakes and seas.
- The upper boundary can be specified as a no-flow boundary where the model is covered by permafrost; as a constant inflow boundary, where the basal melt

water infiltrates into the subsurface; and, as a constant potential boundary where the groundwater system is hydraulically connected with rivers, lakes and seas, or where the permafrost is discontinuous.

6.4 Practical approach in the simulations

In the geomechanical sense the mechanical behaviour of all units, including the Rupel Clay and Asse Member (the RU&AS unit), is represented by the Mohr-Coulomb material model. Mechanical behaviour of the fault is described by the Coulomb friction model (*DIANA, User's Manual, Nonlinear Analysis*). Normal and shear stiffness of the fault are calculated using the following empirical relationships:

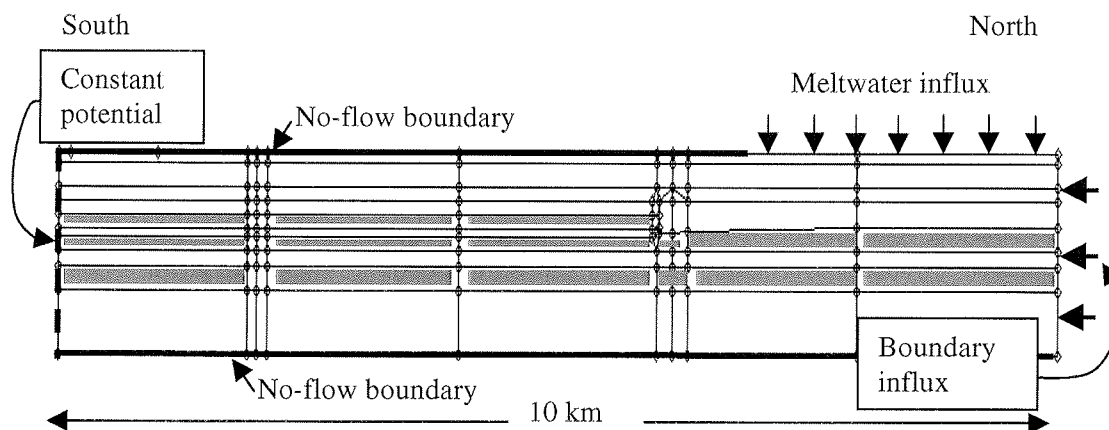


Figure 6.3 Geohydrological boundary conditions.

$$D_n = \frac{(1-\nu)}{(1+\nu)(1-2\nu)} \frac{E}{h} \quad (6.3)$$

$$D_s = \frac{1}{2(1+\nu)} \frac{E}{h} \quad (6.4)$$

where: D_n = normal stiffness
 D_s = shear stiffness
 E = Young's modulus
 ν = Poisson's ratio of the soil surrounding the fault
 h = thickness of the fault.

Simulation of the effects of a future glaciation using the simplified finite element model is carried out through the two main stages:

- First, the *in situ* distribution of stresses and pore pressures for the entire model is calculated. This determines the initial state of the model that corresponds to the present situation when the ice is absent.
- In the second stage various ice-loading scenarios are defined and calculated. These simulate various glacial situations by imposing appropriate loading of the hydromechanical model and changes in the boundary conditions of the model.

Ice-loading scenarios

Various ice-loading scenarios can be defined to simulate the effects of ice loading on the Rupel Clay and Asse Member and the groundwater system. In order to define the ice-loading scenarios the following assumptions have been made:

- An ice-loading scenario consists of three phases:
 - Ice sheet is absent - this corresponds to the initial present conditions.
 - Ice sheet steadily advances over the area until it reaches maximum thickness.
 - Ice sheet of maximum thickness covers the whole area.
- Ice-loading scenarios are divided into three major groups on the basis of the speed of ice sheet movement. These simulate slow, medium fast and very fast advance of ice (Figure 6.4). A set of scenarios corresponding to the medium fast speed of ice sheet movement will be used as a reference.
- Model parameters that will be kept unchanged in all the scenarios are as follows:
 - Geomechanical and geohydrological parameters, which characterise differentiated model units (given in Table 6.1 to Table 6.3), apart from parameters describing the Rupel Clay and Asse Member (the RU&AS model unit).
 - The form and maximum thickness of ice sheet.
 - Ice load, which is applied through five load cases.
 - The geometry and dynamics of the permafrost (Figure 6.5). The permafrost extends laterally 2 km on either side from the ice sheet margin. Permafrost is 60 m thick. It is characterised by a very low hydraulic conductivity $K=1 \times 10^{-10}$ m/s.
 - Vertical inflow due to meltwater infiltration, with a melting rate of 20 mm/year.
 - Constant potential, equal to the ground surface, prescribed along the lateral (southern) boundary of the model.
- Model parameters that can be varied in particular scenario are as follows:
 - Lateral influx.
 - Geomechanical parameters of the Rupel Clay and Asse Member.

- Hydraulic conductivity of the Rupel Clay and Asse Member.
- Hydraulic conductivity of the fault (conduit/seal).
- Presence of a high permeability zone in the Rupel Clay and Asse Member.
- Presence of a river beyond the margin of permafrost.
- By combining model parameters, a set of 15 scenarios has initially been selected to run on the simplified geomechanical model assuming medium fast advance of ice sheet, i.e. reference case (Table 6.4). In the course of first runs, the obtained results will be examined and the total number of scenarios will be possibly limited to about 10.

For two other speeds of the ice sheet movement, namely for very fast and very slow advance of ice sheet, only one or two most interesting scenarios will be run.

Approach

Simulation of the effects of ice loading on the subsurface consists of two major steps. In the first, preparatory step the initial stress and groundwater flow have been initialised in the model (Section 6.3). In the second step, ice-loading scenarios have been simulated using the initialised model (Section 6.4).

The initial stress and groundwater flow conditions have been generated by a linear elastic (static) finite element (FE) analysis. Then a nonlinear transient (i.e. time-dependent) analysis has been used to simulate the hydrodynamical processes in the subsurface caused by ice loading. For a detailed description of the mathematical background and the analysis steps refer to Section 5.1.

The results of a preliminary linear elastic analysis have been presented first (Section 6.5). The results of a nonlinear transient FE analysis have been presented separately for each of the three major groups of the defined ice loading scenarios, which are described in Section 6.3. The hydromechanical effects of the loading by ice for a medium fast, for a very fast and for a very slow advance of an ice sheet have been presented in Section 6.6, Section 6.7 and Section 6.8, respectively. The results from the scenarios with a medium fast advance of an ice sheet have been discussed most extensively. The results from the other two sets of scenarios have been presented only if they significantly differ from those obtained by running the scenarios with a medium fast advance of an ice sheet.

In the defined ice-loading scenarios (see Section 6.4) the parameters determining the weight of soils are kept unchanged, while the initial geohydrological boundary conditions vary. Consequently, the initial stress distributions will also vary. Therefore the results of initialisation, and later the results of the loading by ice, will

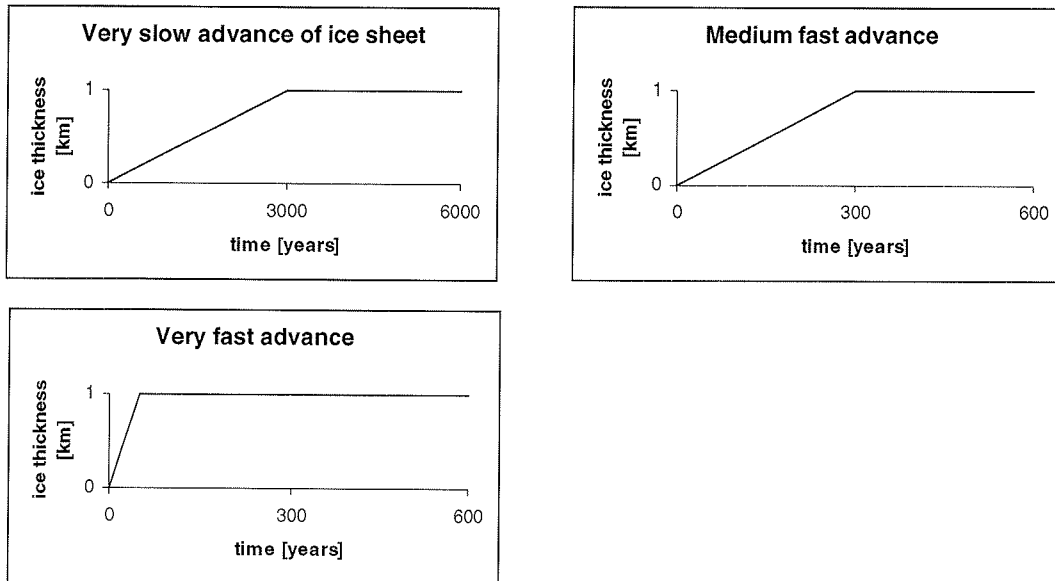


Figure 6.4 Division of ice-loading scenarios into three major groups on the basis of the speed of ice sheet movement

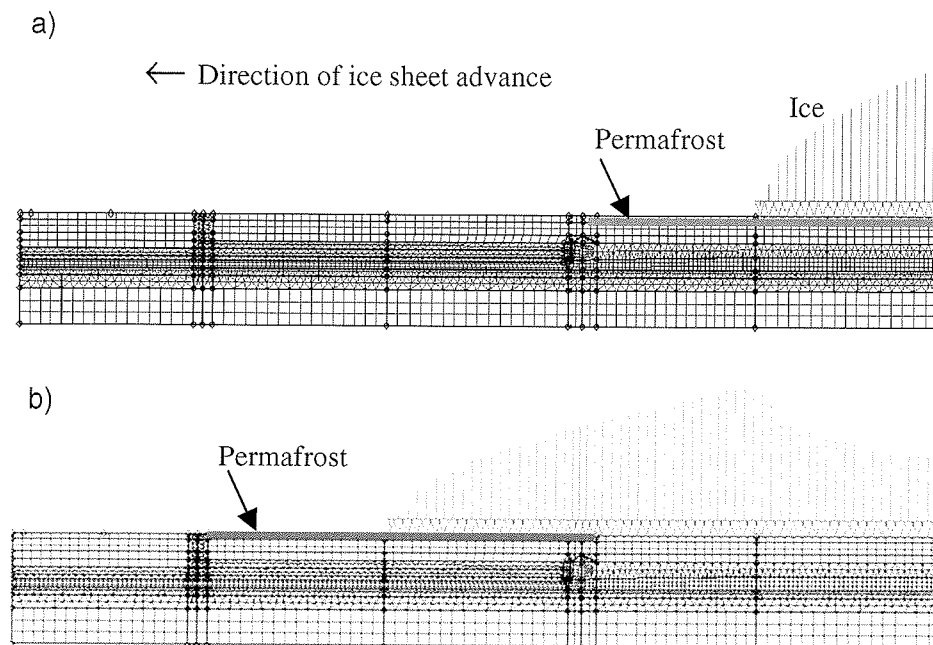


Figure 6.5 Loading of the model by a steadily advancing and thickening ice sheet is achieved through five load cases. Only the first two are presented here. Ice load is not to scale.

be discussed separately for the scenarios with a low lateral influx and the scenarios with a high lateral influx of groundwater into the model.

The scenarios initially selected to be run, listed in Table 6.4, were calculated. The scenarios in which the fault zone functions as a barrier were not calculated, as further explained in Section 6.5.2. However, some of the results are not presented in this report. The scenarios with a medium lateral influx were omitted from the discussion as these depict a medium state of the model. The other two presented sets of scenarios, those with a low and those with a high lateral influx into the model, illustrate the two extreme geohydrological situations. Any intermediate geohydrological situation yields a model response within the two extremes. As the analysis of a medium model state practically would not contribute to this study, the scenarios with a medium influx were omitted from further discussion. Other than that, the scenario with a river at the permafrost margin was also not presented as the river had influenced the groundwater flow pattern in the top aquifer only.

6.5 Initialisation of the stress and groundwater flow in the model

The initial distribution of stresses and pore pressures in the model is determined by the weight of the sediments, pressure of fluids present in the subsurface and the geological history of the modelled area. It was assumed that the area has been normally consolidated and that a simple relationship exists between the horizontal and vertical stresses (Equation 6.1).

Initialisation of the stress and pore pressure in a linear elastic FE analysis is carried out through three loading steps. In the first loading step the initial dead weight is introduced by applying the gravity acceleration on the model (Section 6.5.1). In the second step geohydrological boundary conditions are imposed on the model in order to generate the pore pressure and additional (neutral) stress in the model (Section 6.5.2). In the third step the influence of two previously defined steps is linearly combined. The third loading step introduces the initial state of stress and pore pressure in the model (Section 6.5.3). This loading step will be used in a nonlinear transient analysis to introduce the initial state of stress and pore pressure into the model before loading the model by an ice sheet.

The Quaternary deposits and permafrost are modelled by an ideally elastic material model in order to avoid numerical instabilities during calculations. For all other modelled units an ideally elastic-perfectly plastic Mohr-Coulomb material model was used (Section 6.4).

Table 6.4 Overview of the defined ice-loading scenarios. The scenarios initially selected to be run are marked. Legend: L=low; M=medium; H=high; C=conduit; S=seal.

Varying parameter	Relative values											
	L (low)				M (medium)				H (high)			
Lateral influx	L (low)				M (medium)				H (high)			
Geom. param. Rupel Clay and Asse Member	L	M	L	M	L	M	L	M	L	M	L	M
Hyd. cond. Rupel Clay and Asse Member	H	M	H	M	H	M	H	M	H	M	H	M
Hyd. cond. fault	C	S	C	S	C	S	C	S	C	S	C	S
Scenarios to run	•	•	•		•	•	•	•	•	•	•	•
Additional parameters												
High perm. zone Rup. Clay	Y				Y				Y			
Scenarios to run							•					
River at the perm. margin	Y				Y				Y			
Scenarios to run			•									

Key for the above table:

Varying parameter	Absolute values		
Lateral influx	Low (L)	$i=5 \times 10^{-4}$	Influx is calculated taking into account present, small hydraulic gradient (i).
	Medium (M)	$i=4 \times 10^{-3}$	Influx under increased hydraulic gradient, app. equal to one half of the max. gradient.
	High (H)	$i=8 \times 10^{-3}$	Influx under maximal hydraulic gradient.
Note: Max. hydraulic gradient is calculated by running the supraregional model. Boundary conditions of the supraregional model were adjusted to correspond to those of the simplified hydromechanical model.			
Geomechanical parameters Rupel Clay and Asse Member	Low (L)	$c=100 \text{ kPa}$, $\Phi=20^\circ$	
	Medium (M)	$c=200 \text{ kPa}$, $\Phi=27^\circ$	
Hydraulic conductivity Rupel Clay and Asse Member	Medium (M)	$K=1 \times 10^{-10} \text{ m/s}$	
	High (H)	$K=1 \times 10^{-9} \text{ m/s}$	
Hydraulic conductivity Fault:	Conduit (C)	$K=1 \times 10^{-3} \text{ m/s}$	
	Seal (S)	$K=1 \times 10^{-10} \text{ m/s}$	
High permeability zone Rupel Clay and Asse Member		$K=1 \times 10^{-5} \text{ m/s}$	

6.5.1 Loading by gravity

Loading of the model by applying gravity acceleration in a preliminary linear elastic analysis creates an initial stress field that is identical for all defined scenarios (Figure 6.6 and Figure 6.7). The effective stresses initialised in the model must match the lithostatic stresses for hydrostatic conditions. These stresses can also be calculated manually at any point below the ground surface from the depth below the ground surface and the unit weights of the model units above the point considered. In this manner the initial stress field and the settlements that it causes, obtained by FE calculation, can be checked and verified against the results of simple analytical calculations. By carrying out such a check, a very close agreement between the stresses calculated numerically and analytically has been found. The total settlement of the ground surface, which amounts to 32.46 m in the middle of the model, was also confirmed by the outcome of the analytical method.

6.5.2 Hydrodynamic loading

In the second loading step the pore pressure distribution is initialised in different scenarios for a low, a medium and a high influx through the northern lateral boundary. The southern lateral boundary in all scenarios represents a constant potential boundary. The fault zone is highly permeable, i.e. a conduit.

The field of pore pressures generated for the case of a low influx is shown in Figure 6.8. Checks on generated pore pressures along the four sections show a good agreement with the defined boundary conditions (Figure 6.8,b through e). Calculated pore pressure of approximately 50 kPa (i.e. 5 m hydraulic head) along the northern lateral boundary (Figure 6.8c) is indeed expected to be generated, assuming a small hydraulic gradient ($i=5 \times 10^{-4}$) and a zero potential along the southern lateral boundary of the model.

The field of pore pressures generated for the case of a high influx is shown in Figure 6.9. High hydraulic gradients in this case cause much higher pore pressures, especially in the overpressured Mesozoic aquifer. For the top aquifer a pore pressure of about 800 kPa (i.e. 80 m hydraulic head) along the northern lateral boundary (Figure 6.9c) is indeed expected to be generated under a high hydraulic gradient ($i=8 \times 10^{-3}$), with a zero potential along the southern lateral boundary. For the bottom aquifer the pore pressure is calculated by applying a constant potential of 4400 kPa (440 m hydraulic head) along the southern lateral boundary and by defining a constant inflow along the northern lateral boundary initiated by the same high value of hydraulic gradient. The expected maximum value of pore pressure of about 5200 kPa (520 m hydraulic head) along the northern boundary of the

Mesozoic aquifer was, however, not reached (Figure 6.9c, e). This is due to a high difference in pore pressures between the two aquifers, which causes the upward flow of groundwater through the semipervious Tertiary clay layers towards the top aquifer. In this manner the Mesozoic aquifer is partly being drained and depressurised. The maximum pore pressures would have been reached if the aquitard had been practically impervious, as it was confirmed by a check run.

The runs in which the fault zone functions as a hydraulic barrier to the groundwater flow, i.e. as a seal, were numerically unstable and could not be completed. During the initialisation stage, very high pore pressures were generated in aquifers that were fed by a lateral influx but with no possibility to be drained. In reality, high pore pressures would eventually be released perhaps by flushing out the impervious infill of the fault zone or by hydrofracturing of adjacent aquitards and forming of preferential pathways for groundwater flow. In a simple scenario, which can be regarded as adequate in the current phase of this study, a high permeability fault zone was assumed. For this pragmatic reason the scenarios in which the fault zone acts as a barrier, are abandoned.

6.5.3 Initialisation of stresses for a nonlinear transient analysis

The initial stress conditions at the beginning of a nonlinear transient FE analysis are generated by superimposing the effects of the two previous loading steps from a linear analysis. Thus, a linear combination of the gravity load and the hydrodynamic load will create the initial state of stress and pore pressure in the model.

Common way to introduce the initial stresses in the model at the start of a nonlinear FE geomechanical analysis is to apply a linear load, or, as in our case, a combination of linear loads, while suppressing the model deformations. This is usually desirable because the ground surface preserves its 'original' position at the start of a FE analysis. The initial stresses in this study were also calculated while the displacements in the model were suppressed.

The effective vertical stresses generated for a high influx through the northern lateral boundary of the model are shown in Figure 6.10. Due to high pore pressures in the Mesozoic aquifer a considerable drop in effective stresses with depth can be observed (Figure 6.11). In the case of the scenarios with a low influx, there is practically no change in the effective stresses with depth relative to the effective stresses for hydrostatic conditions, i.e. to the stresses initialised by applying the gravity acceleration. This is because the magnitude of the pore pressures is very small with respect to the magnitude of the lithostatic stresses.

6.6 Loading by ice for a medium fast advance of ice sheet

A simplified hydromechanical model with the initialised stresses and pore pressures was used to simulate various ice-loading scenarios. The initialised stresses are representative of the situation when the toe of an advancing ice sheet has almost reached the northern edge of the model. This point in time is chosen as the beginning of a relative time-scale. The results of the nonlinear finite element analysis presented in this section are related to this time-scale.

6.6.1 Stress and deformation

Vertical and horizontal stresses approximately coincide with the directions of principal stresses. The major principal stress acts in vertical direction and the minor principal stress acts in horizontal direction. An exception to this are superficial parts of the model where the above mentioned global stress pattern can be distorted due to the movement of ice and possible upwards flow of groundwater. Less attention will be paid to these superficial effects as this study focuses on the hydromechanical behaviour of the deeper Tertiary clays and the overall response of the groundwater system.

The calculated vertical displacement does not represent the absolute value of settlement. It rather indicates the order of magnitude of settlement that would occur under the load of ice. This is because the values of the input parameters for settlement calculations for several units were not available and had to be estimated. For all the units the average values of input parameters were used in calculations (Table 3.4).

6.6.1.1 Scenarios with a low lateral influx

The increase in vertical effective stresses caused by the weight of ice for selected time steps is shown in Figure 6.12. Besides the compressive stresses (negative values in the figure), which increase proportionally with depth and the weight of ice, some stresses of tensile type also develop. These occur ahead of the ice margin and represent an elastic response of the model partly loaded by ice. Overpressured shallow aquifers also play an important role here as it will be discussed later in this section. Maximum tensile stresses range from 128 kPa after 10 years, to 195 kPa after about 30 years. In the subsequent stages of ice advance, after 50 years, the whole model is covered by ice and all the stresses become compressive.

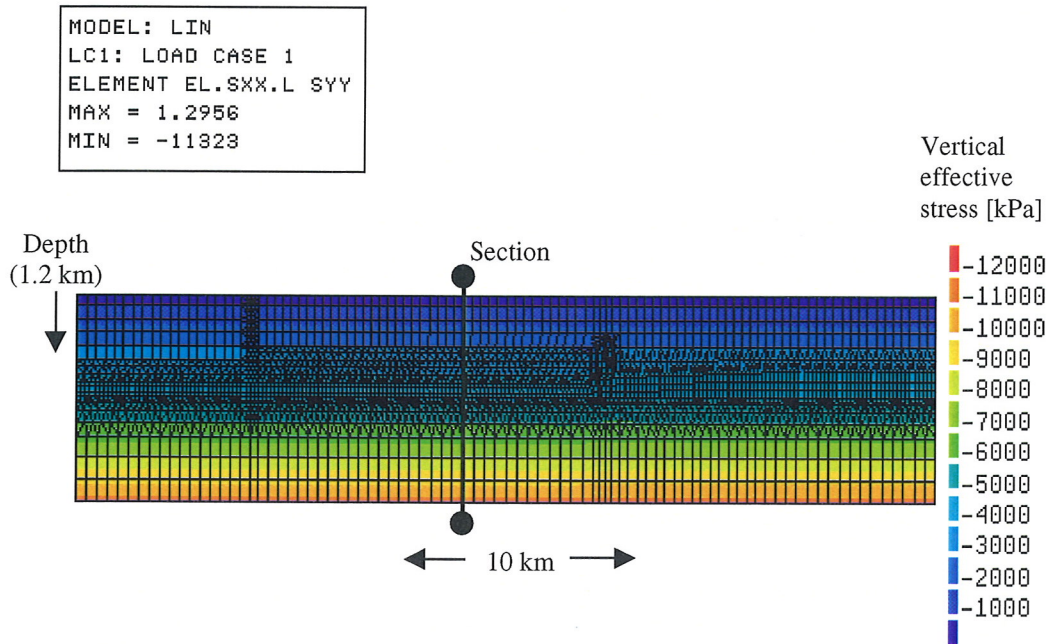


Figure 6.6 Effective vertical stresses in the model initialised in a linear elastic finite element analysis. The stresses are obtained by applying the gravity acceleration on the model and therefore represent lithostatic stresses for hydrostatic conditions.

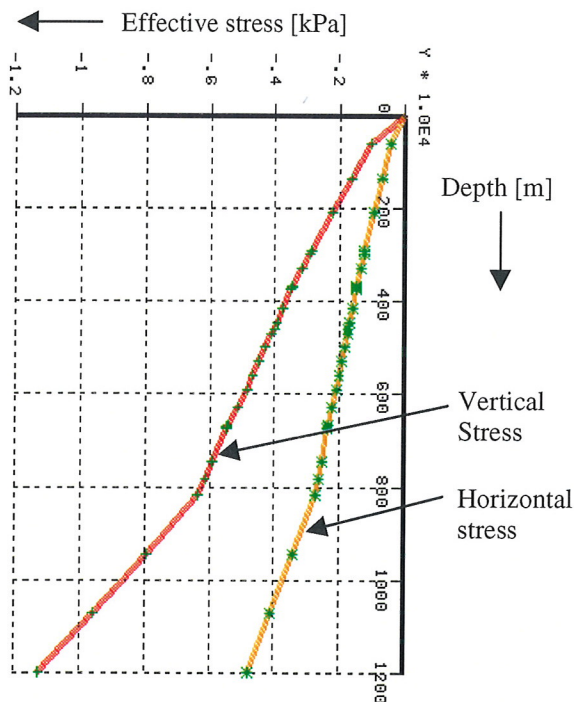
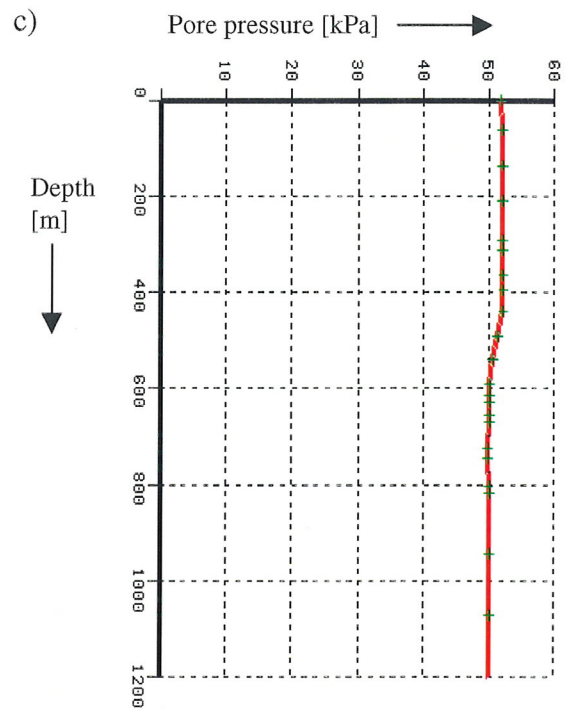
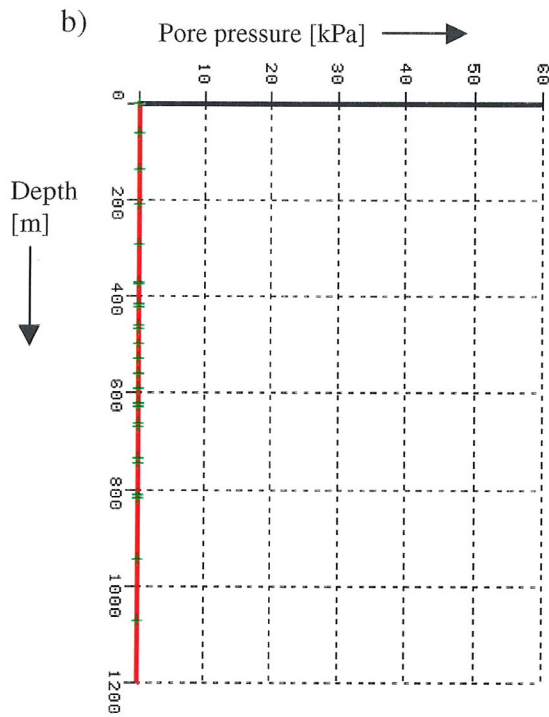
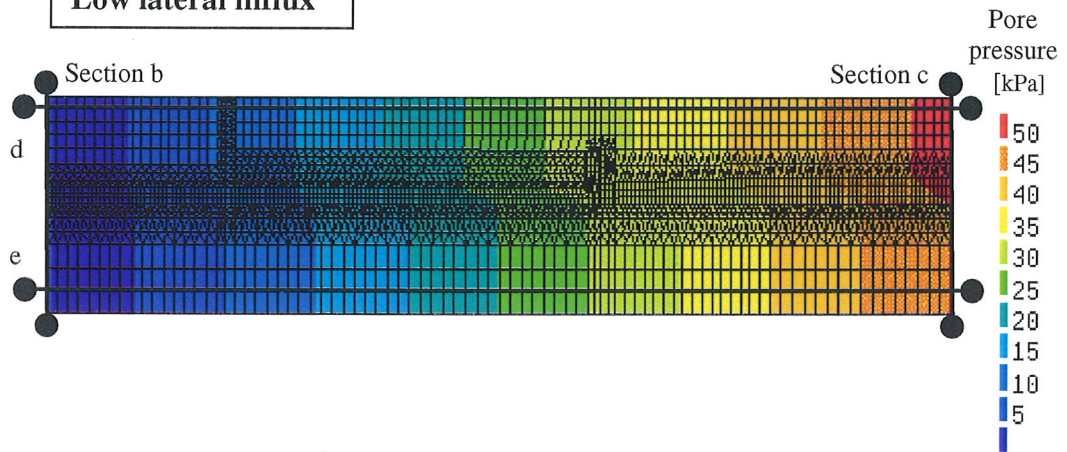


Figure 6.7 Effective stresses for hydrostatic conditions along a vertical section shown in Figure 6.6.

a) MODEL: LIN
 LC2: LOAD CASE 2
 NODAL DPRPH..G DPRPO
 MAX = 52.2 MIN = 0

Low lateral influx



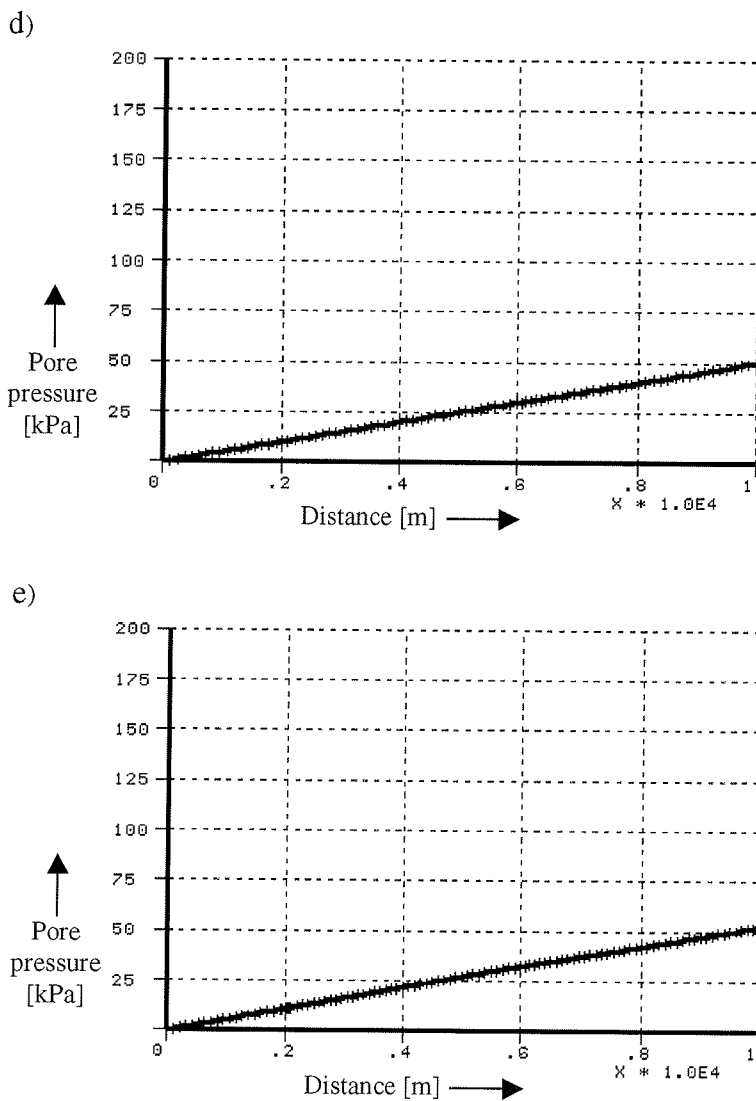


Figure 6.8 Pore pressure distribution initialised for a low influx through the northern lateral boundary.

a) Pore pressure distribution in the model initialised for a low influx through the northern lateral boundary (marked as section c). The influx is based on the present, low hydraulic gradients ($i=5 \times 10^{-4}$). A constant potential boundary, with a potential of zero, is prescribed along the southern lateral boundary of the model (section b).

b) Pore pressure as a function of depth along the southern lateral boundary of the model (section b).

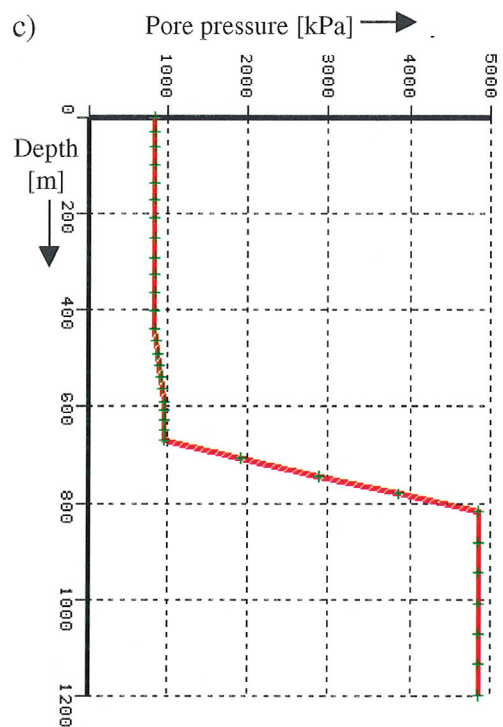
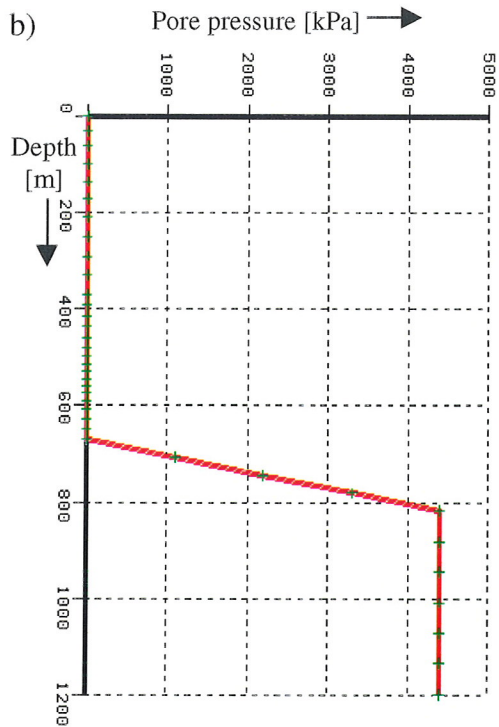
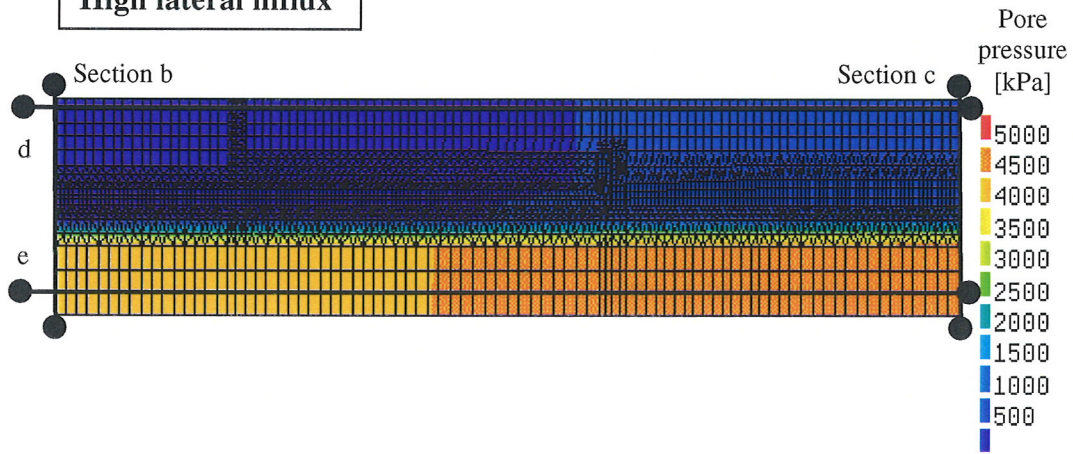
c) Pore pressure as a function of depth along the northern lateral boundary of the model (section c).

d) Pore pressure along a horizontal section d through the top (Quaternary and Tertiary) aquifer.

e) Pore pressure along a horizontal section e through the Mesozoic aquifer.

a) MODEL: LIN
LC2: LOAD CASE 2
NODAL DPRPH. .G DPRPO
MAX = 4845 MIN = 0

High lateral influx



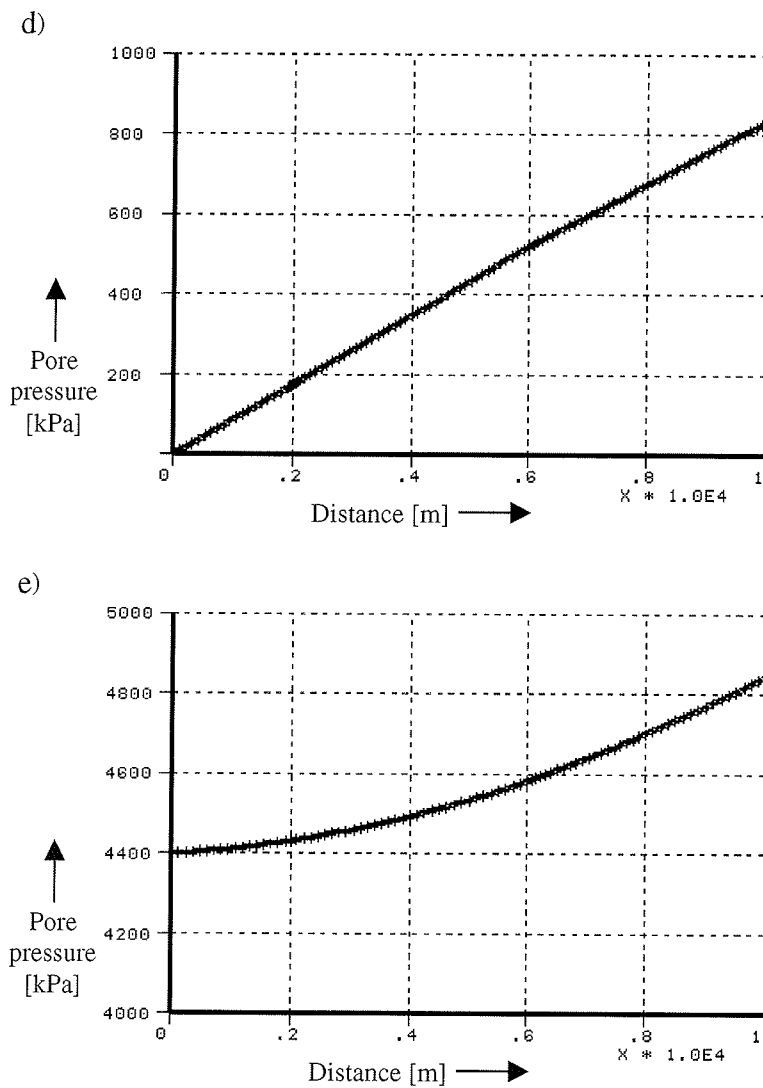


Figure 6.9 Pore pressure distribution initialised for a high influx through the northern lateral boundary.

- a) Pore pressure distribution in the model initialised for a high influx through the northern lateral boundary (marked as section c). The influx is derived from the supra-regional model. Constant potential boundary is prescribed along the southern lateral boundary (section b), with a potential of zero for the (top) Quaternary aquifer, and a potential of 4400 kPa (corresponds to a hydraulic head of about 440 m) for the Mesozoic aquifer.
- b) Pore pressure as a function of depth along the southern lateral boundary of the model (section b).
- c) Pore pressure as a function of depth along the northern lateral boundary of the model (section c).
- d) Pore pressure along a horizontal section d through the top (Quaternary and Tertiary) aquifer.
- e) Pore pressure along a horizontal section e through the Mesozoic aquifer.

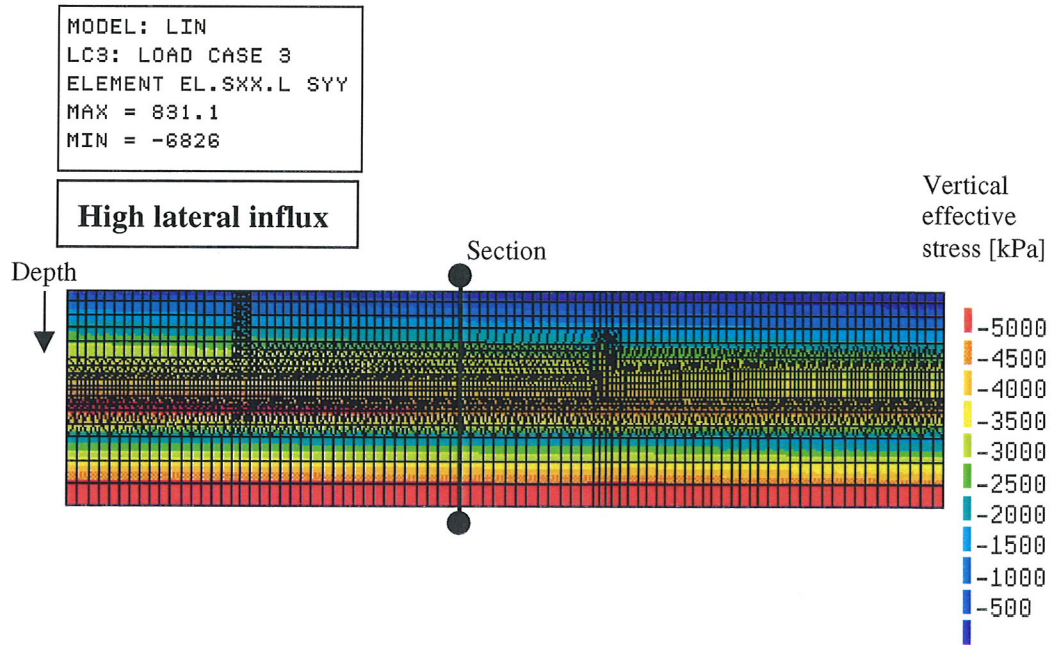
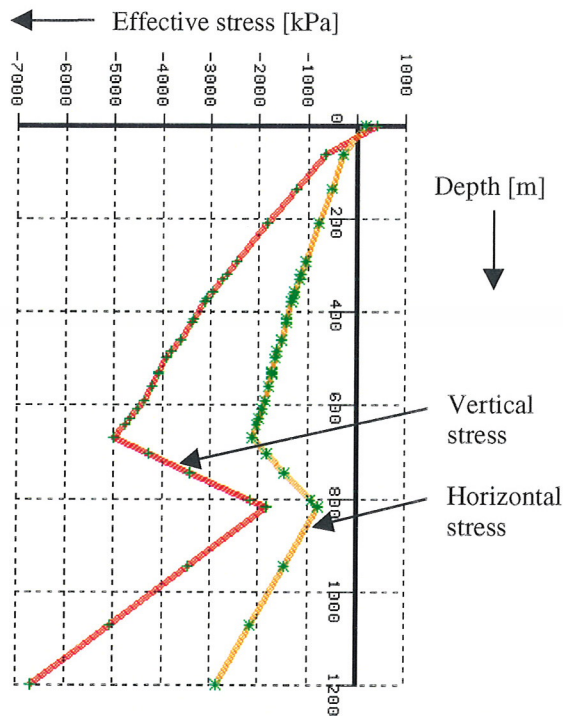


Figure 6.10 Initial effective vertical stresses in the model at the beginning of a nonlinear transient finite element analysis. The stresses are obtained by superimposing the effective stresses for hydrostatic conditions Figure 6.6) and the pore pressure initialised for a high influx through the northern lateral boundary



(Figure 6.9).

Figure 6.11 Initial effective stresses at the beginning of a nonlinear transient finite element analysis along a vertical section shown in Figure 6.10.

The consequence of tensile stresses is the heaving and bulging of the ground surface ahead of the ice margin (Figure 6.13). Deformations of these kind are indeed common in areas affected by glaciation. The magnitude of settlement increases with an increase in the ice load and reaches 66 m, measured at the ground surface, after 300 years. Additional settlement occurs under a constant ice load and reaches 75 m after 600 years (Figure 6.14c). This settlement under a constant load is mainly due to the consolidation of the Tertiary clay layers (the Rupel and Asse model unit and the Ieper and Landen model unit). In the low permeability clay layers the pore water initially takes over the ice load. As the overpressured pore water dissipates from the clay layers the pore pressure decreases and a continuous build-up of effective pressures throughout the clay layers takes place (Figure 6.14a, b). However, the stress equilibrium was not reached at the end of the simulation indicating that the process of consolidation under a 1 km thick ice sheet would last for more than 600 years.

6.6.1.2 Scenarios with a high lateral influx

The calculated stress fields (Figure 6.15) show a similar pattern to those obtained for the scenarios with a low lateral influx into the model (Figure 6.12). The range of effective stresses is here different, mainly due to the different pore pressure fields. Maximum compressive stresses at greater depths are considerably smaller because of the increased pore pressure in the Mesozoic aquifer. Tensile stresses, which occur in the superficial parts of the model ahead of the ice margin, are higher and reach 806 and 611 kPa after 10 and 30 years, respectively. The increase in tensile stresses is due to higher pore pressure and pressure gradients in the top (Quaternary and Tertiary) aquifer, which rests underneath the permafrost.

Settlement under the ice sheet and heaving ahead of the ice margin (Figure 6.16, Figure 6.17c) show practically the same pattern and the order of magnitude as for the scenarios with a low lateral influx into the model (Figure 6.13). This also applies to the development of stresses and pore pressures in the clay layers in time (Figure 6.17a, b). As in the case of low lateral influx, the stress equilibrium was not reached at the end of simulation indicating that the process of consolidation under a 1 km thick ice sheet would last for more than 300 years. Further, the process of consolidation does not appear to be significantly influenced by the order of magnitude of the pore pressures occurring in the adjacent aquifers, assuming a high lateral influx into the model.

Detailed analysis of displacements was carried out for the characteristic nodes in the clay layers (Figure 6.18a). In this manner, settlement of each individual layer can be differentiated. The Breda Formation and Veldhoven (represented as one unit in the model) would settle about 13 m after 600 years (total thickness of this unit is 90 m). The Rupel Clay and Asse Member would settle also about 13 m (total

thickness 90 m) and the Ieper and Landen clay would settle about 21 m (total thickness 150 m). The sum of the total settlement of these three clay layers in the central part of the model is about 46 m. Having in mind that the total settlement of all the layers is about 76 m, the remaining difference of 30 m is due to the settlement of sand layers.

Relatively large settlement of the sand layers is caused by a relatively low value of Young's modulus for sand material ($E=125$ MPa). Comparing with the overlying complex of clays and sands, the total settlement of the Mesozoic unit is small and amounts to 0.27 m.

Another interesting response of clay layers is related to the period of pre-loading when positive displacement (i.e. heaving) occurs. This takes place in the part of the model ahead of the ice margin, which was not yet covered by ice, thus is not yet loaded. For the nodes presented in Figure 6.18 heaving occurs during the first 30 years. As mentioned before, heaving is a consequence of the relaxation of stresses in a non-loaded part of the model. Response of the model to the load is elastic. Settlement under a loaded part of the model is in a way compensated by heaving, which occurs in a non-loaded part of the model.

The influence of hydromechanical parameters on the mechanical behaviour of the Rupel Clay and Asse Member was analysed by using two values of the hydraulic conductivity for this clay layer. A medium value of $K=1 \times 10^{-10}$ m/s was used in most scenarios and a value of $K=1 \times 10^{-9}$ m/s was used in the scenario with a high hydraulic conductivity of the clay. For these two scenarios the vertical strain for a middle element in the clay layer is plotted in Figure 6.18b. The general qualitative conclusion that can be derived from the graphs is that a clay with a higher conductivity responds faster to a change in load and needs a shorter period of time to consolidate.

6.6.2 Plasticity

Plastic deformation has not been detected in the scenarios with a low lateral influx into the model. For the scenarios with a high lateral influx, plastic deformation occurs locally in the Tertiary sand layers close to the northern lateral boundary of the model (Figure 6.19). Vertical plastic strain vectors are dominant and coincide with the direction of the major stress vectors. Negative sign of the principal strain vectors shows that these were formed under a compressive regime. Plastic strain of tensile type was developed in the horizontal direction that corresponds with the direction of the minor principal stress.

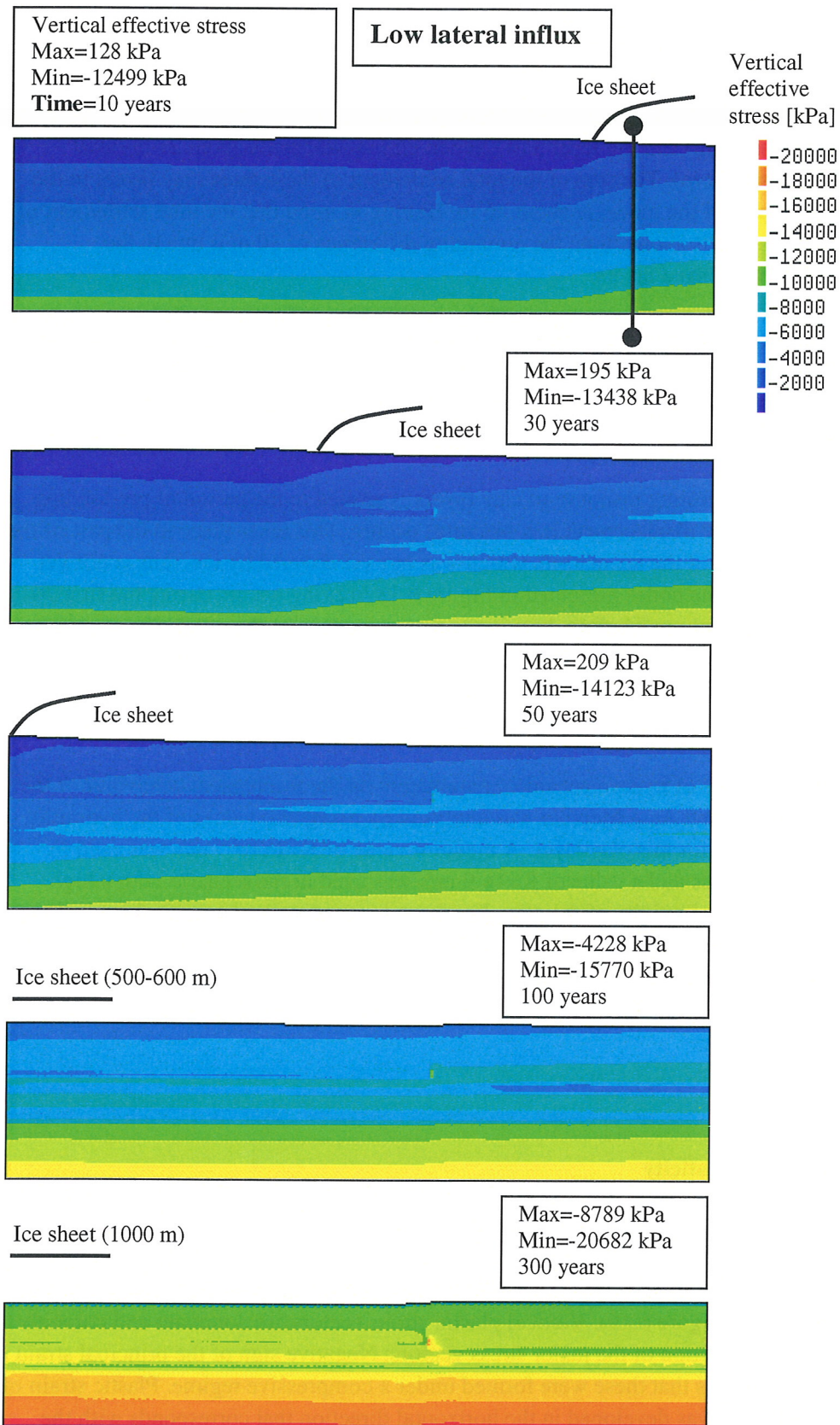


Figure 6.12 Effective vertical stresses during a medium fast advance of ice sheet for a low lateral influx in the model.

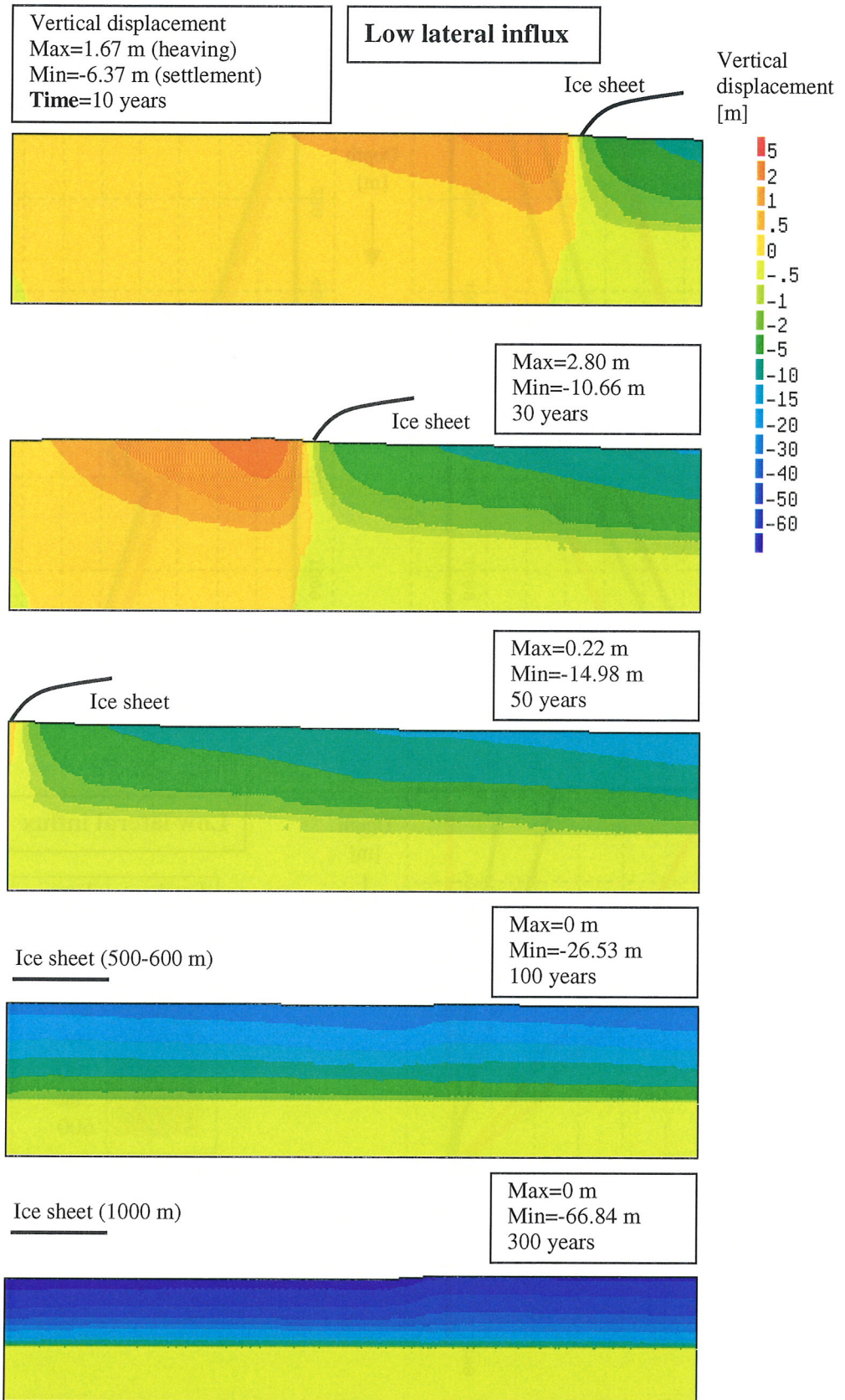


Figure 6.13 Vertical displacement during a medium fast advance of ice sheet for a low lateral influx in the model.

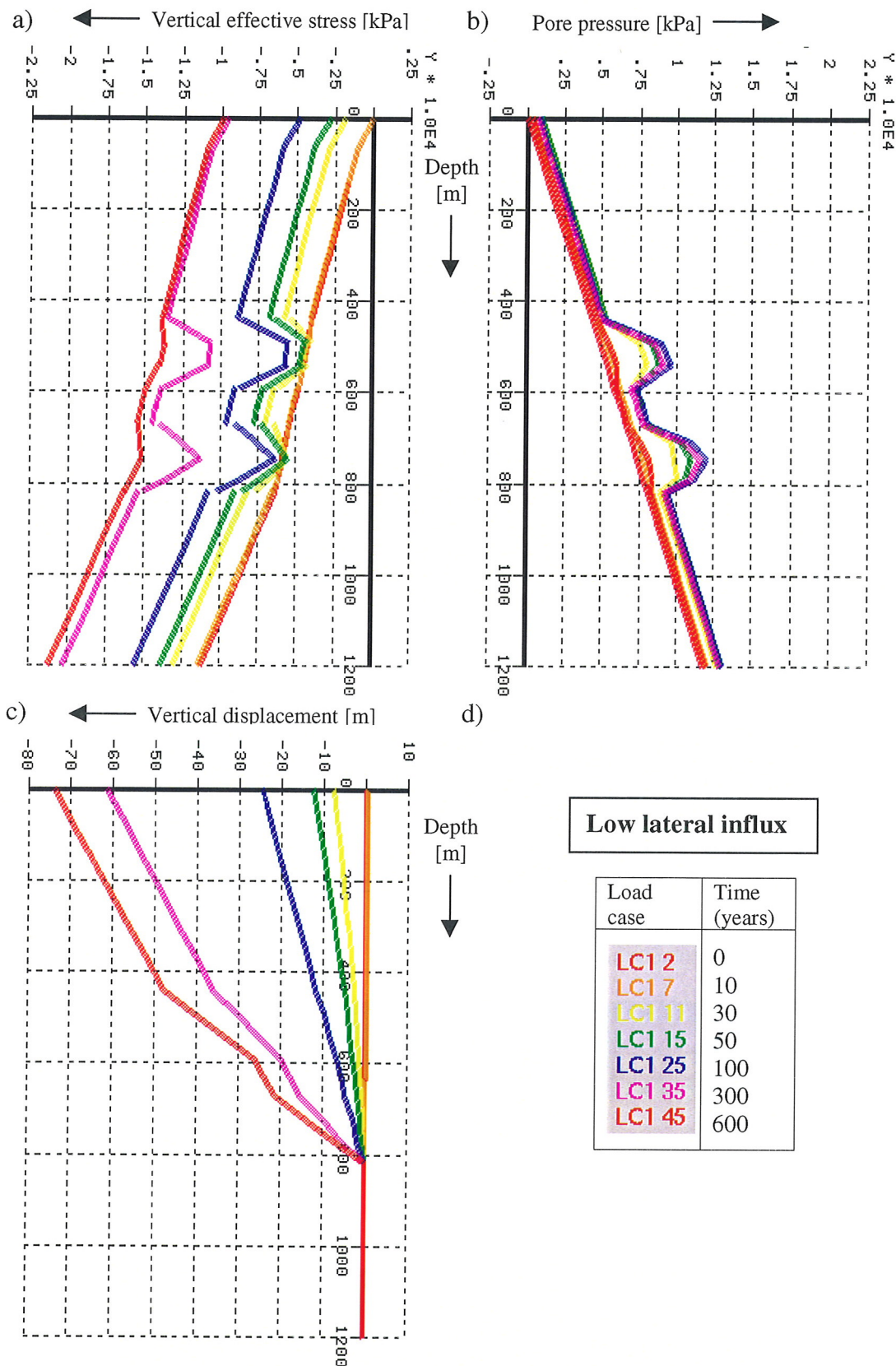


Figure 6.14 a) Vertical effective stress, b) pore pressure, and c) vertical displacement with depth during a medium fast advance of ice sheet for a low lateral influx in the model. d) Key for the graphs. Location of the vertical section is shown in Figure 6.12.

The zone of plasticity is localised within that part of the model where the pore pressure, caused by the lateral influx in the model, is highest. The pore pressure in the top (Quaternary and Tertiary) aquifers pushes up the overlying, impermeable permafrost in the initial stages of ice loading. Permafrost has a confining effect and groundwater in the top aquifer exhibits hydraulic heads that rise above ground surface. Increasing thickness of ice plays here a stabilising role as the plastic deformations practically cease to grow after the northern part of the model has been covered by ice.

The scenario with low values for the geomechanical parameters of the Rupel Clay and Asse Member is meant to be critical for plastic deformation. By trying a few sets of values for cohesion (c) and angle of internal friction (Φ), the critical values of these two parameters were determined as $c=100$ kPa and $\Phi=20^\circ$. These low values very likely underestimate the real values of both parameters for the Rupel Clay and Asse Member.

Development of the plasticity zone throughout the Rupel Clay and Asse Member, characterised by these critical values of the geomechanical parameters, is shown in Figure 6.20. Some plastic deformation of the layer already occurs during the initialisation of stresses, before ice loading. As the ice load increases the zone of plasticity develops progressively and systematically throughout the whole Rupel and Asse model unit. Such a simple pattern of deformation is realistic considering that the thickness of layers in the model is uniform and the geomechanical parameters of the layers are homogeneous.

6.6.3 Groundwater flow in aquifers

The ice-driven pattern of ground water flow is presented separately for aquifers and aquitards. The permafrost, which represents an aquitard, initially covers the superficial part of the model to a depth of 60 m. During advance of the ice the permafrost melts underneath the ice sheet as explained before in description of the ice-loading scenarios. This results in a recharge, specified as a vertical basal meltwater influx, which amounts to 20 mm/year. This recharge is prescribed along the upper model boundary located under the ice sheet where the permafrost is absent. The initial pore pressure distribution in the model is generated as explained in section 6.5.1.

The patterns of groundwater flow in the aquifers obtained by running the scenarios with a low lateral influx and the scenarios with a high lateral influx will be discussed separately.

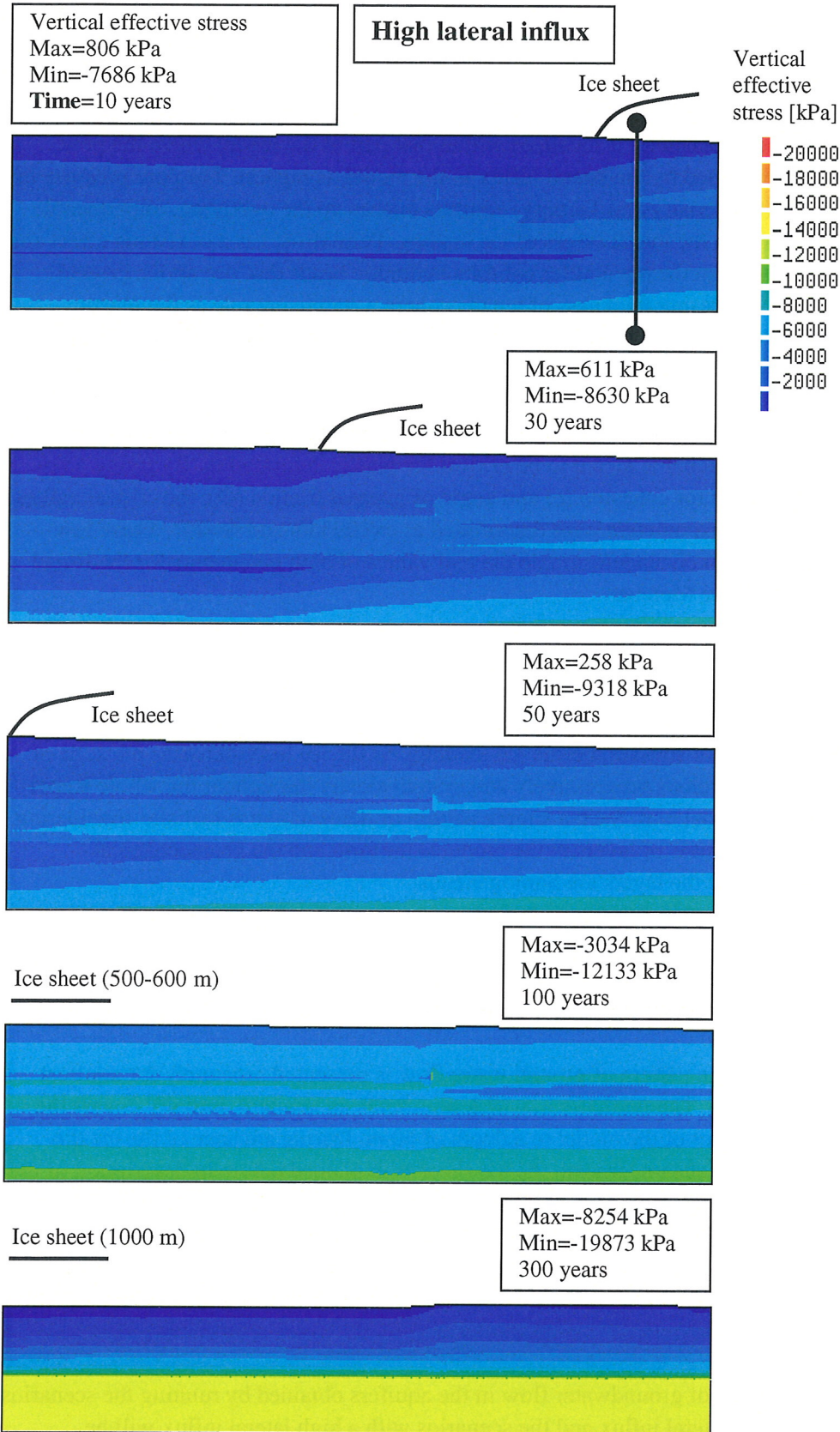


Figure 6.15 Effective vertical stresses during a medium fast advance of ice sheet for a high lateral inflow into the model.

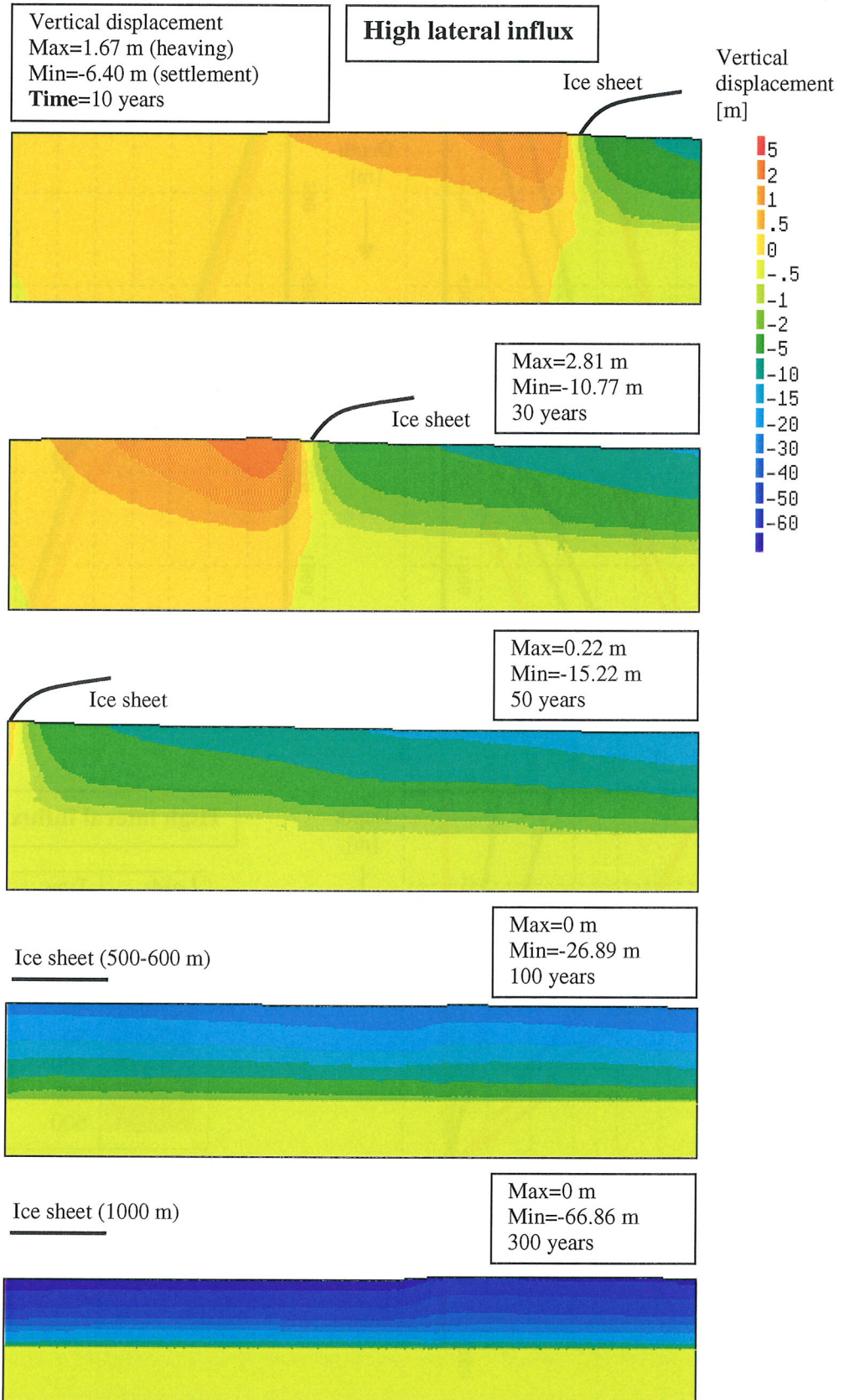


Figure 6.16 Vertical displacement during a medium fast advance of ice sheet for a high lateral influx in the model.

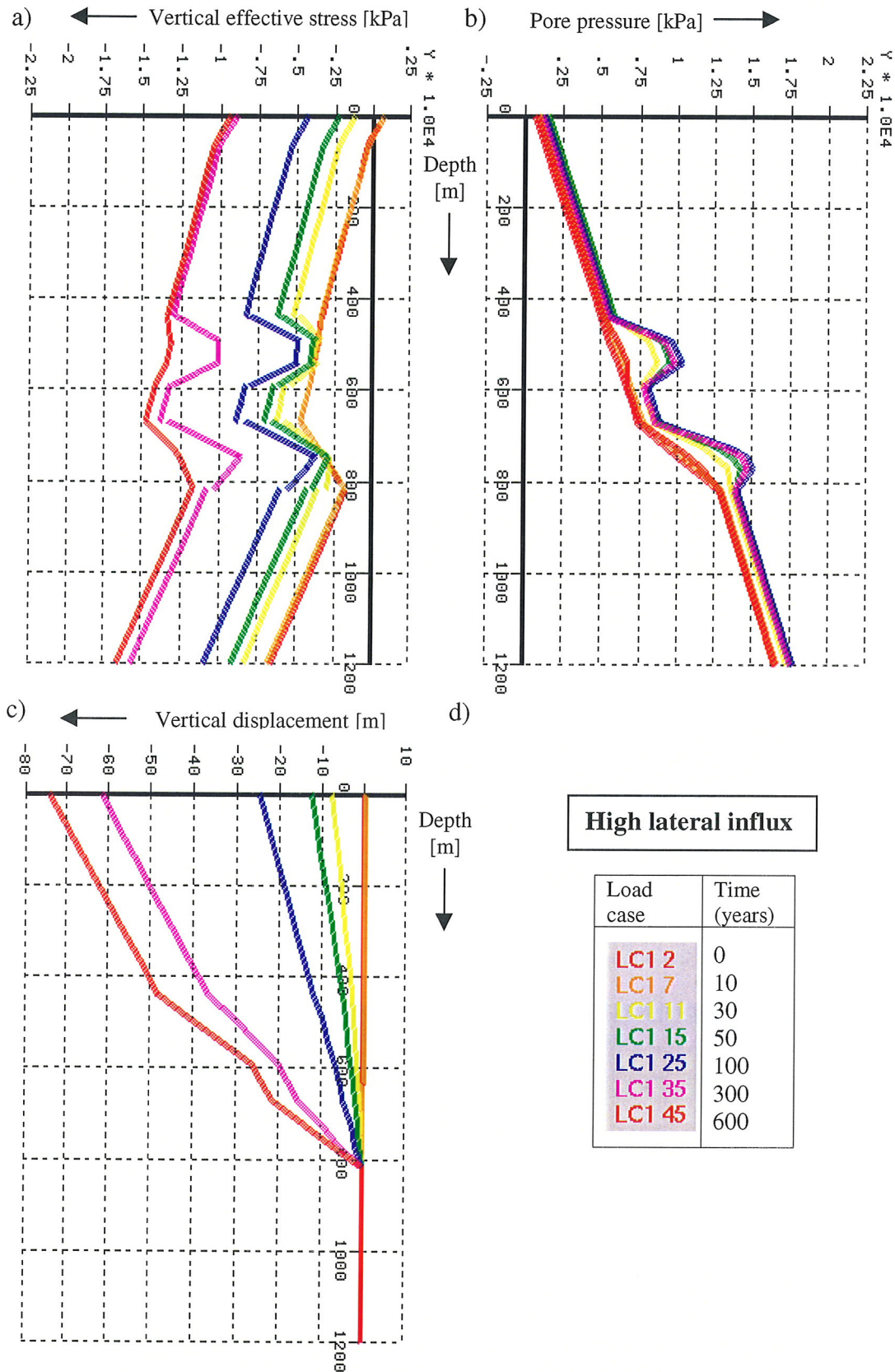


Figure 6.17 a) Vertical effective stress, b) pore pressure, and c) vertical displacement with depth during a medium fast advance of ice sheet for a high lateral influx in the model. d) Key for the graphs. Location of the vertical section is shown in Figure 6.15.

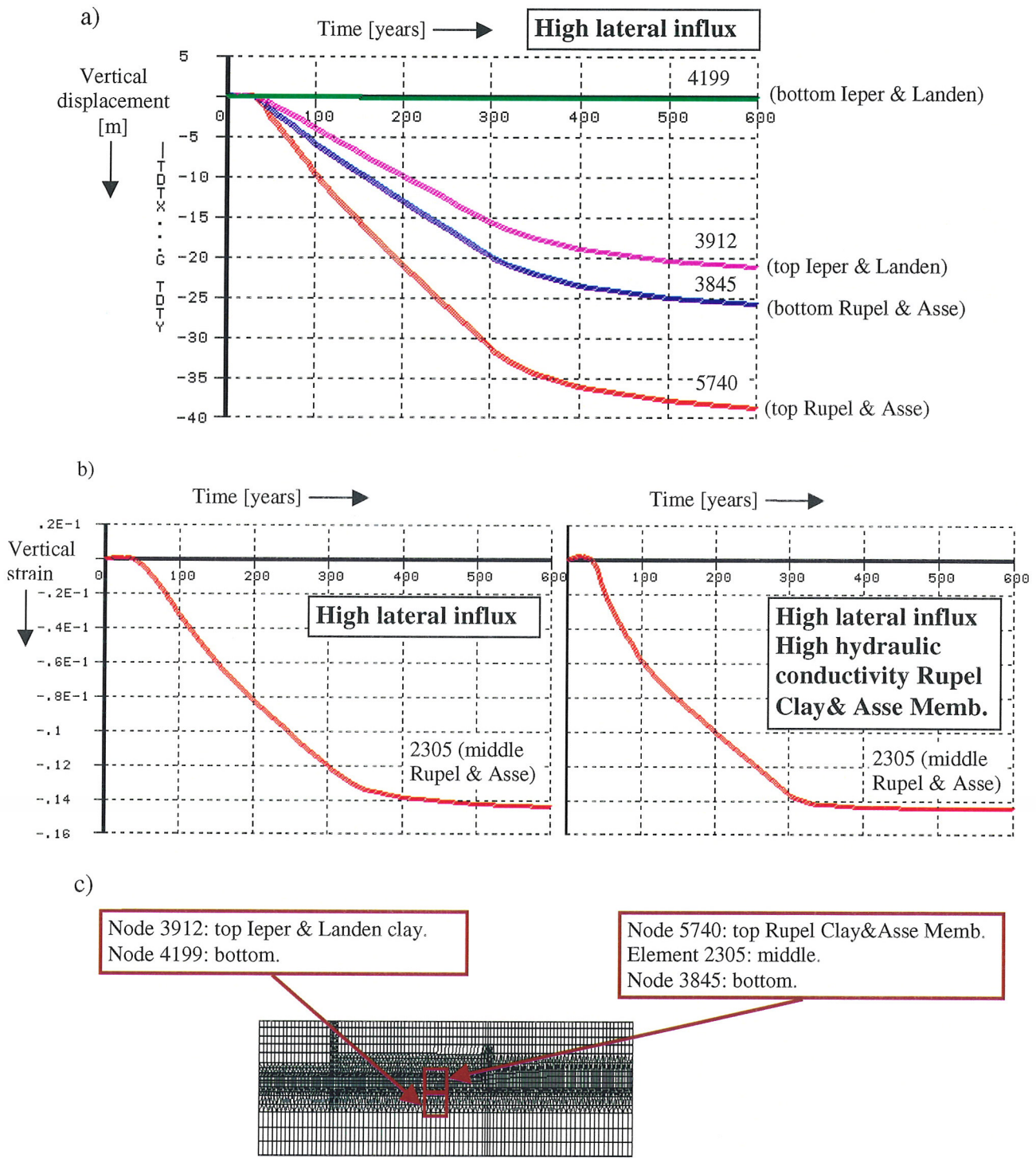


Figure 6.18 a) Vertical displacement of the characteristic nodes in the clay layers during a medium fast advance of ice sheet for a high lateral inflow in the model. b) Vertical strain for a middle element of the Rupel Clay and Asse Member layer, for medium ($K=1 \times 10^{-10}$ m/s) and high hydraulic conductivity ($K=1 \times 10^{-9}$ m/s) of the Rupel Clay and Asse Member. c) Location of the nodes and elements in the model.

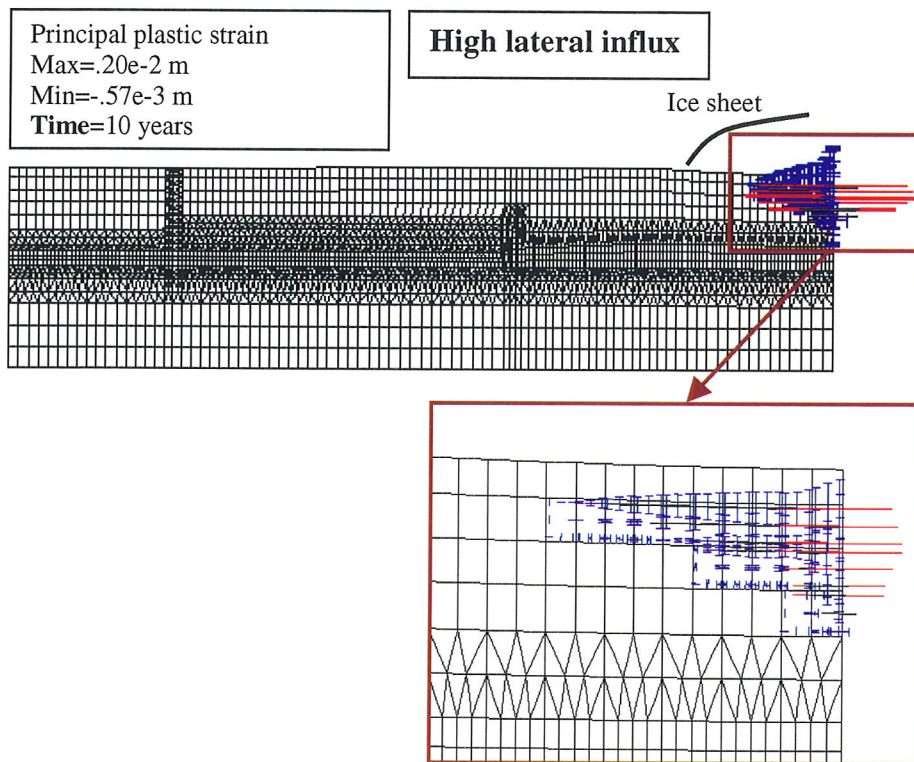


Figure 6.19 Principal plastic strain in the Tertiary sand layers during a medium fast advance of ice sheet for a high lateral influx in the model. The blue vectors denote plastic strain formed under compressive stresses while the red vectors denote plastic strain formed under tensile stresses

6.6.3.1 Scenarios with a low lateral influx

The initial conditions in the model are characterised by a low velocity of groundwater flow, i.e. Darcy flux (or specific discharge), as hydraulic gradients (and pressure gradients) throughout the two main aquifers are small (Figure 6.8). The horizontal Darcy flux in the top (Quaternary and Tertiary) aquifer is -0.3 m/year and in the Mesozoic aquifer about -0.01 m/year (a negative sign denotes that the groundwater flows in the southern direction).

Loading by the ice accelerates groundwater flow in aquifers, mainly in a horizontal direction towards the ice sheet margin (Figure 6.21). The superficial parts of the top aquifer freeze and form permafrost, characterised by a low permeability. The permafrost acts as a confining layer. Darcy flux generally increases and reaches the

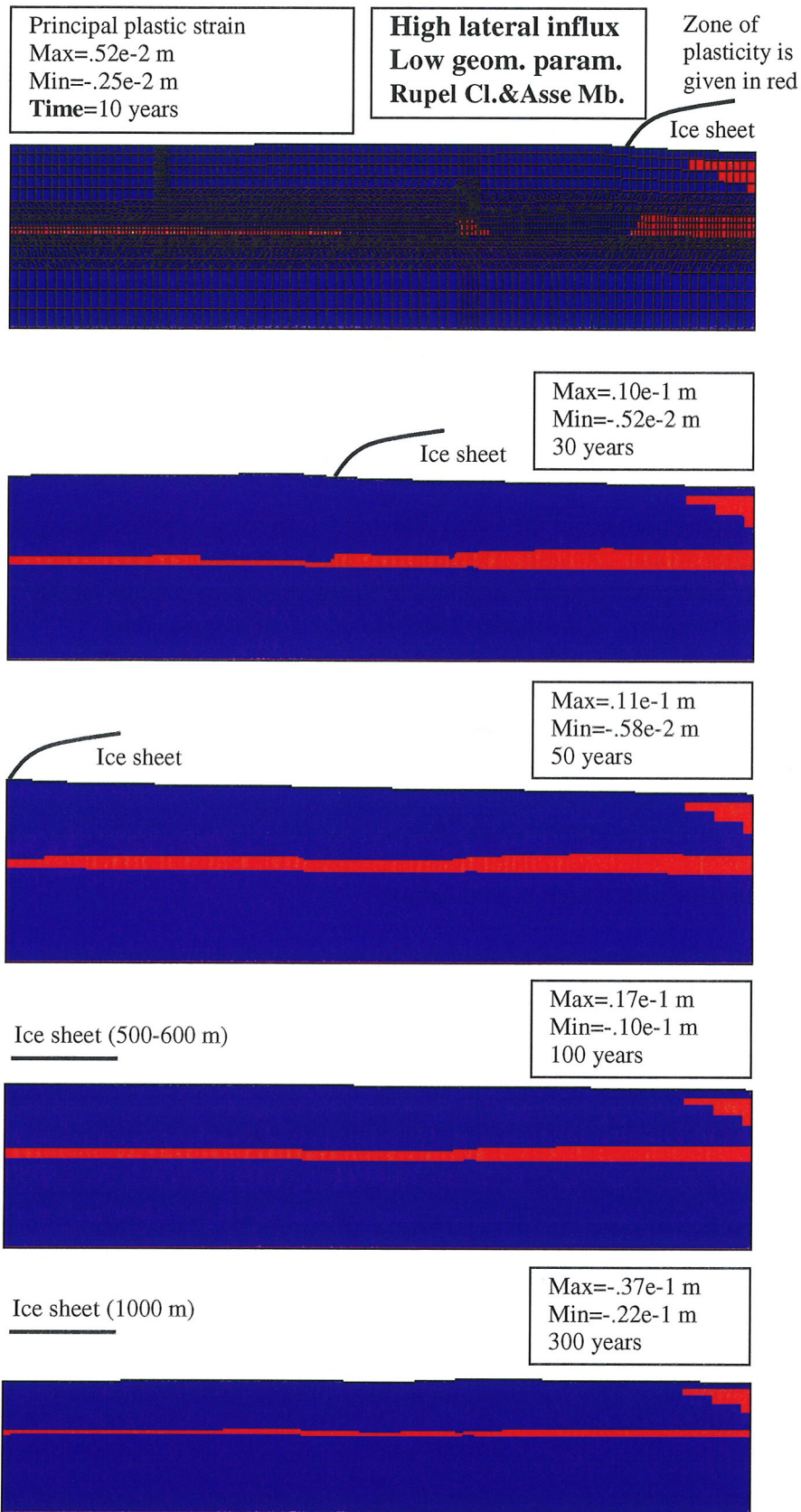


Figure 6.20 Formation of the zone of plasticity during a medium fast advance of ice sheet, for low values of cohesion ($c=100$ kPa) and the angle of internal friction ($\Phi=20^\circ$) for the Rupel Clay and Asse Member and a high lateral influx.

maximum value of -10.4 m/year in the top aquifer after 50 years. In the Mesozoic aquifer the maximum flux of -1 m/year is reached after 100 years. With respect to the initial conditions, this represents an increase of 35 to 100 times.

Increase in the pore pressures with respect to the initial conditions is also manifold. In the top aquifer, at a depth of 95 m, the maximum pore pressure under the ice load, reached after 50 years, amounts to 2000 kPa (Figure 6.22a). The net hydraulic head above the ground surface is thus 105 m. In the middle of the Mesozoic aquifer, at a depth of 990 m, the maximum pore pressure is about 11300 kPa and the net hydraulic head above the ground surface is 140 m (Figure 6.22b).

Darcy flux and pore pressure in the top aquifer and the Mesozoic aquifer decrease respectively after 50 and 100 years (Figure 6.22). Such a response of the model could possibly be explained by the influence of a prescribed zero potential at the southern lateral boundary of the model. This boundary condition becomes unrealistic for the positions of the ice sheet beyond the southern edge of the model. Calculated groundwater flow in the aquifer systems is therefore not representative once the margin of the modelled ice sheet has moved beyond the edge of the model. This limitation can be avoided by developing a longer hydromechanical model, as it will be shown in chapter 7.

6.6.3.2 Scenarios with a high lateral influx

The initial field of pore pressure is calculated by imposing the boundary conditions from the supra-regional model as explained in section 6.5.1. The initial pore pressures, pressure gradients and velocities of ground water flow are higher with respect to the scenarios with a low lateral influx in the model (Figure 6.9). The calculated horizontal Darcy flux (i.e. the specific discharge) in the top (Quaternary and Tertiary) aquifer is -4.7 m/year and in the Mesozoic aquifer -0.3 m/year.

Loading by the ice accelerates the groundwater flow in the aquifers, mainly in a horizontal direction towards the ice sheet margin (Figure 6.23). Darcy flux increases as the ice sheet moves towards the edge of the model. The magnitudes of flux in this case are higher than for the scenarios with a low lateral inflow into the model. The maximum value of Darcy flux of -14.8 m/year is reached in the top aquifer after 50 years. In the Mesozoic aquifer the maximum flux of -1 m/year is reached after 100 years. This represents an increase of three to four times with respect to the initial conditions.

Increase in pore pressures shows the same trend. In the top aquifer, at a depth of 95 m, the maximum pore pressure under the ice load, reached after 50 years, amounts to 2700 kPa (Figure 6.24a). The hydraulic head above the ground surface thus

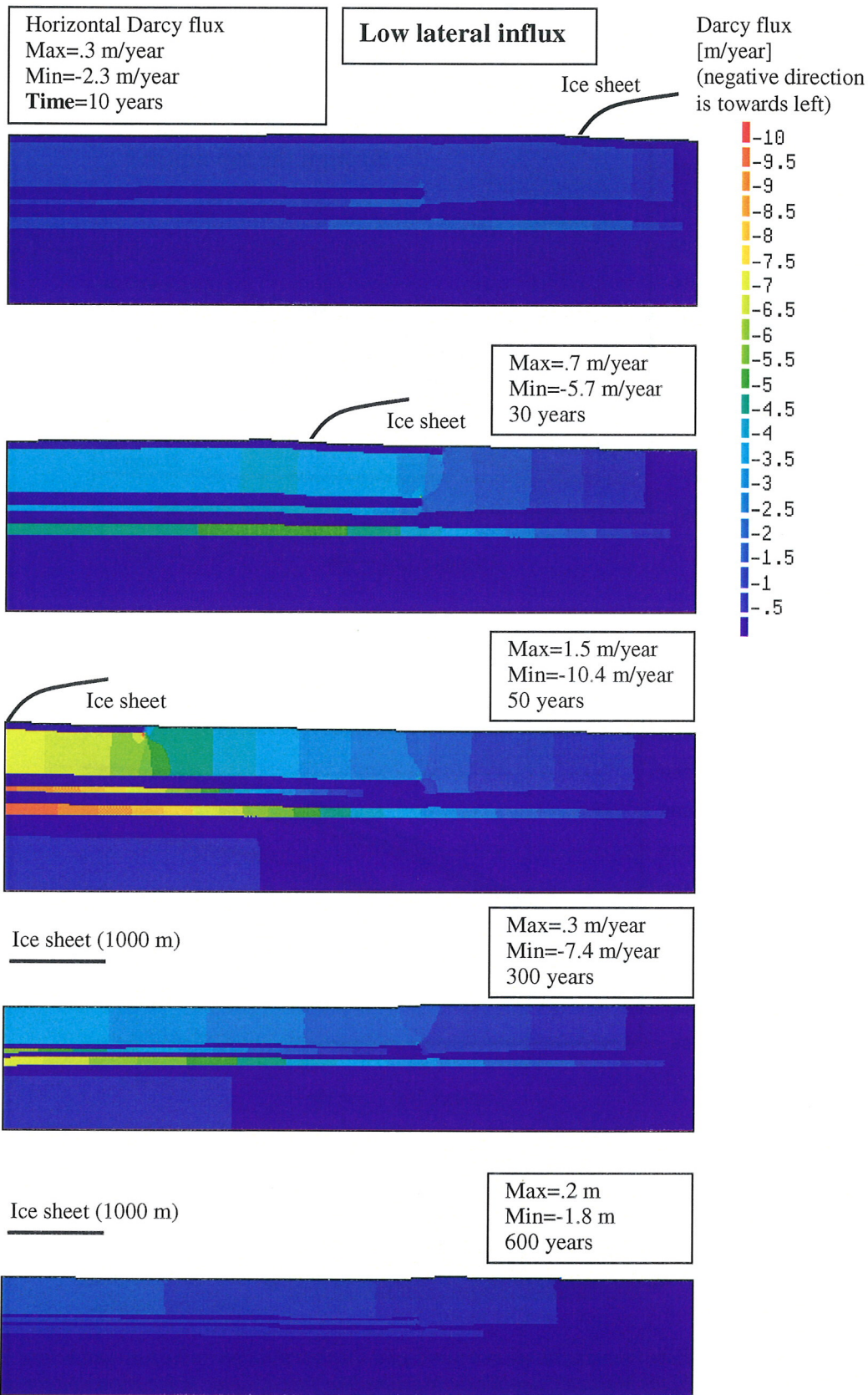


Figure 6.21 Horizontal Darcy flux during a medium fast advance of ice sheet for a low lateral inflow into the model.

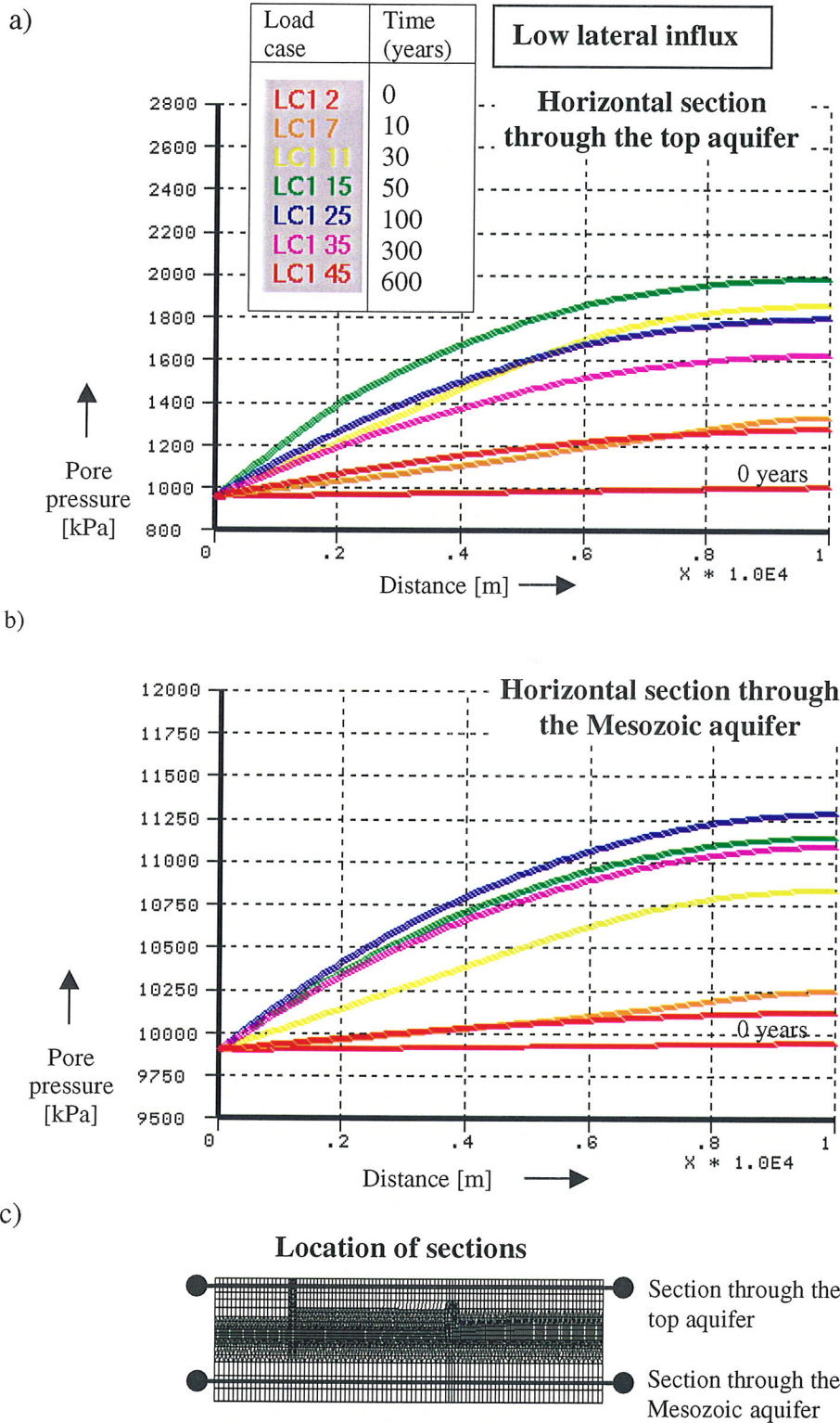


Figure 6.22 Pore pressure along two horizontal sections through a) the top aquifer and b) the Mesozoic aquifer during a medium fast advance of ice sheet and for a low lateral influx into the model. c) Location of the sections for which the pore pressure is shown.

reaches 175 m. With respect to the initial conditions this represents an increase of 95 m. In the middle of the Mesozoic aquifer, at a depth of 990 m, the maximum pore pressure is about 16100 kPa and hydraulic head above the ground surface is 620 m (Figure 6.22b). This represents an increase of 240 m with respect to the initial conditions.

Darcy flux and pore pressure in the top aquifer and the Mesozoic aquifer decrease respectively after 50 and 100 years (Figure 6.24). This is due to the influence of the boundary conditions, in particular due to the southern lateral boundary with a prescribed fixed potential. This boundary condition becomes unrealistic for the positions of the ice sheet beyond the southern edge of the model as explained in the previous subsection.

In conclusion, the groundwater flow pattern through the aquifer system during glaciation is generally characterised by the hydraulic gradients and the groundwater flow velocities that are far greater than at present. Due to a small length of the simple hydromechanical model the calculated increase of the groundwater flow velocities, which amounts to 3 to 10 times of the initial value, likely underestimates the real increase.

6.6.4 Groundwater flow in aquitards

The response of a low permeability layer, i.e. aquitard, to the ice loading is significantly different from that of an aquifer. An increase in load upon an aquitard is initially taken over by the pore water that becomes overpressured. This creates the excess water pressure initially equal to the increase in load. Excess pore pressure generated in an aquitard decreases with time as the overpressured pore water dissipates from the aquitard into adjacent aquifers. This process of consolidation generally results in a manifold increase in the velocity of the pore water flow in an aquitard with respect to the pre-loading conditions, when the pore water flow is driven by the natural hydraulic gradients.

Development of the excess pore pressure in the three aquitards present in the model (clays of the Breda Formation and Veldhoven clay; Rupel clay and Asse Member; and Ieper Member and Landen Clay) is shown in Figure 6.25. In the beginning of loading the pore water completely bears the ice load. After 10 years the maximum excess pore pressure is approximately equal to the applied ice load. In the subsequent two time steps the pore water bears over 90% of the applied ice load. After 50 years the increase of ice load in time is slower. When the ice sheet reaches its maximum thickness after 300 years, the aquitards partly consolidate and the excess pore pressure equals to about 40% of the ice load. Another period of 300 years under a constant ice load is not sufficient for the process of consolidation to be fully completed. At the end of simulation, after 600 years, 8% of the maximum ice load is still carried by the pore water.

For transport of radionuclides disposed in an aquitard it is of primary interest to estimate the Darcy velocity of the pore water throughout the aquitard. In the initial state, before the model is loaded by ice, the velocity of groundwater flow through an aquitard is very small. The flow is driven by natural pressure gradients caused by a difference in pressures between overlying and underlying aquifer. For scenarios with a low lateral influx into the model Darcy velocities through the aquitards are equal to a few hundredths of millimetre per year. For scenarios with a high lateral influx into the model Darcy velocities of groundwater flow in the Rupel and Asse unit are 0.4 mm/year and in the Ieper and Landen unit 9 mm/year. The vertical velocity vectors are in both cases directed upward as the pore pressure in the underlying Mesozoic aquifer is larger than the pore pressure in the overlying Quaternary and Mesozoic aquifer.

When the loading of the model by ice starts, consolidation-driven flow becomes a dominant factor that influences the overall pattern of the pore water flow in aquitards. This can be shown by plotting the vertical component of Darcy flux against time for characteristic elements of the Rupel Clay and Asse Member (Figure 6.26 and Figure 6.27). The pattern and the magnitude of Darcy flux are practically the same regardless of the initial pore pressure distribution generated in the scenario with a low lateral influx (Figure 6.26) and the scenario with a high lateral influx into the model (Figure 6.27).

Another important conclusion can be drawn about the direction of the Darcy flux in the Rupel Clay and Asse Member. During consolidation the pore water dissipates from the loaded parts of an aquitard towards the nearest aquifer. In the elements in the upper part of the Rupel and Asse unit (marked red in Figure 6.26 and Figure 6.27) Darcy flow is directed upwards. In the elements in the bottom part of the unit (marked grey) Darcy flow is directed downwards. This implies that during consolidation flushing out of the Rupel and Asse unit by an upward flow from the highly pressurised Mesozoic aquifer is unlikely to take place. Contrary to consolidation, during unloading of previously loaded parts of the model, the pore water is being taken into the Rupel Clay and Asse Member. This can be seen close to the origin of the second graph and the third graph, until 30 years. The same response of the model would have been obtained if an unloading stage had been included in an ice-loading scenario.

The magnitude of Darcy flux increases manifold with respect to the initial conditions and reaches an average of 2 cm/year. This value was obtained by using a value of $K=1 \times 10^{-10}$ m/s for the hydraulic conductivity of the Rupel Clay and Asse Member (scenario with a medium hydraulic conductivity). In another scenario a value of $K=1 \times 10^{-9}$ m/s was used for the Rupel Clay and Asse Member (scenario with a high hydraulic conductivity). The calculated vertical Darcy flux in the latter case shows an increase to 5 cm/year (Figure 6.28). Another difference with respect to the scenario with a medium hydraulic conductivity is related to the direction of

Darcy flux in the Rupel Clay and Asse Member. The vertical Darcy flux vectors in the middle cells of the Rupel Clay and Asse Member (marked in yellow in Figure 6.28) are directed upward. Even the flux vectors in the bottom cells become directed upward (marked in grey) after the maximum thickness of ice sheet has been reached. This implies that during consolidation flushing out of the Rupel Clay and Asse Member by an upward flow from a highly pressurised Mesozoic aquifer may be possible.

6.7 Loading by ice for a very fast advance of ice sheet

In the scenario with a very fast advance of the ice sheet, the maximum thickness of the ice sheet is reached in 50 years. The initial conditions are the same as in the case of the scenario with a medium fast advance of the ice sheet and a high lateral influx into the model (Section 6.5.1). The hydraulic conductivity of the Rupel Clay and Asse Member is high ($K=1 \times 10^{-9}$ m/s).

Shortened loading time used in this scenario has an important effect on the modelling results. The most important differences with respect to the scenario with a medium fast advance of the ice sheet are related to the forming of plasticity zones, to the flow of groundwater in the aquifers and to the hydromechanical response of the aquitards.

Plasticity

In the initial stage of loading plastic deformations occur locally in the Tertiary sand layers close to the northern lateral boundary of the model (Figure 6.29). The location and extent of deformation is practically the same for all scenarios with a high lateral influx into the model regardless of the speed of ice advance.

Distinctive to the scenario considered here is the occurrence of plasticity zones in the upper part of the Tertiary aquifer complex (Hardewijk and Maasluis Formations), which is located just beneath the permafrost zone and ahead of the ice sheet margin. Plastic zones occur consistently in the initial stages of ice loading when ice sheet partly covers the model. The reason for the forming of plasticity zones is the buoyancy force and the increased pore pressures in the top (Quaternary and Tertiary) aquifer caused by ice loading. Permafrost has a confining effect and groundwater in the top aquifer exhibits hydraulic heads that rise above ground surface. Manifestations of the plasticity in the form of heaving and bulging of the ground surface are commonly present in the areas affected by glaciation.

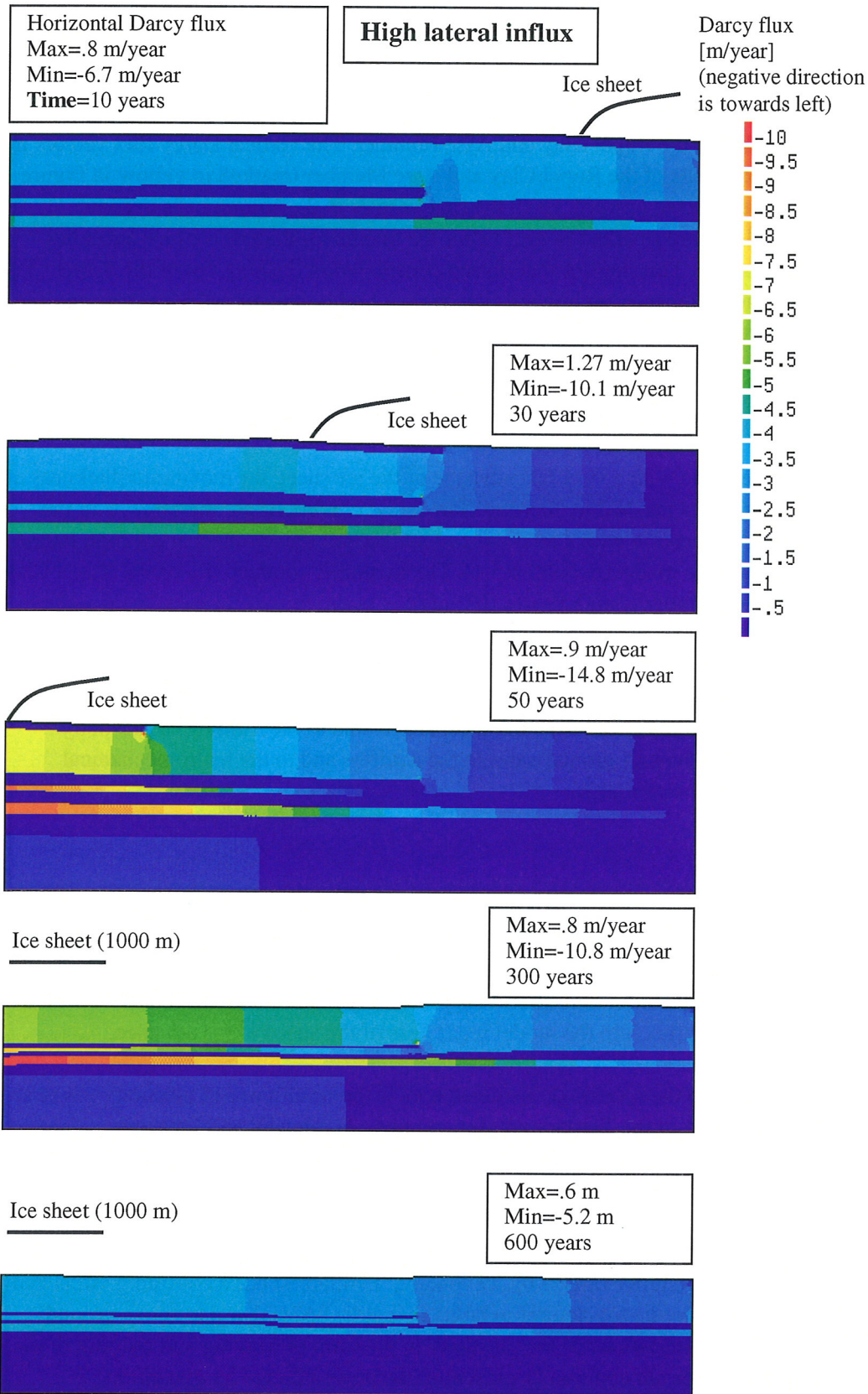


Figure 6.23 Horizontal Darcy flux during a medium fast advance of ice sheet for a high lateral influx into the model.

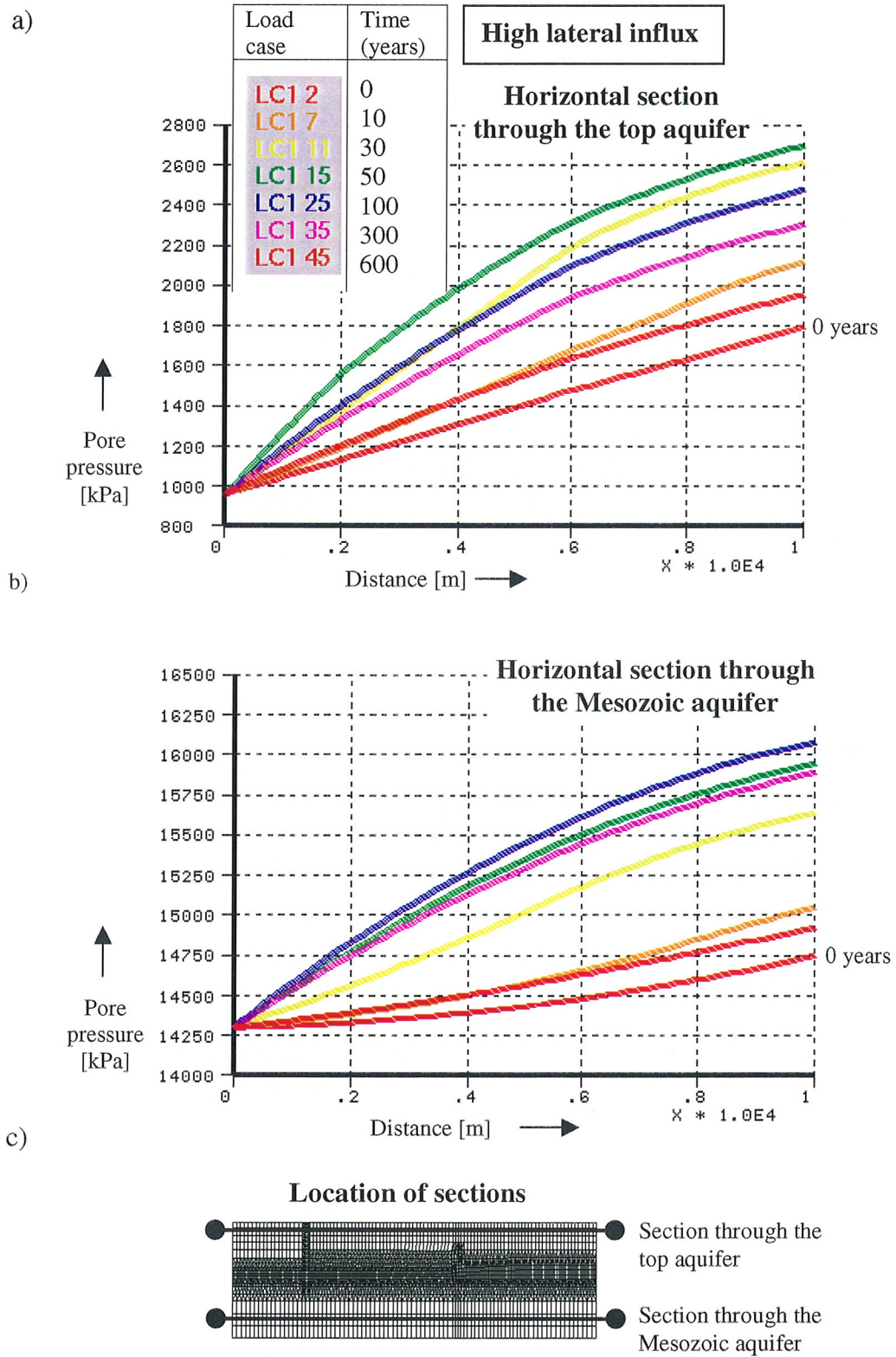


Figure 6.24 a) Pore pressure along two horizontal sections through a) the top aquifer and b) the Mesozoic aquifer during a medium fast advance of ice sheet and for a high lateral influx into the model. c) Location of the sections for which the pore pressure is shown.

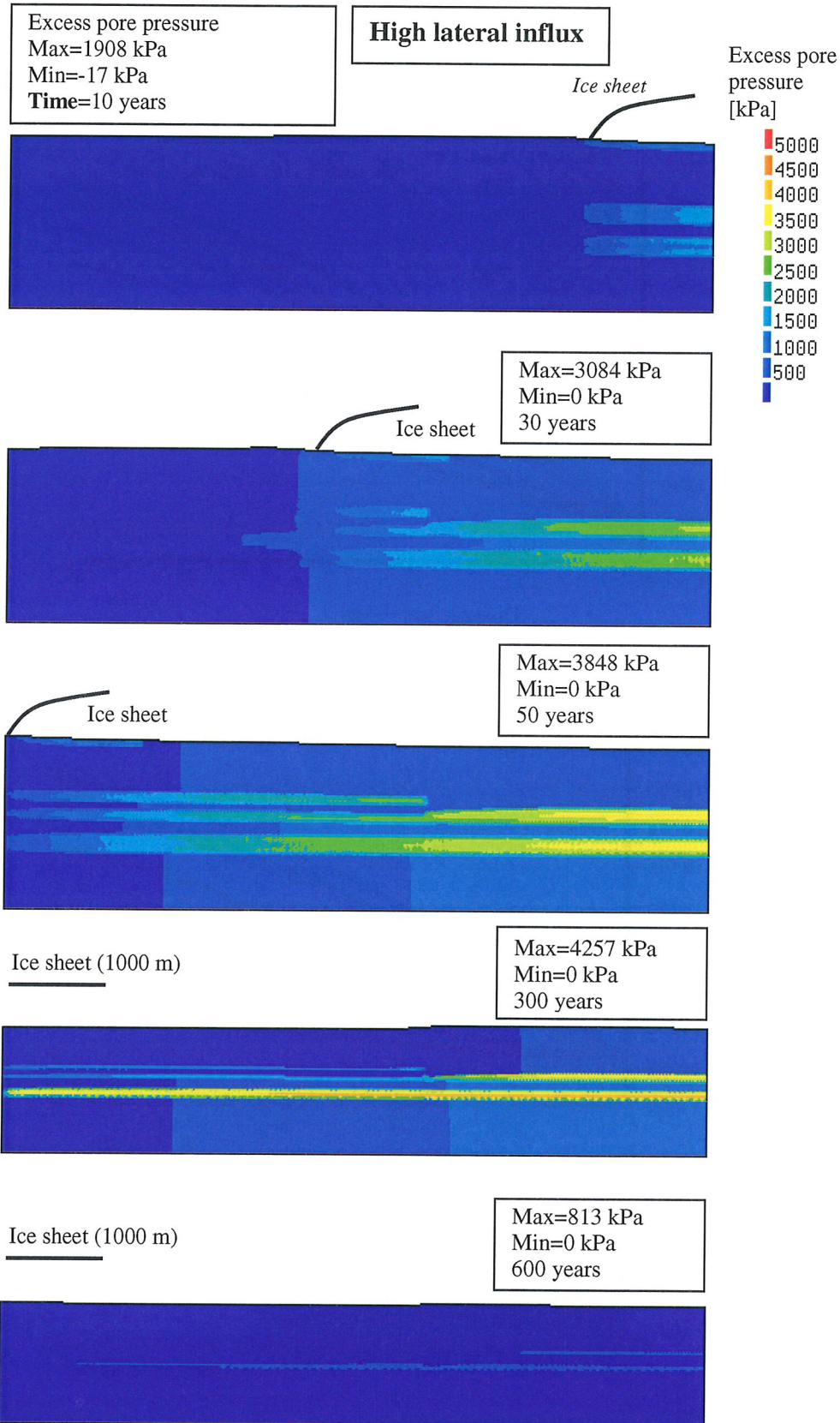


Figure 6.25 Excess pore pressure during a medium fast advance of ice sheet for a high lateral influx into the model.

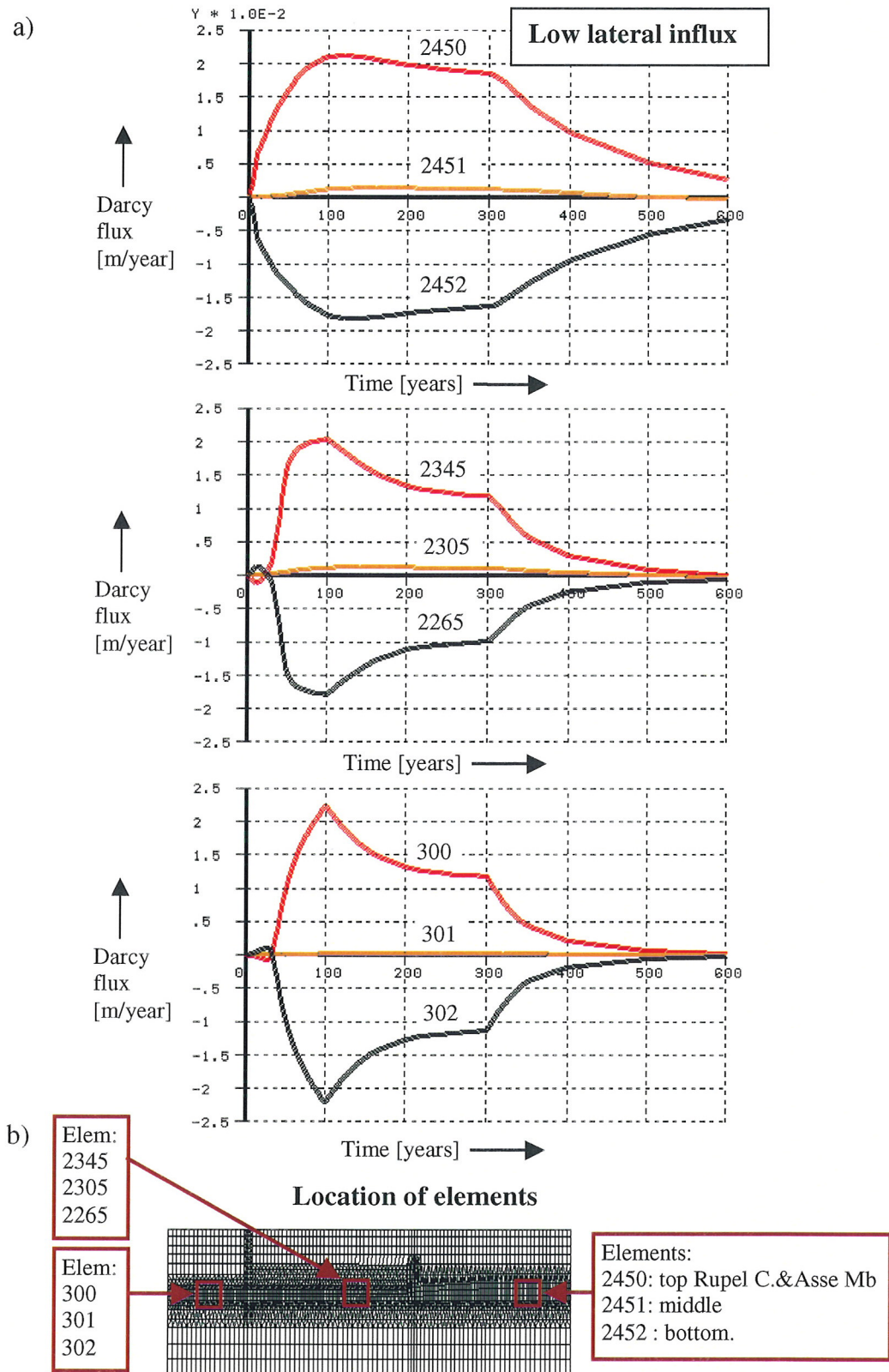


Figure 6.26 a) Vertical Darcy flux in the Rupel Clay and Asse Member during a medium fast advance of ice sheet for a low lateral influx into the model. b) Location of the elements for which the flux is shown.

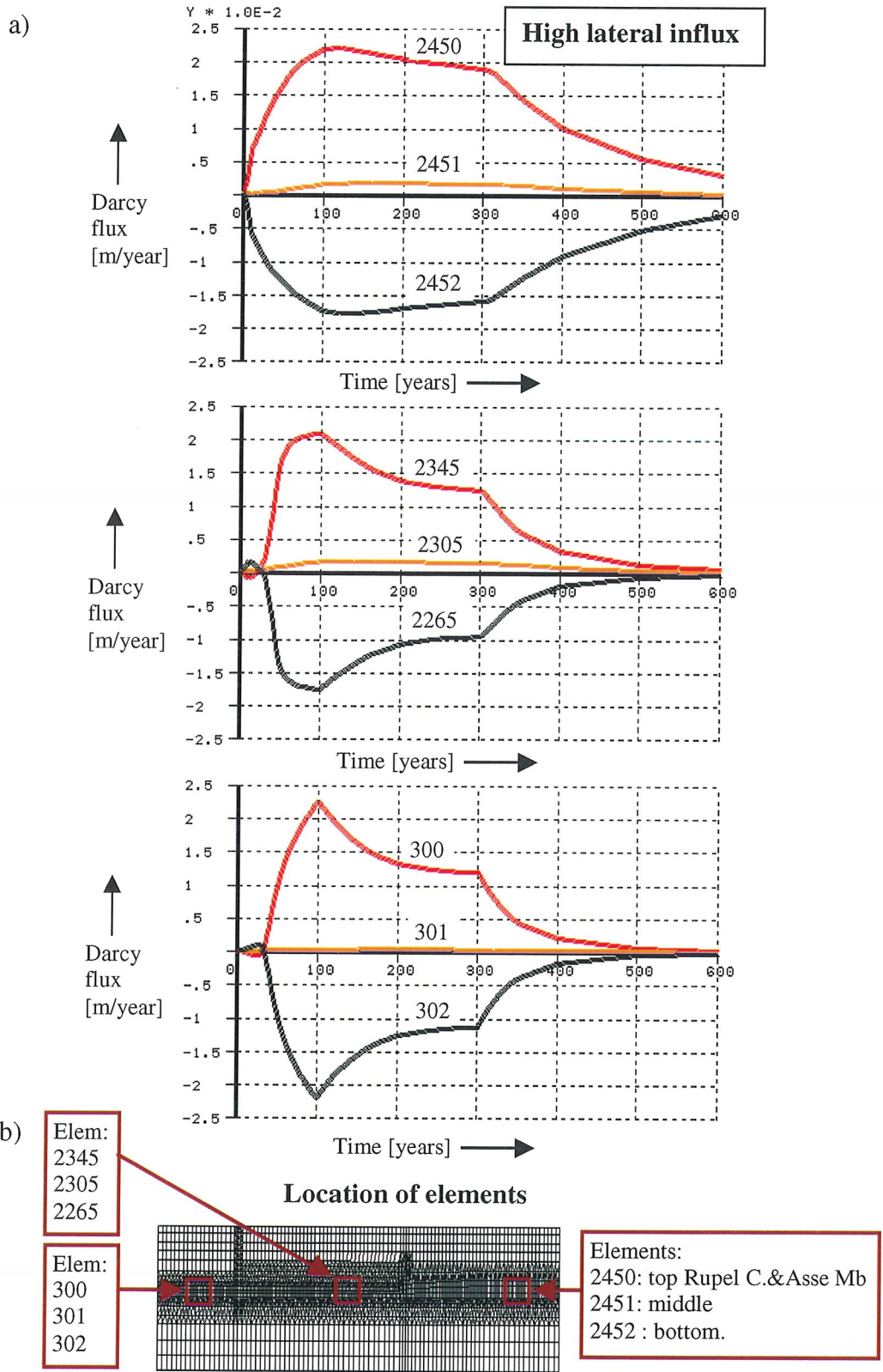


Figure 6.27 a) Vertical Darcy flux in the Rupel Clay and Asse Member during a medium fast advance of ice sheet for a high lateral influx into the model. b) Location of the elements for which the flux is shown.

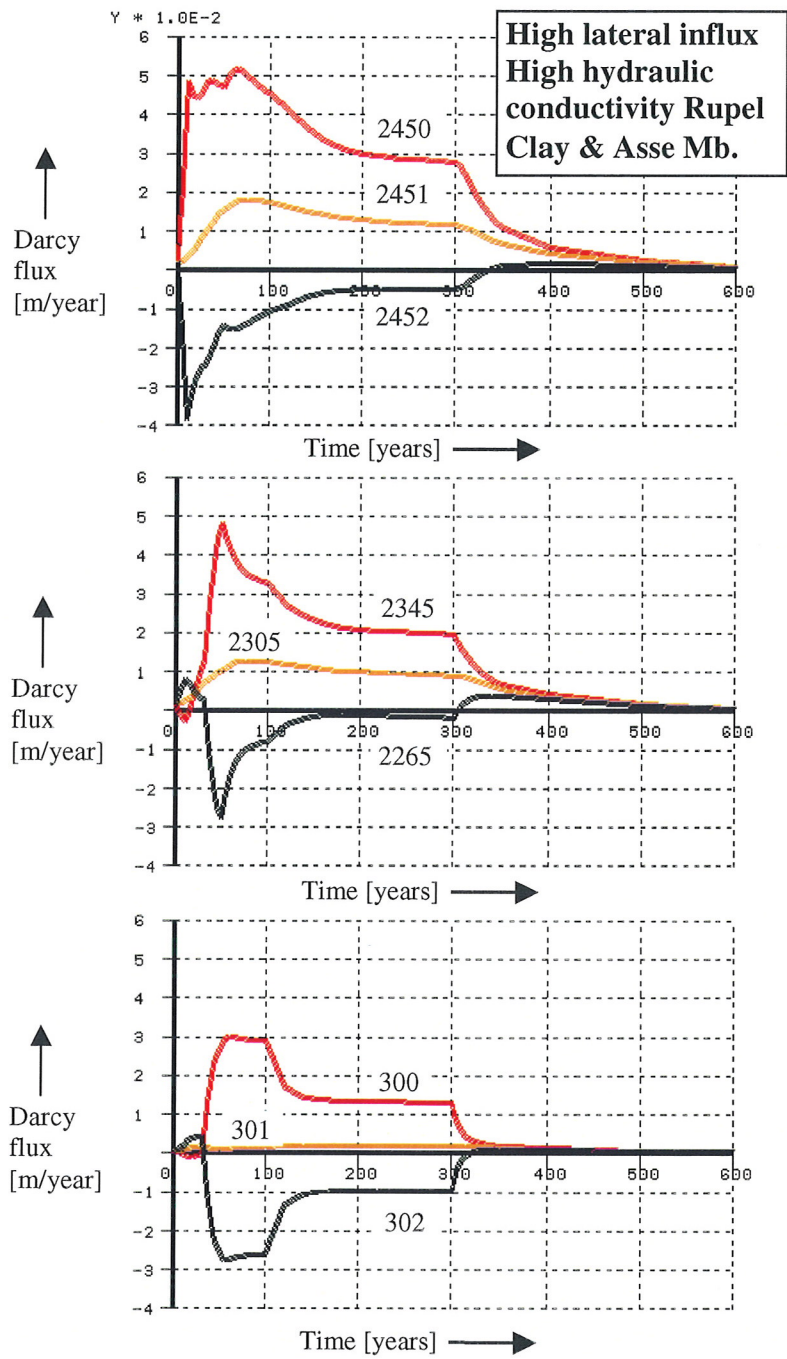


Figure 6.28 Vertical Darcy flux in the Rupel Clay and Asse Member during a medium fast advance of ice sheet and for a high lateral influx into the model and high hydraulic conductivity of the Rupel Clay and Asse Member. For the location of the elements for which the flux is shown see Figure 6.27.

Groundwater flow in aquifers

The initial pore pressures, pressure gradients and velocities of ground water flow are the same as in the scenarios with a medium fast advance of the ice sheet and with a high lateral influx in the model. The initial horizontal Darcy flux (i.e. the specific discharge) in the top (Quaternary and Tertiary) aquifer is -4.7 m/year and in the Mesozoic aquifer -0.3 m/year.

Loading by ice significantly accelerates groundwater flow in aquifers mainly in horizontal direction towards the ice sheet margin (Figure 6.30). Darcy flux increases as the ice sheet moves towards the edge of the model. The rate of acceleration is here higher than for the scenarios with a medium fast advance of ice sheet. The maximum value of Darcy flux of -42 m/year is reached in the top aquifer after 16.6 years when a 500 m thick ice sheet loads the model. This velocity occurs in the Voort Member. In the Mesozoic aquifer the maximum flux of -2.2 m/year is reached after 50 years, at the time when the ice sheet reaches its maximum thickness. This represents an increase of one order of magnitude with respect to the initial conditions.

Increase in pore pressures shows the same trend. In the top aquifer, at a depth of 95 m, the maximum pore pressure under the ice load, reached after 16.6 years, amounts to 4800 kPa (Figure 6.31a). This corresponds to a hydraulic head of 385 m above the ground surface, which is a fourfold increase with respect to the initial head of 80 m. The Mesozoic aquifer responds in a similar way. In the middle of this aquifer, at a depth of 990 m, the maximum pore pressure is about 18000 kPa. Hydraulic head thus increases from an initial value of 480 m to 810 m above the ground surface. The maximum pore pressure occurs after 50 years, when the maximum thickness of ice sheet has been reached (Figure 6.31b).

Groundwater flow in aquitards

Before loading by ice, Darcy velocities of groundwater are 2 mm/year in the Rupel Clay and Asse Member and 9 mm/year in the Ieper and Landen clay. The velocity vectors are directed upward as the pore pressure is higher in the underlying Mesozoic aquifer than in the overlying Quaternary and Mesozoic aquifer.

The development of the excess pore pressure in the aquitards present in the model is shown in Figure 6.32. The maximum excess pore pressure throughout the loading stages is approximately equal to the stresses caused by the applied ice load. At the last stage of the ice load increase, after 50 years, the shape of the ground surface is convex indicating that a considerable part of the consolidation settlement is yet to take place. At the end of the simulation, after 350 years, the excess pore pressure decreases to about 18% of the ice load.

The maximum excess pore pressure occurs in the Ieper and Landen clay. The hydraulic conductivity of this clay is one order of magnitude lower than that of the Rupel Clay and Asse Member. For that reason the pore water dissipates faster and the excess pore pressure decreases faster in the Rupel Clay and Asse Member. After 50 years, when the maximum thickness of ice sheet has been reached, the excess pore pressure in the Rupel Clay and Asse Member amounts to about 50% of the ice load. At the end of simulation, after 350 years, it reduces to 2%.

Graphs plotting the vertical component of Darcy flux against time for characteristic elements of the Rupel Clay and Asse Member are shown in Figure 6.33. In the initial state the pore water flow through this clay is directed upwards. In the initial stages of ice loading, when the model is partly covered by ice, two patterns of pore water flow can be detected. Consolidation-driven flow occurs in the elements that are being loaded, and swelling-driven flow occurs in the elements that are not yet loaded by the ice. Depending on the location of an element in the model, the swelling phase can last between 0 and 50 years. During swelling an element takes up the pore water from the neighbouring aquifers. For the elements shown in the first graph in Figure 6.33 the swelling phase is absent. For the elements shown in the second graph, it lasts 1.65 years. For the elements shown in the third graph, it lasts 5 years. During consolidation the maximum vertical Darcy flux, directed out of the Rupel Clay and Asse Member, amounts to about 14 cm/year. This represents a threefold increase in Darcy flux with respect to the scenario with a medium fast advance of the ice sheet. The pattern of pore water flow in the Rupel Clay and Asse Member at the end of simulations becomes close to the pattern characteristic for the initial state.

6.8 Loading by ice for a very slow advance of ice sheet

The maximum thickness of ice sheet is reached after 3000 years in the scenario with a very slow advance of the ice sheet. The initial conditions in this scenario are the same as in the case of the scenarios with a medium fast advance of ice sheet and a high lateral influx into the model (Section 6.5.1). The hydraulic conductivity of the Rupel Clay and Asse Member is high ($K=1 \times 10^{-9}$ m/s).

Prolonged loading time decreases some effects of loading on the subsurface. Plastic deformations in the top aquifer, underneath the permafrost and ahead of the ice sheet margin, do not occur. Darcy velocities of groundwater flow in the aquifers and the velocities of consolidation-driven flow in the aquitards are far smaller than in the scenarios with a fast and a very fast advance of the ice sheet. The results related to the response of the groundwater system will shortly be presented below.

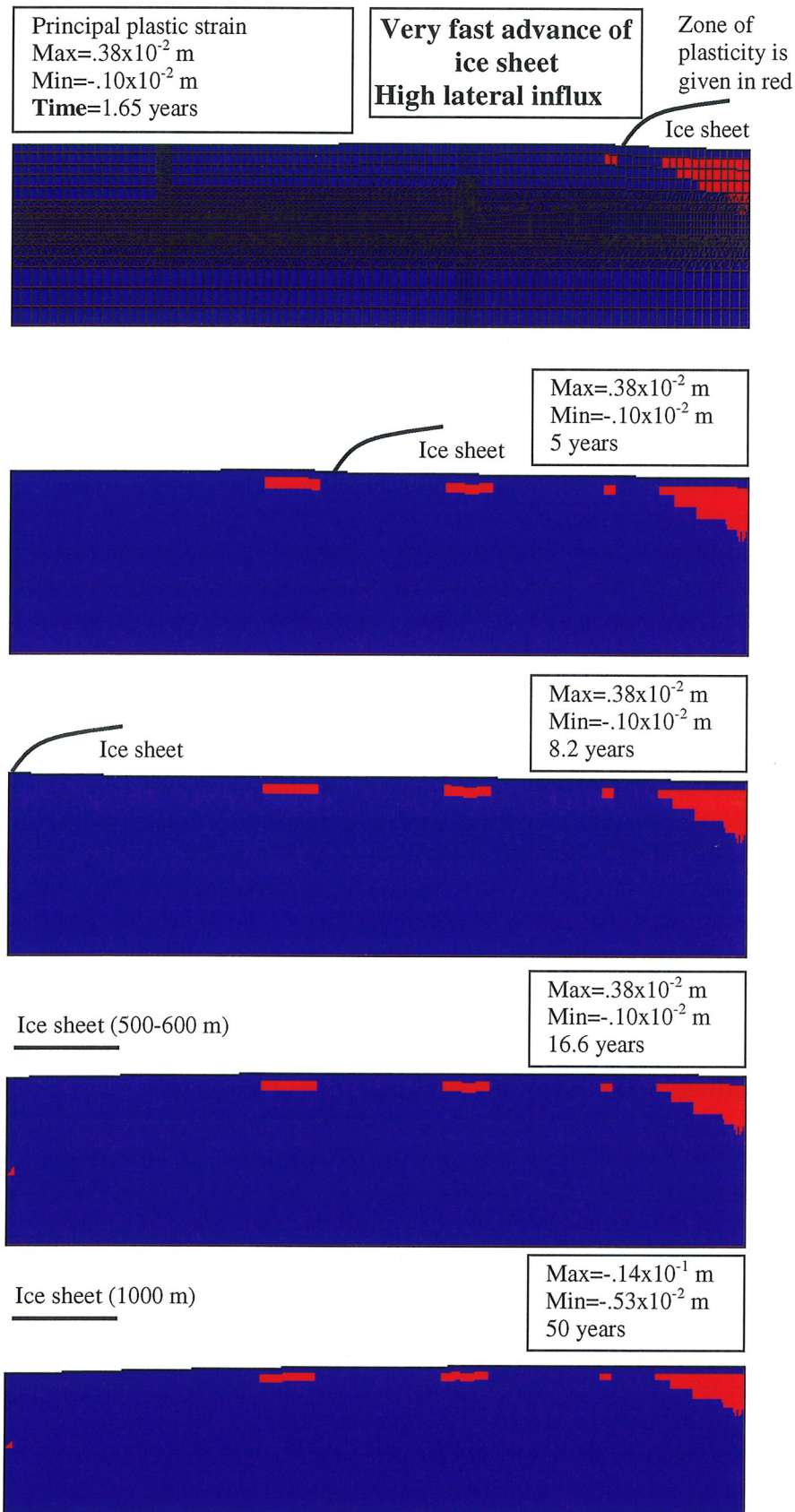


Figure 6.29 Formation of the zone of plasticity during a very fast advance of ice sheet for a high lateral influx into the model.

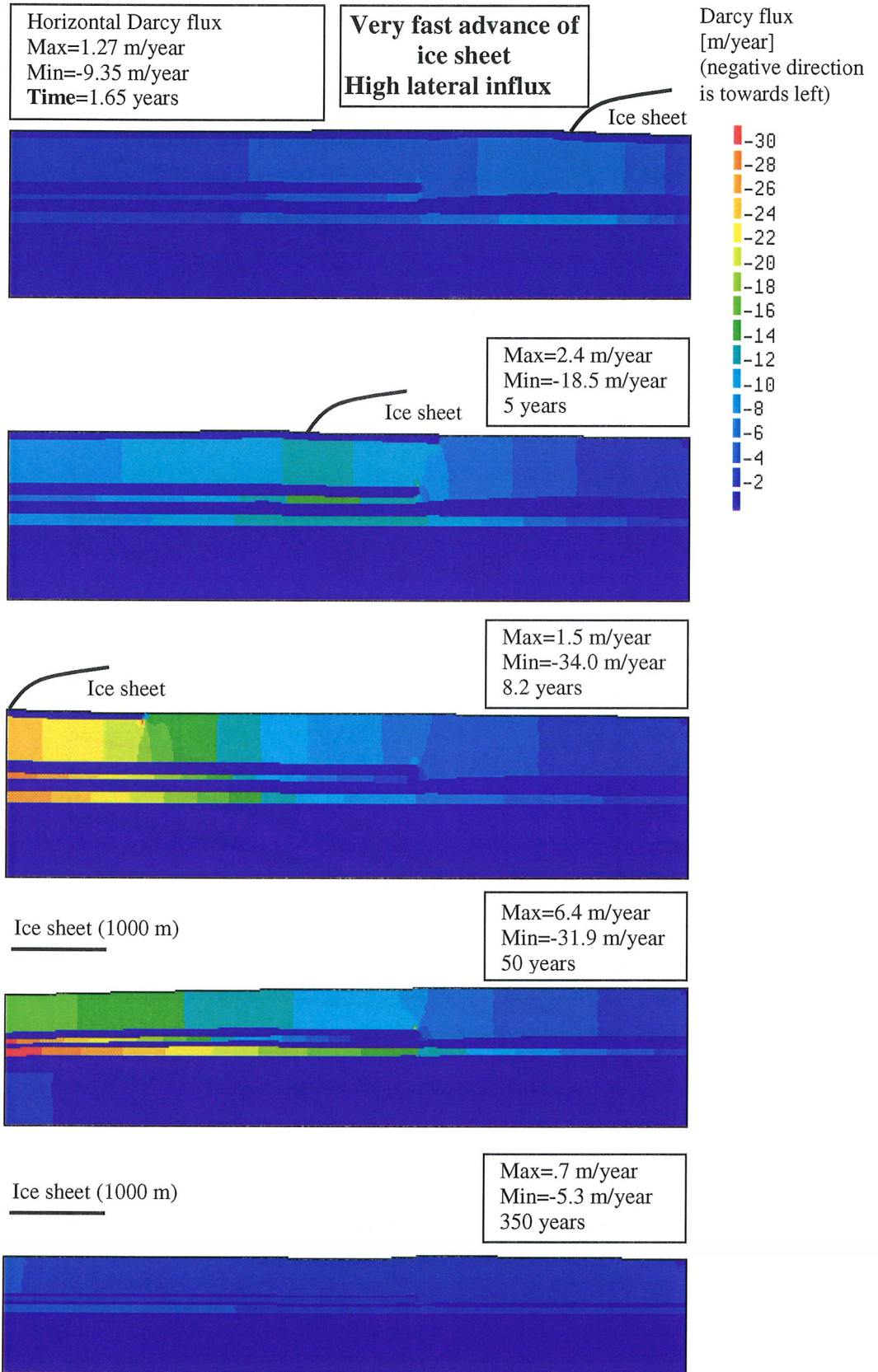


Figure 6.30 Horizontal Darcy flux during a very fast advance of ice sheet for a high lateral inflow into the model.

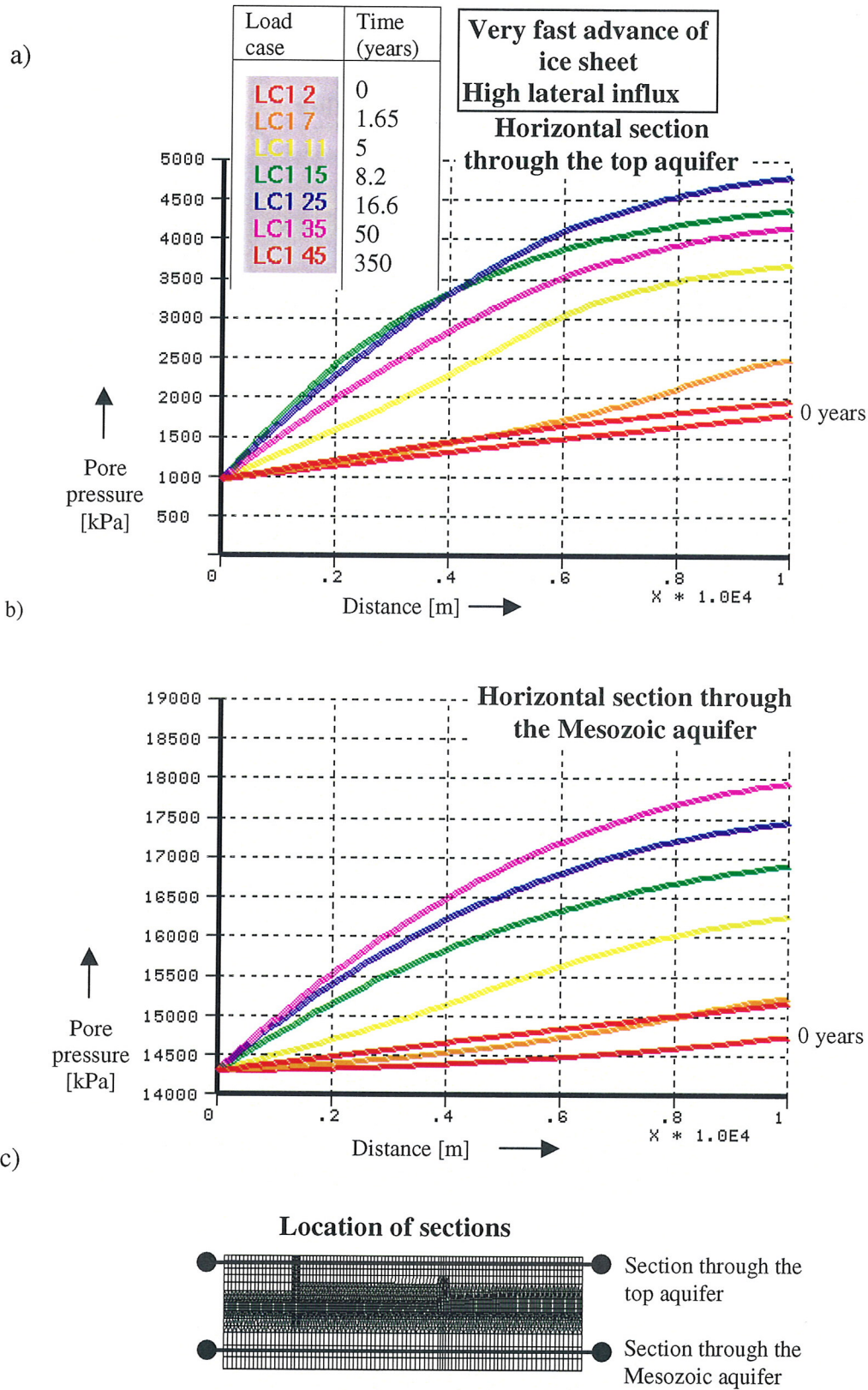


Figure 6.31 Pore pressure along two horizontal sections through a) the top aquifer and b) the Mesozoic aquifer during a very fast advance of ice sheet and for a high lateral influx into the model. c) Location of the sections for which the pore pressure is shown.

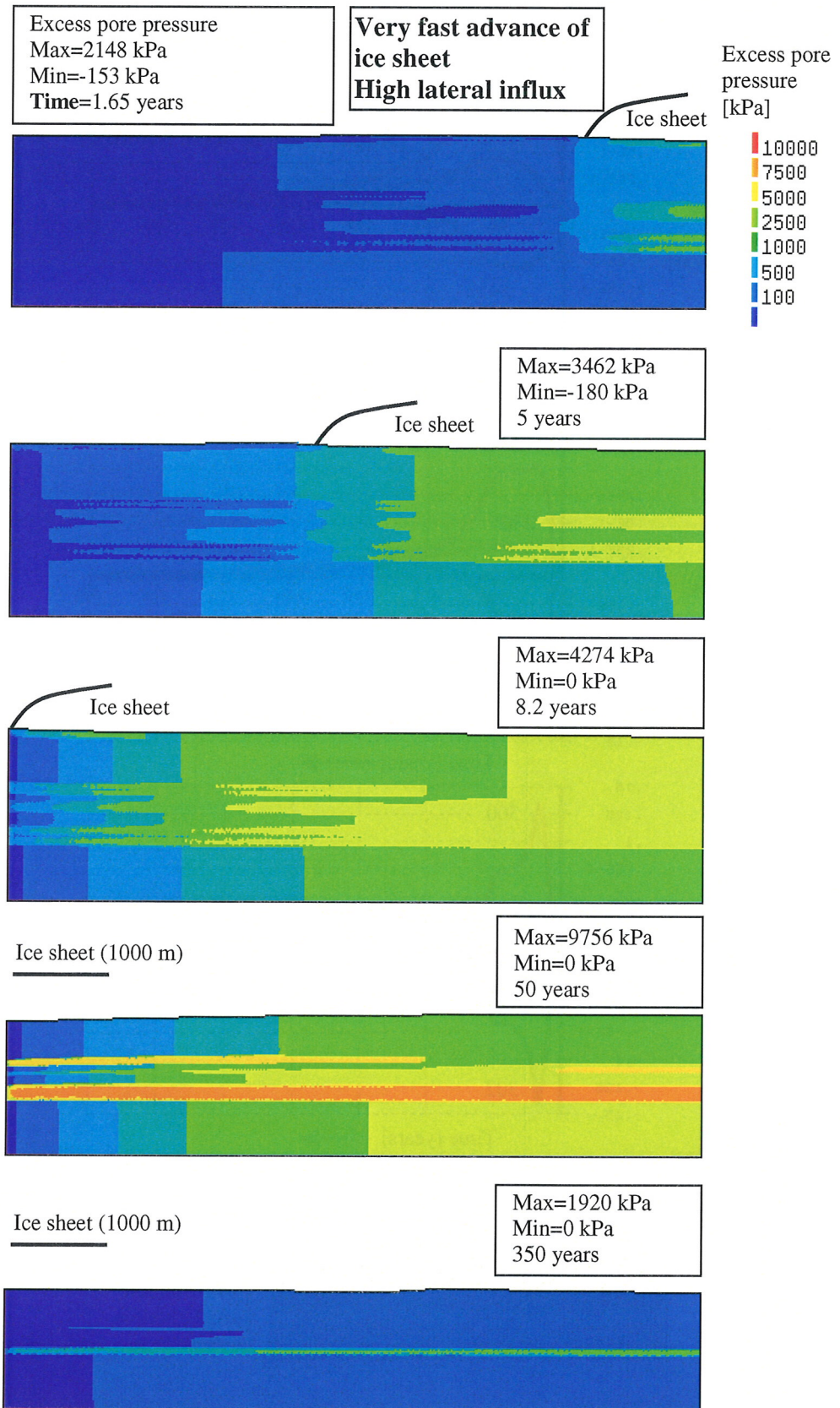


Figure 6.32 Excess pore pressure during a very fast advance of ice sheet for a high lateral influx into the model.

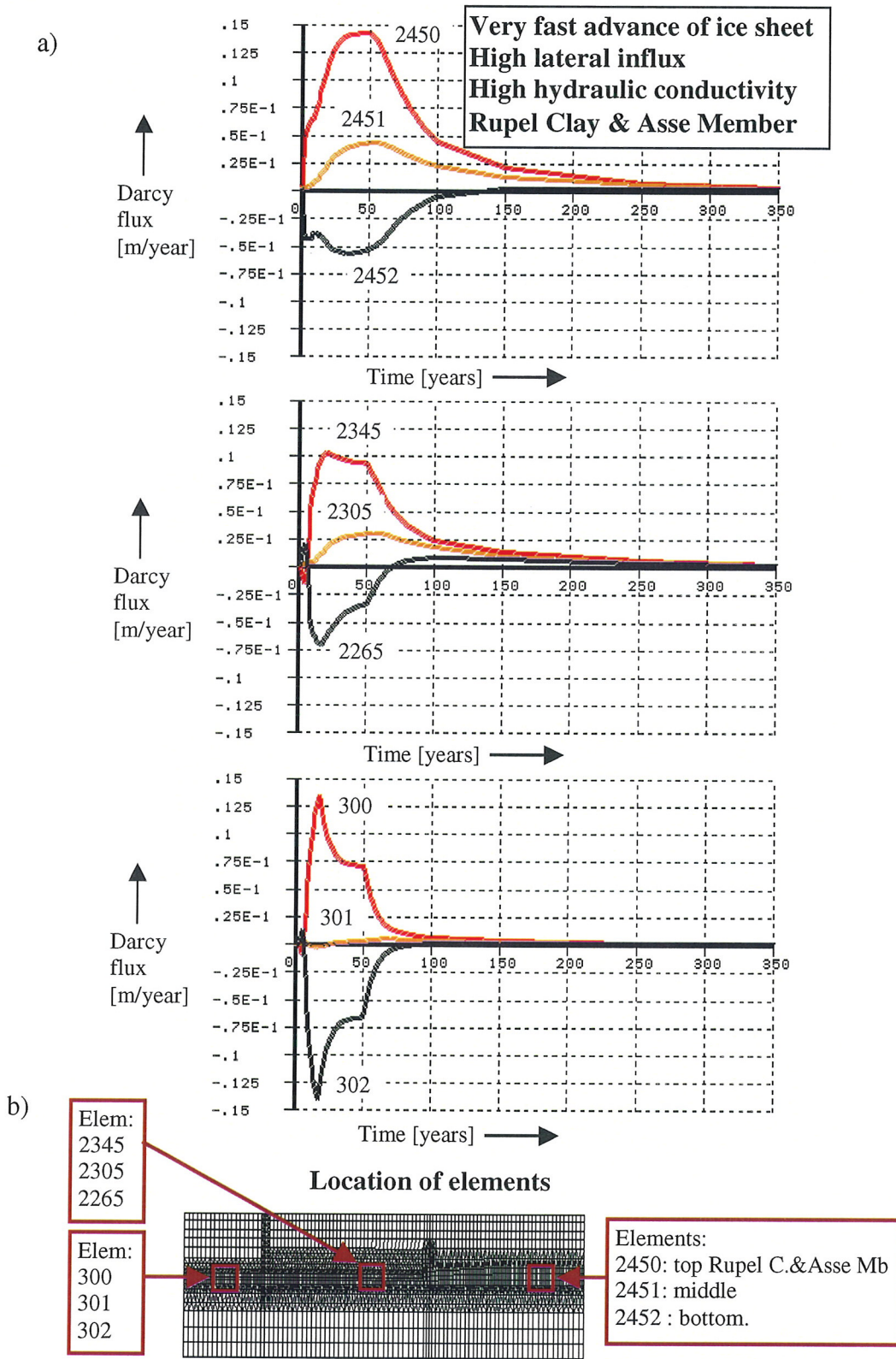


Figure 6.33 a) Vertical Darcy flux in the Rupel Clay during a very fast advance of ice sheet, for a high lateral influx into the model and high hydraulic conductivity. b) Location of the elements for which the flux is shown.

Groundwater flow in aquifers

The initial velocities of groundwater flow in the aquifers, pore pressures and pressure gradients are the same as in the other scenarios with a high lateral influx in the model. The initial horizontal Darcy flux (i.e. the specific discharge) in the top (Quaternary and Tertiary) aquifer is -4.7 m/year and in the Mesozoic aquifer -0.3 m/year.

Loading by ice accelerates the groundwater flow in aquifers to a small degree, mainly in a horizontal direction and towards the ice sheet margin. The maximum value of Darcy flux of -5.4 m/year is reached after 3000 years in the sands of the Breda Formation, which is a part of the top aquifer. In the Mesozoic aquifer there is a very small change in Darcy velocities throughout the loading.

Increase in pore pressures shows the same trend as in the Breda Formation. In the top aquifer, at a depth of 95 m, the maximum pore pressure under the ice load, reached after 3000 years, amounts to 2000 kPa (Figure 6.34a). This corresponds to a hydraulic head of 105 m above the ground surface, which is an increase of 25 m with respect to the initial head. The Mesozoic aquifer responds in a similar way. In the middle of this aquifer, at a depth of 990 m, the maximum pore pressure is about 15100 kPa (Figure 6.34b). This is equivalent to an increase in hydraulic head of about 40 m.

Groundwater flow in aquitards

Before loading by ice, Darcy velocities of groundwater are 2 mm/year in the Rupel Clay and Asse Member and 9 mm/year in the Ieper Member and Landen Clay. The velocity vectors are directed upwards because the pore pressure in the underlying Mesozoic aquifer is higher than in the overlying Quaternary and Mesozoic aquifer.

The development of the excess pore pressure in the model during the loading stages is shown in Figure 6.35. The maximum excess pore pressure is the highest in the first loading stage (69% of the stresses induced by the additional load) and generally decreases through the loading stages. After 3000 years, when the maximum thickness of ice sheet has been reached, the excess pore pressure is only about 4% of the stresses induced by the ice load. The maximum value of the excess pore pressure occurs in the Ieper Member and Landen Clay, which is ten times less permeable than the Rupel Clay and Asse Member. The excess pore pressure in the Rupel Clay and Asse Member is lower and ranges from 18% (of the stresses induced by the ice load) in the first loading stage to almost 0% in the last loading stage.

The vertical component of Darcy flux against time for characteristic elements of the Rupel Clay and Asse Member is plotted in Figure 6.36. In the previous

scenarios with a medium fast and a fast advance of ice sheet two patterns of the pore water flow were detected during the initial stages of ice loading. These are the consolidation-driven flow, which occurs in the elements being loaded, and the swelling-driven flow, which occurs in the elements not loaded by the ice. In the scenario with a very slow advance of ice sheet the swelling phase is not present (Figure 6.36). This can be explained by very small pressure gradient in the Rupel Clay and Asse Member caused by a very slow consolidation of the clay. Gradients caused by consolidation are much smaller than the natural pressure gradients caused by a difference in the pore pressures between the top aquifer and the Mesozoic aquifer. The initial groundwater flow through the Rupel Clay and Asse Member is directed upwards. This flow prevails over the consolidation-driven flow directed out of the clay. The maximum vertical Darcy flux out of the Rupel Clay and Asse Member, directed upwards, is about 1.5 cm/year. The average value is considerably smaller and close to the initial value of Darcy flux of 2 mm/year.

6.9 Discussion

The simplified hydromechanical model has been developed in order to simulate the effects of a potential future glaciation on the Tertiary clays. The process of consolidation and glacially driven changes in the groundwater system were simulated. Both processes cause a manifold increase of the velocity of the pore water flow. Consolidation of the Tertiary clays, that takes place under the weight of ice sheet, causes the flow of pore water from the clay layers into adjacent aquifers. The groundwater flow pattern through the aquifer system during glaciation is generally characterised by hydraulic gradients and groundwater flow velocities that are far greater than at present.

The obtained results provide a quantitative insight into the effects of the hydromechanical processes in the Tertiary clays and the groundwater system caused by advance of an ice sheet over a generic study area. The results obtained by running a set of scenarios on this model are preliminary and will be used to develop a more complex finite element model in the second phase of this study.

The simplified hydromechanical model is adequate as a tool for preliminary assessment of the hydromechanical processes in the subsurface caused by a future glaciation and the weight of an ice sheet. As a tool for assessments of the regional groundwater flow, this model is of a limited value. The length of the model is relatively small with respect to the length of the ice sheet. Because of that the geohydrological boundary conditions defined along the lateral sides of the model become unrealistic once the ice sheet has moved beyond the edge of the model.

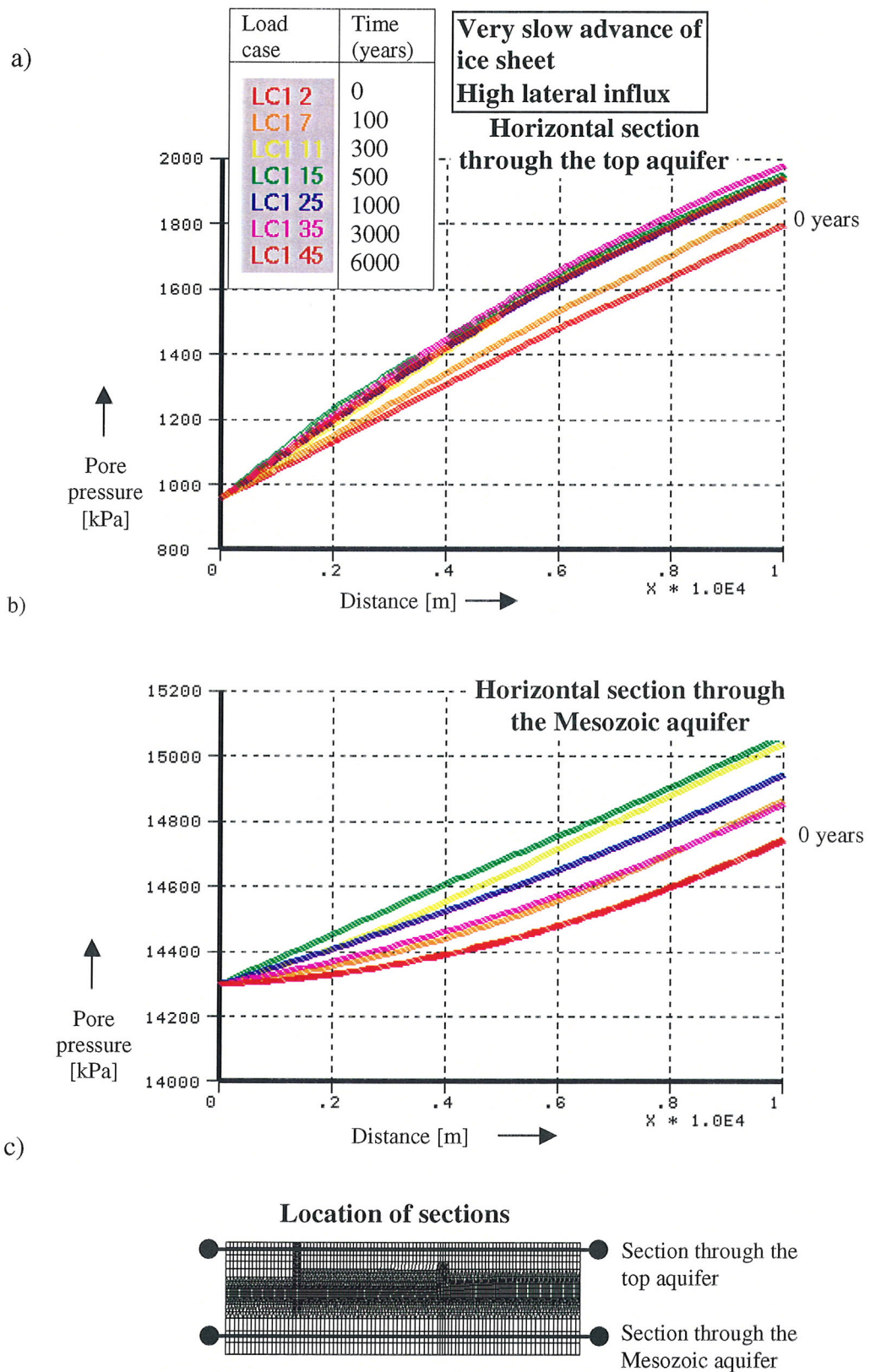


Figure 6.34 Pore pressure along two horizontal sections through a) the top aquifer and b) the Mesozoic aquifer during a very slow advance of ice sheet and for a high lateral influx into the model. c) Location of the sections for which the pore pressure is shown.

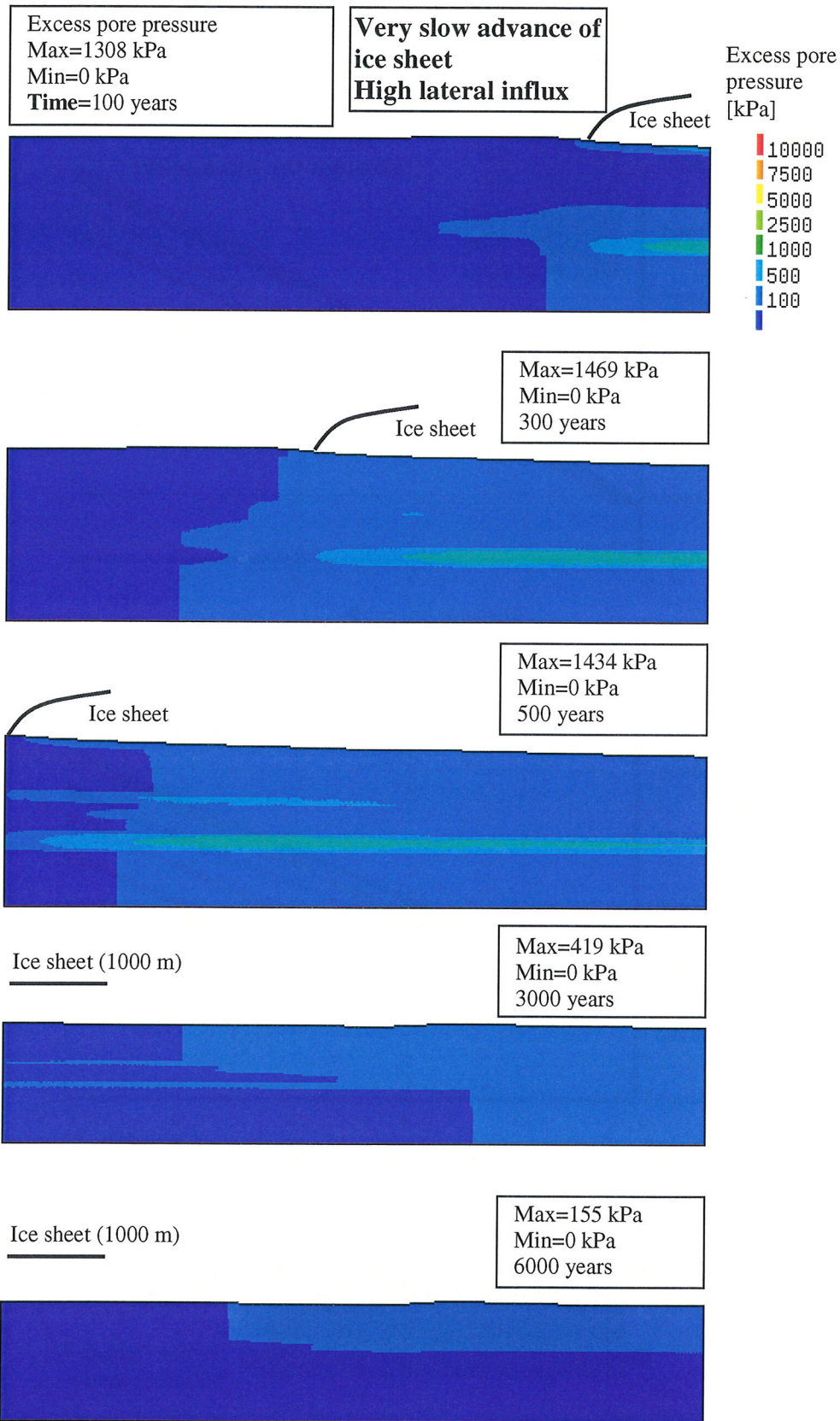


Figure 6.35 Excess pore pressure during a very slow advance of ice sheet for a high lateral influx into the model.

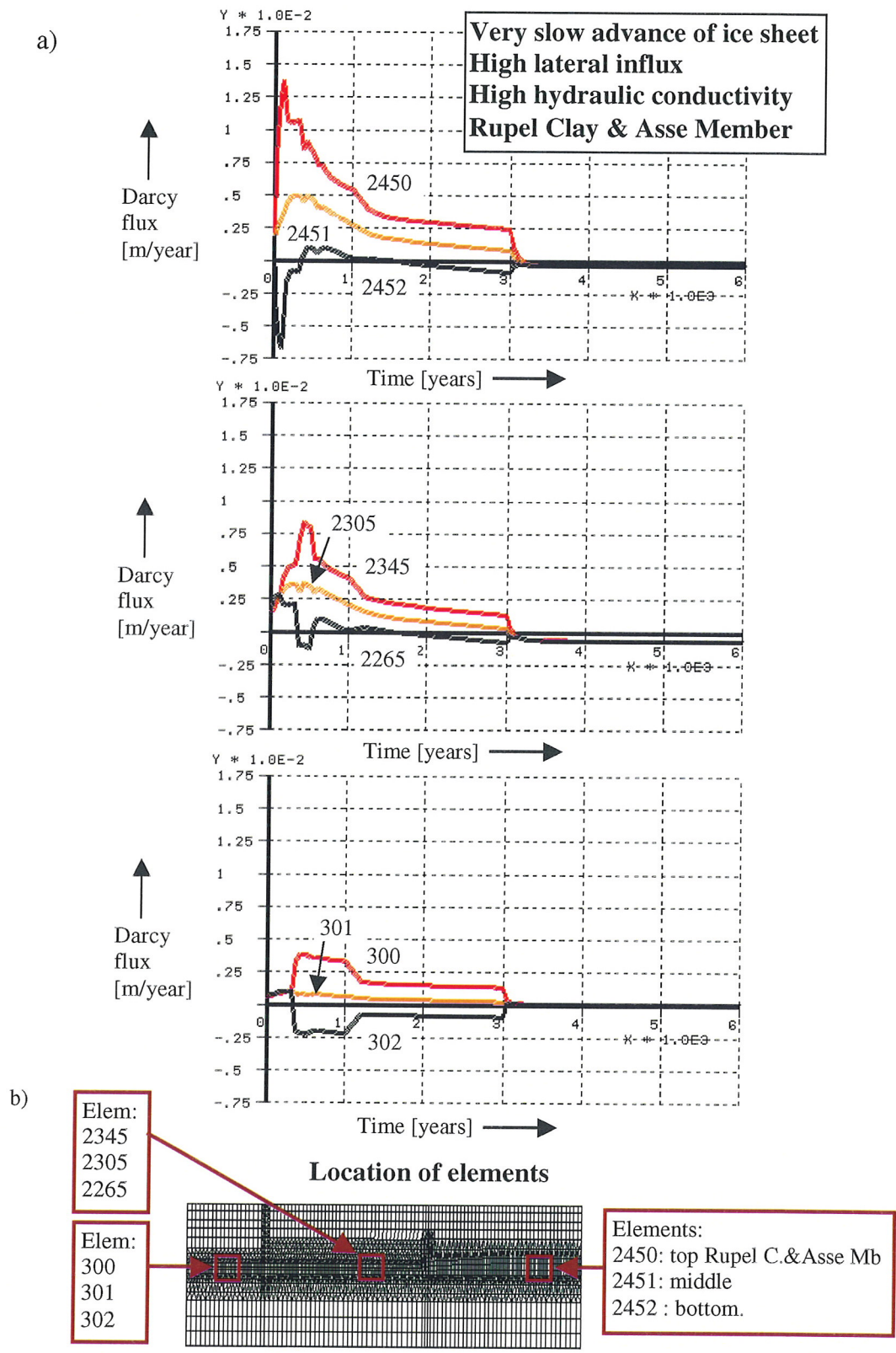


Figure 6.36 Vertical Darcy flux in the Rupel Clay and Asse Member during a very slow advance of ice sheet, for a high lateral influx into the model and high hydraulic conductivity of the Rupel Clay and Asse Member. b) Location of the elements for which the flux is shown.

Sensitivity analysis of the model is carried out by defining a set of scenarios in which important input parameters were varied over a range of values (low, medium and high values). By carrying out the sensitivity analysis, the response of the model to the varying input parameters was assessed. The critical model parameters were identified, which helped to reduce the number of input parameters to be varied in runs on a detailed finite element model. The critical model parameters are the hydraulic conductivity of the Rupel clay, their geomechanical properties and the material model used to model the mechanical behaviour of the clay.

Based on the conclusions from the first part of this study the following recommendations related to the preparation of a more detailed hydromechanical model can be given:

- Prepare a more detailed finite element model that will extend beyond the terminus of the ice sheet. In this manner prescribed hydraulic boundary conditions will be realistic throughout a whole ice-loading scenario. Taking into account the parameters that determine the geometry of the ice sheet adopted in this study, such a model has to be at least 70 km long
- Characterise the Rupel Clay and Asse Member by geomechanical parameters obtained by the experimental programme carried out within this study.

7 Simulation of glacially-driven hydromechanical processes using a detailed model

7.1 Approach

A detailed hydromechanical model has been developed in order to simulate the hydromechanical and geohydrological response of the subsurface to the loading by the ice during glaciation. Simulations calculated by using the detailed hydromechanical model are described in this chapter. These simulations provide input data, in the form of groundwater velocity fields, to the transport model. Simulations of the transport of radionuclides from the repository to the biosphere, carried out by using the METROPOL code (RIVM, 1993), are described in the next chapter.

The modelling methodology for a detailed hydromechanical model generally follows the methodology applied to develop a simple hydromechanical model. The detailed model is based on the same conceptual model and it incorporates the same physical processes and key features as the simple hydromechanical model. For detailed explanations refer to the Chapter 6.

The major enhancements and differences incorporated in the detailed hydromechanical model with respect to the simple hydromechanical model are as follows:

- Model adjustment.
 - The geometry of the detailed hydromechanical model has been adjusted by increasing its length to 70 km. In this manner the model has become more suitable to simulate the response of the regional groundwater system to a glaciation. The model has been built as a nested model by re-using a simple hydromechanical model (Figure 7.1; Section 7.2.1).
 - The values of the hydro- and geomechanical parameters, which characterise the Rupel Clay and Asse Member, were derived from the available laboratory tests carried out within the scope of the TRUCK-II project and the TRACTOR project (Section 7.2.2).
 - Loading and boundary conditions were adjusted to accommodate for the increased length of the model (Section 7.2.3).
- A small number of transient ice-loading scenario has been defined and calculated (Section 7.2.4). The simulation results are presented in Section 7.4.
- The detailed model established the basis for the subsequent simulation of radionuclide transport.
- A procedure has been developed to exchange data and results between the detailed hydromechanical model (Diana package) and the transport model (METROPOL package). The procedure is described in Section 7.4.5. For each of the scenarios that were calculated on the detailed hydromechanical model,

three representative groundwater velocity fields were defined. These characterise:

- the present-day situation (i.e. reference case),
- the pre-glaciation period with permafrost and increased fluxes,
- the glaciation period.

The representative groundwater velocity fields form the basis for the simulation of the radionuclide migration from the clay barrier to the biosphere as it will be discussed in the following chapter.

7.2 Description of the hydromechanical model

Preparation of the detailed hydromechanical model comprises building of a finite element mesh, characterising of the model units by the representative values of hydromechanical properties and definition of the boundary and loading conditions. A brief description of the above-mentioned steps follows. The section ends with description of the ice-loading scenarios selected to be run on the detailed hydromechanical model.

7.2.1 Schematisation and mesh

The length of the finite element model amounts to 70 km and its width to 1.2 km (Figure 7.1). The length of the model has been determined taking into account prescribed boundary conditions, geometry of the ice sheet and location of the repository. Boundary conditions are assumed realistic throughout a whole ice-loading scenario if the ice sheet terminus does not extend beyond the model boundaries when the ice over the repository reaches a maximum thickness of 1 km. These conditions are indeed met for the chosen length of the model.

The detailed hydromechanical model has been built by re-using the simple hydromechanical model and then extending it laterally. The mesh is made coarser where possible to decrease the number of elements and the computational time. The mesh consists of over 5000 quadratic plane-strain elements and over 12000 nodes. The element types used are CQ16E (quadrilateral with 8 nodes, based on quadratic integration according to a 2 x 2 integration scheme). To a much smaller degree the element type CT12E (triangle with 6 nodes, based on quadratic integration according to a 3- point integration scheme; Diana Manuals, 1999) was used.

The model units differentiated on the section correspond to those differentiated in the simple hydromechanical model. An exception is a 10 m wide fault zone, which is here modelled by the plane strain finite elements instead of the interface

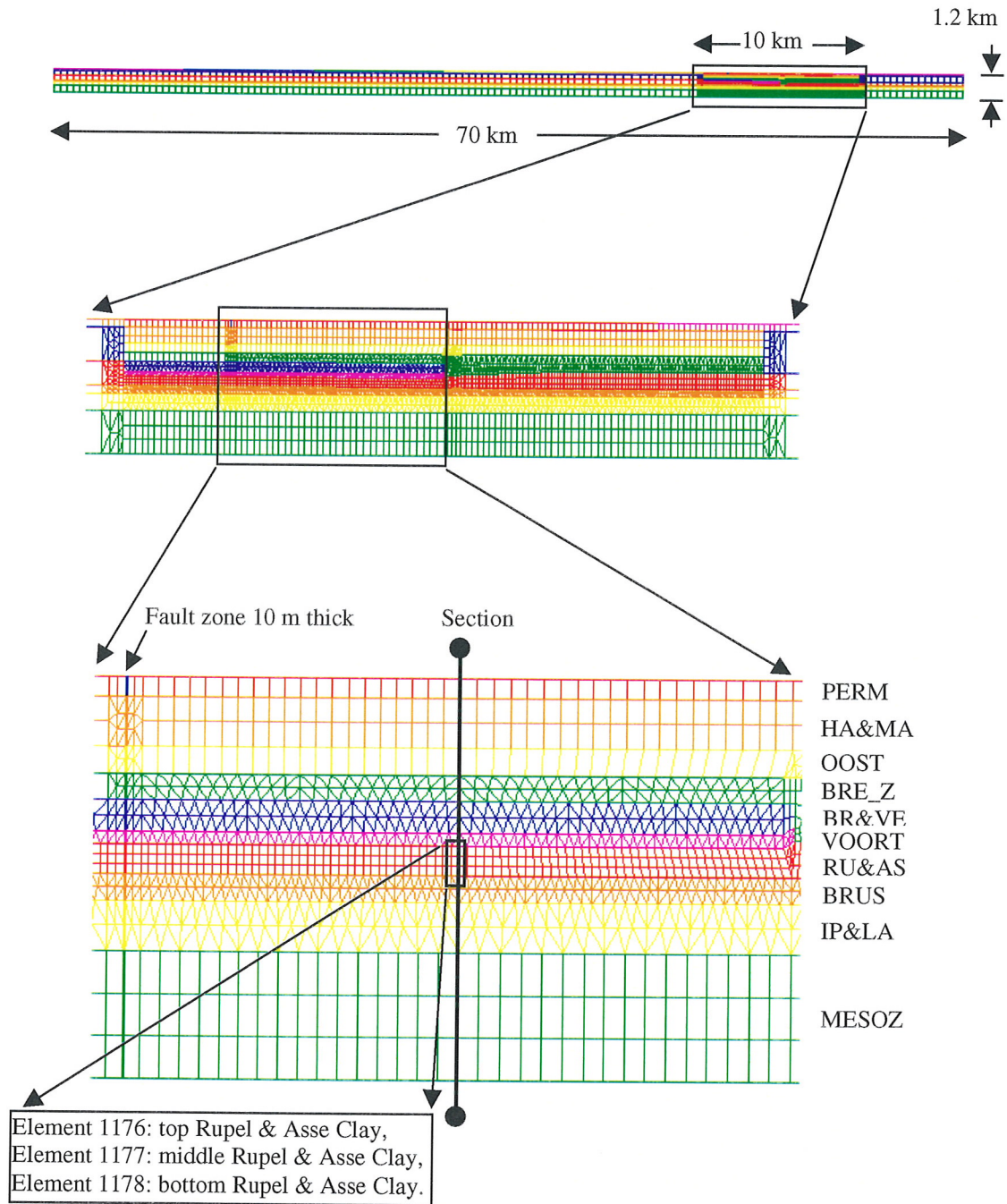


Figure 7.1 Finite element mesh for the detailed hydromechanical model. Model schematisation is the same as in case of the simplified hydromechanical model. The repository is assumed to be located in the middle of the element 1177.

elements used in the simple hydromechanical model. In this way the velocities of groundwater flow throughout the fault zone could also be obtained, as the interface elements do not allow for output of groundwater velocities, i.e. fluxes.

7.2.2 Material models and hydromechanical parameters

The experimental programme carried out within the scope of the TRUCK II project resulted in a set of geomechanical parameters for the Mohr-Coulomb model and the Modified Cam-Clay model of the Rupel Clay and Asse Member (Thimus et al, 1999). Both models will be used in the loading scenarios to describe the behaviour of the Rupel Clay and Asse Member (see Section 7.2.4). For the other Tertiary aquitards and aquifers the Mohr-Coulomb material model was used. The permafrost, the top (Quaternary and Tertiary) aquifer and the Mesozoic aquifer were assumed to behave purely elastic.

The most representative parameters are those obtained on samples taken at a large depth, which closely corresponds to a depth of the potential repository. For a projected repository depth of 500 to 800 m, the geomechanical parameters determined on samples from the locations Weelde, taken at a depth of 313 m, and from Blija, taken at depths of 454 and 478 m, are the most representative and will be used in this model study. The estimates are thought to be realistic averages characteristic of the model units. The values of geomechanical and geohydrological parameters used to characterise differentiated model units are given in Table 7.1.

In estimation of the Young's modulus a simple empirical relation was used:

$$E = c \sigma' \quad (7.1)$$

where: E = Young's modulus [$ML^{-1}T^2$, e.g. Pa]

σ' = average effective stress in the layer [$ML^{-1}T^2$, e.g. Pa]

c = correction factor, ranging from 20 to 100 for sand and 100 to 500 for clay [-].

For frozen unconsolidated sediments of the permafrost, the value of Young's modulus has been estimated to be approximately one order of magnitude greater than in unfrozen sediments. This in analogy with frozen clay, which shows a fivefold increase in Young's modulus in comparison with unfrozen clay (Thimus, 1989). For frozen sand the increase is likely greater due to a dominant macroscopic porosity of sand and larger quantities of pore water that can easily be frozen.

Table 7.1 Geomechanical and geohydrological parameters for the model units in the detailed hydromechanical model.

Stratigraphic unit	Model unit	γ [kN/m ³]	E [MPa]	Degree of consolidation	ν [-]	c [kPa]	ϕ [°]	K [m/s]
Quaternary	KWAR	20	125	Low	0.3	-	-	1×10^{-5}
	PERM	20	1000	-	0.3	-	-	1×10^{-10}
Harderwijk, Maasluis	HA&MA	20	150	Low	0.3	-	-	1×10^{-5}
Oosterhout	OOST	20	250	Low	0.3	-	-	1×10^{-5}
Breda (sand)	BRE_Z	20	320	Low	0.3	-	-	1×10^{-5}
Haarderwijk, Oosterhout, Breda	HA&OO&BR	20	250	Low	0.3	-	-	1×10^{-5}
Breda (clay), Veldhoven	BR&VE	19	240	Medium	0.3	200	27	1×10^{-10}
Voort	VOORT	20	1400	Medium	0.3	10	35	1×10^{-5}
Rupel Clay & Asse Member	RU&AS	19	520	High	0.3	200	12	3×10^{-12}
						-	15	1×10^{-11}
Brussel	BRUS	20	3000	High	0.3	10	35	1×10^{-5}
Ieper, Landen	IP&LA	19	750	High	0.3	200	27	3×10^{-12}
Mesozoic	MESOZ	23	10000	- (rock mass)	0.3	-	-	1×10^{-6}
Fault zone (above Mesoz.)	FZONE	20	150		0.3	-	-	1×10^{-3}

Parameters for the Modified Cam-Clay model

Stratigraphic unit	Model unit	λ [-]	K [-]	Pc' [kPa]	n [-]	γ_d [kN/m ³]
Rupel Clay & Asse Member	RU&AS	0.119	0.021	6900/10350	0.4	1.5

Legend:

n - initial porosity,	ϕ - angle of internal friction,
K - hydraulic conductivity,	c - cohesion,
γ - unit weight, saturated,	λ - compression index,
γ_d - unit weight, dry,	κ - swelling index,
E - Young's modulus,	p_c' - preconsolidation stress.
ν - Poisson's ratio,	

7.2.3 Boundary conditions

Initial geohydrological boundary conditions are derived from the developed conceptual model for the glacial groundwater system presented Section 2.2. Structural boundary conditions as well as the rates of potentials prescribed along the model boundaries are equivalent to those used in the case of the simplified hydromechanical model (Figure 7.2). The lateral fluxes were enlarged to accommodate for the length of the model, which was increased with respect to the simple hydromechanical model (Table 7.2). The lateral fluxes were calculated assuming that the maximal hydraulic gradient $i=8 \times 10^{-3}$ extends over a length of 20 km across the model and then it reduces to about one half of the maximal value. The prescribed lateral flux into the top aquifer (the HA&OO&BR model unit) results in a hydraulic head of about 350 m measured along the northern lateral boundary of the model.

Loading of the model by the ice during glaciation was simulated by using 18 load cases (Figure 7.2). The loads were applied subsequently simulating a steadily advancing ice sheet. The location of the ice sheet terminus, the lateral extension of the permafrost and the length over which the infiltration of the meltwater takes place are dependent on the loading stage. The permafrost was assumed to extend partly underneath the ice sheet, approximately 10 km beyond its terminus. Further away, at the contact between the ice sheet and the ground surface infiltration of the meltwater takes place.

With regard to the dynamics of loading, it was assumed that the ice sheet steadily advances over the model until its terminus reaches the southern model edge (Figure 7.3). The thickness of the ice over the repository is then about 1 km. This maximum thickness of the ice resides for the whole duration of the glacial period, which is assumed to last for 20,000 years. The speed of ice advance amounts to 200 m/year as in the case of a medium fast advance of the ice in the simplified hydromechanical model.

7.2.4 Ice-loading scenarios

Three ice-loading scenarios were defined to be run on the detailed hydromechanical model:

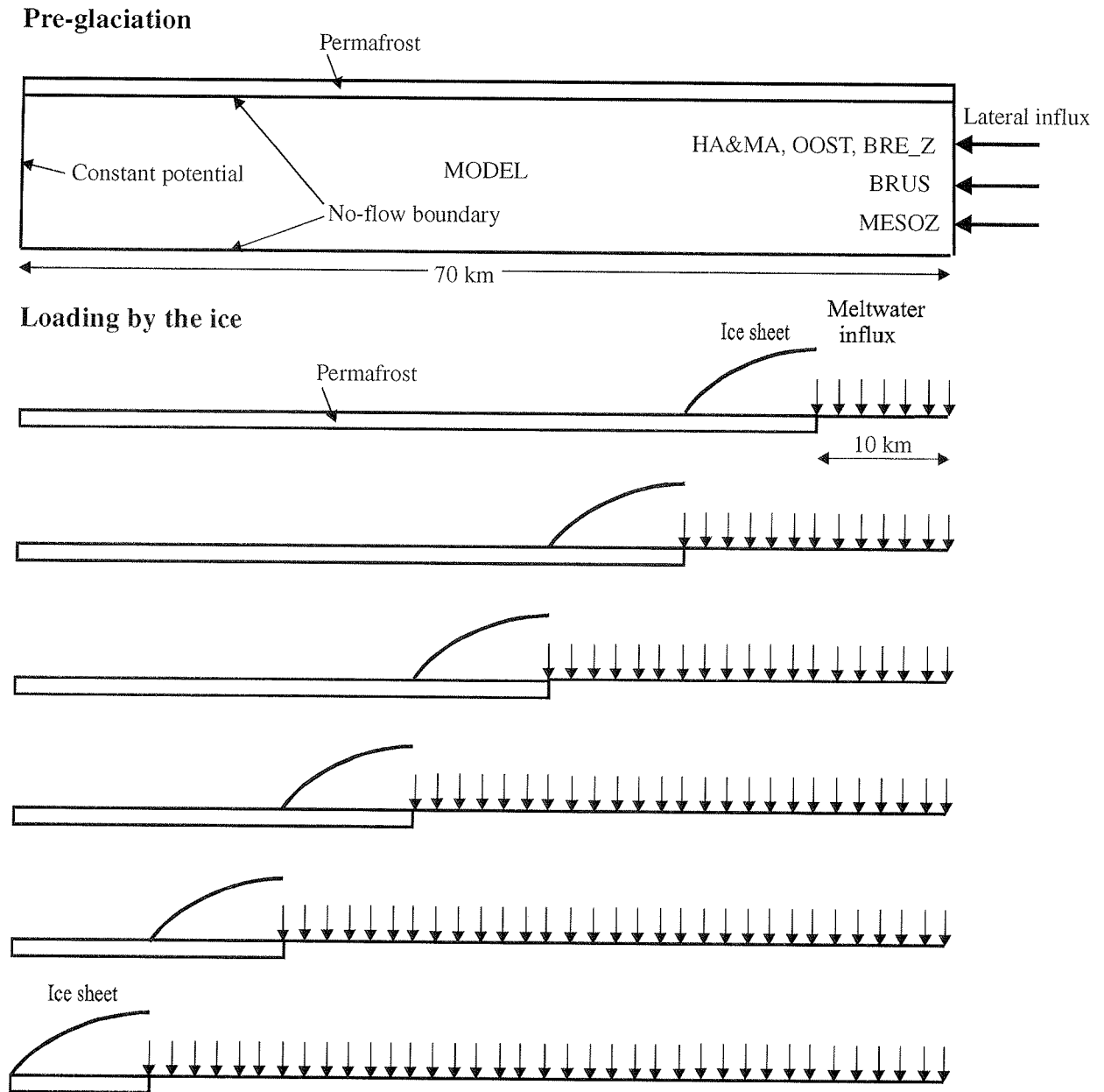


Figure 7.2 Geohydrological boundary conditions in the detailed hydromechanical model. Initial, pre-glacial phase (top) and glacial phase. Lateral extension of the permafrost and the zone of meltwater infiltration beneath the ice sheet depend on the location of the ice sheet margin.

Table 7.2 Fluxes and potentials used to define geohydrogeological boundary conditions in the detailed hydromechanical model (refer also to Figure 7.2).

Stratigraphic unit - aquifer	Model unit	Type of geohydrogeological boundary		
		q - constant influx [m/year]	p - constant potential [kPa]	
		Right (northern) lateral boundary	Left (southern) lateral boundary	Top boundary
Quaternary	KWAR		$p=0$	$q=0.02$
	PERM	No-flow		
Harderwijk, Oosterhout, Breda	HA&OO&BR	$q=1.14$	$p=0$	-
		(q total =342*)		
Brussel	BRUS	$q=0.9$	$p=0$	-
		(q total=72)		
Mesozoic	MESOZ	$q=0.09$	$p=4400$	-
		(q total=34)		

* q and p represent the unit influx and the unit potential, respectively, while the q total represents the total influx into the unit over its whole thickness.

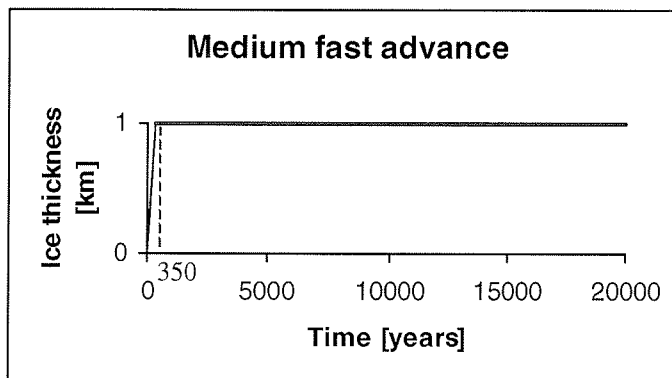


Figure 7.3 Dynamics of the ice sheet movement.

- Scenario with the Modified Cam-Clay model for the Rupel Clay and Asse Member, with average values of the Cam-Clay parameters and an average value of the hydraulic conductivity. The values of the parameters used are as follows: $\phi=15^\circ$, $p_c'=10350$ kPa, $\lambda=0.119$, $\kappa=0.021$ and $K=3 \times 10^{-12}$ m/s (where ϕ is the friction angle, p_c' is the preconsolidation stress, λ is the compression index, κ is the swelling index and K is the hydraulic conductivity).
- Scenario with the Modified Cam-Clay model for the Rupel Clay and Asse Member, with low values of the Cam-Clay parameters and a high value of the hydraulic conductivity. The values of the parameters used are as follows: $\phi=12^\circ$, $p_c'=6900$ kPa, $\lambda=0.119$, $\kappa=0.021$ and $K=1 \times 10^{-11}$ m/s.

- Scenario with the Mohr-Coulomb model for the Rupel Clay and Asse Member. The values of the parameters used are as follows: $\phi=12^\circ$, $c=200$ kPa and $K=3 \times 10^{-12}$ m/s (where c is the cohesion).

The parameters varied in the ice loading scenarios are the type of material model and the hydraulic conductivity of the Rupel Clay and Asse Member. These parameters are critical for determining the representative groundwater velocity fields in the model during loading by the ice. Sensitivity of the hydromechanical model to a material model used for the Rupel Clay and Asse Member is assessed through the usage of a Mohr-Coulomb model and an advanced Modified Cam-Clay model. Sensitivity to the permeability of the Rupel Clay and Asse Member is assessed by using two different values of the hydraulic conductivity, namely $K=3 \times 10^{-12}$ m/s and $K=1 \times 10^{-11}$ m/s (in the scenario with the high conductivity). The former value is referred to as representative in the METRO safety study (Grupa & Houkema, 2000) while the latter value is recommended as a representative field (*in situ*) value by GeoDelft (GeoDelft Report nr. CO-383970/06, 1999).

7.3 Initialisation of the stress and groundwater flow

The initial effective stresses and pore pressures have to be introduced into the detailed hydromechanical model before loading it by the ice. The initial conditions are representative for the period of pre-glaciation (Figure 7.2) and can be imposed by applying the hydrostatic and hydrodynamic loading on the model. This is done by loading the model by the gravity acceleration and by imposing the geohydrological boundary conditions (Section 7.2.3). The present-day situation (i.e. reference case) is calculated by a single stationary run of the detailed hydromechanical model with a prescribed low lateral influx into the model (as explained earlier in Sections 6.3 and 6.4).

Figure 7.4 illustrates the effects of a high permeable fault zone on the spatial distribution of the initialised pore pressures. The fault zone acts as a drainage path which to a certain extent releases the pore pressure in the Mesozoic aquifer. This affects the general groundwater flow pattern, especially in the Mesozoic aquifer. In this aquifer, the groundwater flow is mainly horizontal, from either side of the fault zone towards the fault. Then the ground water flows upwards through the fault zone and discharges into the Top Quaternary and Tertiary aquifer. The fault zone represents a direct hydraulic link between the two aquifers.

By combining the stresses caused by the gravity loading and the initialised pore pressures the initial effective stresses have been generated in the model. The effective horizontal stresses in the Rupel Clay and Asse Member were calculated assuming that the lateral pressure ratio is a function of the angle of internal friction of the Rupel Clay and Asse Member. The following expression was used:

$$K_0 = 1 - \sin \phi \quad (7.2)$$

where: K_0 = the lateral pressure ratio,
 ϕ = the angle of internal friction.

Due to a low value of the friction angle the horizontal stresses in the Rupel Clay and Asse Member are larger than in the neighbouring layers (Figure 7.5).

7.4 Loading by ice

At the beginning of a loading simulation, the model is in the initial state of stresses and pore pressures, which were imposed as described in the previous Section. The initial state is characteristic for a pre-glacial period with the permafrost. Glaciation starts with the loading of the model by ice. Simulation results obtained by running three ice-loading scenarios, described in Section 7.2.4, on the detailed hydromechanical model are presented and discussed below.

7.4.1 Stress and deformation

Changes in the effective vertical stress, pore pressure and vertical displacement along a vertical section running through the location of a potential repository site are shown in Figure 7.6 to Figure 7.8. In all cases is the increase in the effective vertical stress delayed with respect to the increase in the ice load. For example, after 350 years the ice load has reached its maximum value while the effective vertical stress is still about one half of the load being applied (Figure 7.6a to Figure 7.8a). The pore water in the aquifers and aquitards takes over a significant part of the ice load (Figure 7.6b to Figure 7.8b). As the time progresses the pore pressure continuously decreases and the effective stress builds up. At the end of the simulations, the effective stress has increased for the full amount of the maximum applied ice load (1MPa) and the pore pressure has returned to the initial state.

The equalisation of the effective stresses in the aquitards over time is much slower. The response of the Rupel Clay and Asse Member depends not only on their hydraulic conductivity but also on the material model used. For example, in the case of the Mohr-Coulomb model ($K=3 \times 10^{-12}$ m/s) the stress equilibrium has been achieved practically after about 1000 years (the upper anomaly in graphs on Figure 7.6a,b). In the case of the Modified Cam-Clay model and the same value of the hydraulic conductivity as above the equalisation of the effective stresses and simultaneous decrease in the pore pressure last far longer and likely extend over the whole duration of simulation, i.e. over the whole glaciated period (Figure 7.7a,b). In the case of the Modified Cam-Clay model and high hydraulic

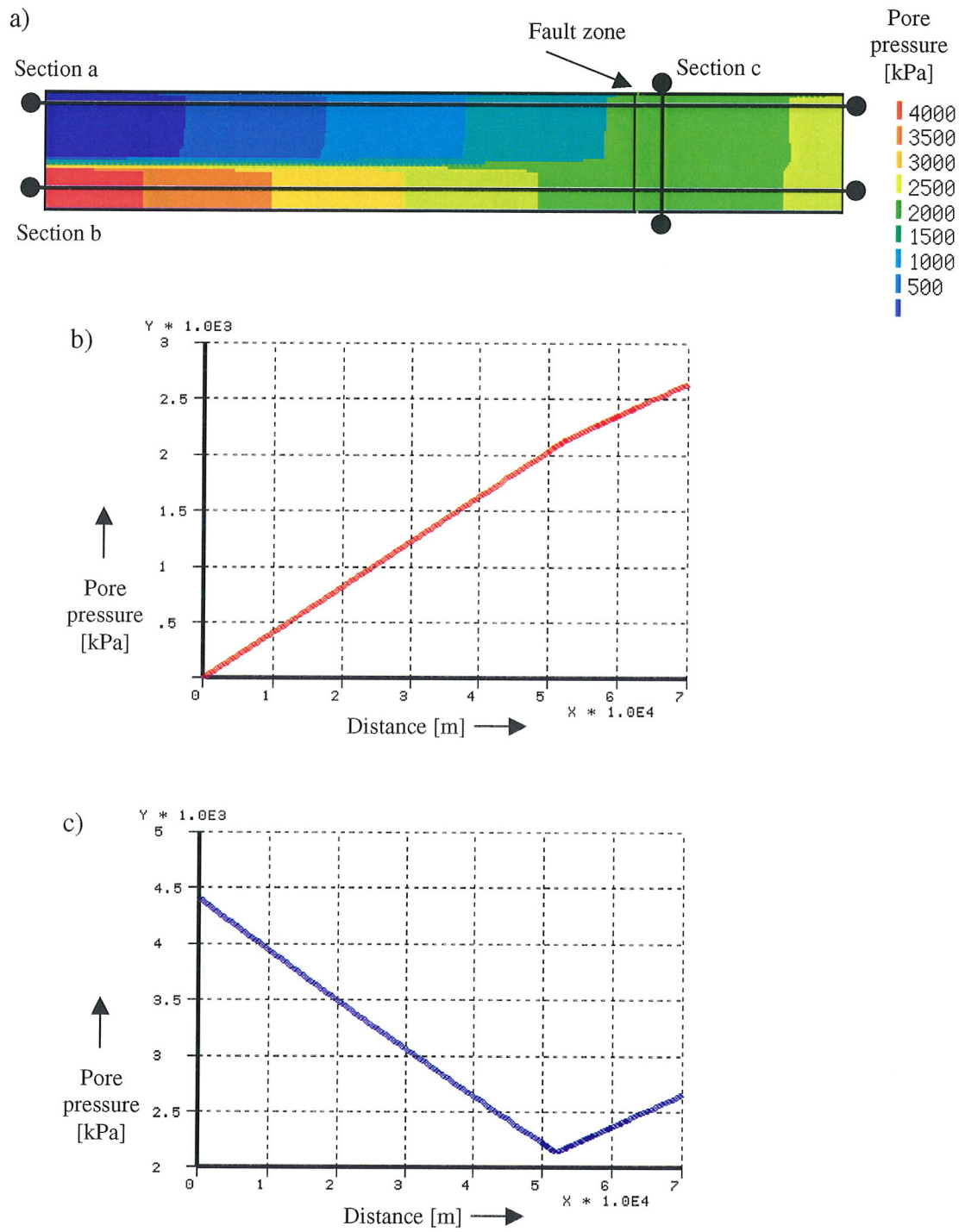


Figure 7.4 Initial hydrodynamic pore pressures a) in the detailed hydromechanical model, b) along a horizontal section a through the Top (Tertiary and Quaternary) aquifer, and c) along a horizontal section b through the Mesozoic aquifer. Note the influence of a high permeable fault zone on the distribution of the pore pressure.

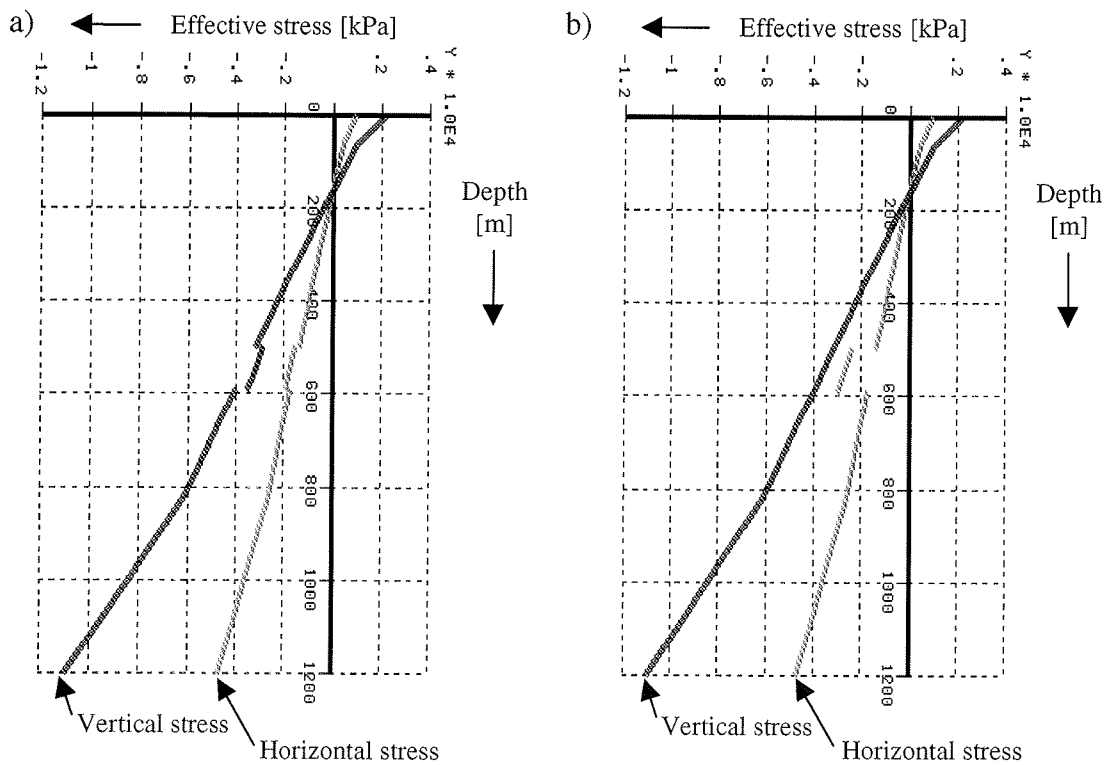


Figure 7.5 Initial effective stresses in the model along a vertical section *c* shown in Figure 7.4. The Rupel Clay and Asse Member are modelled by a) the Mohr-Coulomb material model and b) by the Modified Cam-Clay material model.

conductivity ($K=1 \times 10^{-11}$ m/s) the response of the Rupel Clay and Asse Member is similar to that obtained by using the Mohr-Coulomb model (Figure 7.8a,b).

The total settlement caused by the ice loading amounts to about 20 m (Figure 7.6c to Figure 7.8c). The Young's moduli of the model units were empirically estimated (Section 7.2.2) and they are generally higher than in the case of the simplified hydromechanical model. Consequently, the calculated settlement rates are here lower than in the case of the simplified hydromechanical model.

7.4.2 Plasticity

Geomechanical parameters of the material model for the Rupel Clay and Asse Member were determined by a series of laboratory tests (TRUCK II, 1999). As the experimental programme of the TRUCK II project and the TRACTOR project were running simultaneously with the numerical modelling study presented here,

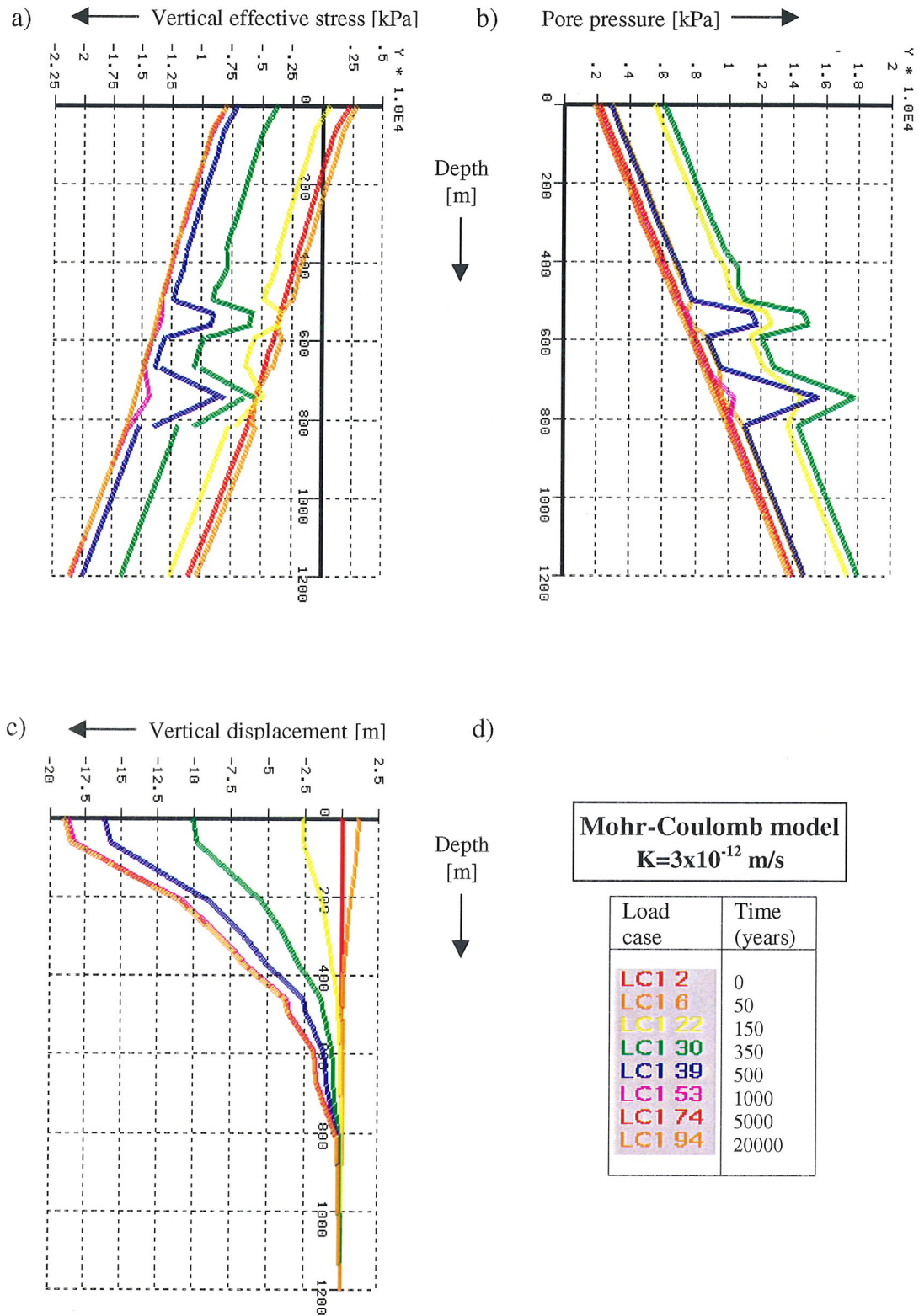


Figure 7.6 a) Vertical effective stress, b) pore pressure, and c) vertical displacement with depth along a vertical section c shown in Figure 7.1 (Mohr-Coulomb model).

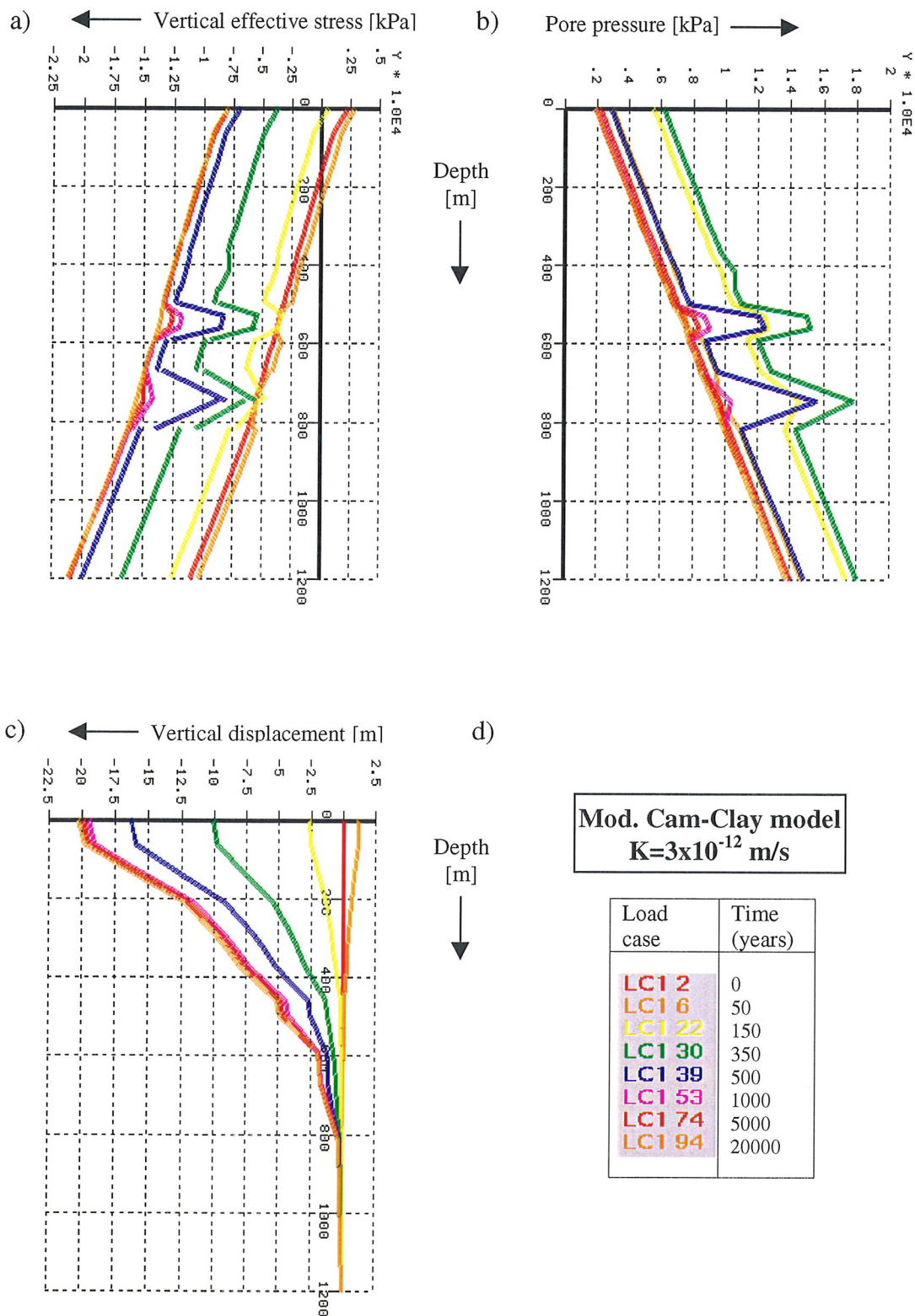


Figure 7.7 a) Vertical effective stress, b) pore pressure, and c) vertical displacement with depth along a vertical section c shown in Figure 7.1 (Cam-Clay model) Average values of the Cam-Clay parameters were used. ($\phi=15^\circ$, preconsolidation stress, $p_c'=10.35$ MPa; see Section 7.2.4).

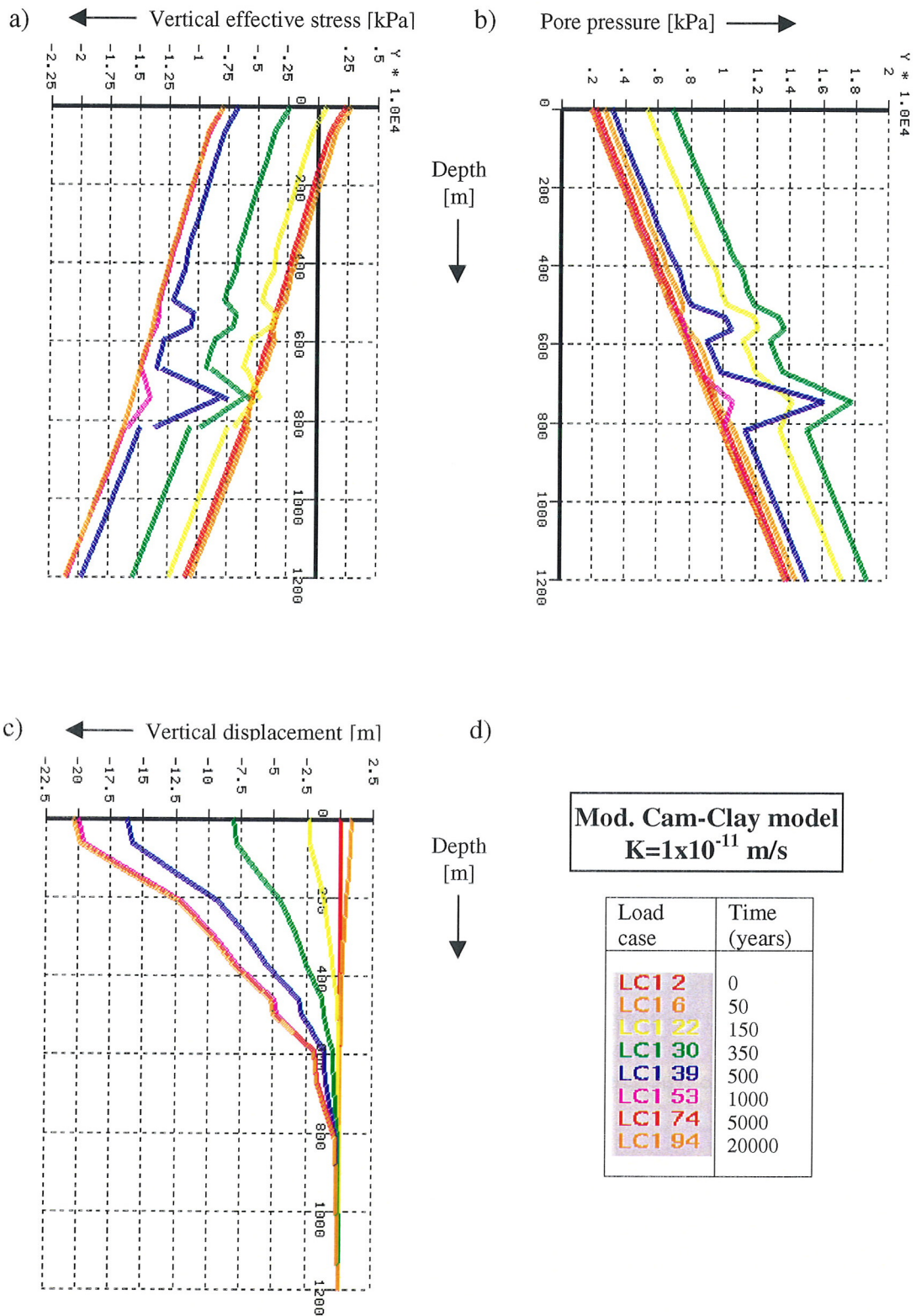


Figure 7.8 a) Vertical effective stress, b) pore pressure, and c) vertical displacement with depth along a vertical section c shown in Figure 7.1 (Cam-Clay model). Low values of the Cam-Clay parameters were used ($\phi=12^\circ$, preconsolidation stress, $p_c'=6.9$ MPa; see Section 7.2.4).

not all the laboratory test had been completed at the time when the modelling study started. The input parameters for the detailed hydromechanical model were therefore derived from the partially available lab test results. The range of values of the angle of internal friction and the cohesion are generally lower than it would be expected for overconsolidated clay located at a depth of 500 m. The consequence of low values of the model parameters is the appearance of plastic deformations in the Rupel Clay and Asse Member during early phases of loading by the ice.

In the scenario with the Mohr-Coulomb model for the Rupel Clay and Asse Member, the values of the Mohr-Coulomb parameters are relatively low. This caused development of the plasticity throughout the Rupel Clay and Asse Member during initialisation of the stresses. Figure 7.9 shows that the point that represents the initial stress in element 1177 lies on the Mohr-Coulomb failure line. The initial stress is thus sufficiently large to induce shear failure in the clay. This has been confirmed during initialisation of the stresses in the model when the Rupel Clay and Asse Member have been affected almost completely by plastic deformation.

In both scenarios with the Modified Cam-Clay model for the Rupel Clay and Asse Member initialisation of the stresses in the model does not cause plastic deformation of the clay. This is illustrated by the p' - q' diagram in Figure 7.10 (p' – isotropic stress, q' – deviatoric stress; for definition of these parameters see DIANA User's Manual or a textbook on soil mechanics, e.g. Britto & Gunn, 1987). The point that represents the initial stress in element 1177 lies within the yield locus and below the critical state line. This indicates that the plasticity does not occur during initialisation of stresses and that the initial deformation of the clay during loading by the ice is elastic.

During loading by the ice the effective stress continuously changes defining an effective stress path as shown in Figure 7.11. In both cases shown in the figure the effective stress paths for element 1177 increase from the initial position and reach the critical state line. The stress path then steadily decreases following the elliptical yield locus.

For a low value of the friction angle ($\phi=12^\circ$) of the Rupel Clay and Asse Member, initial elastic strain is likely followed by plastic strain before the material begins to yield (Figure 7.11a). For average values of the Cam-Clay parameters ($\phi=15^\circ$ and preconsolidation stress $p_c'=10.35$ MPa) the stress path reaches the critical state line approximately at the top of the initial yield locus (Figure 7.11b and Figure 7.10b) suggesting that the initial elastic strain is immediately followed by the yielding.

Development of plastic deformation in the Rupel Clay and Asse Member is illustrated by a few snap-shots in Figure 7.12. Plastic strain, which indicates

yielding of the clay, is evident throughout the whole clay layer after 1000 years from the beginning of glaciation.

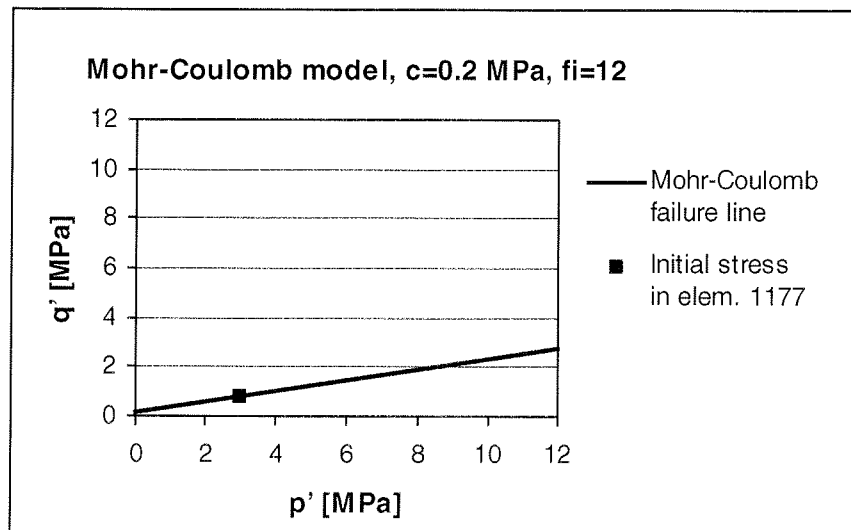


Figure 7.9 Mohr-Coulomb material model for the Rupel Clay and Asse Member used in an ice-loading scenario. The initial stresses in element 1177, which is located in the middle of the clay layer, cause plastic deformation of the element. Legend: p' – isotropic stress, q' – deviatoric stress.

7.4.3 Groundwater flow in aquifers

The pattern of groundwater flow in a pre-glacial period is considerably affected by an increased lateral influx into the model, presence of the permafrost and presence of a highly permeable vertical fault zone. Calculated pre-glacial groundwater velocity field shows that the fault zone acts as a drainage path which allows upward flow of groundwater from the Mesozoic aquifer towards the Top (Quaternary and Tertiary) aquifer (Figure 7.13, 0 years). This releases the pore pressure in the Mesozoic aquifer (Figure 7.14b, 0 years).

During glaciation the groundwater velocity field and the pore pressure field dynamically change. Loading of the aquifers by the ice pushes the ground water ahead of the ice margin and accelerates the groundwater flow. Horizontal groundwater velocities increase for at least one order of magnitude with respect to the pre-glacial period (Figure 7.13). The pore pressure in both aquifers also increases with an increase in the ice load (Figure 7.14). The pattern of the pore pressure field is additionally influenced by the vertical meltwater recharge, which flattens down the pore pressure curves.

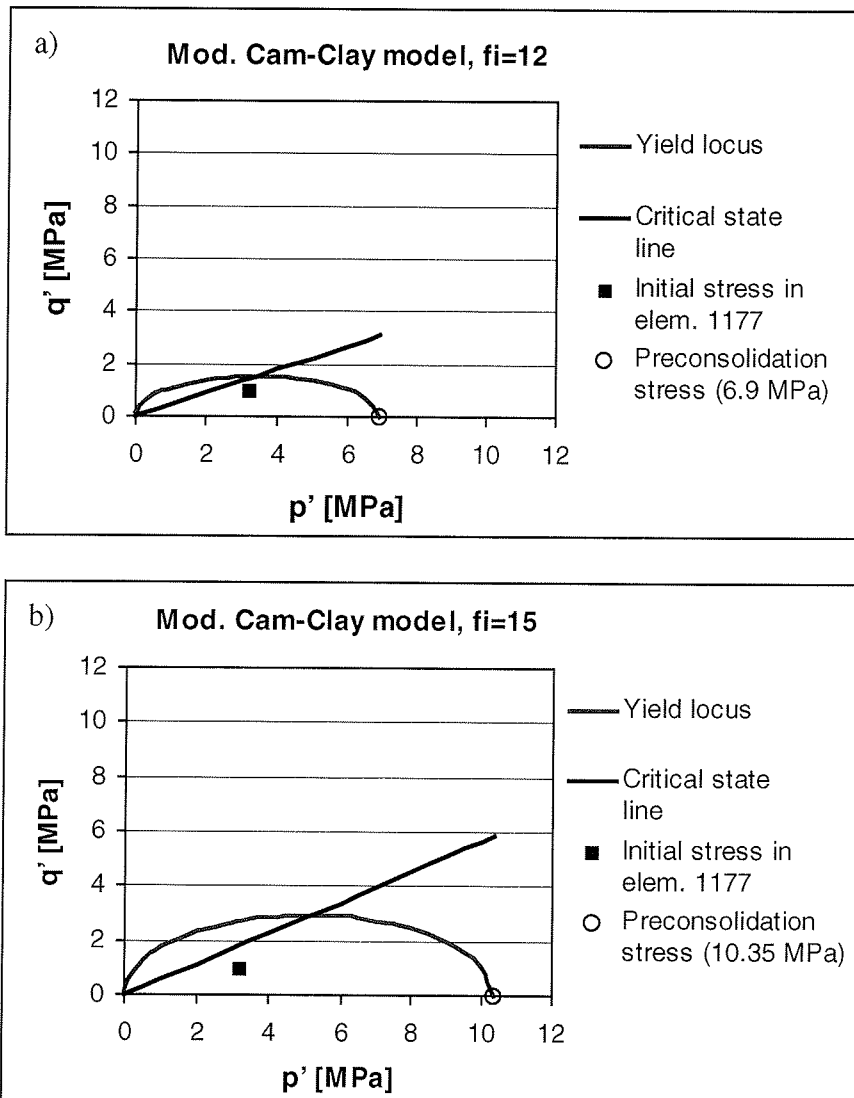


Figure 7.10 Modified Cam-Clay material model for the Rupel Clay and Asse Member used in two ice-loading scenarios. a) Scenario with low parameters ($\phi=12^\circ$, preconsolidation stress $p_c'=6.9$ MPa), b) scenario with average parameters ($\phi=15^\circ$, $p_c'=10.35$ MPa). The initial stresses in element 1177, which is located in the middle of the clay layer, do not cause plastic deformation of the element. Legend: p' – isotropic stress, q' – deviatoric stress.

An increase in the groundwater velocity and pore pressure in the aquifers is limited to the period during which the magnitude of the ice load being applied increases.

This is because the consolidation of highly permeable sediments occurs practically instantaneously with the application of the load. Once the maximum ice load has been reached, the pore pressure steadily decreases until it eventually reaches the

initial pre-glacial state. The response of the Mesozoic aquifer is in this respect somewhat slower than the response of the Top (Quaternary and Tertiary) aquifer.

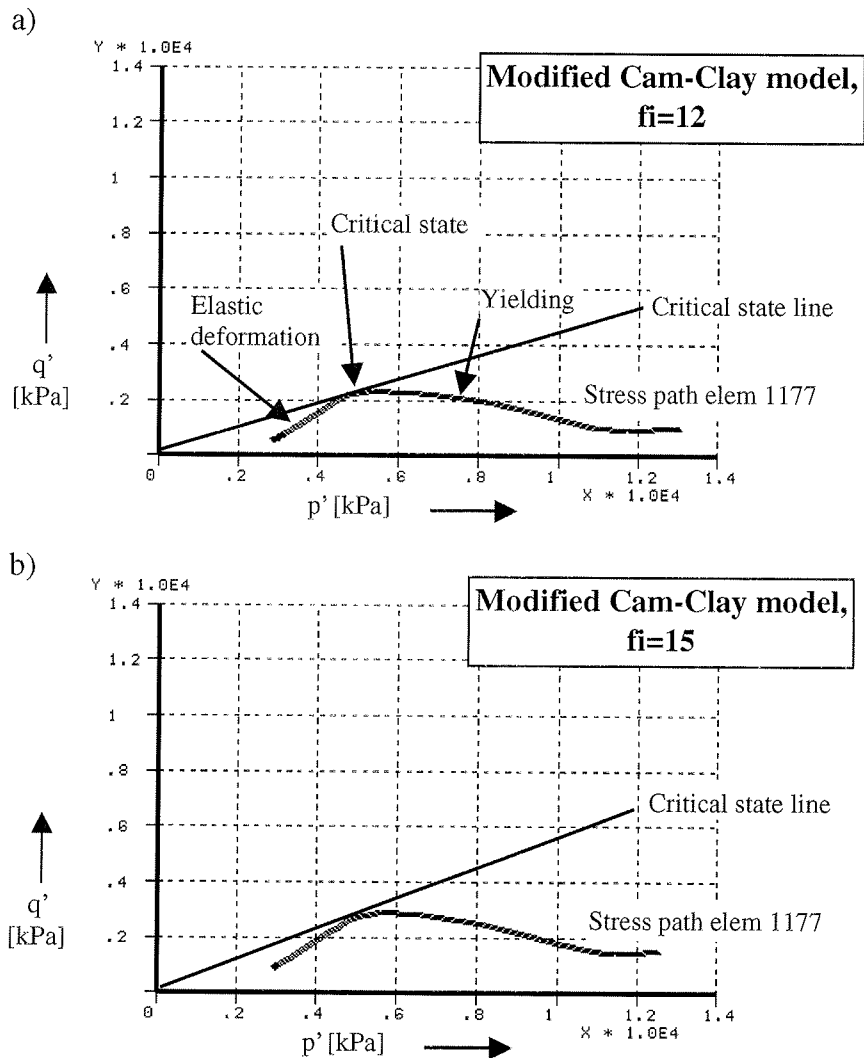


Figure 7.11 Effective stress path for element 1177 located in the middle of the Rupel Clay and Asse Member. a) Ice-loading scenario with low Cam-Clay parameters: $\phi=12^\circ$, preconsolidation stress $p_c'=6.9$ MPa. b) Scenario with average parameters: $\phi=15^\circ$, $p_c'=10.35$ MPa. Legend: p' – isotropic stress, q' – deviatoric stress.

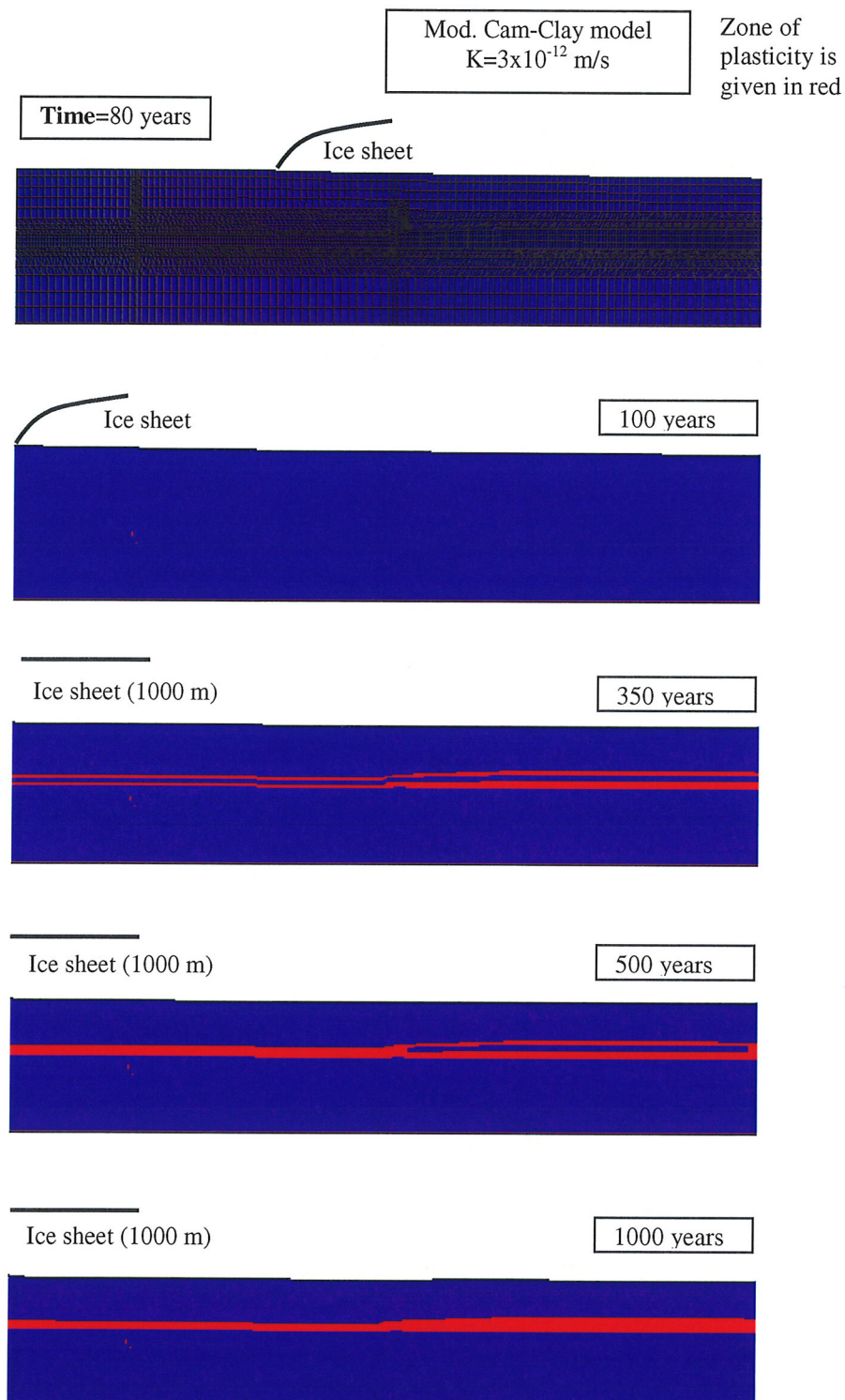


Figure 7.12 Formation of the plasticity zone in the Rupel Clay and Asse Member modelled by a Cam-Clay model.

7.4.4 Groundwater flow in aquitards

In the present-day situation and during the period of pre-glaciation the pore water flow in the Tertiary clays is governed by the hydraulic and pressure gradients between the Tertiary/Quaternary aquifer above and Tertiary Brussel sand below the clays. As the permeability of the aquitard is generally very low, the velocities of pore water flow will also be very low. Calculated velocities of the pore water in the Rupel Clay and Asse Member in element 1177 amount to 4×10^{-7} m/year, assuming that the hydraulic conductivity of the clay is $K=3 \times 10^{-12}$ m/s. The velocity vectors are directed downwards as the pore pressure in the overlying aquifer (the Voort model unit) exceeds the pressure in the underlying aquifer (the Brussel model unit).

During glaciation, the consolidation-driven flow becomes a dominant factor that influences the overall pattern of the pore water flow in the clay. Consolidation-driven flow is generally vertical upwards or downwards, as the overpressurised pore water in the clay follows the shortest path towards the over- or underlying aquifer. During glaciation, the velocity of the vertical flow in the Rupel Clay and Asse Member increases a few orders of magnitude with regard to the pre-glaciated period.

Dynamics of the consolidation-driven flow in element 1177 is shown in Figure 7.15. Important differences in the magnitude and duration of the consolidation-driven flow can be observed between the calculated ice-loading scenarios. The maximum magnitude of the groundwater velocity ranges between 1.2 and 2.2 mm/year, while the duration of the consolidation process varies from 2000 to 20000 years.

In the scenario with the Mohr-Coulomb model the consolidation process lasts for about 2000 years (Figure 7.15a). This scenario is assumed to be the least reliable as the plastic strain and yielding already occur in the pre-glaciated period during initialisation of the stresses. This is unlikely to happen in natural conditions having in mind that the Tertiary clays at greater depths (>500 m) are stiff and likely overconsolidated (GeoDelft, 1999). Simulations of the ice loading by using such a model with the initiated stresses and the plasticity is therefore also questionable.

The scenario with the average values of the Cam-Clay parameters and $K=3 \times 10^{-12}$ m/s results in the longest duration of consolidation. The ground water velocities are increased over the whole glaciated period of 20,000 years (Figure 7.15b). The scenario with the low values of the Cam-Clay parameters and $K=1 \times 10^{-11}$ m/s results in increased velocities. Duration of consolidation is far shorter and does not exceed 2000 years (Figure 7.15c). Shorter consolidation is a consequence of higher hydraulic conductivity of the Rupel Clay and Asse Member.

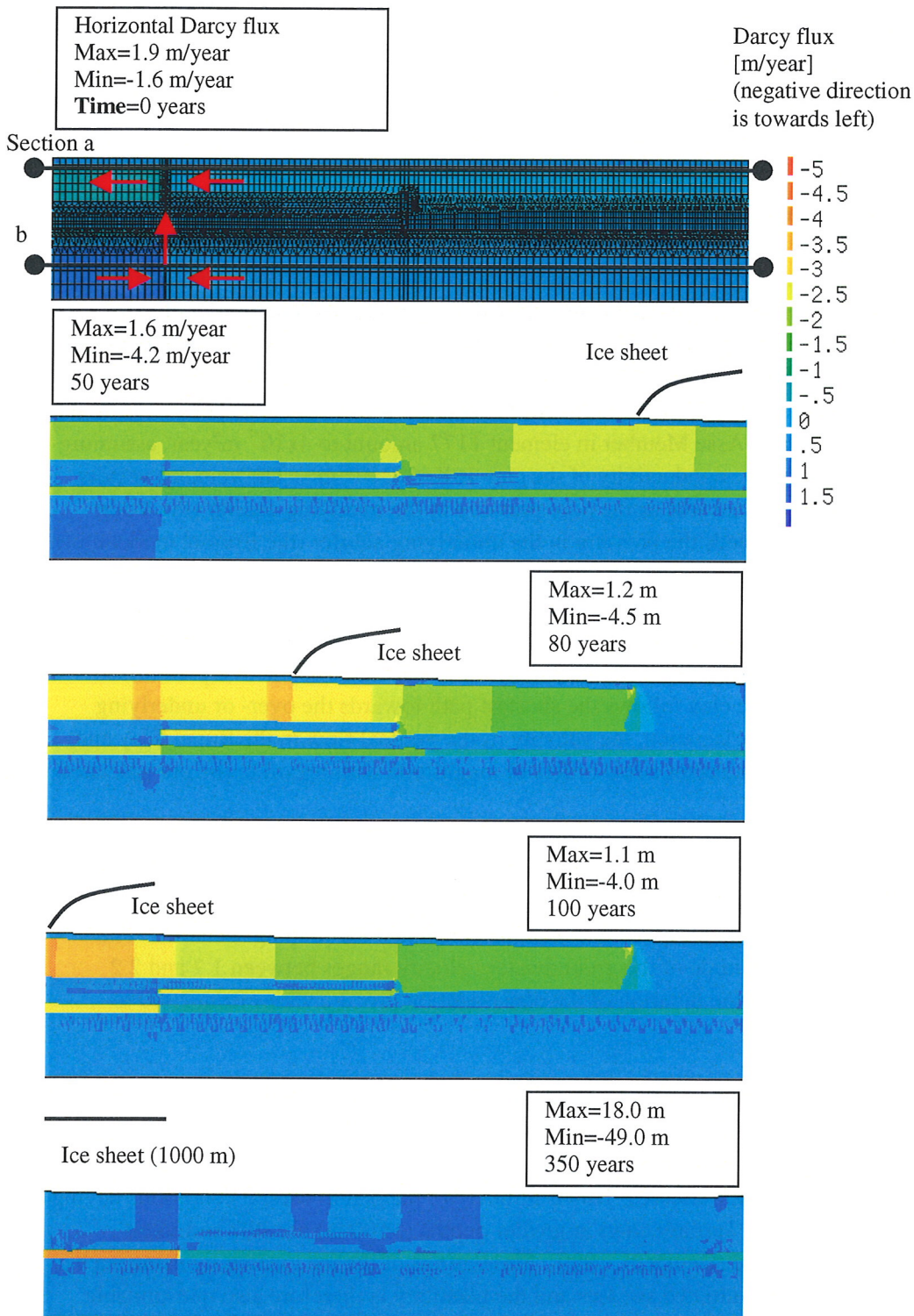


Figure 7.13 Horizontal Darcy flux shown for a 10 km long refined part of the detailed hydromechanical model. Location of the refined part of the model is shown in Figure 7.1.

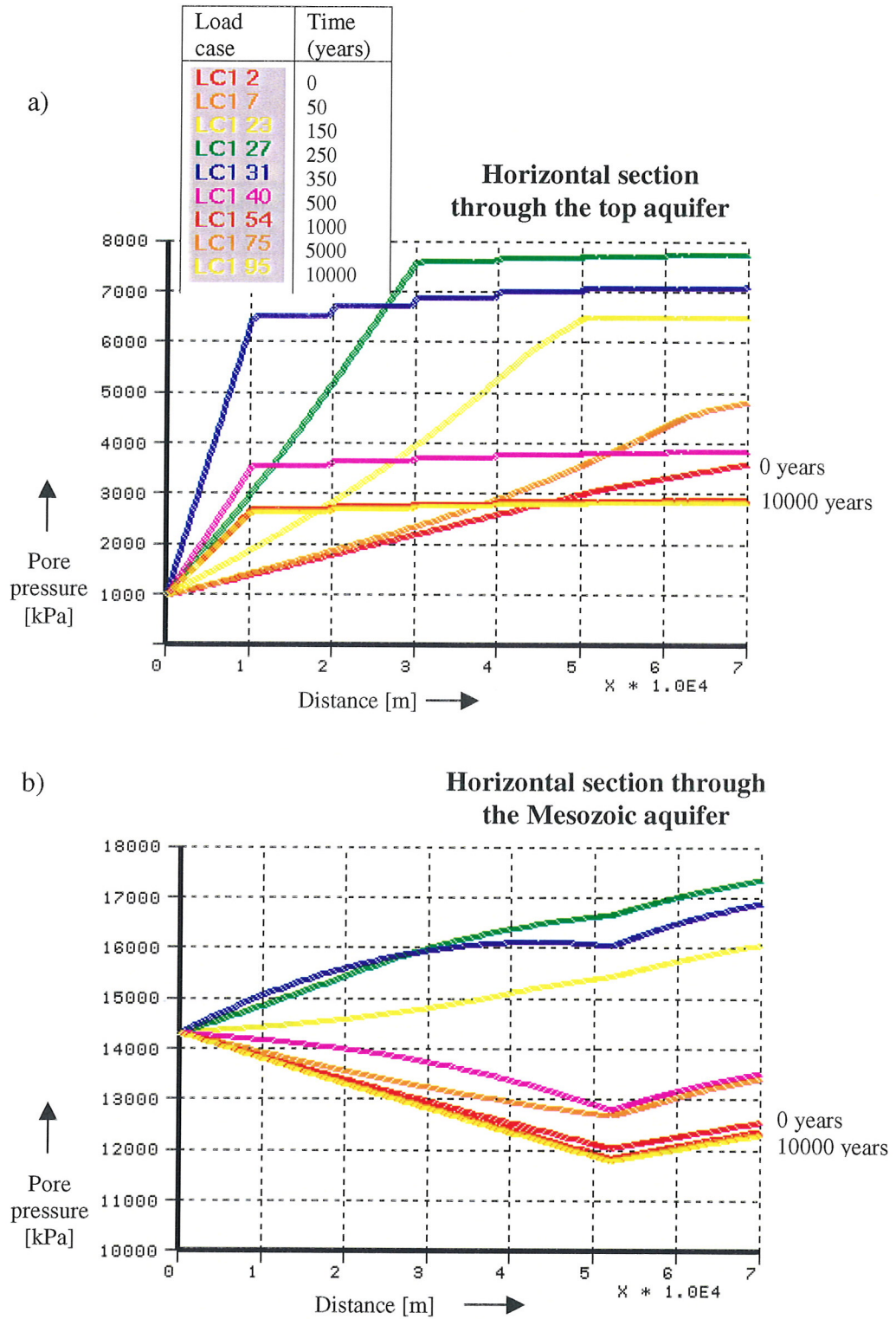


Figure 7.14 Pore pressure along horizontal sections through a) the Top (Quaternary and Tertiary) aquifer, and b) the Mesozoic aquifer during glaciation. Location of the sections for which the pore pressure is shown is given in Figure 7.13.

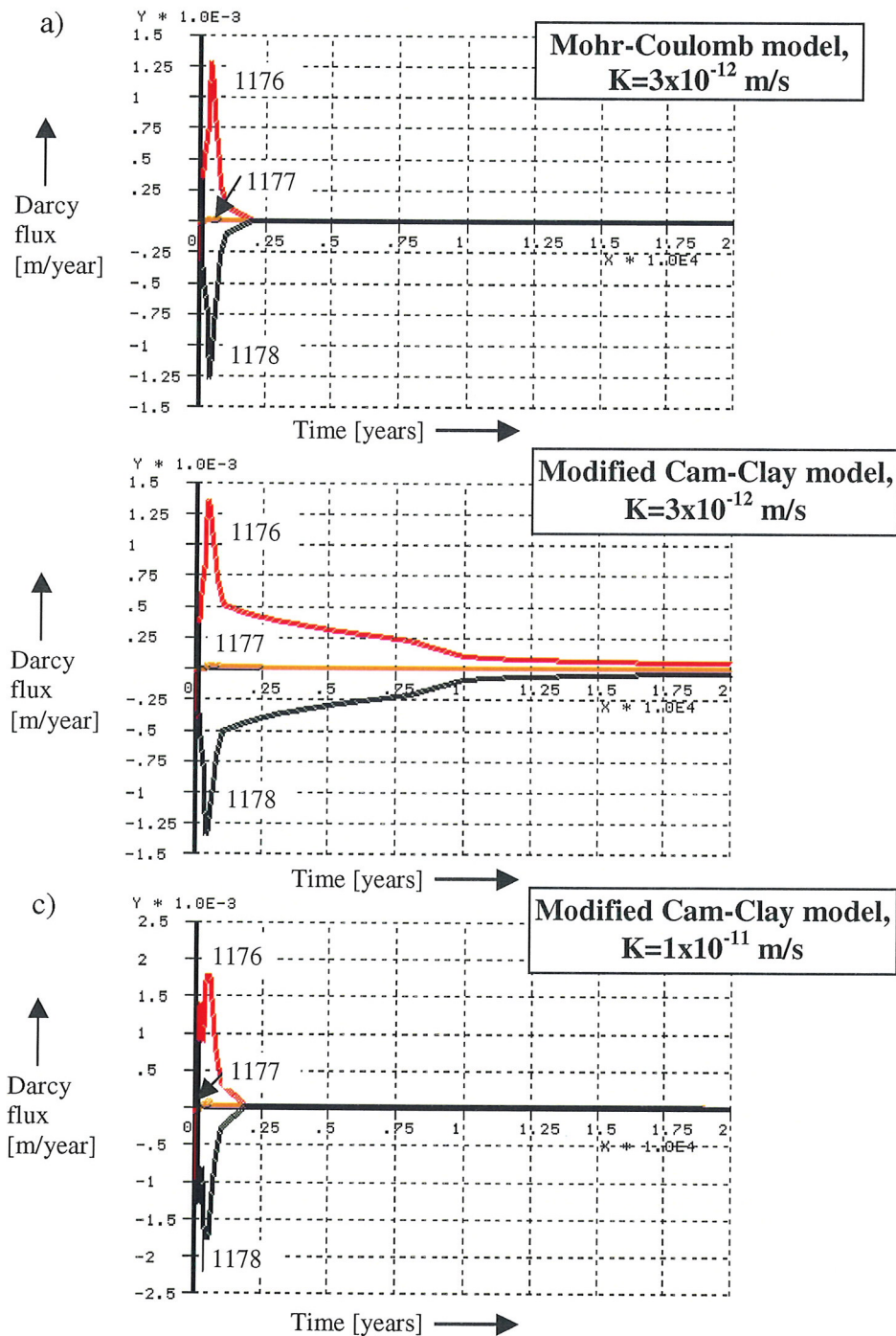


Figure 7.15 Vertical Darcy flux in the Rupel Clay and Asse Member during glaciation. The material model and hydraulic conductivity (K) of the clay were varied as follows: a) the Mohr-Coulomb model and $K=3 \times 10^{-12}$ m/s, b) the Modified Cam-Clay model and $K=3 \times 10^{-12}$ m/s, and c) the Modified Cam-Clay model and $K=1 \times 10^{-11}$ m/s. For the location of elements for which the flux is shown see Figure 7.1.

7.4.5 Preparation of the groundwater velocity fields for the transport model

Three representative groundwater velocity fields were defined for the transport model (Figure 7.16). These fields characterise:

- the present-day situation (i.e. reference case),
- the pre-glaciation period with the permafrost and increased fluxes,
- the glaciation period.

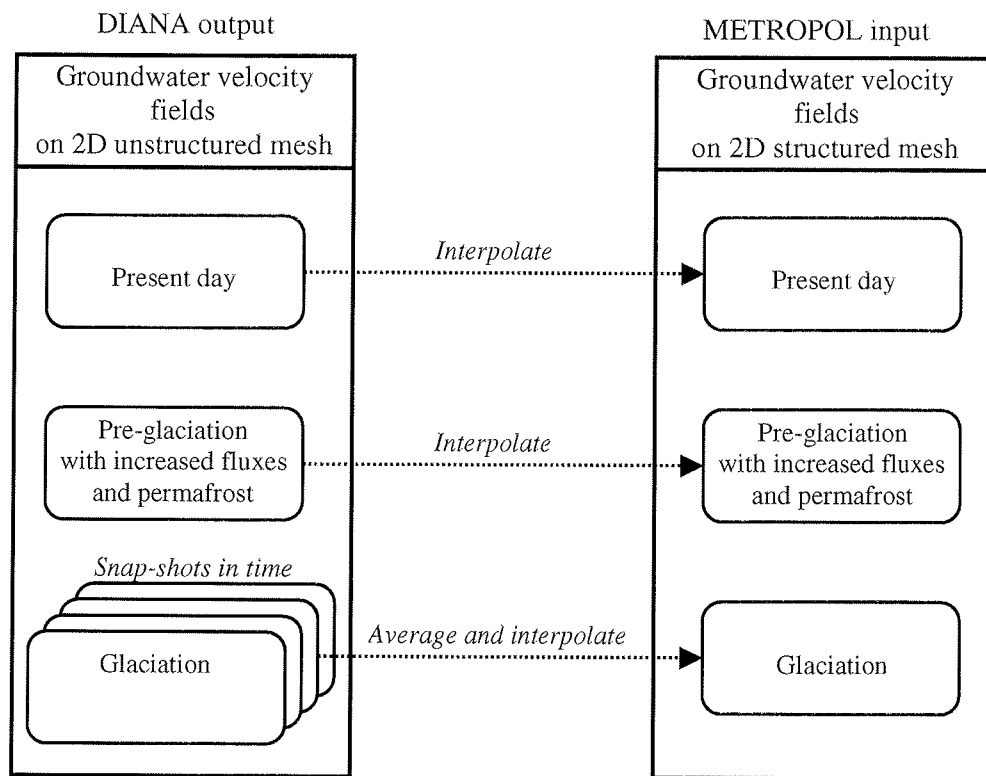


Figure 7.16 Preparation of the groundwater velocity fields, calculated by the detailed hydromechanical model (Diana), for the transport model (METROPOL).

Present day groundwater velocity field is calculated by imposing a low lateral influx in the model caused by a small, present-day hydraulic gradient ($i = 5 \times 10^{-4}$).

Pre-glaciated groundwater velocity field is characterised by an increased lateral influx into the model and the presence of permafrost, which extends over the whole model. The pre-glaciated velocity field is calculated from the detailed

hydromechanical model by initialising the initial stresses and pore pressure in the model.

The groundwater velocity field during ice loading is obtained by averaging a number of snap-shots taken from the transient simulations. These three representative groundwater velocity fields will be used to define the scenarios for the calculation of radionuclide migration as discussed in the following chapter.

Each of the three scenarios runs has resulted in a set of three groundwater velocity fields. Each of the three velocity fields was then converted, i.e. mapped, from a Diana unstructured mesh to a METROPOL structured mesh. The data conversion was carried out for a 10 km long refined part of the hydromechanical model. Conversion included interpolation of the components of the Darcy velocity at each node of the METROPOL mesh. The nearest neighbour interpolation technique was used as the density of the input Diana mesh was far greater than the density of the METROPOL mesh. The interpolation was geologically controlled. This means that, in order to be considered in the interpolation, data from which interpolation is to be carried out must belong to the same geological unit (i.e. model unit) as the node to be estimated.

8 Migration of radionuclides

8.1 Introduction

In this chapter we describe the simulations with the program METROPOL-4, developed at the RIVM (National Institute of Public Health and Environmental Protection, Bilthoven, The Netherlands). A description of the program is given in Section 8.2, the description of the input in Section 8.3, the results in Section 8.3.2, and the discussion is presented in Section 8.5.

8.2 Description of METROPOL-4

The following is taken from the User's Guide of METROPOL-4 (Sauter *et al.*, 1993). METROPOL-4 is a program for the simulation of the transport of tracers (low concentration solutes) by groundwater. METROPOL-4 computes mass fractions of the solutes, taking into account linear adsorption and decay. The flow field is given by the user, e.g. as a uniform flow or as a result of earlier computations of METROPOL-1, -2, -3, or by an other program. The mass balance equation for a tracer reads, for n and ρ constant in

$$Rn\rho \frac{\partial \omega}{\partial t} = \nabla \cdot (\rho D \cdot \nabla \omega) - \nabla \cdot (\rho q \omega) - Rn\rho \omega + \rho_{in} \omega_{in} I_{in} - \rho \omega I_{ex} + R_{prod} \quad (8.1)$$

where:

- R = retardation factor [1],
- n = porosity [1],
- ρ = liquid density [kg/m^3],
- ω = mass fraction of the tracer in the system [1],
- t = time [y],
- q = Darcy velocity vector [m/y],
- J = dispersive/diffusive mass flux vector [kg/m^3],
- λ = decay rate [1/y],
- ρ_{in} = density of injected fluid [kg/m^3],
- ω_{in} = mass fraction of the tracer in the injected fluid [1],
- I_{in} = injection rate of fluid [1/y],
- I_{ex} = extraction rate of fluid [1/y],
- R_{prod} = production rate for the tracer per unit volume, i.e. the production of mass by decay of the mother nuclide in a decay chain [$\text{kg}/\text{m}^3/\text{y}$],
- D = dispersive/diffusive tensor [m^2/y].

The dispersive/diffusive mass flux J is given by Fick's Law:

$$J = -\rho D \cdot \nabla \omega \quad (8.2)$$

The dispersive/diffusive tensor is defined in the classical way as a function of the Darcy velocity and the longitudinal and transversal dispersivities. The effective molecular diffusion D_m is included in the dispersive/diffusive tensor:

$$D_{xx} = D_m + (\alpha_l - \alpha_t) \frac{q_x^2}{|q|} + \alpha_t |q|, \quad (8.3)$$

$$D_{yy} = D_m + (\alpha_l - \alpha_t) \frac{q_y^2}{|q|} + \alpha_t |q|,$$

$$D_{zz} = D_m + (\alpha_l - \alpha_t) \frac{q_z^2}{|q|} + \alpha_t |q|,$$

$$D_{xy} = D_{yx} = (\alpha_l - \alpha_t) \frac{q_x q_y}{|q|},$$

$$D_{xz} = D_{zx} = (\alpha_l - \alpha_t) \frac{q_x q_z}{|q|},$$

$$D_{yz} = D_{zy} = (\alpha_l - \alpha_t) \frac{q_y q_z}{|q|},$$

where:

- D_{xx}, \dots, D_{zy} = components of dispersive/diffusive tensor [m^2/y],
- D_m = effective molecular diffusion coefficient [m^2/y],
- α_l = longitudinal dispersivity [m],
- α_m = transversal dispersivity [m],
- q_x, q_y, q_z = x, y, z components of Darcy velocity [m/y],
- $|q|$ = length of the Darcy velocity vector [m/y].

Adsorption is taken into account by the retardation factor, which is given by the relation:

$$R = 1 + K_d \frac{1-n}{n} \rho_r \quad (8.4)$$

where:

$$\begin{aligned}\rho &= \text{rock density [kg/m}^3\text{]}, \\ K_d &= \text{adsorption distribution coefficient [m}^3\text{/kg]}.\end{aligned}$$

The porosity and liquid density may vary in space but are constant in time. They are computed according to the following constitutive equations:

$$\rho = \rho_0 \exp(\beta(p - p_0) + \gamma\omega_s), \quad (8.5)$$

$$n = n_0 \exp(C_r(p - p_0)), \quad (8.6)$$

where:

$$\begin{aligned}\rho_0 &= \text{reference density [kg/m}^3\text{], at pressure } p = p_0 \text{ and salt mass} \\ &\quad \text{fraction } \omega_s = 0, \\ \beta &= \text{liquid compressibility [m.y}^2\text{/kg]}, \\ p_0 &= \text{reference pressure [kg/m.y}^2\text{]}, \\ \gamma &= \text{constant relating density with salt mass fraction [1]}, \\ \omega_s &= \text{salt mass fraction [1]}, \\ n &= \text{reference porosity at } p = p_0 \text{ [1]}, \\ C_r &= \text{compressibility of the rock matrix [m.y}^2\text{/kg]}.\end{aligned}$$

Retardation factors and decay constants can vary in space and are different for the different tracers. Sources and sinks are point sources and point sinks, respectively and must be located in nodal points. The velocity field is stepwise constant in time. It is possible to specify a no flow boundary and to fix the mass fraction at the boundary. A constant mass flux at the boundary can be simulated by introducing point sources at this boundary.

8.3 Input description

8.3.1 METROMESH and METROREF

A representative subsurface window of horizontal extension of 10 km, and vertical extension of 1200 m has been considered. This cross-section is copied from part of the hydromechanical model (see Section 7.2). The transversal extension was chosen as 150 m. A coarse mesh was created by METROMESH, with 6*3*10 layers (in the horizontal *X*-direction, transversal *Y*-direction and vertical *Z*-direction, respectively). The 10 vertical layers follow the geological structure defined for the hydromechanical model. With the program METROREF the mesh has been refined to 57*4*22 elements, giving 5016 elements and 6670 nodal

points. In each horizontal layer there are 228 elements and 290 nodal points. This refinement has been more intense in that part of the domain where most of the nuclide-transport in the chosen time frame will take place.

Moreover, the middle clay layer BR&VE stops at 6070 m, the clay-layer RU&AS becomes thicker between $X = 6000$ m and $X = 10000$ m. At the location $X = 2000$ m, a fault has been modelled with horizontal extension of 1 m. The structure of the finite element mesh is presented in Table 8.1.

Table 8.1 Structure of the finite element mesh used for the transport simulations. The shortened names of the geological units are explained in Section 6.2.

X [m]	X [m]	Number of sub-layers	Width per sub-layer [m]	
0	2000	5	400	
2000	2001	1	1	Fault with name ZONE_BR
2001	6000	40	99.975	
6000	6070	1	70	
6070	8000	5	386	
8000	10000	5	400	

Y [m]	Y [m]	Number of sub-layers	Width per sub-layer [m]
0	50	1	50
50	100	2	22.5
100	150	1	50

Z [m]	Z [m]	Name	Number of sub-layers	Height per sub-layer [m] ($0 \leq X \leq 6000$ m)
0	-60	KWAR	1	60
-60	-210	HA&MA	2	75
-210	-290	OOST	1	80
-290	-370	BRE_Z	2	40
-370	-460	BR&VE	2	45
-460	-500	VOORT	3	13.333
-500	-590	RU&AS	4	22.5
-590	-670	BRUS	2	40
-670	-820	IP&LA	2	75
-820	-1200	MESOZ	3	126.666

For $6000 \text{ m} \leq X \leq 10000 \text{ m}$, the width of the layers depends on the position, because the clay-layer RU&AS thickens for increasing X .

In the area where the nuclides are thought to be stored ($X = 4005$ m, $Y = 75$ m, $Z = 545$ m) the horizontal dimension of the elements is $3999 \text{ m} / 40 = 99.975$ m, the vertical dimension is 22.5 m and the lateral dimension is 25 m (see above). See Figure 8.1.

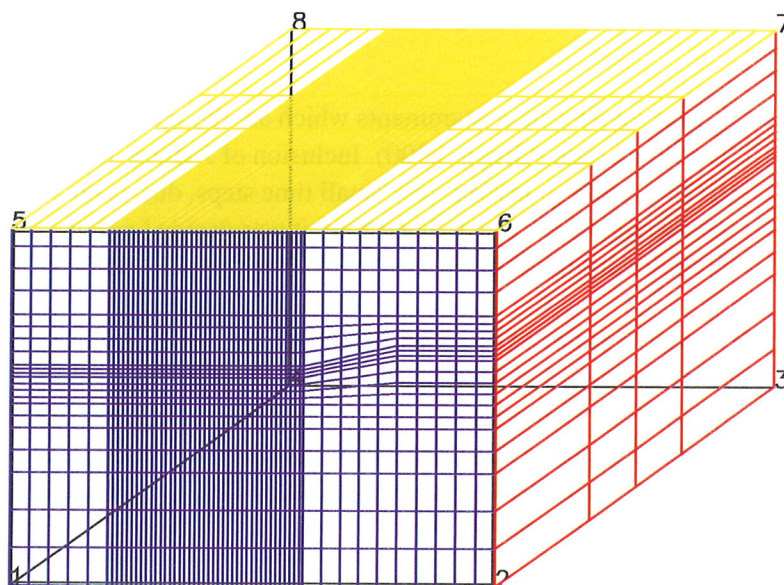


Figure 8.1 Mesh used in the transport model.

8.3.2 METROPOL-4

For the three runs with METROPOL-4 the following input has been compiled. Below are given the relevant record names from the input description.

Mathematics

MATH2:

JODE = 3

i.e. the program determines size based on the required precision.

EPSODA = 1.10^{-10}

i.e. the absolute precision.

EPSODR = 1.10^{-2}

i.e. the relative precision.

MATH3:

TSTEP = 5.10^{-1}

i.e. the initial time step [year].

DTMIN = 1.10^{-1}

i.e. the minimal time step [year].

DTMAX = 2.10^4

i.e. the maximal time step [year].

Contaminants

CON1:

NCONT = 17 *i.e.* the number of contaminants which are thought to be the most important (Grupa, 2000). Inclusion of Jodium-129 (I129) caused to invoke very small time steps, due to the retardation factor $R = 1$. Therefore, it was decided not to consider this nuclide.

CON2:

The following nuclides and chains have been considered as suggested by Grupa (2000). The half-life values are specified (principal source Nichols & Hunt (1999), secondary source Hacker (1997)). The half-life of Se79 is a rather uncertain, because the two sources give different values. It turned out that there exists some confusion about this half-life value in the literature (Nichols, 2000). The choice has been made for the value $6.5 \cdot 10^4$ y (Grupa, 2000).

Nuclide	Half-life [y]	Name of chain
Am243	$7.37 \cdot 10^3$	Americium chain
Pu239	$2.4113 \cdot 10^4$	Americium chain
U235	$7.038 \cdot 10^8$	Americium chain
Pa231	$3.2760 \cdot 10^4$	Americium chain
Sn126	$1.0 \cdot 10^5$	
Se79	$6.5 \cdot 10^4$	
Am241	$4.327 \cdot 10^2$	
Pu242	$3.735 \cdot 10^5$	
Cm246	$4.75 \cdot 10^3$	
Cm245	$8.5 \cdot 10^3$	Neptunium chain
Np237	$2.14 \cdot 10^6$	Neptunium chain
U233	$1.5925 \cdot 10^5$	Neptunium chain
Th229	$7.34 \cdot 10^3$	Neptunium chain
U238	$4.468 \cdot 10^9$	Uranium-Radium chain
U234	$2.457 \cdot 10^5$	Uranium-Radium chain
Th230	$7.54 \cdot 10^4$	Uranium-Radium chain
Ra226	$1.6 \cdot 10^3$	Uranium-Radium chain

In the following Table 8.2 the retardation factor R [1] (Grupa & Houkema, 2000, Table 3.4) and the distribution coefficient K_d [m^3/kg] is given. METROPOL-4 requires K_d , while the R has been specified for the clay (= aquitards). The relation between R , K_d , ρ_r and n is given by formula (8.4). Based on the values of R , ρ_r and the n (= 0.2, 0.35 or 0.4 in the domain) an overall K_d has been calculated in such a way that the resulting R (used by METROPOL-4) has a conservative value with respect to the transport of the nuclides (*i.e.* that the resulting R is a little bit smaller than the listed value below).

Table 8.2 Retardation factor and K_d .

Nuclide	R [1]	K_d [m^2/kg]
Am243	2000	$5 \cdot 10^{-1}$
Pu239	1000	$2.5 \cdot 10^{-1}$
U235	300	$7.5 \cdot 10^{-2}$
Pa231	400	$1 \cdot 10^{-1}$
Sn126	20	$5 \cdot 10^{-3}$
Se79	300	$7.5 \cdot 10^{-2}$
Am241	2000	$5 \cdot 10^{-1}$
Pu242	1000	$2.5 \cdot 10^{-1}$
Cm246	1000	$2.5 \cdot 10^{-1}$
Cm245	1000	$2.5 \cdot 10^{-1}$
Np237	2000	$5 \cdot 10^{-1}$
U233	300	$7.5 \cdot 10^{-2}$
Th229	500	$1.25 \cdot 10^{-1}$
U238	300	$7.5 \cdot 10^{-2}$
U234	300	$7.5 \cdot 10^{-2}$
Th230	500	$1.25 \cdot 10^{-1}$
Ra226	50	$1.25 \cdot 10^{-1}$

For each nuclide the input source has been specified at $t = 0$, at the location where the nuclides are thought to be stored ($X = 4005$ m, $Y = 75$ m, $Z = 545$ m). That is nodal point #2753. In the Table 8.3 the amount of nuclide in each container is given [Bq] (Grupa, 2000, Table 3.3). We recall that 1 Becquerel is 1 event of radiation emission per second. Since METROPOL-4 requires as input a mass fraction, firstly, the amount of Bequerel has to be transformed in an amount of mass. Therefore we need the specific activity A_{nuclide} [1/(g.s)]. The specific activity is defined as:

$$A_{\text{nuclide}} = \lambda_{\text{nuclide}} * N_{\text{avogadro}} / M_{\text{nuclide}}, \quad (8.7)$$

where:

$$\lambda_{\text{nuclide}} = \ln(2) / T_{1/2, \text{nuclide}} \text{ [1/s]} \quad \text{the decay rate, with } T_{1/2, \text{nuclide}} \text{ the half life time of the nuclide,}$$

$$N_{\text{avogadro}} = 6.022137 \cdot 10^{23} \text{ [1/mol]}$$

$$M_{\text{nuclide}} \quad \text{the mass number of the nuclide [g/mol].}$$

With the knowledge of A the amount of x Bq is equivalent with y gram as follows:

$$y \text{ [g]} = x / A_{\text{nuclide}} \text{ [1/s / (1/(g.s))].}$$

To determine the mass fraction, the so found amount of grams has to be attributed to some volume in the domain, namely to 1/8 of each of volume of the surrounding elements. In that way a density appears. The volume to which the initial mass is

attributed in nodal point #2753, the radionuclide point source, equals $V_{2753} = 99.975 * 25 * 22.5 \text{ m}^3 = 5.62359375 * 10^4 \text{ m}^3$. Moreover, this density has to be divided by the density of water ($\rho = 10^6 \text{ g/m}^3$). That means that $x \text{ Bq}$ is equivalent with [1] mass fraction as follows:

$$\begin{aligned} \omega &= x / A_{\text{nuclide}} / V / \rho && [1/\text{s} / (1/(\text{g.s}) 1/\text{m}^3 \text{ m}^3/\text{g})] \\ &= x / A_{\text{nuclide}} / 5.62359375 * 10^{-4} * 10^{-6} && [1] \\ &= x / A_{\text{nuclide}} * F, \quad \text{with } F = 1.77822233 * 10^{-11} && [1]. \end{aligned}$$

For the input of METROPOL-4 the factor F (see above) has been disregarded to prevent that the program had to run with very small numbers. This is allowed since it is just a constant factor for all results. Only, one has to realise that if one wants to calculate the equivalent amount of Becquerel at some particular location (at some nodal point # ip), one has to take into account the V_{ip} of that nodal point. This V_{ip} can be different from V_{2753} . In the Table 8.3 the amount has been calculated for the nuclides, without taking into account the factor F (input $\omega_f = \omega / F$). There will be 300 containers with waste (Grupa & Houkema, 2000). We have used the number of 400. At the calculation of the radiation doses this will be corrected.

Table 8.3 Amount of nuclides per container.

Nuclide	Amount/container [Bq]	$\omega_f = \omega / F$ for 400 containers [1]
Am243	$8.5 * 10^{11}$	$4.600269 * 10^4$
Pu239	$1.2 * 10^{11}$	$2.089878 * 10^4$
U235	$1.6 * 10^6$	$7.997010 * 10^3$
Pa231	$8.2 * 10^5$	$1.875255 * 10^{-1}$
Sn126	$4.6 * 10^{10}$	$1.751535 * 10^4$
Se79	$2.0 * 10^{10}$	$3.103566 * 10^3$
Am241	$3.9 * 10^{13}$	$1.229020 * 10^5$
Pu242	$7.4 * 10^8$	$2.021288 * 10^3$
Cm246	$1.1 * 10^9$	$3.884292 * 10^1$
Cm245	$5.9 * 10^9$	$3.713022 * 10^2$
Np237	$1.6 * 10^{10}$	$2.452294 * 10^5$
U233	$7.7 * 10^4$	$8.634090 * 10^{-2}$
Th229	$4.5 * 10^3$	$2.285781 * 10^{-4}$
U238	$2.4 * 10^7$	$7.712441 * 10^5$
U234	$9.3 * 10^7$	$1.615826 * 10^2$
Th230	$3.1 * 10^6$	$1.624618 * 10^0$
Ra226	$5.3 * 10^3$	$5.791550 * 10^{-5}$

Source

Since there is not a continuous extra amount of nuclide put into the system, the source terms are all zero.

Chain

As mentioned above, 8 chains are taken into account, 3 with 4 members, and 5 with just one member, as suggested by Grupa (2000), see Table 8.4.

Table 8.4 Nuclide chains.

Nuclide chains
Americium chain $Am243 \rightarrow Pu239 \rightarrow U235 \rightarrow Pa231$
Tin126 chain Sn126
Selenium79 chain Se79
Americium241 chain Am241
Plutonium242 chain Pu242
Curium246 chain Cm246
Neptunium chain $Cm245 \rightarrow Np237 \rightarrow U233 \rightarrow Th229$
Uranium-Radium chain $U238 \rightarrow U234 \rightarrow Th230 \rightarrow Ra226$

Boundary conditions

The boundary condition "no dispersive/diffusive mass flux" has been applied to all boundaries. One has to realise that the boundaries are far away of the domain of interest and moreover that there is no information available for any other type of boundary condition.

Velocities

The runs with METROPOL-4 have been performed for three different scenarios:

1. Current situation during 10^6 y. This is a reference scenario with present-day boundary conditions to be used for the evaluation of the more realistic scenario 3.
2. Permafrost situation during 10^6 y. This is a second reference scenario with glacial boundary conditions to be used for the evaluation of scenario 3.
3. Combination of the current situation during $6 \cdot 10^4$ y, permafrost situation during $2 \cdot 10^4$ y, glaciation situation during $2 \cdot 10^4$ y, and this sequence repeated 10 times, so that the end time is also $1 \cdot 10^6$ y.

For each scenario a velocity field has been supplied by earlier calculations with DIANA (see section 7.4.5). In this way the influence of the glaciation period can be assessed by comparing the three results.

Flux

No surfaces have been specified for which a flux has to be calculated.

Transport

TRANS1:

A number of points has been specified for which time profiles of the radionuclide dosis in Sv per year are required (All with $Y = 75$ m). These points are the release point #2753, 16 points around this point, three points near the interface between the aquitard RU&AS and VOORT and three near this of RU&AS and BRUS, and 10 points around the fault in the layers VOORT, RU&AS and BRUS. Moreover, one point in VOORT and one in BRUS, halfway between the fault and the vertical through the release point. Finally, 2 points at the surface ($Z = 0$ m) along the fault and just above the release point and 2 in the same way in BRE_Z.

TRANS2:

The time instances for which print out is required are the begin and time times of the respective periods, so $6 \cdot 10^4$, $8 \cdot 10^4$, $1 \cdot 10^5$, $1.6 \cdot 10^5$, $1.8 \cdot 10^5$, $2 \cdot 10^5$, ..., $9 \cdot 10^5$, $9.6 \cdot 10^5$, $9.8 \cdot 10^5$, $1 \cdot 10^6$ y.

8.4 Results

The main result about the spread of the nuclides is given in Figure 8.2, which gives the contours of the mass fraction ω_f (i.e. ω divided by the factor $F = 1.77822233 \cdot 10^{-11}$). So, to find the real mass fractions one has to multiply by F . In this figure, the levels are $1 \cdot 10^6$ (near the release location), $1 \cdot 10^5$, $1 \cdot 10^4$, $1 \cdot 10^3$, $1 \cdot 10^2$, $1 \cdot 10^1$, $1 \cdot 10^0$, $1 \cdot 10^{-1}$, $1 \cdot 10^{-2}$, $1 \cdot 10^{-3}$. The blue colour represents the simulation with current boundary conditions, the red colour the simulation with permafrost conditions and the green colour the more realistic cyclic alternation of present-day, permafrost and ice-loading conditions.

As can be seen in this figure, the transport in the aquitard is mainly diffusive, since the contour lines are centred around the release point. This follows also from the values of the parameters. Since the molecular diffusion coefficient $D_m = 6.3072$

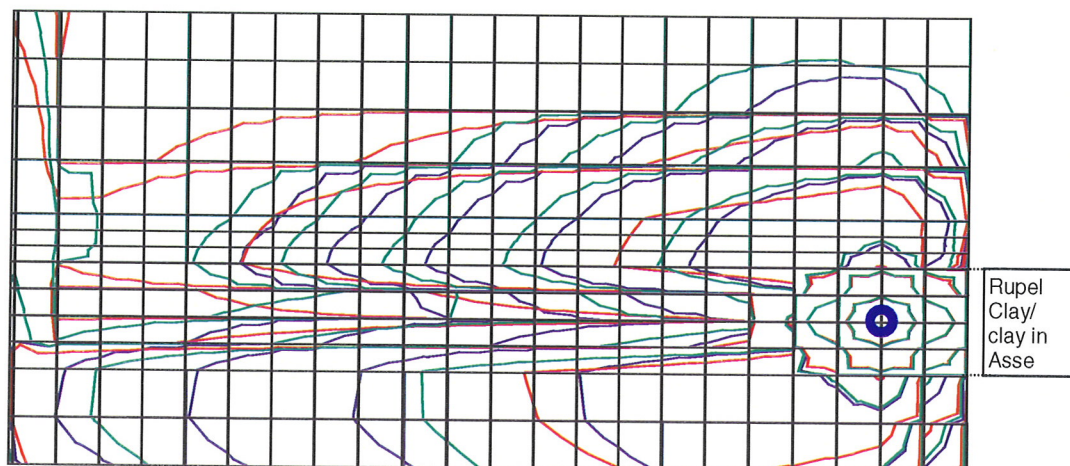


Figure 8.2 Contours mass fractions; blue = present-day conditions; red = permafrost conditions; green = cyclic alternation of present-day, glacial and ice-loading conditions.

Levels are: $1 \cdot 10^6$, $1 \cdot 10^5$, $1 \cdot 10^4$, $1 \cdot 10^3$, $1 \cdot 10^2$, $1 \cdot 10^1$, 1 , $1 \cdot 10^{-1}$, $1 \cdot 10^{-2}$, $1 \cdot 10^{-3}$. For the real mass fractions these levels values have to be multiplied by $F = 1.77822233 \cdot 10^{-11}$. Result corrected for 300 containers. Fault is at the left side of the window. Top two layers represent BRE_Z, next two BRE_VE (clay), next three VOORT, next four RU_AS (clay), last two layers BRUS.

$10^{-3} \text{ m}^2/\text{y}$, the longitudinal dispersivity $\alpha_1 = 50 \text{ m}$ and the order of magnitude of the absolute velocities in the aquitard are 10^{-7} m/y , $2.5 \cdot 10^{-7} \text{ m/y}$, and $1.7 \cdot 10^{-5} \text{ m/y}$, respectively for the initial, permafrost and glacial conditions, the contribution of the dispersive transport into the total diffusion coefficient is about 0.08%, 0.2% and 14%.

To exhibit the relative difference of the three scenarios time plots have been produced of the ratio of the mass fractions at nodal point #3333 (just above the release point, at the interface of the aquitard and the upper lying aquifer) for 6 different nuclides (Pu238, Np236, Se79, Sn126, Th230, and U 238), see Figure 8.3 to Figure 8.8. The present-day conditions have been taken as the reference scenario. Due to the higher velocities in the aquifers during the permafrost conditions the transport of the nuclides is faster and so the nuclides have been spread out over a larger area. For the scenario with cyclic changes, the mass fractions at the selected locations are 2 to 9 times higher at a maximum.

8.5 Discussion

The effect of the cyclic velocity field is quite clear from the Figure 8.3 to Figure 8.8. The situation of continuous permafrost which gives rise to a higher velocity in the clay layers produces a lower level of mass fractions in the reference points, just above the release point.

The cyclic scenario consists of a sequence of three velocity fields, which are coupled to each other. Each velocity field itself is the mean of the corresponding period. That means that at the start time of each subperiod the velocity field makes a rather large change, without a continuous transition. Due to shortage in time it was not possible to perform this study with a more continuously changing velocity field.

From Figure 8.2 it can be seen that once the nuclide material has reached the aquifer above or below the aquitard with the release point, the propagation is much faster than in the aquitard. Diffusion is the dominant process of transport in the clay. The presence of the fault induces also a faster spreading of the nuclides than has been presented here.

The scope of the present study was a regional simulation of the nuclides through the aquitard-aquifer system. Due to hardware memory restrictions and time restrictions it has not been possible to focus properly with the METROPOL-4 program into the behaviour of the nuclide transport in the aquitard in which the radioactive waste is stored. From the actual knowledge it is clear that during the present day conditions the transport process in this aquitard is diffusive. From this study the absolute velocities in this aquitard are increased somewhat (about a factor 2.5) during permafrost conditions and quite largely (about a factor 200) during glacial conditions. Still, the transport in the aquitard is not much influenced by advection and dispersion. However, the influence of this increase becomes only apparent in the concentrations in the upper and lower lying aquifer, due to the prevailing higher velocities there.

A comparison with the results from the METRO-III study learns that there are differences with the TRACTOR research. The main one is the fact that in that study the times at which the recharge of the nuclides into the aquifer occurs later than in this study. Possible reasons for this discrepancy are the following:

- In this study the number of elements is rather low to model the transport through the aquitard. The reason for this choice has been dictated by the scope of the underlying study, namely a subregional study of a domain of 10 km width and over the full height of the aquifer-aquitard system.

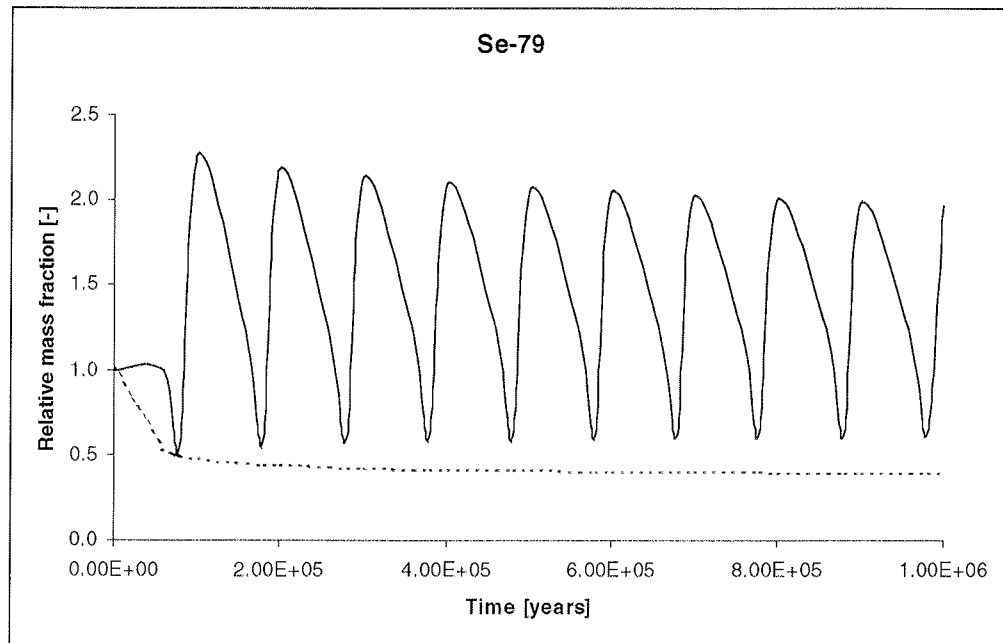


Figure 8.3 Mass fraction of radio-isotope Se-79 relative to present-day condition; solid line = relative mass fraction for scenario with cyclic changes; dashed line = relative mass fraction for permafrost scenario.

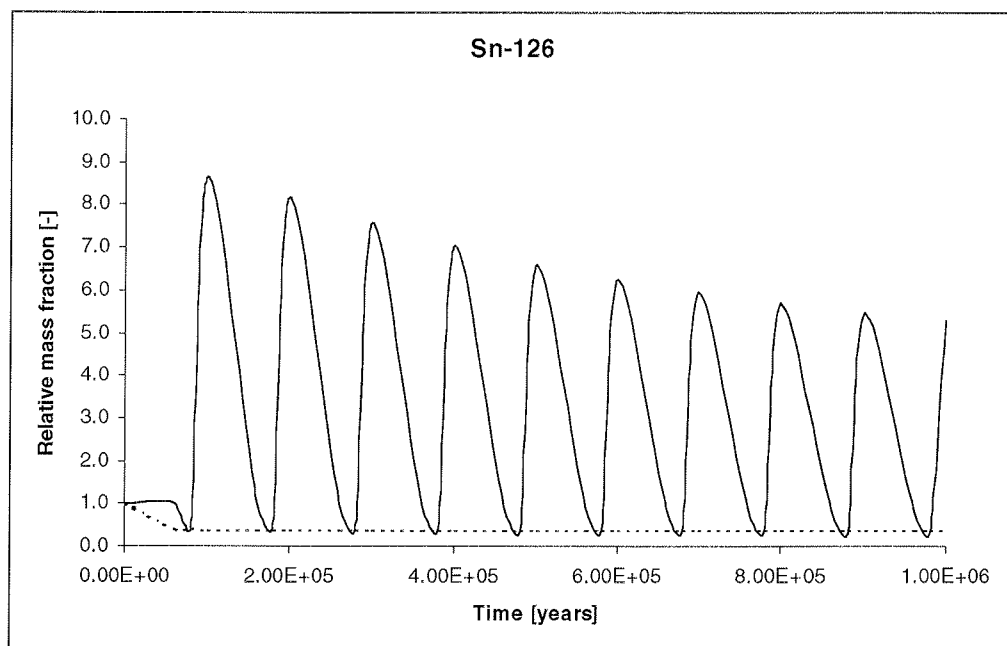


Figure 8.4 Mass fraction of radio-isotope Sn-126 relative to present-day condition; solid line = relative mass fraction for scenario with cyclic changes; dashed line = relative mass fraction for permafrost scenario.

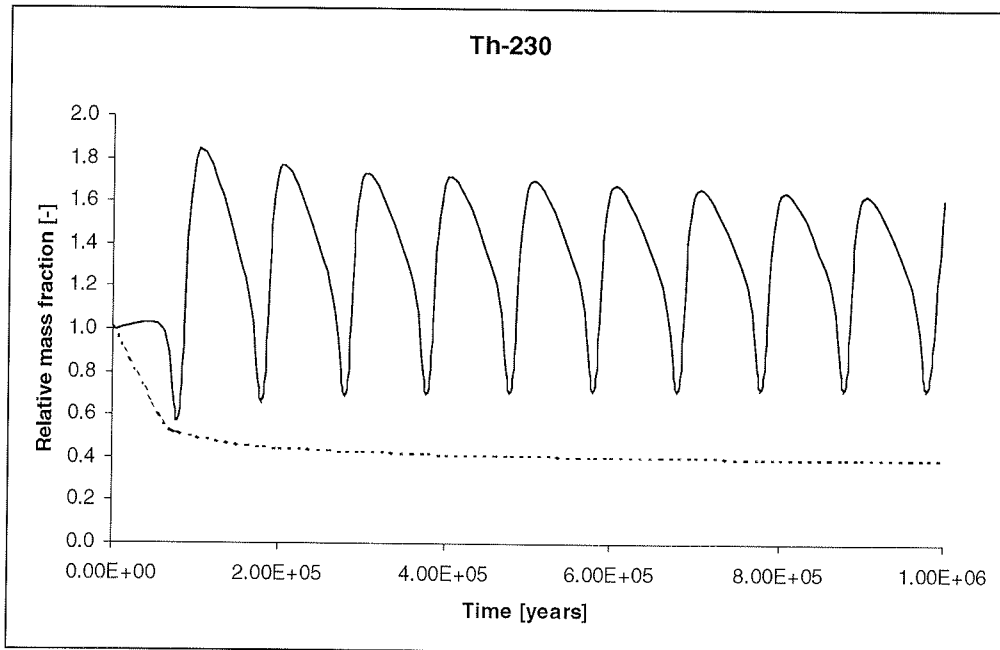


Figure 8.5 Mass fraction of radio-isotope Th-230 relative to present-day condition; solid line = relative mass fraction for scenario with cyclic changes; dashed line = relative mass fraction for permafrost scenario.

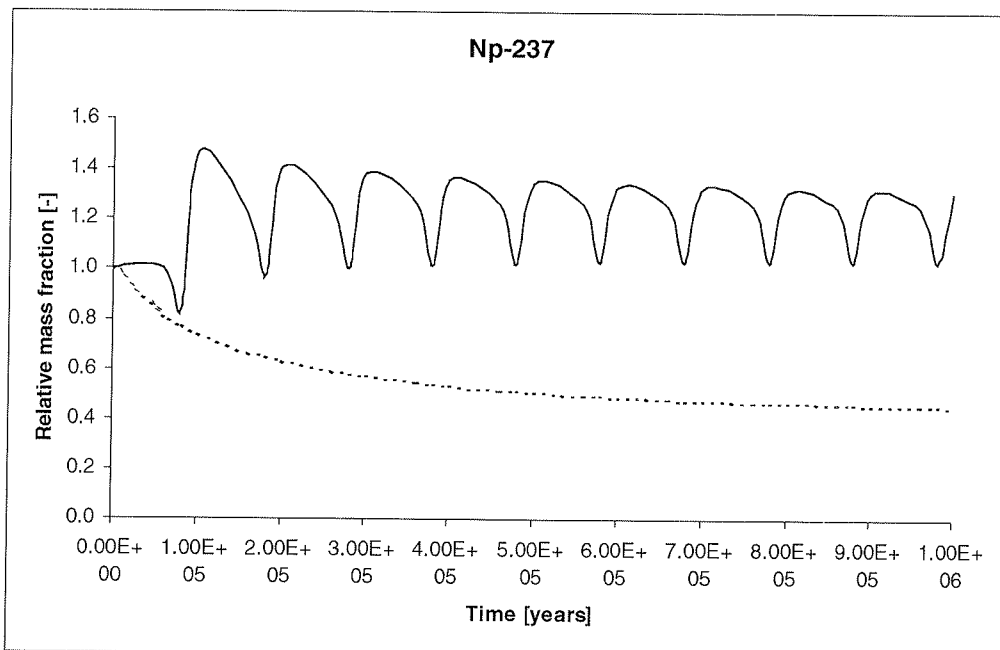


Figure 8.6 Mass fraction of radio-isotope Np-237 relative to present-day condition; solid line = relative mass fraction for scenario with cyclic changes; dashed line = relative mass fraction for permafrost scenario.

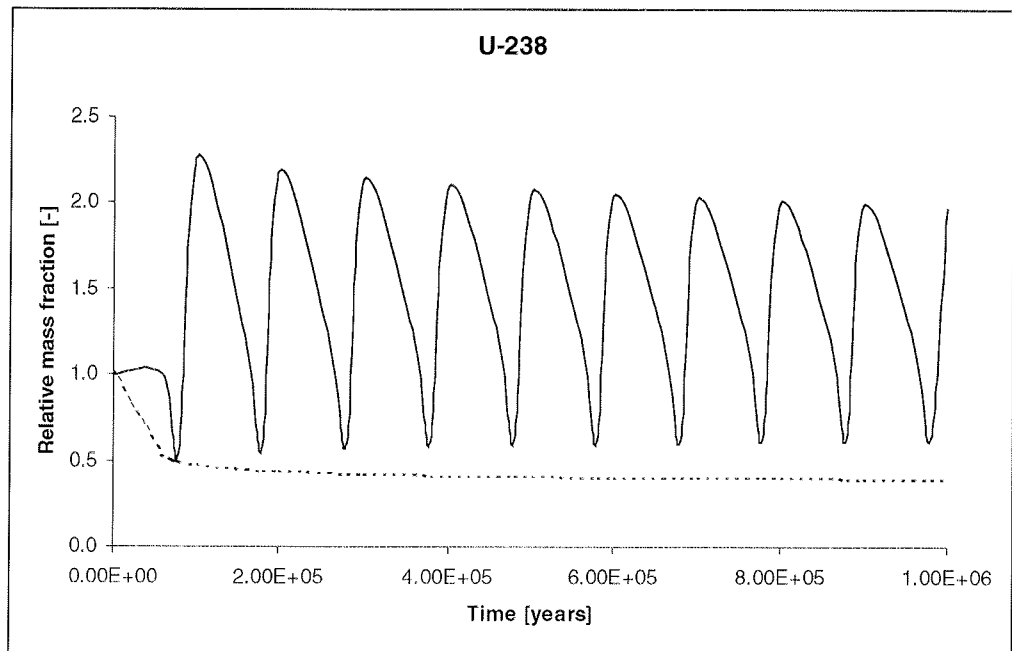


Figure 8.7 Mass fraction of radio-isotope U-238 relative to present-day condition; solid line = relative mass fraction for scenario with cyclic changes; dashed line = relative mass fraction for permafrost scenario.

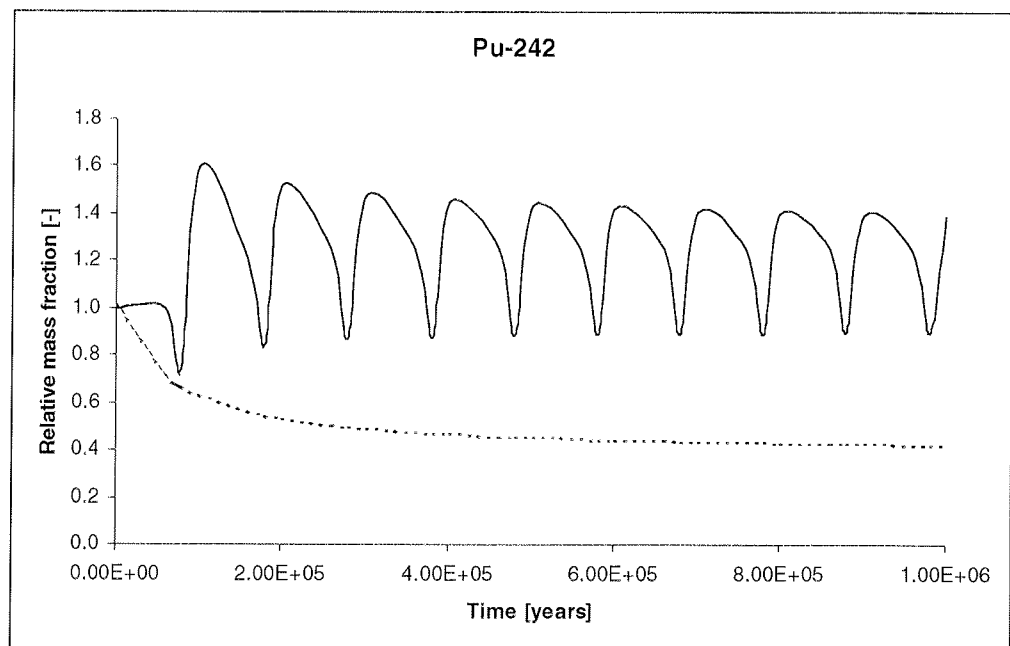


Figure 8.8 Mass fraction of radio-isotope Pu-242 relative to present-day condition; solid line = relative mass fraction for scenario with cyclic changes; dashed line = relative mass fraction for permafrost scenario.

- For the transport through the clay-layer in the METRO-III study (Grupa & Houkema, 2000) the choice has been made for the boundary condition at the interface of the aquitard and the aquifer that the concentration is fixed at 0. The time at which the maximum value for the flux into the aquifer occurs is listed in Grupa & Houkema (2000; Table 3.9 and Fig. 3.5 & 3.6). In the present study such a condition has not been posed, but, since the covering aquifer is part of the model, the recharge of the aquitard into the aquifer has been calculated by the program METROPOL-4 based on the velocity field supplied by DIANA. The mathematical model for the transport through the clay by Grupa & Houkema (2000) can be written as:

$$\begin{aligned}
 R \frac{\partial c}{\partial t} &= D \frac{\partial^2 c}{\partial x^2} - \lambda R c, & 0 \leq x \leq B, & \quad t > 0, \\
 c(x, 0) &= 0, & 0 \leq x \leq B, & \\
 c(0, t) &= \exp(-\lambda t), & t \geq 0, & \\
 c(B, t) &= 0, & t \geq 0. &
 \end{aligned} \tag{8.8}$$

The analytical solution of this mathematical problem is

$$c(x, t) = \frac{2}{\pi} \exp(-\lambda t) \sum_{n=1}^{\infty} \frac{1}{n} \left(1 - \exp\left(-\frac{n^2 \pi^2 D t}{R B^2}\right) \right) \sin\left(\frac{n \pi x}{B}\right) \tag{8.9}$$

see Sneddon (1972, formula (3-15-15)). Conceptually, this approach is different from the current study.

- In contrast to the METRO-III study, the release of the nuclides into the aquitard has been thought to take place already at $t = 0$, whereas the METRO-III study takes into consideration that the containers are deteriorating in 75000 years. For the shorter living nuclides, this fact gives rise to both a delay and a lower exposure of the aquitard by the nuclides in the METRO-III study.
- It turned out that for the total exposure at $t = 0$ in this study the retardation factor R has not been taken into consideration. This decreases the calculated concentrations with just that factor.

9 Conclusions and recommendations

Glaciation and radionuclide migration

- Exploratory calculations show that cyclic ice loading can lead to an acceleration of radionuclide migration in clay. The calculated contributions of dispersive transport to the total diffusion coefficient in clay amounts to 0.08% under present-day conditions, 0.2% under glacial conditions without ice loading and 14% under glacial conditions with ice loading. These values are valid under the assumption that the longitudinal dispersivity equals 50 m. They do not reflect the effect of radionuclide retention.
- The episodic occurrence of ice loading with an assumed duration of 20,000 years and a periodicity of 100,000 years increases the radionuclide mass fraction at the interface between the clay barrier and the upper aquifer. The increase of the mass fraction is dependent on the radioisotope mass fraction and its maximum value is 2 to 9 times the mass fraction in the reference scenario (current climate conditions). The increase probably falls within the uncertainty range of the estimated diffusive transport.

Glaciation and groundwater flow

- Large-scale modelling of the groundwater system reveals that ice loading increases the pore pressure in deep-seated aquifers. Loading of the aquifers by the ice accelerates the ground water flow outwards towards the ice margin and ahead of it. Hydraulic gradients, pore pressures and flow velocities are at least one order of magnitude greater during glaciation than in the pre-glacial period. This condition may lead to an amplified flooding of clay bodies with a permeability of 10^{-10} m/s or more. Preferential flow occurs along permeable, vertical faults.
- An increase in the groundwater velocity and pore pressure in the aquifers is limited to the period during which the ice load increases. Once the ice load reaches its maximum value, the pore pressure steadily decreases until it eventually reaches the initial pre-glacial state.
- A glaciation leads to amplified outflow of groundwater from a clay body to the aquifers above and below the clay, also named consolidation-driven flow. The magnitude and dynamics of the consolidation-driven flow is sensitive to the input geomechanical parameters and hydraulic conductivity of the Rupel Clay and the clay of the Asse Member as well as to the initial state of stresses in the subsurface. The knowledge of these site-specific parameters is indispensable

for a possibly improved estimate of the consolidation-driven pore water flow in the Rupel Clay and the clay of the Asse Member.

The outflow increases with higher values of permeability. At the same time, the duration of the outflow is shortened. The outflow rate of the groundwater is proportional to the progradation rate of the ice front.

The type of material model used also influences the outflow rate and the duration of the enlarged outflow. The more realistic Cam-Clay model reduces the rate and enlarges the duration with respect to the Mohr-Coulomb model.

- The most realistic ice-loading scenario is the situation in which the Cam-Clay material model was applied with a permeability of the clay of $3 \cdot 10^{-12}$ m/s, an effective friction angle of 15° and an effective pre-consolidation pressure of 10.4 MPa. The consolidation of the Rupel Clay and the clay of the Asse Member extends over the whole period of ice loading. The maximum value of the outflow rate amounts to 1 mm per year. This value is about three orders of magnitude higher than the flow rate before ice loading started.

Glaciation and mechanical behaviour of the clay

- The total settlement caused by the ice loading amounts to about 20 m.
- Increased hydraulic gradients, pore pressures and velocities of the groundwater flow cause heaving and plastic deformations of the shallow subsurface ahead of the ice sheet margin. The sediments affected by these deformations belong to Quaternary formations. The ice front advances with a fast or medium fast velocity.

Mechanical laboratory experiments on clay

- The experiments on Rupel Clay samples from the depth range of 313 to 454 metre have resulted in the following mechanical parameter ranges:

<i>Parameter</i>	<i>Range</i>
ϕ'	8.1 – 13.1°
c'	0.09 – 0.72 MPa
p'_c	6 - 8 MPa
λ	0.14 – 0.24
κ	0.06 – 0.07

- Analysis of a clay sample from the Asse Member has revealed a ϕ' -value of 2° . This extreme low value must be checked in additional experiments.

- Calculation of the permeability of the Rupel Clay in the same depth interval has resulted in values between $1,1 \cdot 10^{-13}$ tot $7,6 \cdot 10^{-14}$ m/s.
- Some mechanical parameters, such as the friction angle, cohesion and the shear modulus, tend to change with depth. The available amount of data however is too small to draw definite conclusions. This complicates the extrapolation of Belgian data on Tertiary clays to stratigraphically comparable clays in the deeper subsurface of the Netherlands.
- The analysed clays are all overconsolidated. The cause of the overconsolidation cannot be determined unequivocally. Diagenetic changes, creep or overloading, or a combination of these processes, might have caused the overconsolidated behaviour of the clays. Effective loading by an ice sheet with a thickness of 1,000 m will result in further consolidation of the Rupel Clay.

Laboratory experiments and computer modelling

- The parameter values for the most realistic scenario that has been analysed have been derived from the experiments for the mining engineering study TRUCK-II. The experimental results for the TRACTOR project itself were not available at the time of the hydromechanical simulations.
- The parameter values used in this scenario are:

<i>Parameter</i>	<i>Value</i>
ϕ'	15°
p'_c	10.4 MPa
λ	0.12
κ	0.02
K	$3 \cdot 10^{12} \text{ m/s}$

- The used value for the friction angle is higher than the experimentally determined values. In Cam-Clay models a higher ϕ -values is used to compensate for the cohesion parameter, which is not included in the Cam-Clay model.
- The lower experimental value for the effective pre-consolidation pressure p'_c and the higher experimental value for the compression-index λ would result in a somewhat higher Darcy-flux than has been simulated for the most realistic scenario in the TRACTOR project.

Characterisation of the Rupel Clay

- It is strongly recommended to characterise the Rupel Clay for the objectives of retrievable radioactive waste storage. The characterisation should be based on material from the proper depth range and region. In this respect, we advise to use well-log measurements, which need to be calibrated with information from drill cores. Mechanical and hydraulic properties of the clay cores have to be analysed in the laboratory. The natural stress conditions of the clays must be measured *in situ*.

Additional experiments and simulations

- More field data are also needed for assessing the usefulness of other Tertiary clays for retrievable waste storage, like the clays from the Asse and Ieper Members.
- We recommend additional hydromechanical simulations which will be based on the latest mechanical data for the Rupel Clay (see also conclusion below 'Laboratory experiments and computer modelling').
With the experience of this study, we recommend further transport simulations zoomed in more closely into the neighbourhood of the release point of the nuclides to make more profit of the possibilities of the METROPOL-4 program.

10 References

- Anonymous (1992). *Geologie rondom ijstijden*. Open Universiteit Heerlen, vol. 1-3.
- Biot, M.A. (1941). General theory of three-dimensional consolidation. *Journal of Applied Physics*, Vol. 12, 155-164.
- Bishop, A.W., D.L. Webb, and P.I. Lewin (1965). Undisturbed samples of London Clay from the Ashford Common shaft: strength-effective stress relationships. *Géotechnique*, 15, no.1, 1-31.
- Boulton, G.S. & K.E. Dobbie (1993), Consolidation of sediments by glaciers: relations between sediment geotechnics, soft-bed glacier dynamics and subglacial ground-water flow. In: *Journal of Glaciology*, vol. 39, no. 131, 26-44.
- Boulton, G.S. & R.C.A. Hindmarsh (1987). Sediment deformation beneath glaciers: rheology and geological consequences. *Journal of Geophysical Research*, vol. 92, no. B9, 9059-9082.
- Boulton, G.S., Slot, T., Blessing, K., Glasbergen, P., Leijnse, T. & K. van Gijssel (1993). Deep circulation of groundwater in overpressured subglacial aquifers and its geological consequences. In: *Quaternary Science Reviews*, vol. 12, 739-745.
- Boulton, G.S. & F. Curle (1997). Simulation of the effects of long-term climatic changes on groundwater flow and the safety of geological disposal sites. University of Edinburgh, RIVM & RGD, European Commission, Nuclear Science and Technology, EUR 17793 EN.
- Britto, A.M, Gunn, M.J., 1987. *Critical State Soil Mechanics via Finite Elements*. John Wiley & Sons, New York.
- Brown, R.J.E. (1966). The relation between mean annual air and ground temperatures in the permafrost regions of Canada. In: *Proceedings, 1st International Conference on Permafrost*. Ottawa: National Academy of Science, National Research Council of Canada, Publication 1287.
- Certes, C., Escalier des Orres, P., Goblet, P., Levassor, A. & J. Marivoet (1997). *Evaluation of elements responsible for the effective engaged dose rates associated with the final storage of radioactive waste: Everest project. Volume 2b: Clay formation, site in France and common conclusions on clay*. European Commission, rep. no. EUR 17449/2b, 532p.
- De Moor, G. (1983). Cryogenic structures in the Weichselian deposits of Northern Belgium and their significance. *Polarforschung*, 53(2), 79-86.
- French, H.M. (1996). *The periglacial Environment*. In: Poser, H., 1948, *Boden- und Klimaverhältnisse in Mittel- und Westeuropa während der Würmeiszeit*. Erdkunde, 2.
- GeoDelft (1999a). Aut.: C.Lehnen-de Rooij. *Analyse van de doorlatendheid van de Klei van Boom bij hoge belastingen*. Rapportnr. CO 383970/4, 21 p.

- GeoDelft (1999b). *Bronnenonderzoek naar Overconsolidatie van Dikke Tertiaire Kleipakketten in Nederland: Klei van Boom*. Rapportnr. CO 383970/06.
- Gomit, J.M., Marivoet, J., Raimbault, P. & F. Recreo (1997). *Evaluation of elements responsible for the effective engaged dose rates associated with the final storage of radioactive waste: Everest project. Volume 1: Common aspects of the study*. European Commission, rep. no. EUR 17449/1, 418p.
- Grupa, J.B., M. Houkema (2000). Consequenties van de implementatie van langdurige terughaalbaarheid voor opberging van radioactief afval in de diepe ondergrond. Concept Eindrapport METRO-III, NRG, Petten.
- Grupa, J.B.(2000). E-mail message *d.d.* February 11, 2000.
- Hacker, Charles (1997). *RADIATION DECAY, version 2, March 1997*. Griffith University, Queensland, Australia. [Windows95 computer programme].
- Lerche, I., Yu, Z., Tørudbakken, B.& R.O. Thomsen (1997). Ice loading effects in sedimentary basins with reference to the Barents Sea. In: *Marine and Petroleum Geology*, vol. 14, p.277-338.
- Marivoet, J., Volckaert, G., Walravens, J., Wemaere, I. & R. Beaufays (1996). *Geological disposal of conditioned high-level and long lived radioactive waste. Hydrogeological modelling and long-term performance studies. Annex 1: Simulation of the permafrost thickness during glaciations*. Progress report to NIRAS/ONDRAF for 1995, SCK-CEN, R-3088, vol. 3, 12p.
- Marivoet, J., Volckaert, G., Wemaere, I. & J. Wibin (1997). *Evaluation of elements responsible for the effective engaged dose rates associated with the final storage of radioactive waste: Everest project. Volume 2a: Clay formation, site in Belgium*. European Commission, rep. no. EUR 17449/2a, 328p.
- Modaressi, H., Gentier, J., Fourniguet, J. & P.Peaudecerf (1990). *Géoperspective: développement de la modélisation*. Volume 3, Simulation de l'influence d'une glaciation sur les déformations et les écoulements dans une série sédimentaire. Commission des Communautés européennes, Sciences et techniques nucléaires, EUR 12503 FR/3, 77p.
- Mooers, H.D. (1990). Ice-marginal thrusting of drift and bedrock: thermal regime, subglacial aquifers, and glacial surges. *Canadian Journal of Earth Sciences*, 27, 849-862.
- Nederlands Instituut voor Toegepaste Geowetenschappen TNO (1998). *Inventarisatie geomechanische en geohydrologische eigenschappen van Tertiaire kleipakketten –CAR Fase II*. Haarlem, TNO-rapport NITG 98-90 B, 73p.
- Nichols, Alan L., Emma Hunt (1999). *Nuclear Data Table*. AEA Technology plc, Analytical Services, Didcot, Oxfordshire, United Kingdom. [file nuclides.pdf].
- Nichols, Alan L. (2000). E-mail message *d.d.* March 14, 2000.
- Prij, J., Benneker, P.B.J.M. (1989). *Invloed van een Tijdelijke Temperatuurdaling en Landijsbedekking op de Gesteentetemperatuur en –druk*. Stichting Energieonderzoek Centrum Nederland, Rap. ECN-89-12, 122p.

- Rijks Geologische Dienst (1992). *(Hydro)Geologische Karakteristieken van Breuken*. Haarlem, rap. Nr. 30103B, 33p.
- Rijks Geologische Dienst en TNO (1983), *Geologische en hydrogeologische inventarisatie van tertiaire en onder-kwartaire afzettingen in Midden-Nederland t.b.v. ondergrondse opslag en winning van warm water*. Haarlem, rap. nr. 83KA20EX, 131p.
- Rijks Geologische Dienst (1984), *Inventarisatie van slecht-doorlatende laagpakketten in de ondergrond van het Nederlandse vasteland*. Haarlem, rap. nr. OP 6009, 105p.
- Rijks Geologische Dienst en TNO (1984), *Geologische en hydrogeologische inventarisatie van tertiaire en onder-kwartaire afzettingen in Noord-Nederland t.b.v. ondergrondse opslag en winning van warm water*. Haarlem, rap. nr. 84KAR08EX, 150p.
- Rijks Geologische Dienst (1985). *Aardwarmtewinning en grootschalige warmteopslag in tertiaire en kwartaire afzettingen*. Haarlem, rapp. nr. 85 KAR 02 EX, 103p.
- Sauter, F.J. (1987). *User's manual METROPOL, Mathematical description*. National Institute of Public Health and Environmental Protection, Bilthoven, RIVM Report 728514002.
- Sauter, F.J., S.M. Hassanizadeh, 1989. Verification of METROPOL-code for groundwater flow in inhomogeneous porous media, Hydrocoin project level1, cases 1 and 2, RIVM report 728528001.
- Sauter F.J., S.M. Hassanizadeh, A. Leijnse, P. Glasbergen, A.F.M. Slot (1990). METROPOL: a computer code for the simulation of contaminants with groundwater, Report of the European Communities, EUR 13073 EN, Luxemburg.
- Sauter, F.J., A. Leijnse, A.H.W. Beusen (1993). *METROPOL, User's guide*. National Institute of Public Health and Environmental Protection, Bilthoven, RIVM Report 725205003.
- Rijks Geologische Dienst (1996). *Project 'CAR' - Fase 1: Kartering slecht doorlatende laag-pakketten van Tertiaire formaties*. Heerlen, rapp. nr. GB 2514, 25p.
- Schokking, F. (1990). On estimating the thickness of the Saalian ice sheet from a vertical profile of preconsolidation loads of a lacustroglacial clay. *Geologie en Mijnbouw*, 69, 305-312.
- Schokking, F. (1998). *Anisotropic geotechnical properties of a glacially overconsolidated and fissured clay*. PhD thesis, Delft University of Technology, Delft, The Netherlands, 150p.
- Shoemaker, E.M. (1986). Subglacial hydrology for an ice sheet resting on a deformable layer. *Journal of Glaciology*, vol. 32, no. 110, 20-30.
- Smith, M.W. (1975). Microclimatic influences on ground temperature and frost distribution, Mackenzie Delta, Northwest Territories. *Can.J.Earth Sci.*, 12.
- Sneddon, Ian N. (1972). *The Use of Integral Transforms*, McGraw-Hill Book Company, New York.

- Université catholique de Louvain (1999). Authors: S. de Cock & J.F. Thimus.
Project TRUCK II – Test results. Draft report.
- Vandenberge, N. (1978). *Sedimentology of the Boom Clay (Rupelian) in Belgium*.
Verh. Kon. Acad. Wetensch. Letteren en Schone Kunsten van Belgie, XL,
147, 137p.
- Vandenbergh J. (1993). *Permafrost Changes in Europe During the Last Glacial*.
Permafrost and Periglacial Processes. Vol. 4.
- Van Vliet-Lanoë B. (1989). Dynamics and extent of the Weichselian Permafrost in
Western Europe (Substage 5E to stage 1). *Quaternary International*, Vols.
3/4.
- Van Weert, F.H.A. & A. Leijnse (1996). *Modelling the effects of the Pleistocene
glaciations on the Northwest European geohydrological system*. National
Institute of Public Health and the Environment (RIVM) Bilthoven, The
Netherlands, rep.no. 715401001, 55p.
- Van Weert, F.H.A., K. van Gijssel, A. Leijnse, G.S. Boulton (1997). The effects of
the Pleistocene glaciations on the geohydrological system of Northwest
Europe, *Journal of Hydrology*, 195, pp. 137-159.
- Volckaert, G., Neerdael, B. & Ph. Lalieux (1997). *Characteristics of argillaceous
rocks: Boom Clay*. A catalogue of the Characteristics of Argillaceous Rocks
studied with respect to radioactive waste disposal issues: Belgium, Canada,
France, Germany, Italy, Japan, Spain.
- TNO, Rijksinstituut voor Drinkwatervoorziening, Rijks Geologische Dienst
(1976). *Geohydrologie II, Atlas of The Netherlands, Blad VII-4*.
- Terzaghi, K., Peck, R. (1962). *Soil Mechanics in Engineering Practice*. 12th ed.,
John Wiley & Sons, New York, 566p.

Appendix A Analysis of the permeability of the Boom clay at high pressure

(This is a summary of the report prepared by GeoDelft for the project TRACTOR, GeoDelft, 1999a).

In order to establish the permeability of the Boom Clay at high pressures, an analysis was performed of oedometer tests conducted on Boom Clay samples in the course of the Western Scheld tunnel project.

The permeability was determined on samples from different boreholes at pressures of 4-, 8-, 16-, and 30-times the effective overburden pressures at the respective sample depths. Both Taylor and Casagrande methods were adopted for this purpose.

The corresponding void ratio was calculated from the strain that was registered during the respective loading steps. A linear relationship was established between the logarithm of permeability and void ratio by means of a regression analysis.

Void ratios at high pressures of 6000 kPa to 21000 kPa were determined for each sample by extrapolation of the relationship between the logarithm of pressure and strain for the last two (highest) loading steps. The corresponding permeabilities were then calculated using the previously obtained linear relationship between void ratio and the logarithm of permeability.

Table A.1 Range of permeabilities resulting from the analysis of samples from the Boom Clay in the Western Scheld tunnel project.

Pressure [kPa]	Maximum permeability [m/s]	Minimum permeability [m/s]
6000	3.47×10^{-11}	2.21×10^{-13}
21000	1.18×10^{-11}	5.37×10^{-15}

Permeabilities were also calculated for overburden pressures by backward extrapolation. These values were compared with the results of falling head tests conducted on samples at overburden pressure. Although the latter samples were taken in different boreholes, they provided an insight in the validity of the extrapolation procedure, because falling head tests are considered to give results close to the *in-situ* values. The comparison indicated that the permeabilities extrapolated from the oedometer tests were a factor of 5 lower than the falling head values and should not be used for these pressure ranges (220 kPa – 430 kPa).

Based on general experience the extrapolated permeabilities at high pressures should be increased by a factor of 2. For the present project, where a higher permeability represents a worst-case situation it is advised to adopt the higher values from the analysis, i.e. 1×10^{-11} to 5×10^{-11} .

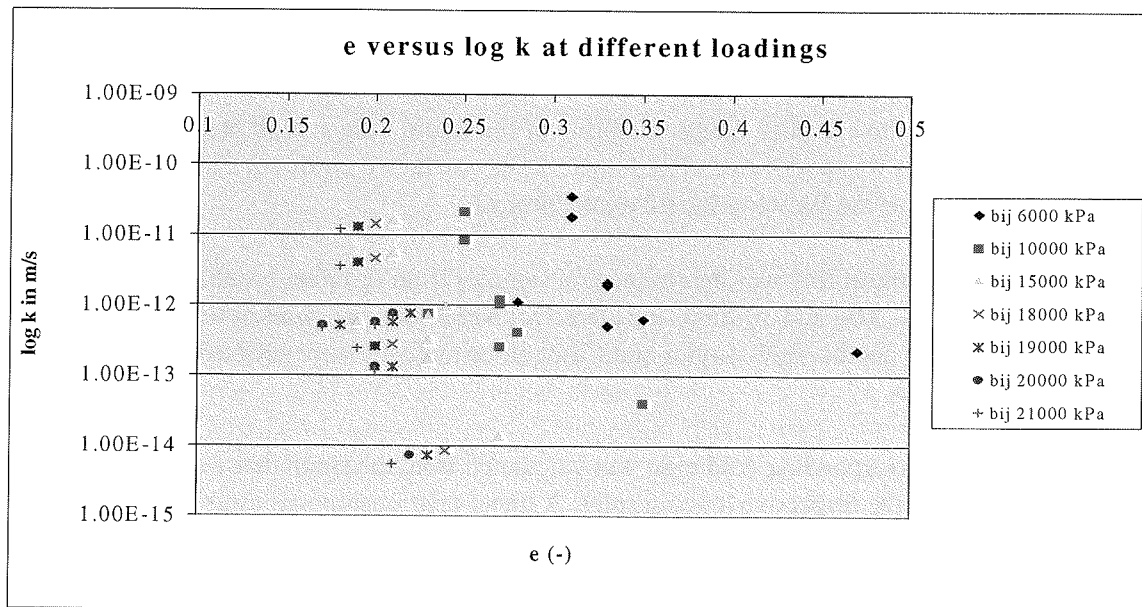


Figure A.1 Graph of void ratio (e) versus logarithm of the permeability (k) at various loadings.

Appendix B Stress paths in the tri-axial tests

The next figures give, for each test, the deviator stress versus the mean effective stress (Figure B.1 to Figure B.6) and the deviatoric stress versus the mean total stress (Figure B.7 to Figure B.12).

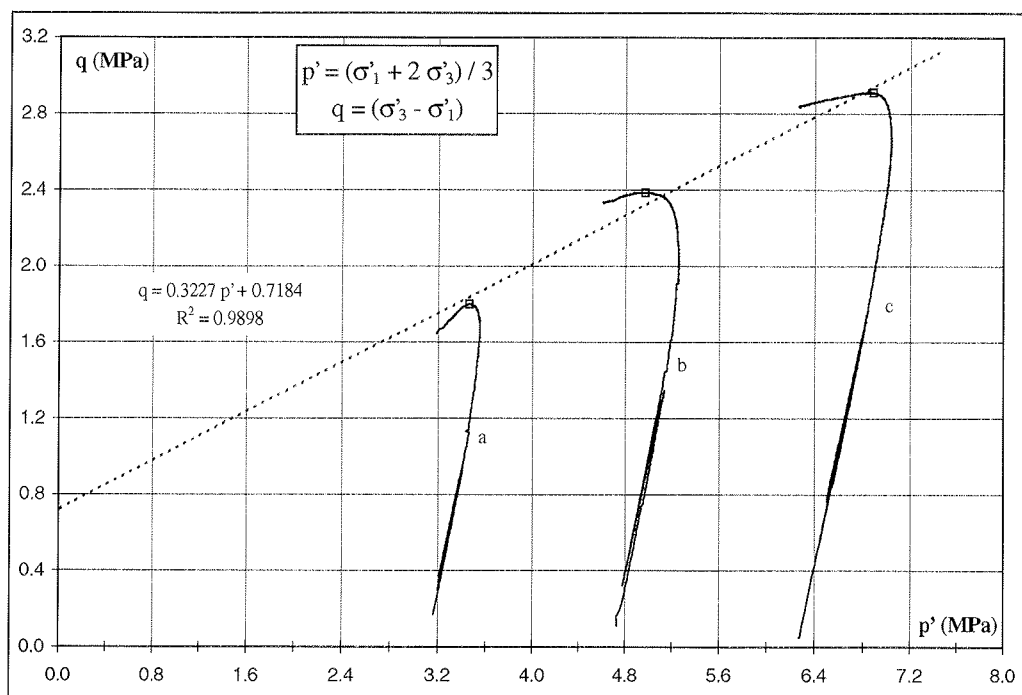


Figure B.1 Deviatoric stress versus the mean effective stress for Weelde (Belgium):
313.22 – 313.55 m (Case 1).

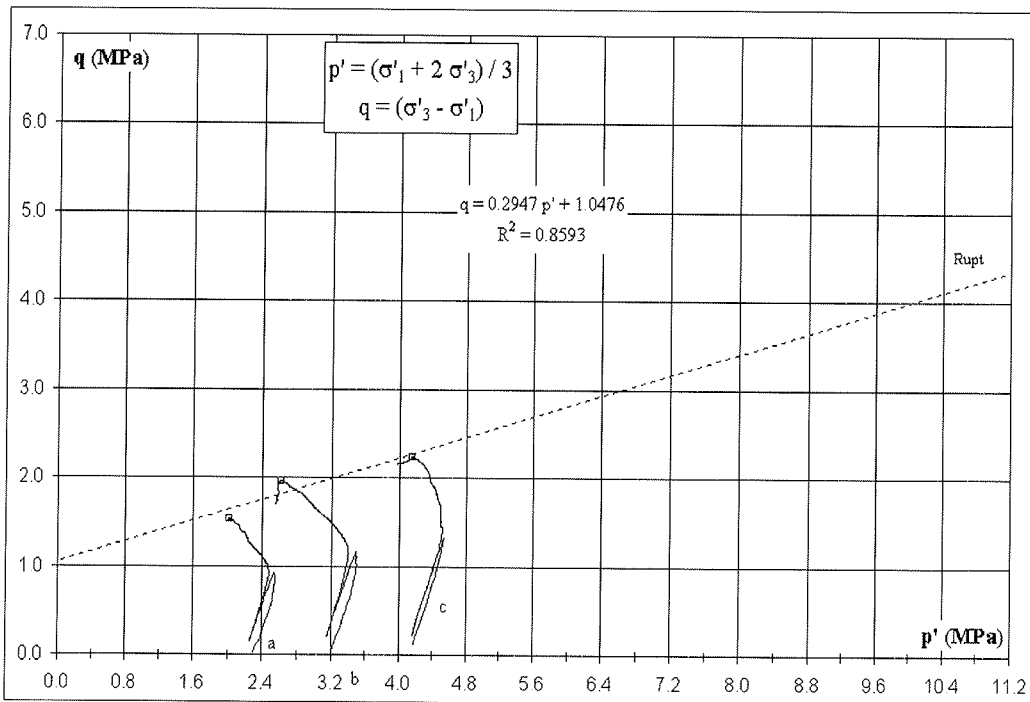


Figure B.2 Deviatoric stress versus the mean effective stress for Weelde (Belgium):
314.22 – 315.10 m (Case 2).

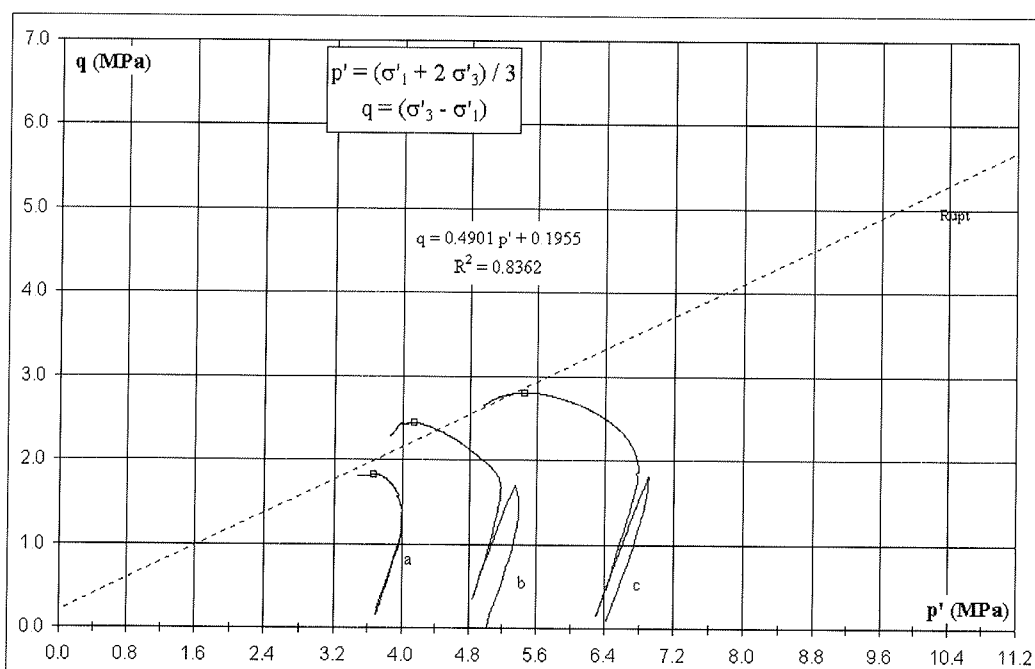


Figure B.3 Deviatoric stress versus the mean effective stress for Weelde (Belgium):
314.22 – 315.10 m (Case 3).

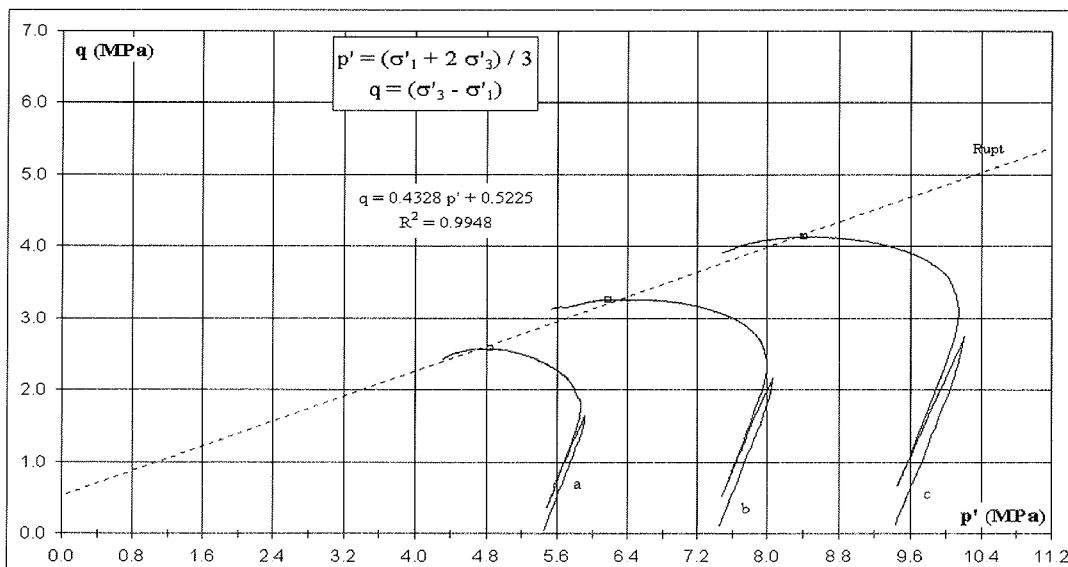


Figure B.4 Deviatoric stress versus the mean effective stress for Weelde (Belgium): 314.22 – 315.10 m (Case 5).

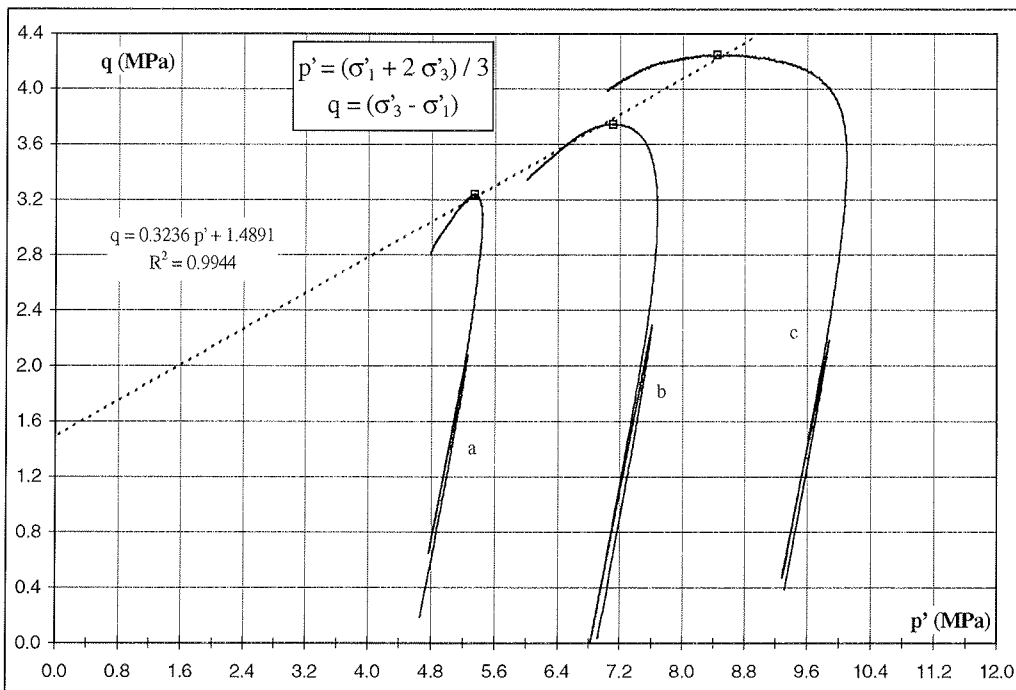


Figure B.5 Deviatoric stress versus the mean effective stress for Blija (The Netherlands): 454.50 - 455.00 m (Case 1).

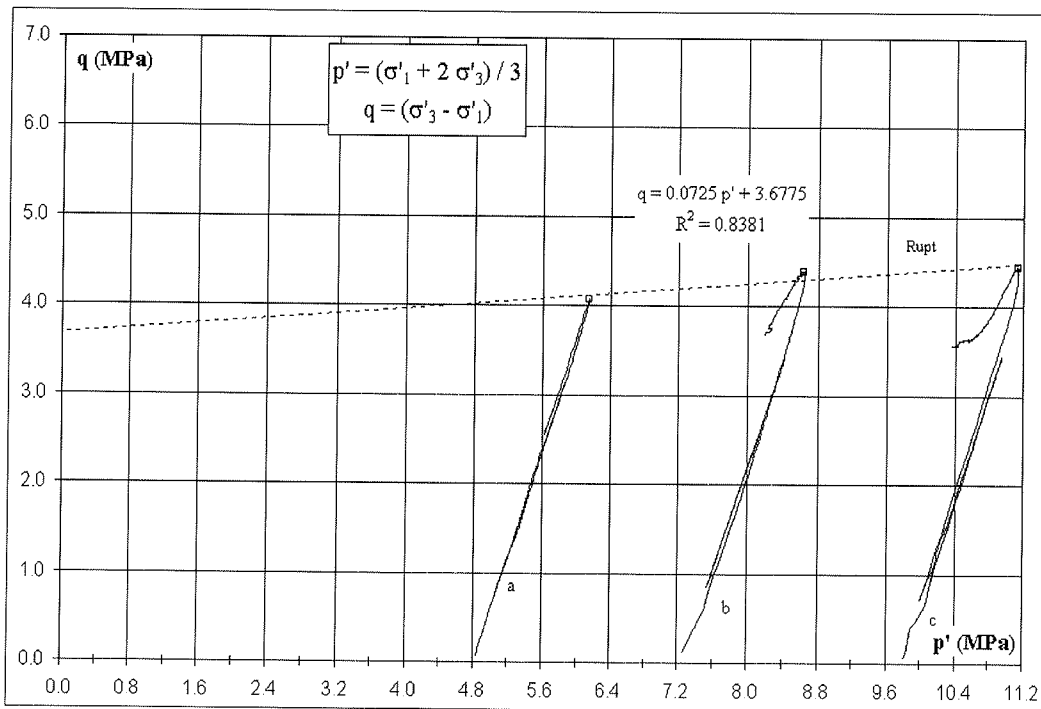


Figure B.6 Deviatoric stress versus the mean effective stress for Blija (Belgium): 561.50 – 561.85 (Case 3).

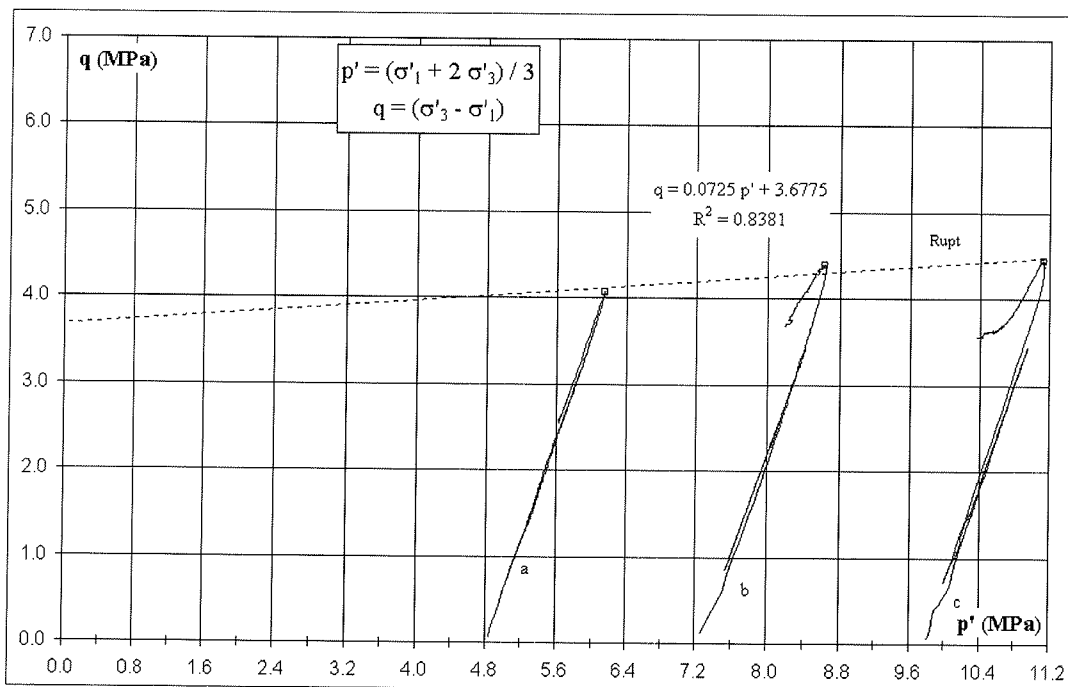


Figure B.7 Deviatoric stress versus the mean total stress for Weelde (Belgium): 313.22 – 313.55 m (Case 1).

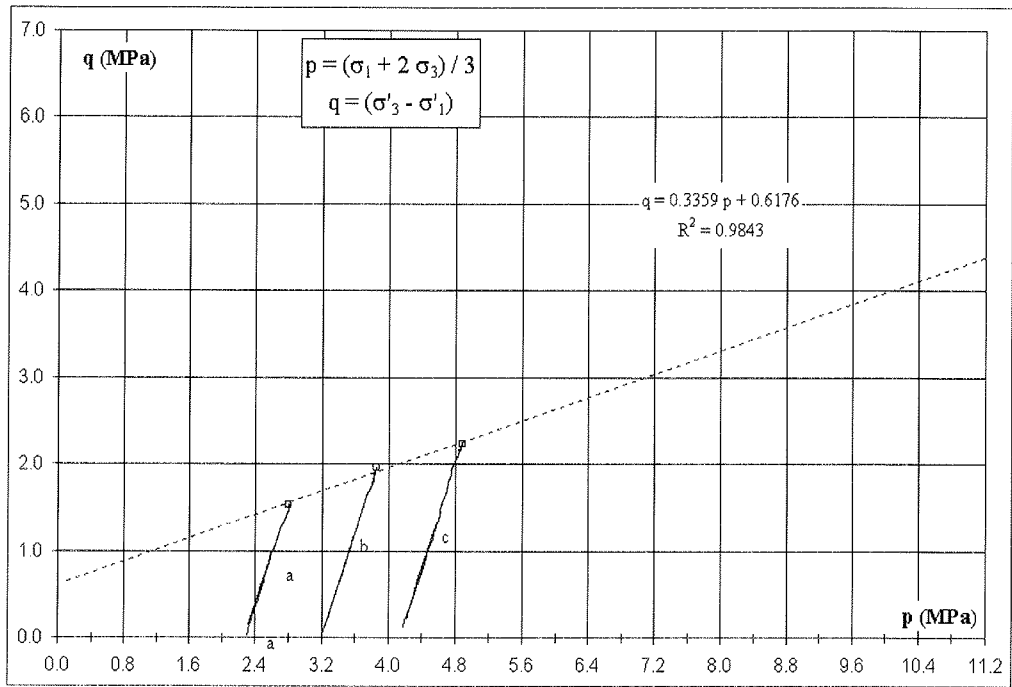


Figure B.8 Deviatoric stress versus the mean total stress for Weelde (Belgium): 314.22 – 315.10 m (Case 2).

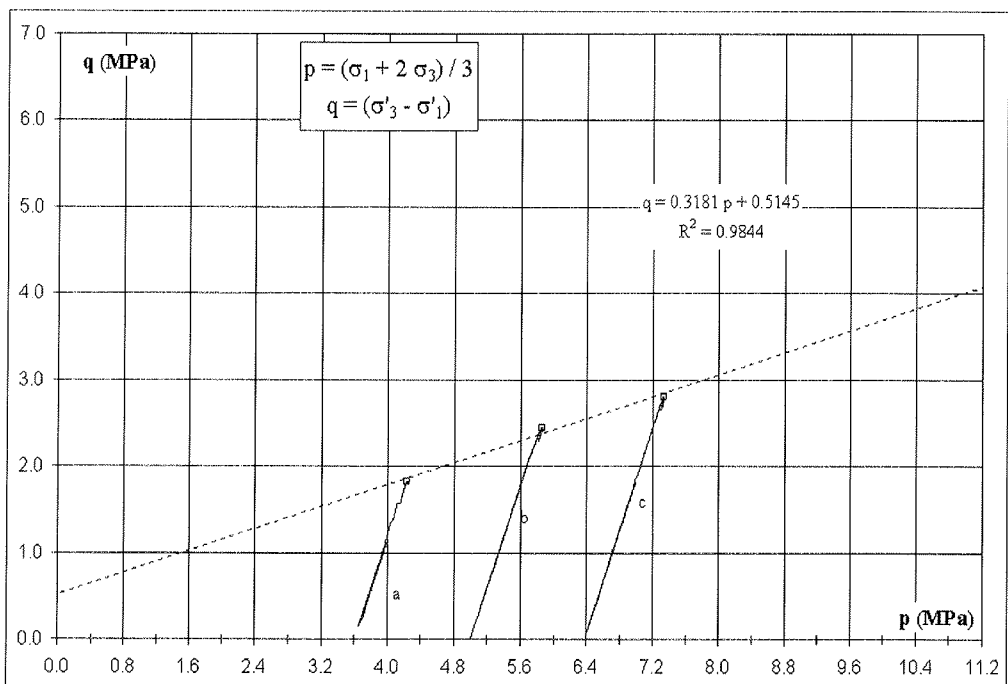


Figure B.9 Deviatoric stress versus the mean total stress for Weelde (B): 314.22 – 315.10 m (Case 3).

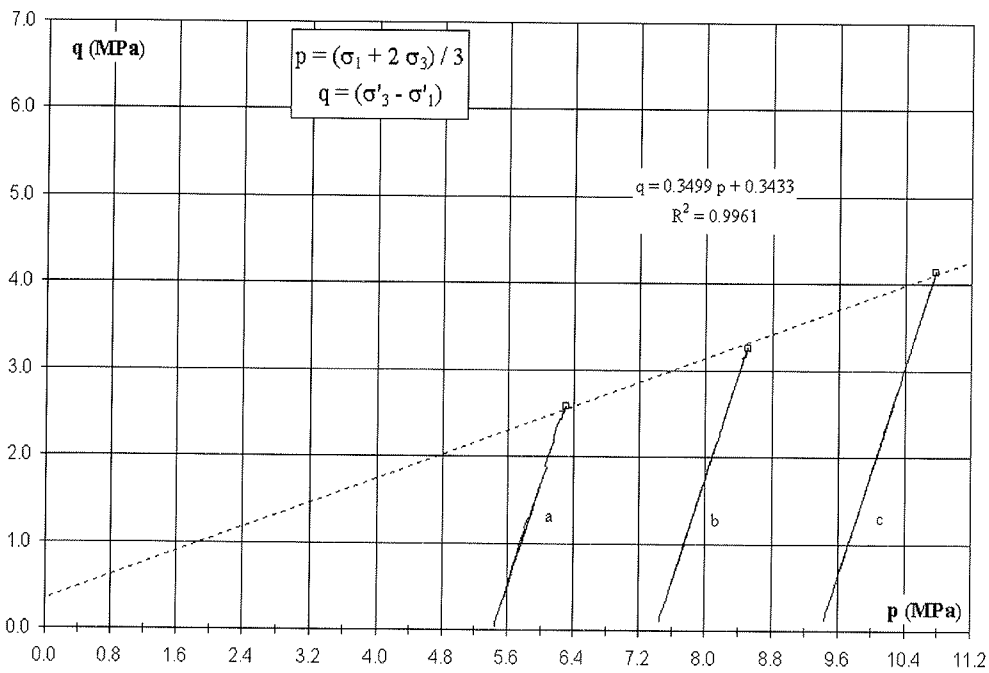


Figure B.10 Deviatoric stress versus the mean total stress for Weelde (Belgium) 314.22 – 315.10 m (Case 5).

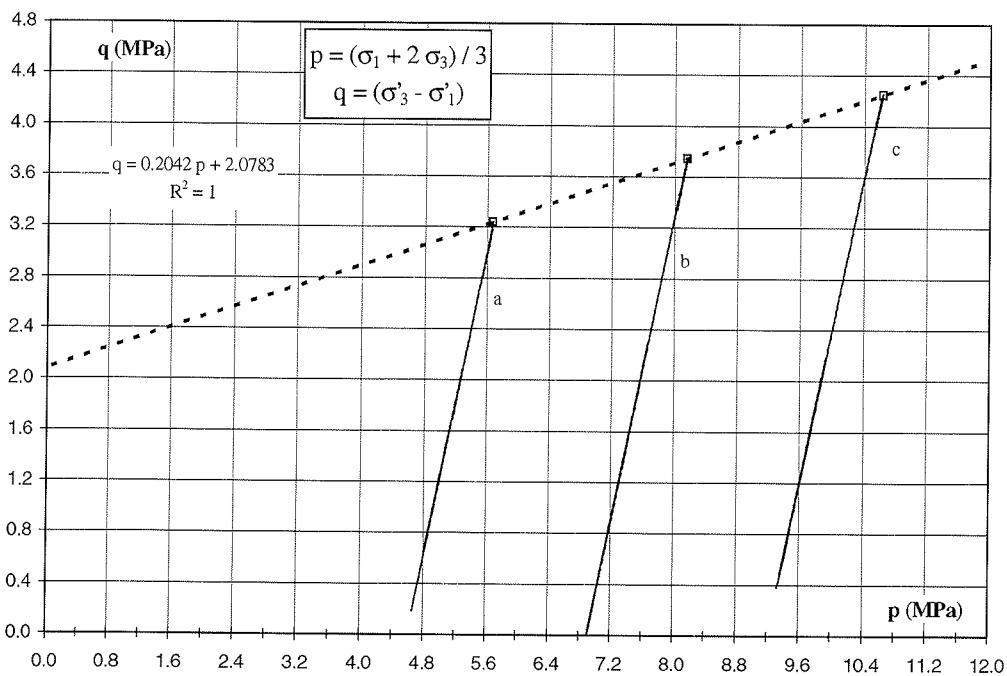


Figure B.11 Deviatoric stress versus the mean total stress for Blija (The Netherlands): 454.50 - 455.00 m (Case 1).

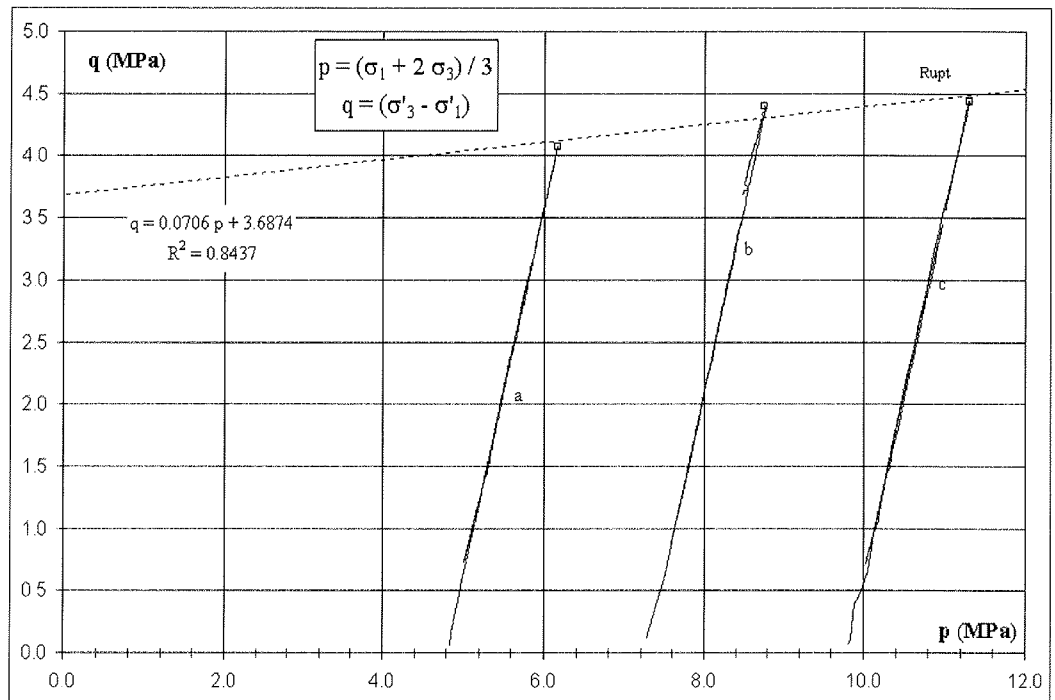


Figure B.12 Deviatoric stress versus the mean total stress for Blija (The Netherlands):
561.50 – 561.85 m (Case 3).

Appendix C Mineralogical analyses

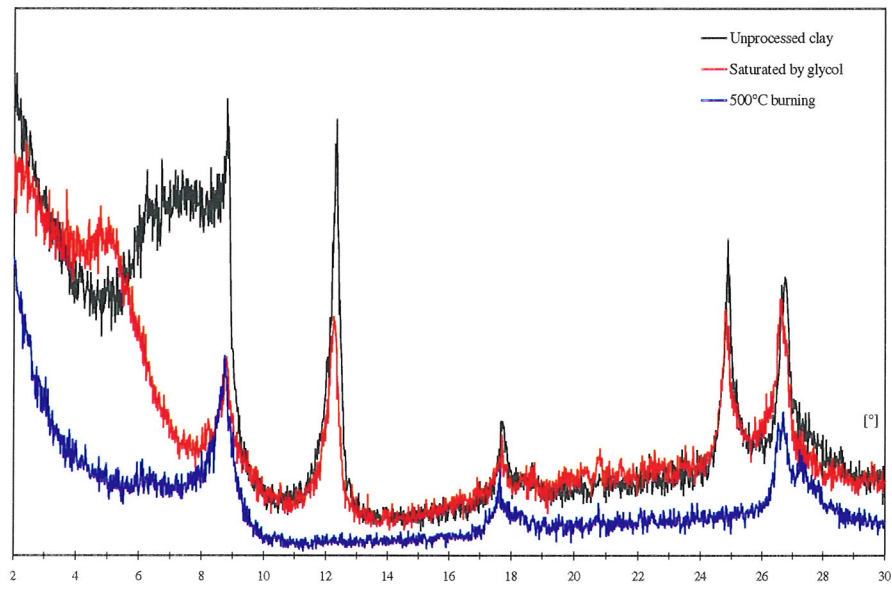


Figure C.1 Mineralogical analysis: Spectra on the clay for Weelde (B) - 313 m.

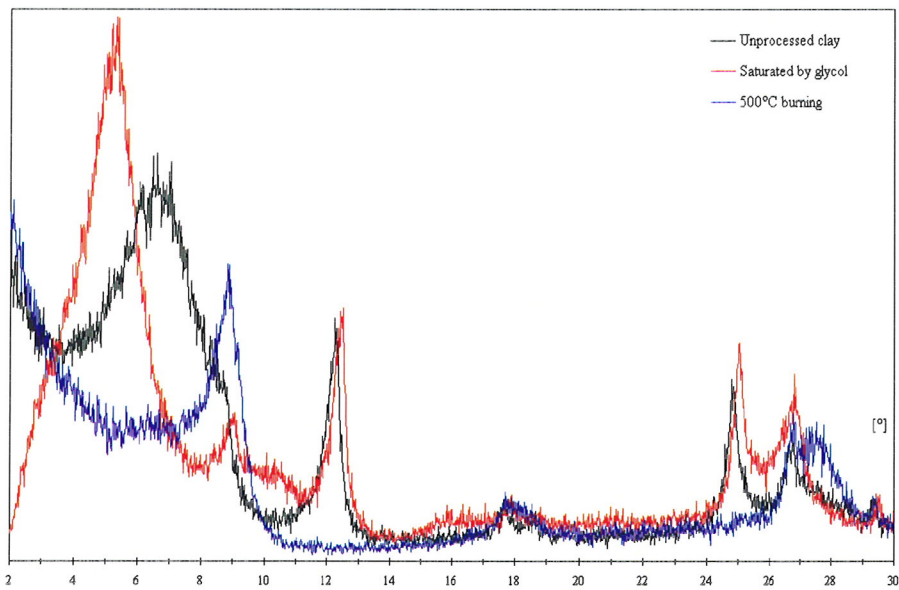


Figure C.2 Mineralogical analysis: Spectra on the clay for Blija (NL) - 561 m.

Appendix D Physical input parameters of METROPOL

Physics

PHYS1:

- PRESSR = $1 \cdot 10^{21}$ *i.e.* the reference pressure p_0 [kg/m/y²]; this is *c.* $1 \cdot 10^6$ Pa. The program will not use this value, see below under PHYS6.
- DENSR = $1 \cdot 10^3$ *i.e.* the reference density ρ_0 [kg/m³]; this value will not be used by the program, see below under PHYS6.
- COMPR = 0. *i.e.* the fluid compressibility β [m.y²/kg]; the program will not use this value, see below under PHYS6.
- GAMMA = 0. *i.e.* coefficient in density-salt mass fraction relation γ [1]; the program will not use this value, see below under PHYS6.

PHYS2:

The steady state pressure p [kg/m/y²] is put equal to the reference pressure p_0 , because there is no information available about this value after the hydromechanical calculations and because these values will not be used, since the porosity has been fixed during the simulation. The pressure could be used to define the actual porosity, see (2.5).

PHYS3:

The steady state mass salt mass fractions ω_s [1] is put to 0., since the influence of density effects are not considered in this study.

PHYS4:

The rock density ρ_r [kg/m³] is put to $2 \cdot 10^3$. This value will be used in the calculation of the retardation factor R [1], see (2.4).

PHYS5:

The rock compressibility C_r [m.y²/kg] is put to 0. This value will be used otherwise in the calculation of the porosity n [1], see (2.6).

PHYS6:

The reference porosity n_r [1] for all elements. For the aquitards (IP&LA, RU&AS, BRAVE) $n_r = 0.4$; for the aquifers (BRUS, VOORT, BRE_Z, OOST, HA&MA, KWAR) $n_r = 0.35$, for the bottom layer (MESOZ) $n_r = 0.2$, and for the fault ZONE_BR $n_r = 0.35$. These values will not be changed during the simulation time due to the choice of the rock compressibility $C_r = 0$. and due to the fact that the steady state pressure p equals the reference steady state p_0 in (2.6).

PHYS7:

The longitudinal dispersivity [m] is chosen to be 50 m for all elements. By this choice the Peclet number $P = \Delta x v/D \approx \Delta x v/\alpha_1 v = 2$, since the horizontal width of the elements is about 100 m around the release point of the nuclides.

This is a requirement to prevent numerical dispersion.

PHYS8:

The transversal dispersivity [m] is chosen to be 5 m for all elements.

PHYS9:

The molecular diffusion coefficient D_m [m²/y] is chosen to be $2 \cdot 10^{-10} \text{ m}^2/\text{s} = 6.3072 \cdot 10^{-3} \text{ m}^2/\text{y}$ for all elements; see Grupa & Houkema (2000; Table 3.4).